ABSTRACT

Title of Dissertation: IN OPERANDO MECHANISTIC STUDIES OF HETEROGENEOUS ELECTROCATALYSIS ON SOLID OXIDE ELECTROCHEMICAL CELL MATERIALS

Aaron Isaac Geller, Doctor of Philosophy, 2017

Directed by: Professor Bryan W. Eichhorn
Department of Chemistry and Biochemistry

This dissertation details the development and utilization of *in operando* protocols for observing electrochemical reactions on solid oxide electrochemical cells (SOCs) in order to better understand the fundamental chemistry governing their operation.

Two key reactions in SOC processes are studied using ambient pressure X-ray photoelectron spectroscopy (AP-XPS), the oxygen reduction and evolution reactions (ORR and OER). Measurements made on lanthanum strontium manganite ($La_{1-x}Sr_xMnO_{3\pm\partial}$, LSM), a standard electrode material show that the surface composition does not match the bulk stoichiometry. Sr extrudes onto the LSM surface in the form of SrO and greater Mn reduction is observed. These phenomena are further augmented by application of a cathodic bias (promoting ORR), while an anodic bias (promoting OER) results in the oxidation of Mn and no significant changes in Sr segregation.

Surface potentials on the LSM are measured to locate regions of electrochemical activity when promoting ORR and OER. These measurements yield *in operando* spectroscopic evidence that all electrochemical activity occurs at the electrode/electrolyte interface and that LSM is more electrocatalytically active toward ORR than OER.

We further compare surfaces between a pure LSM material and a composite of LSM and yttria-stabilized zirconia ($(ZrO_2)_{1-2x}(Y_2O_3)_x$, YSZ) in different gaseous environments which approximate standard operating conditions. The LSM/YSZ composite exhibits a larger concentration of surface oxygen vacancies in each environment allowing for greater oxygen reactivity.

A method for measuring surface Co oxidation states with XPS is explored. *In situ* thermal redox studies on cathode material, lanthanum cobaltite ($LaCoO_{3-\partial}$), show a potential correlation between Co reduction and the Auger parameter.

An *in operando* technique for monitoring SOCs with near infrared (NIR) imaging is presented. Ce oxidation states are tracked in an operating SOC using ceria (CeO_{2-x}) electrodes in studies analogous with previous AP-XPS research. However, the NIR experiments take place in fully ambient conditions as opposed to the model, near ambient conditions used in the AP-XPS experiments. Ce reduction is observed within an electrochemically active region commensurate with that found with AP-XPS, simultaneously supporting the use of NIR imaging for *in operando* studies on these SOCs, and the model AP-XPS experiments previously conducted.

IN OPERANDO MECHANISTIC STUDIES OF HETEROGENEOUS ELECTROCATALYSIS ON SOLID OXIDE ELECTROCHEMICAL CELL MATERIALS

by

Aaron Isaac Geller

Dissertation submitted to the Faculty of the Graduate School of the
University of Maryland, College Park in partial fulfillment
Of the requirements for the degree of
Doctor of Philosophy
2017

Advisory Committee:

Professor Bryan Eichhorn, Chair
Professor Sang Bok Lee
Professor Zhihong Nie
Professor Efrain Rodriguez
Professor Eric Wachsman

Acknowledgements

First and foremost, I must express my extreme gratitude to Professor Bryan Eichhorn for his constant support and mentorship throughout my Graduate School experience. Secondly, I must thank the members of the Eichhorn Research group that I have had the pleasure of working with throughout the years, Dr. Chunjuan Zhang, Dr. Yang Peng, Dr. Dennis Mayo, Dr. Domonique Downing, Dr. Christopher Sims, Dr. Yi Yu, Dr. Samantha DeCarlo, Dr. Hao Lei, Dr. Christopher Snyder, Dr. Junkai Hu, Dr. Yi Wang, Dr. Angelique Jarry, Jonathan Senn, Kim Huynh, Lauren Stevens, Luning Wang, Noah Masika, Cody Sherlock, Sarah Gibbons, and Aviva Mazurek. A special thanks must be made to members who have contributed directly to my project, Dr. Chunjuan Zhang, Dr. Yi Yu, Dr. Angelique Jarry, and Luning Wang; particularly Dr. Yi Yu for her role in my mentorship.

I am also thankful to members of the University of Maryland without whom I could not have completed my work: Dr. Karen Gaskell for her constant input on data analysis, experimental plans, and sample characterization. Dr. Yi-lin Huang and Dr. Christopher Pelligrinelli for their collaborative efforts and Dr. Xiaohong Zhang and Yangang Liang for sample preparation. I also thank Professors Robert Walker, Ross Salawich, and Alice Mignerey, for playing a strong role in my coming to the University, and their continued guidance from then on. Finally, I thank my committee, Professors Sang Bok Lee, Zhihong Nie, Efrain Rodriguez, and Eric Wachsman.

My work also consisted of collaborations outside of the University of

Maryland. I am grateful to researchers at the Advance Light Source in the Lawrence Berkeley National Laboratory, Dr. Ethan Crumlin, Dr. Hendrik Bluhm, and Dr. Zhi Liu without whom I could not have run the majority of experiments presented in this work. This work also owes a debt of gratitude to Dr. Jefferey Owrutsky, Dr. Michael Pomfret, and Dr. Daniel Steinhurst at the Naval Research Laboratory.

Lastly I thank my sources of funding, the Office of Naval Research and the US Department of Education.

Table of Contents

List of Figures

List of Tables

List of Abbreviations

A	Area of sample under study with XPS
A	Absorbance
AFC	Alkaline fuel cells
Al_2O_3	Alumina
ALS	Advanced light source
AP	Auger parameter
AP-XPS	Ambient pressure x-ray photoelectron spectroscopy
BE	Binding energy
CCD	Charged couple device
CE	Counter electrode
$CeO_{(2-x)}$	Ceria
cps	Counts per second
DMFC	Direct methanol fuel cell
$E^{(o)}$	Electromotive Force (o = at standard conditions)
E_o	Edge (in NEXAFS scans)
E/R	Emissive and reflective
EC	Electrolyzer cell
EELS	Electron energy loss spectroscopy
E_F	Fermi Level
EIS	Electrochemical impedance spectroscopy
EMF	Electromotive Force
E_{vac}	Vacuum level

EXAFS	Extended X-ray absorption fine structure
f	Photon flux
F	Faraday's Constant (96485 C/ mol e^-)
FC	Fuel Cell
FWHM	Full width half maximum
ΔG	Gibbs Free Energy change
GDC	Gadolinium-doped ceria
HT	High Temperature
$h\nu$	Photon energy
I or i	Electrical current
I	Intensity
ICE	Internal Combustion Engine
IMFP	Inelastic mean free path
IT	Intermediate temperature
IT-SOFC	Intermediate temperature solid oxide fuel cell
j	Spin+orbit quantum number
j	Electrical current density
KE	Kinetic energy
l	Angular momentum quantum number
LINAC	Linear accelerator
LBNL	Lawrence Berkeley National Laboratory
LSC	Lanthanum strontium cobaltite ($La_{1-x}Sr_x\ CoO_{3-\partial}$)
LSCF	Lanthanum strontium cobalt ferrite ($La_{1-x}Sr_xCo_{1-y}Fe_yO_{3-\partial}$)

LSM	Lanthanum strontium manganite ($_{La1-x}Sr_xMnO_{3\pm\partial}$)
LSV	Linear sweep voltammetry
LT	Low Temperature
MCFC	Molten carbonate fuel cell
MIEC	Mixed ionic/electronic conductor
MS	Mass spectrometry
n	Number of atoms/cm^3
n	Moles (of electrons)
NEXAFS	Near edge X-ray absorption fine structure
NIR	Near infrared
NRL	Naval Research Laboratory
OCV	Open circuit voltage
OER	Oxygen evolution reaction
ORR	Oxygen reduction reaction
OSC	Oxygen storage capacity
PAFC	Phosphoric acid fuel cell
PEMEC	Proton exchange membrane electrolyzer cells
PEMFC	Proton exchange membrane fuel cells
PEY	Partial electron yield
PLD	Pulsed laser deposition
R	Conduction resistance
R	Universal Gas Constant (8.314 J/ mol * K)
R	Reflectance (NIR radiation)

R_a	Intra-atomic relaxation energy
R_a	Intra-atomic relaxation energy
R_B	Bulk resistance
R_{CT}	Charge transfer resistance
RP	Ruddlesden-Popper
rr	Ramp rate
rt	Room temperature
s	Spin quantum number
s	Sensitivity factor for XPS atomic measurements
S (unit)	Siemens (Ω^{-1})
S	Vacant surface site
ΔS	Entropy change
SOC	Solid oxide electrochemical cell
SOEC	Solid oxide electrolyzer cell
SOFC	Solid oxide fuel cell
T	Temperature
T	Detection efficiency for electrons in spectrometer
T	Transmittance (NIR radiation)
TEC	Thermal expansion coefficient
TEY	Total electron yield
TGA	Thermogravimetric analysis
TPB	Three-phase boundary
UHV	Ultra high vacuum

V	Cell voltage
V_L	Local surface potential
V_o	Oxygen Vacancy
$w_{el,\ max}$	Maximum electrical work possible
WE	Working electrode
XAS	X-ray absorption spectroscopy
XPS	X-ray photoelectron spectroscopy
XRD	X-ray powder Diffraction
XRR	X-ray reflectivity
Y_2O_3	Yttria
YSZ	Yttria-stabilized zirconia
Z	Nuclear charge
ZrO_2	Zirconia
α	Auger parameter
α'	Modified Auger parameter
ε	Emissivity
ε_F	Hartree-Fock calculated energy
λ	Inelastic mean free path
η_{an}	Anodic overpotential / polarization loss
η_{cath}	Cathodic overpotential / polarization loss
η_{ohm}	Ohmic overpotential / polarization loss
Ψ	Charging
Φ	Workfunction

Ω (unit)	Ohm
θ	Angular efficiencies of spectrophotometer
γ	Efficiency of photoelectric process
σ	Photoionization cross sections

1 Introduction

1.1 General Introduction

The oxygen reduction reaction (ORR, see forward R1.1) is a crucial reaction for the current technological demands of society. The reaction simply consists of the reduction of oxygen gas into oxide ions and yet it impacts energy storage (metal air batteries), automotive and medical applications (oxygen sensors), or the utilization of alternative fuels like hydrogen (solid oxide electrochemical cells, SOCs). For example, ORR tends to be the rate-limiting step in SOC processes,[1-5] making optimization of cathode materials toward ORR essential. Despite the reaction's simplicity and importance, very little is understood about the ORR mechanism on different materials due to typical high operating temperatures (T > 600 ^{o}C)[6,7] and gaseous environments that preclude standard high vacuum characterization techniques[8,9] (e.g. X-ray photoelectron spectroscopy, XPS).

$O_{2(g)} + 4e^{-} \rightleftharpoons 2O^{2-}_{(lat)}$ (**R1.1** ORR fwd and OER rev)

where $O^{2-}_{(lat)}$ represents an oxide ion in the lattice of a SOC component (*e.g.* cathode, electrolyte).

Likewise, the oxygen evolution reaction (OER, the reverse of R1.1,) is also not well understood despite being critical toward a SOC's ability to produce hydrogen, which could then be used as a fuel, or for industrial purposes such as the production of ammonia[10] or organic compounds (*e.g.* aldehydes and ketones).[11,12]

Most studies on both ORR and OER have consisted of either *ex situ* characterizations on relevant electrocatalysts (*i.e.* catalytic electrodes), or *in operando* studies (*i.e.* studies on an operating SOC) employing electrochemical performance tests.[13-22] These performance tests typically involve changing system parameters (*e.g*. electrode thickness, operating temperature) and measuring changes in electrochemical characteristics such as polarization losses (*i.e.* overpotentials) or resistances. While *ex situ* characterizations provide some information regarding overall changes experienced by the SOC, they do not capture the nature of the materials under *in situ* conditions (*i.e.* at temperature, in appropriate atmospheres, but *not* in operation), let alone the far-from-equilibrium conditions they are subjected to when operating. The *in operando* performance tests may help to improve material performance, but do not necessarily give insight into what mechanistic details allow for those improvements. Several other techniques have been used for *in operando* studies, such as ambient pressure X-ray photoelectron spectroscopy (AP-XPS),[23-29] near infrared (NIR) imaging,[30-38] and isotopic exchange labeling,[39-42] to provide more fundamental details.

This dissertation describes the development of *in operando* protocols for elucidating mechanistic details (*e.g.* electrode oxidation states, regions of electrochemical activity) regarding ORR and OER on common SOC materials: lanthanum strontium manganite (LSM), lanthanum strontium cobaltite (LSC), and ceria. In the remainder of this chapter, the operational principles of SOCs and relevant materials are discussed, followed by more specific details on ORR and OER, and finally a description of the *in operando* techniques used.

1.2 Solid Oxide Electrochemical Cells

A simple SOC consists of the three components common to all electrochemical cells, a cathode, an anode, and an electrolyte (this work does not consider interconnects). The electrolyte is solid and conducts oxide ions, a process which has a high activation barrier necessitating high operational temperatures (> 800 ^{o}C, conventionally).

If the SOC is run in a spontaneous direction (galvanic), it behaves as a solid oxide fuel cell (SOFC), whereas if it is run in the opposite direction (electrolytic) it behaves as a solid oxide electrolyzer cell (SOEC). As such, sometimes the terms "fuel cell mode" and "electrolyzer cell mode" may be used to distinguish SOC operation. Sections 1.2.1 and 1.2.2 will show that a clear distinction between the two modes is that fuel cell mode involves the promotion of ORR while electrolyzer mode promotes OER.

1.2.1 Solid Oxide Fuel Cells

1.2.1.1 General Information

A fuel cell (FC) is an electrical energy conversion device that converts chemical energy directly into electrical energy, unlike an internal combustion engine (ICE) which requires an intermediate step in which chemical energy is first converted into heat and then into mechanical energy.[43,44] SOFC efficiency is generally higher, as SOFCs are not subject to an engine's carnot limitations.[44,45]

The FC works by oxidizing a fuel, with a concurrent reduction of an oxidant. The fuel and oxidant gases are in compartments separated by an electrolyte. The identity of the ions conducted through an electrolyte and its phase defines the FC.

Presently there are six types of FCs, alkaline fuel cells (AFCs), proton exchange membrane fuel cells (PEMFCs), direct methanol fuel cells (DMFC), phosphoric acid fuel cells (PAFC), molten carbonate fuel cells (MCFCs), and SOFCs.

These FCs can largely be divided into two categories, low temperature (LT) and high temperature (HT). LT-FCs (AFC, PEMFC, PAFC) suffer from numerous disadvantages compared to their HT counterparts. The low temperature necessitates the use of H_2 as a fuel[44,46] and noble metal electrocatalysts (namely, Pt) to achieve acceptable kinetics.[44,47] Aside from being expensive and rare, Pt is susceptible to CO poisoning such that the hydrogen, which is likely produced from steam reforming, must be very pure.[7,47]

A SOFC is attractive because high operating temperatures mitigate these problems. At high temperatures, relatively inexpensive electrocatalysts that are less sensitive to impurities than Pt may be used.[43,44] The high temperature also lowers polarization losses[44] (see Section 1.2.1.2) and the energy conversion efficiencies are much higher than LT counterparts, especially if generated waste heat is harnessed for combined heat and power or gas turbine applications.[45] Indeed, Figure 1.1[46,48] shows that SOFCs can generate more power for a given mass or volume than many energy production devices including other FCs and ICEs.

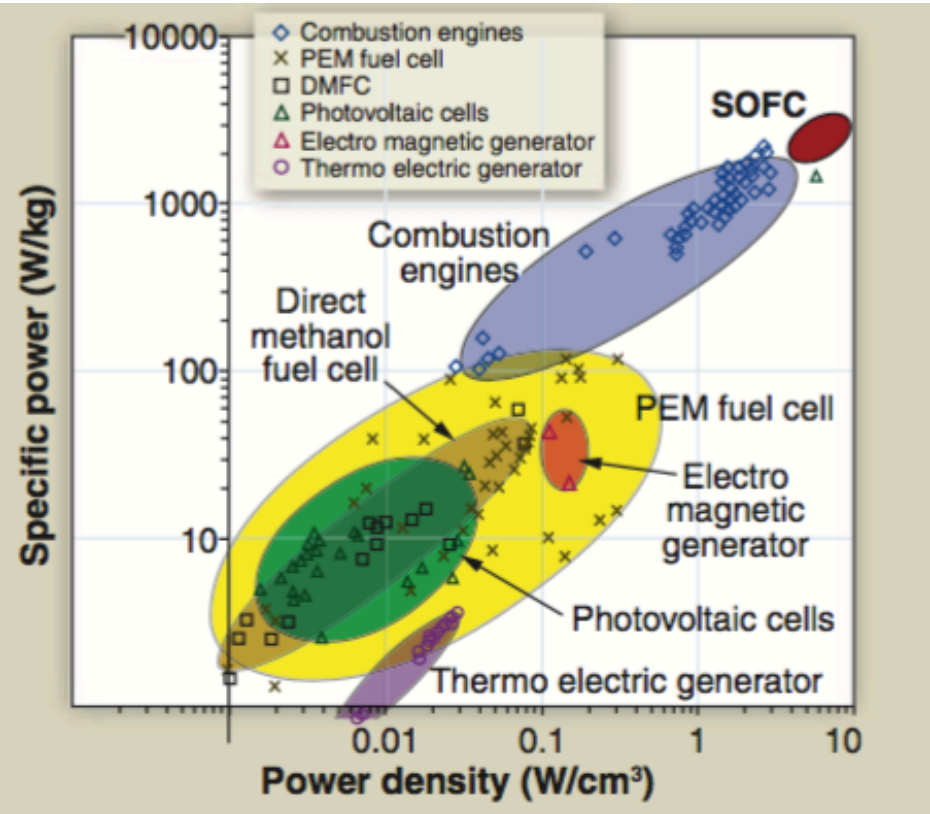

Figure 1.1.[46,48] Specific power vs. power density of various energy conversion devices.

Another advantage of high temperature operation is the allowance for more fuel options than just H_2.[7] While H_2 has the potential to be a "clean" fuel, the ability to use other fuels such as standard hydrocarbons, as shown by Gorte *et al.* and other research groups,[49-52] makes SOFCs more amenable to the current infrastructure and energy sources.

1.2.1.2 Basic Electrochemical and Operational Principles

Figure 1.2 shows a schematic of a simple SOFC in operation using H_2 as a fuel. O_2 gas is reduced at a cathode forming oxide ions which then travel through the electrolyte to the anode. At the anode, the O^{2-} reacts with $H_{2(g)}$ fuel and forms the oxidized product, $H_2O_{(g)}$. The anode reaction liberates electrons which can then flow through the circuit for electrical work.

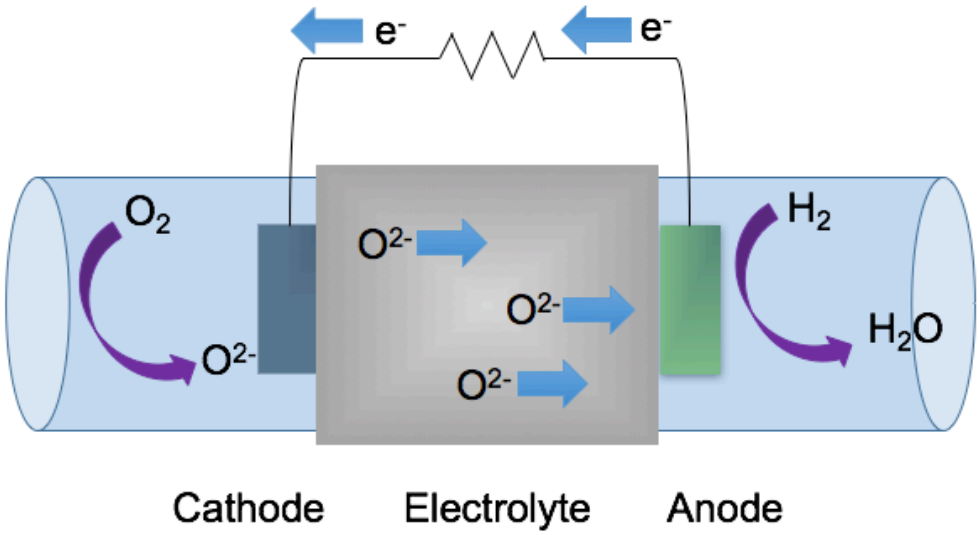

Figure 1.2. Schematic of SOFC operation. O_2 oxidant and H_2 fuel are separated from each other by a solid oxide conducting electrolyte. At the cathode, O_2 is reduced to O^{2-} ions which are drawn to the anode where they oxidize H_2, producing H_2O and electrical current.

Thermodynamic principles can be used to determine the maximum electrical work that can be done by a SOFC. Recognizing that Gibbs Free Energy is equal to the maximum energy available for electrical work at constant temperature and pressure, the following relationship can be determined:

$$w_{el,\,max} = \Delta G = \Delta H - T\Delta S \qquad \textbf{(Eq. 1.1)}$$

where $w_{el,\,max}$ is the maximum electrical energy available for work, ΔG is the change in Gibbs Free Energy, ΔH is the change in enthalpy, T is the temperature, and ΔS is the change in entropy. The total thermal energy available is ΔH, while $T\Delta S$ represents the portion that is unavailable for electrical work. ΔG can also be related to the electromotive force (EMF) between species:

$$-\Delta G = nFE \quad \textbf{(Eq. 1.2)}$$

where n represents the number of electrons transferred in the reaction, F is Faraday's Constant (96,485 C/mol e^-), and E represents the EMF. The EMF that exists between the cathode and anode (which sets the maximum performance of the SOFC[44] as will be discussed below) can also be described as the ideal open circuit voltage (OCV). Recognizing that the two half reactions are:

$$O_{2(g)} + 4e^- \longrightarrow 2O^{2-}_{(lat)} \quad \textbf{(R1.2} \text{ cathode, ORR)}$$

$$2H_{2(g)} + 2O^{2-}_{(lat)} \longrightarrow 2H_2O_{(g)} + 4e^- \quad \textbf{(R1.3}, \text{ anode, } H_2 \text{ electrooxidation)}$$

the two reactions can be summed up to:

$$2H_{2(g)} + O_{2(g)} \longrightarrow 2H_2O_{(g)} \quad \textbf{(R1.4)}$$

The OCV value of R1.4 at operating temperatures and standard partial pressures, *i.e.* E^o, can then be calculated from Eq. 1.2 (typically ~1.1 V).[53,54] The OCV under non-standard partial pressures can be determined from the Nernst Equation:

$$E = E^o + \frac{RT}{4F}\ln\left(\frac{p^2_{H_2,anode}\, p_{O_2,cathode}}{p^2_{H_2O,anode}}\right) \quad \textbf{(Eq. 1.3)}$$

where E is EMF under non-standard pressures, R is the universal gas constant, T is the temperature, 4 is the number of electrons transferred in the reaction, and the p terms are the partial pressures of each gas at their respective electrodes.

Ideally, a SOFC can draw current and the E value would remain stable meaning the power generated by the SOFC would increase linearly with current (P = iV, where i is the current and V equals E). In reality the cell voltage, *i.e.* available electrical energy, is less than the calculated E value due to "polarization losses." These losses are from three contributors, activation polarization, ohmic polarization, and concentration polarization, and each type of loss (described below) dominates at different current regimes as shown in Figure 1.3.[44]

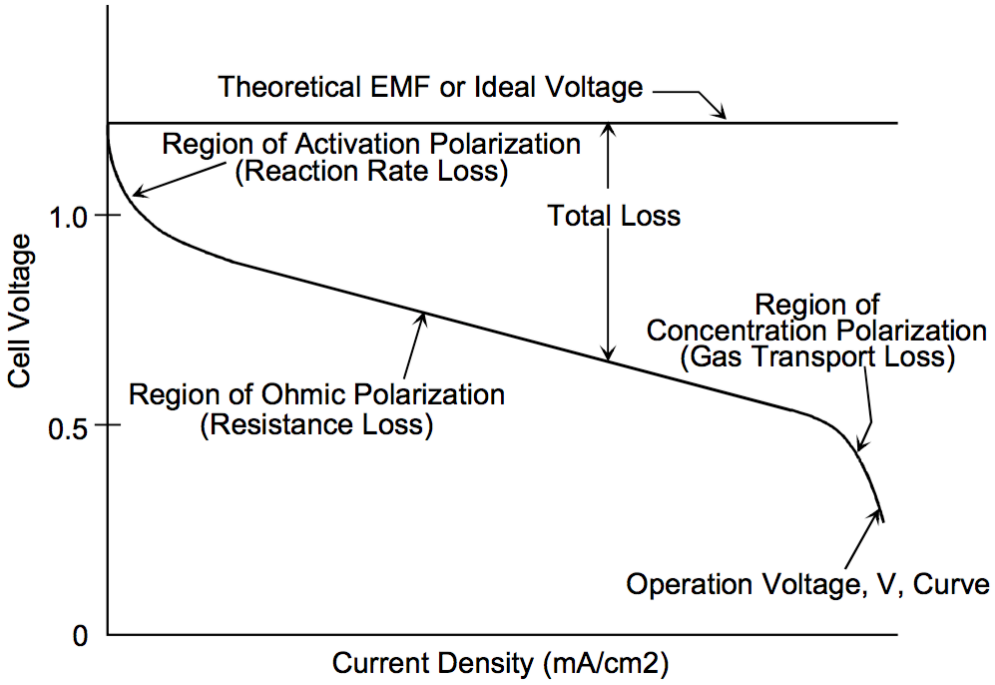

Figure 1.3.[44] A typical FC V-I curve, in which Cell Voltage is plotted against Current Density. The flat line at ~1.1 V represents the ideal voltage, *i.e.* the OCV value determined from Eq. 1.3 at some temperature. As current is drawn, this voltage decreases from polarization losses with different contributors dominating at different currents.

Activation losses: losses related to electrode kinetics. The activation energy of rate-limiting steps in each half-reaction largely determines the magnitude of activation losses. These losses are mostly unaffected by the current drawn.

Ohmic losses: losses related to the resistance of electronic and ionic conduction through the electrodes and electrolyte, respectively. These losses obey Ohm's law:

$$\eta_{ohm} = iR \qquad \textbf{(Eq. 1.4)}$$

where η_{ohm} is the ohmic polarization loss, i is the current drawn, and R is the conduction resistance. In planar SOFCs, the ionic resistance usually dominates.[44] As can be seen from Eq. 1.4 and Figure 1.3, the ohmic loss scales linearly with current, assuming a constant R.

Mass Transport-Related (Concentration) Losses: at high currents, a concentration gradient is produced by the rapid conversion of reactant to products, and mass transport rates limit the replenishment of reactant (or removal of the product).

The effect of these losses on the ideal cell voltage (E) can be described by[43,44,53]:

$$V = E - iR - \eta_{cath} - \eta_{an} \qquad \textbf{(Eq. 1.5)}$$

where V represents that actual cell voltage, iR represents the ohmic loss, and η_{cath}

and η_{an} represent the sum of activation and concentration losses at the cathode and anode, respectively. When the cell is polarized to draw current, the available energy for electrical work is reduced, as is the power. Understanding the reaction mechanisms and components can help to understand the origin of these voltage losses better, particularly the activation losses (which are usually larger at the cathode).

1.2.1.3 Components

In this section, general requirements for suitable materials followed by specific material information for each of the three major SOC components are described. Several key criteria shared between all three parts are: good compatibility between components in contact with each other (*i.e.* low reactivity and similar thermal expansion coefficients, TECs), stability in the atmospheres that the parts are exposed to, and low cost of materials.[7,43,44,55] The electrolyte in particular must be considered carefully as it is in contact with both electrodes and their atmospheres and will largely dictate the electrode materials and performance of the SOFC.[56]

Electrolytes:

The electrolyte is the primary contributor to ohmic polarization losses from their internal resistance of ionic conductivity. Good electrolytes should possess the following characteristics: good oxide ion conductivity ($>10^{-2}$ S/cm)[57] but negligible electron conductivity,[58] high density to prevent gas permeation, and thermodynamic stability at high operating temperatures and different O_2 partial

pressures. Electrolytes are typically fluorite or perovskite structures;[59,60] the most commonly used being yttria-stabilized zirconia (YSZ, $(Y_2O_3)_x(ZrO_2)_{1-x}$).

YSZ: YSZ is zirconia (ZrO_2) material that has been doped with yttria (Y_2O_3). The structure may be seen in Figure 1.4.[61] The purpose of the doping is two-fold, the first being structure-related as pure ZrO_2 is monoclinic at typical operating temperatures,[61] while doping stabilizes the more conductive cubic fluorite phase at ~8 mol % yttria doping.[7,56] The second purpose is to introduce "oxygen vacancies" (V_o) which are spaces in the lattice that can accommodate an oxide ion, which increases oxide ion conductivity.[47,53,58] The vacancies are formed to preserve charge neutrality. However, as can be seen in Figure 1.5,[58] which shows how conductivity of ZrO_2 system changes as a function of doping, the conductivity decreases if more than 8 mol% yttria is used, potentially due to defect ordering, vacancy clustering, or electrostatic interactions.[7,58,62]

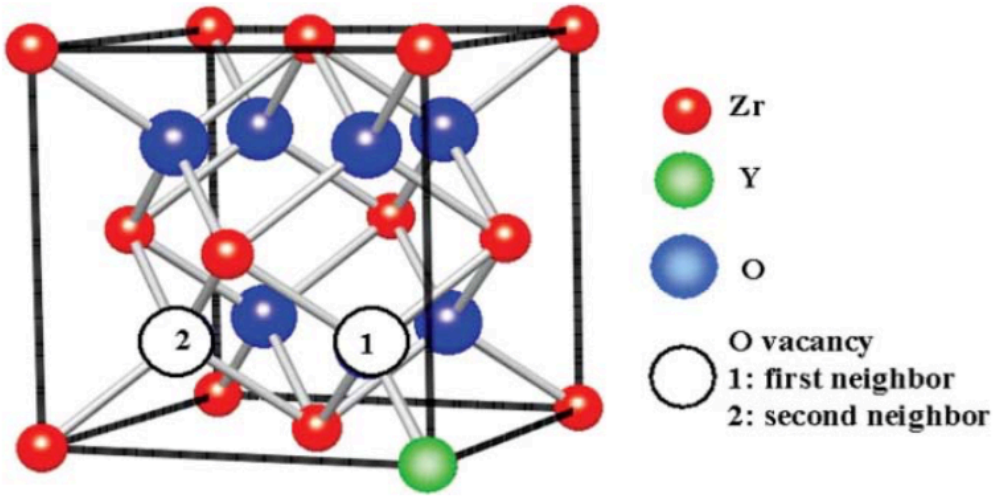

Figure 1.4.[61] YSZ unit cell. The material is a cubic fluorite structure in which some % of Zr sites are doped with Y introducing oxygen vacancies for charge neutrality.

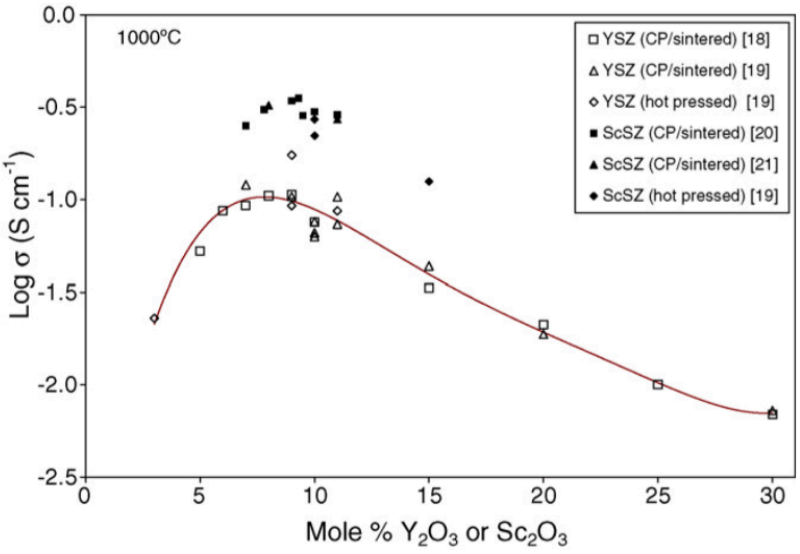

Figure 1.5.[58] Log of oxide ion conductivity as a function of mol % of dopants, Y_2O_3 (open symbols) and Sc_2O_3 (closed symbols), from various studies at 1000 °C. A red trendline is given for Y_2O_3 doping.

It is worth noting that Figure 1.5 shows a higher conductivity when Sc_2O_3 is used as a dopant instead of Y_2O_3. This is attributed to the smaller mismatch in size between Zr^{4+} (72 pm) and Sc^{3+} (74.5 pm),[47,58,63] which lowers the defect formation energy. Increased defects allow for more conductivity, however, the material is not as stable[58] and is far more expensive than YSZ.[47]

Alternate Materials: There is interest in developing new electrolytes that give superior ionic conductivity to YSZ, particularly at intermediate temperatures (IT, 500 – 800 °C). Reducing the operating temperature lowers the constraints on materials selection with regards to TEC compatibility and durability.[44] This materials flexibility not only allows for more conductive and electrocatalytically SOC electrodes and electrolytes to be used (as detailed below), but also allows for stainless steel SOFC casing and interconnects,[64-66] which is much more cost-

effective than using typical ceramics. Figure 1.6[46] shows several popular materials under investigation.

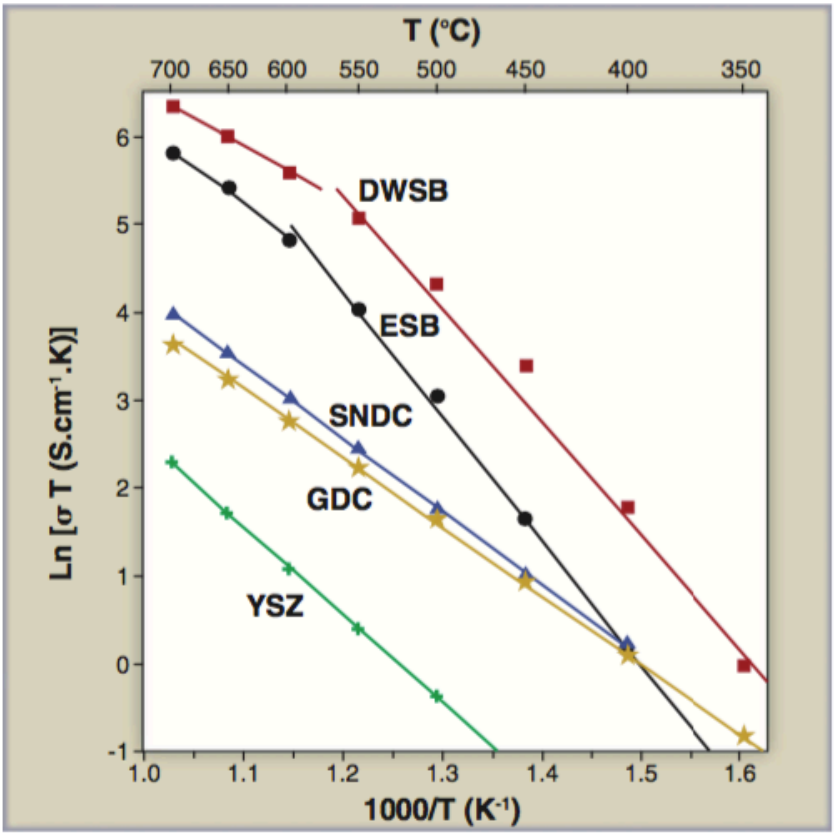

Figure 1.6.[46] Various solid oxide conducting electrolytes' conductivity relationship to temperature.

Gadolinium-doped ceria (GDC) has gained a substantial amount of interest. Ceria (CeO_{2-x}, where x is a measure of oxygen deficiency) has a fluorite structure like YSZ and oxygen vacancies are introduced by substituting Ce^{4+} with divalent alkaline earth or trivalent rare earth ions[67] (**(**Gd^{3+} is closest in size to the Ce^{4+} with ionic radii of 93.5 pm and 87 pm, respectively).[63,68] GDC's greater conductivity compared to YSZ is attributed to the larger ionic radius of Ce^{4+} as compared to Zr^{4+}, which results in larger oxygen channels for conducting oxide ions.[53] However, the stability of ceria in low oxygen partial pressures at the anode side of the SOFC is

inferior.[58,69,70] This is due to the reduction of Ce^{4+} to Ce^{3+} leading to both an expansion of the GDC lattice and an electronic leakage current,[7,46,47,53,71] decreasing the OCV.

Cathodes:

Development of the cathode materials is particularly important because the relevant reaction, ORR, is the rate-limiting step of SOFC processes[1-5] (further details in Section 1.3.1).

Electrodes can be grouped into two types of conductors, electronic conductors and mixed ionic/electronic conductors (MIEC). While both are capable of conducting electrons, only MIEC materials can conduct ions appreciably (due to ion vacancies in the material). The type of conductor determines the importance of three phase boundaries (TPBs), which are interfaces at which the gas, electrolyte, and electrode meet. The importance can be understood by considering Figure 1.7A, which shows ORR on an electronic conductor. $O_{2(g)}$ is adsorbed on the cathode where it is reduced into O^{2-}, and is then incorporated into the electrolyte. In this case, all three phases of the TPB must be present for ORR and the "surface path" is predominantly followed.[43,53,72] But if the cathode is a MIEC, O^{2-} ions can be incorporated directly into the cathode itself, and then move toward the electrolyte. In this case, the gas/cathode interface is acceptable for ORR to occur and the "bulk path" is followed as shown in Figure 1.7B. As such, MIECs have significantly larger active surface areas than electronic conductors.

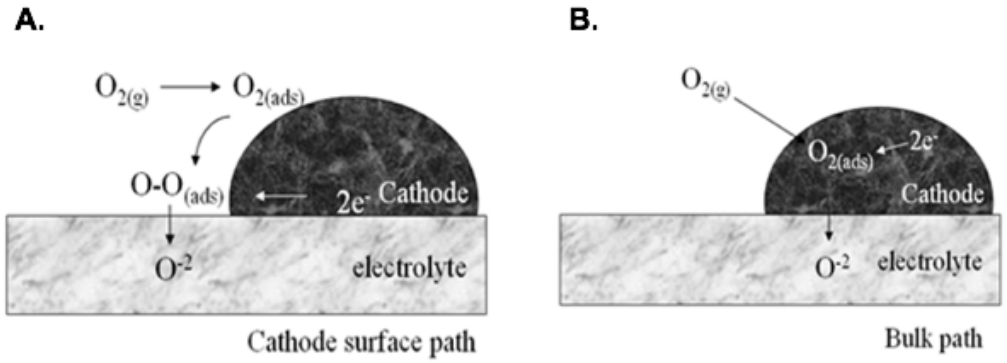

Figure 1.7.[43,72] (A) ORR behavior of an electronic conductor. $O_{2(g)}$ molecules adsorb to the surface of the cathode and migrate to the TPB, where electrons reduce the O_2 and the O^{2-} ions can be incorporated into the electrolyte. (B) ORR behavior of a MIEC in which the adsorbed O_2 can be reduced at the cathode/gas interface and directly incorporate into the cathode and then travel to the electrolyte.

A cathode must thus possess adequate porosity[7,44,53,55] at operating temperatures (~30-40%) to allow oxygen diffusion to TPBs or a large TPB (especially in an electron conducting material). Other requirements include high electrocatalytic activity for ORR, good adhesion to the electrolyte and high electronic conductivity.[44,53,55]

In early SOFC development, noble metals (particularly Pt) were used[73,74,75] but were chemically and physical unstable and incompatible with most electrolytes.[7,44] Furthermore due to the rarity and high cost of Pt, metal oxide materials have been studied for their potential use as cathodes.[76,77] The most promising of these oxides are perovskites such as, lanthanum strontium cobaltite (LSC), which was studied by Button and Archer and was among the first perovskite-cathodes to be reported.[73,78] The most commonly used perovskite cathode at high temperatures is lanthanum strontium manganite (LSM), an

electronic conductor, due to its similar TEC with a YSZ electrolyte, high electron conductivity, and good electrocatalytic activity for ORR.[44,56,79-81]

LSM Perovskite Cathode: The ideal perovskite structure is shown in Figure 1.8.[82] The structure has an ABO_3 formula where larger rare earth ions (*e.g.* La) typically occupy the A-site and smaller transition metals (*e.g.* Mn) occupy the B-site. The ions are arranged in a cubic unit cell in which the A-site cation is coordinated to 12 oxide ions and the B-site cation is octahedrally-coordinated by the oxide ions.[53,55,81,83]

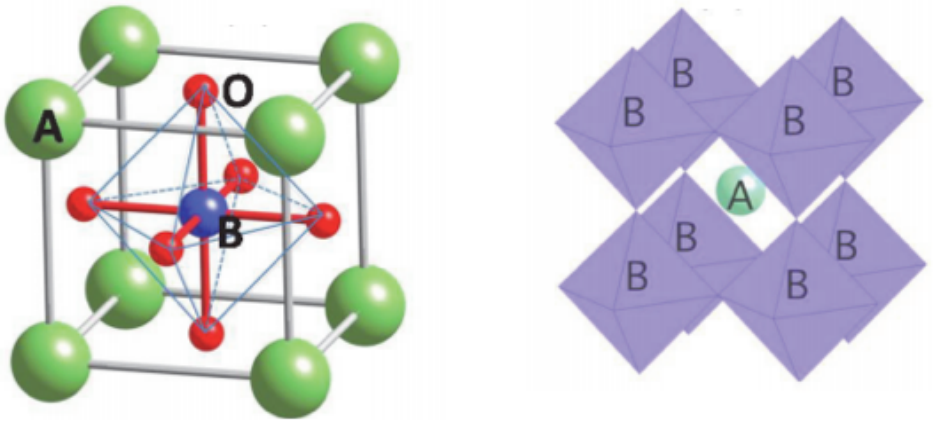

Figure 1.8.[82] Perovskite structures from the perspective of (Left) B-site ion in the center and (Right) A-site ion in the center.

LSM has the formula, $La_{1-x}Sr_xMnO_{3\pm\partial}$, in which the A-site La is doped by Sr by the amount "x," and the ∂ symbol represents an oxygen "excess" or deficiency. The "excess" oxygen phase ($\partial > 0$) was proven by neutron powder diffraction, high-resolution transmission electron microscopy,[21,83-87] and thermodynamic modeling studies[21,88,89] to be a Schottky-type disorder,[90] in which cation vacancies are formed, rather than an actual oxygen excess. When LSM is O-deficient ($\partial < 0$), oxygen vacancies are formed, increasing ionic conductivity in the

material. Whether LSM is in an oxygen "excess" or deficient regime is based on temperature and oxygen partial pressure, as determined by Mizusaki *et al.*[91] (see Figure 1.9).

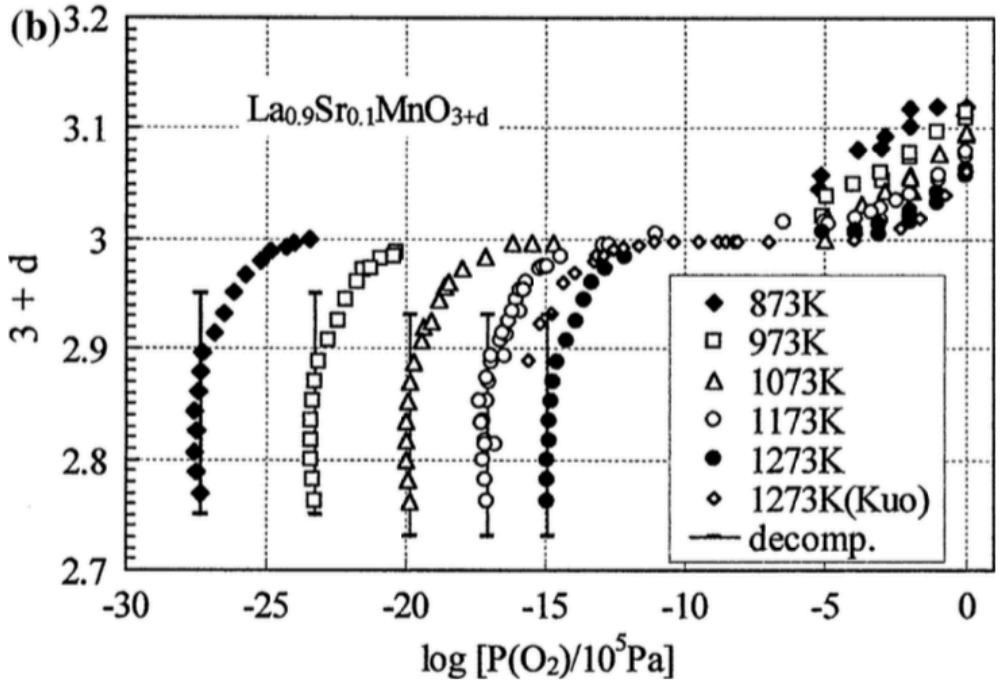

Figure 1.9.[91] 3± ∂ values of LSM (10 mol% Sr doping) as a function of log O_2 partial pressure at different temperatures.

Sr doping of the La site is done to enhance both electrical conductivity[83,92] and catalytic activity[21,83] of lanthanum manganite. Sr has some effect on phase behavior between 20-30% mol doping as shown by Zheng *et al.*[93] who observed a monoclinic structure at those levels. The primary Sr-doping induced change is an increase in electrical conductivity up to 50 mol % Sr doping (*i.e.* x = 0.5), in 1 bar O_2, as shown by Mizusaki *et al.*[92] (Figure 1.10). This enhancement is due to an increase in Mn oxidation state, *i.e.* "electron holes". While any divalent ion can be used in place of Sr for this effect, Sr forms stable compounds with lanthanum

manganite that have high conductivity in the oxidizing atmosphere found in SOFC cathode conditions.[94,95]

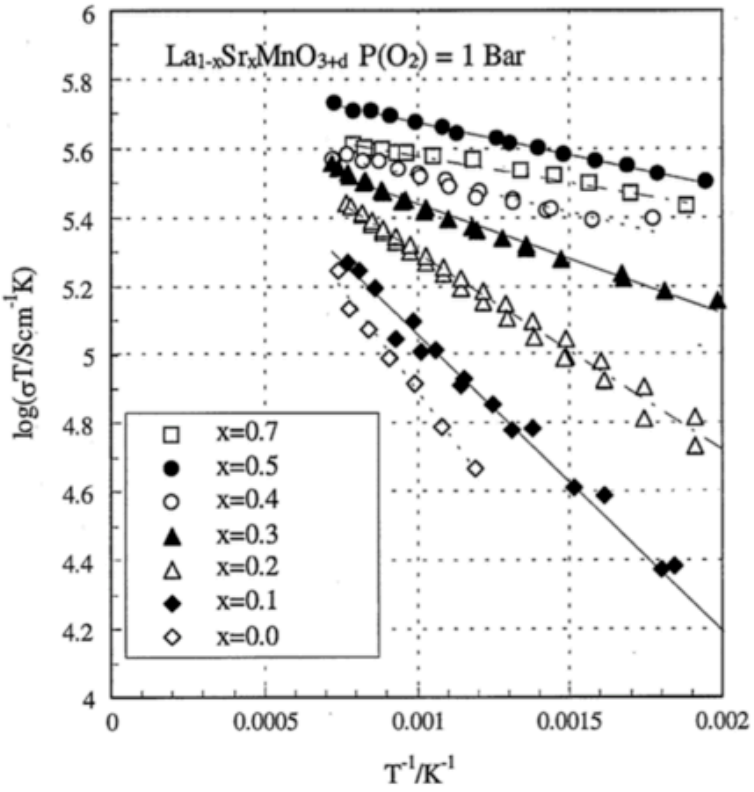

Figure 1.10.[92] Measure of electronic conductivity (σ) as a function of inverse temperature at various Sr doping levels (x).

Studies by Jiang *et al.*[96] (Figure 1.11) show a decrease in electrical current (or an increase in polarization losses) at lower temperatures, likely due to lower oxygen vacancy (V_o) content (see Figure 1.9), as electrocatalytic behavior under high cathodic polarization (*i.e.* bias or applied voltage) is correlated with oxygen vacancy generation at the electrode surface.[21,97-99] In essence, if the LSM cannot effectively incorporate or allow for mobility of oxide ions in the lattice, then the kinetics of ORR are sluggish. Poor kinetics will result in higher activation polarization losses (see Section 1.2.1.2) resulting in a lower electrical current

generation. As such, LSM is not a suitable material for intermediate temperature-SOFC (IT-SOFC) interests. This problem can be mitigated by forming a composite material of LSM and YSZ, which increases the presence of TPBs[56] and increases ionic conductivity via the oxygen vacancies from the YSZ.[44,100,101] Other perovskites may exhibit higher conductivity than LSM (see Figure 1.12[97]), although stability is an issue.

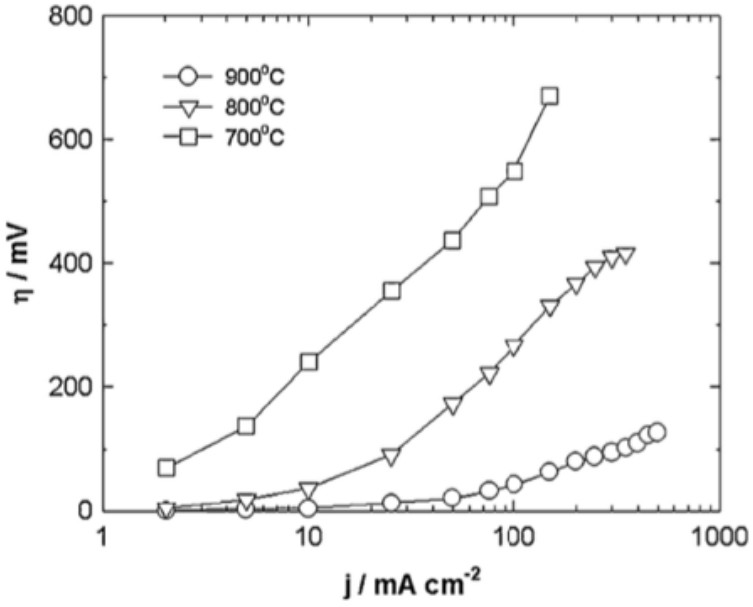

Figure 1.11.[96] Overpotential (*i.e.* polarization losses) as a function of current densities at 900 °C, 800 °C, and 700 °C. At lower temperatures, the overpotential increases with a concurrent decrease in current.

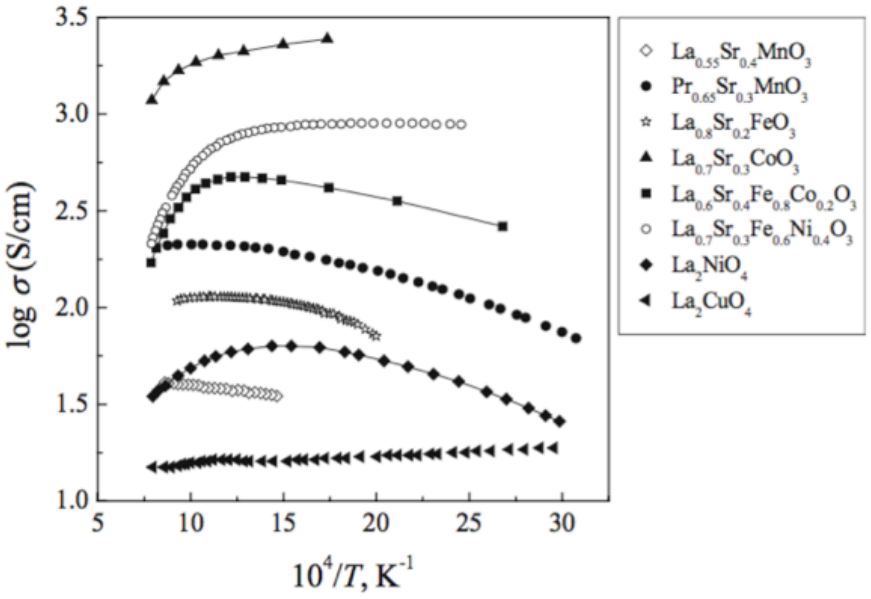

Figure 1.12.[97] Electronic conductivities of various perovskite-related materials in air.

LSC: LSC ($La_{1-x}Sr_xCoO_{3-\partial}$), is a MIEC which shows exceptional electronic conductivity (see Figure 1.12) and electrochemical activity[47,53,56,97] compared to other perovskites and has a relatively compatible TEC with GDC,[53,56] a good IT-SOFC electrolyte (see above). The TEC match between LSC and GDC can be improved by doping LSC with iron,[47,56,102-104] giving LSCF ($La_{1-x}Sr_xCo_{1-y}Fe_yO_{3-\partial}$), a material that still exhibits MIEC properties and good ORR kinetics.

Anodes:

The choice of anode can be more complicated than the cathode in a SOFC due to the wide range of fuels available. As stated above, using hydrogen (as per R1.3) is an option, but a SOFC can burn hydrocarbon fuels directly:

$$C_nH_{2(n+2)} + (3n+1)O^{2-} \rightarrow nCO_2 + (n+1)H_2O + (6n+2)e^- \qquad \textbf{(R1.5)}$$

An anode that is electrocatalytically active for hydrogen oxidation, may have issues with hydrocarbon oxidation (*e.g.* Ni/YSZ). Further considerations include standard electrode requirements: high electrical conductivity, large TPB density, and high porosity (20 – 40%) to allow for efficient mass transport of the fuel, but also removal of the reaction products.[45,53,55] Furthermore, in the case of hydrocarbon fuel usage, the anode should be resistant to coking or sulfur poisoning.[45,53,56,83] Lastly, the anode must be stable in both the overall reducing environment, but also the oxidizing environment localized at active sites (where the oxidized product forms). At operating temperatures, these requirements limit the choice of material drastically.[7] Nickel is a suitable metal for hydrogen oxidation in that it has high catalytic activity, conducts electricity well, and is cost effective,[7,43,45,53,56,105] but the TEC is incompatible with YSZ.[45] Spacil overcame this issue by introducing a Ni/YSZ "cermet"[106] (ceramic and metal) which is currently the most commonly used anode for SOFCs burning hydrogen fuel.

Ni/YSZ: Spacil developed the Ni/YSZ composite for structural purposes,[106] by significantly reducing the anode TEC to be compatible with the YSZ electrolyte[107,108] so that the Ni does not sinter during operation.[7] The insertion of YSZ also improves electrocatalytic activity due to YSZ oxygen vacancies[43,53] and the increased density of TPB sites.[18,47,109-111]

The volume ratio of Ni to YSZ is a critical consideration. Dees *et al.*[110,112] studied the relationship between volume and conductivity and found a percolation limit of 30 vol % Ni, *i.e.* the minimum volume needed for significant electrical conductivity. This has been further corroborated by various studies (see Figure

1.13[97]) which showed that at YSZ volume fractions greater than 70%, the electrical conductivity is very low and the conductivity is primarily ionic. However, while electrical conductivity increases with increasing Ni content, the TEC does as well increasing chances of coarsening of the Ni phase[110,113,114], cracking of the electrolyte, or delaminating from the anode.[7,77,115] As such, the Ni volume % is usually between 35% to 55%.[53]

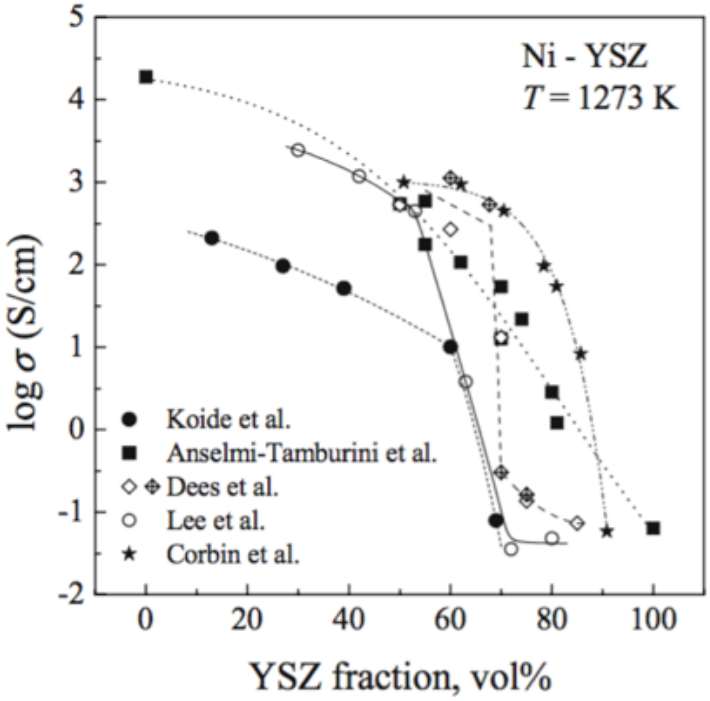

Figure 1.13.[97] A measure of conductivity as a function of YSZ volume fraction in Ni/YSZ at 1273 K from various studies.

Other concerns regarding Ni/YSZ include facile oxidation of Ni if the anode is exposed to air when not in operation, which may cause the anode structure to fail over multiple oxidation/reduction cycles,[43,44] poor IT-SOFC performance,[110,116] and its being ineffective for hydrocarbon fuel use. The inefficacy is due to low electrocatalytic activity toward hydrocarbon oxidation,[81] a strong sensitivity to

sulfur impurities in fuel streams,[44,45,56,107] and coking problems.[7,44,45,47,117]

To address these issues, perovskite materials such as titanates and chromites are being studied,[47,56,118] but a substantial interest has been shown in a cermet made of Cu and ceria.[44,47]

***Ceria and Cu-Ceria cermets*:** Ceria has a fluorite structure, as can be seen in Figure 1.14.[119,120] In 1964, Möbius and Rohland[121] demonstrated ceria's viability as a SOFC anode for H_2 and CO. Ceria is a MIEC due to its ease of oxygen vacancy formation induced by low O_2 partial pressures and elevated temperatures,[119] as can be seen in Figure 1.15.[67] Oxygen vacancies can be further introduced through doping, as observed in the electrolyte, GDC, and as shown in Figure 1.14.[119,120] The ease with which ceria can store and release oxygen (termed, "oxygen storage capacity", OSC) lends to a very high catalytic activity of ceria toward combustion reactions involving oxygen, including the burning of hydrocarbons.[43,97]

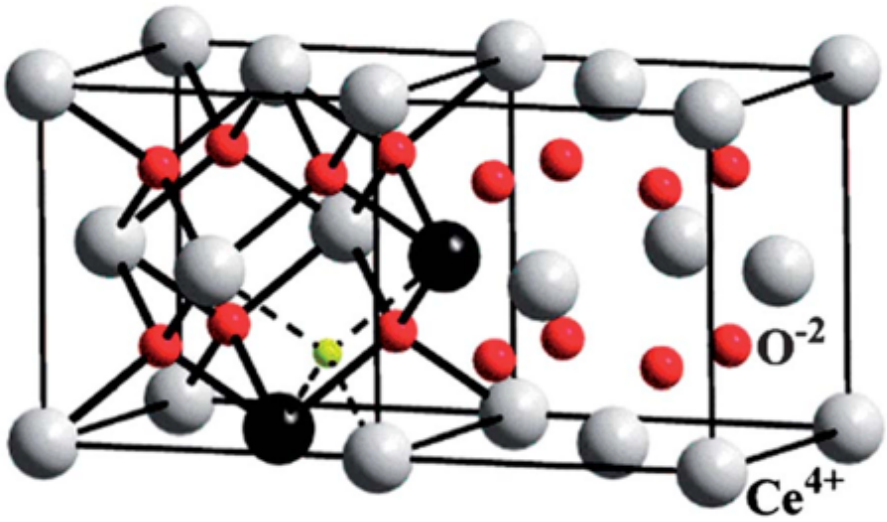

Figure 1.14.[119,120] Two ceria unit cells where the white spheres represent Ce^{4+} and the red spheres are O^{2-}. The black sphere represents a doping of a trivalent ion (*e.g.* Gd^{3+}) in place of Ce^{4+} resulting in an oxygen vacancy (yellow).

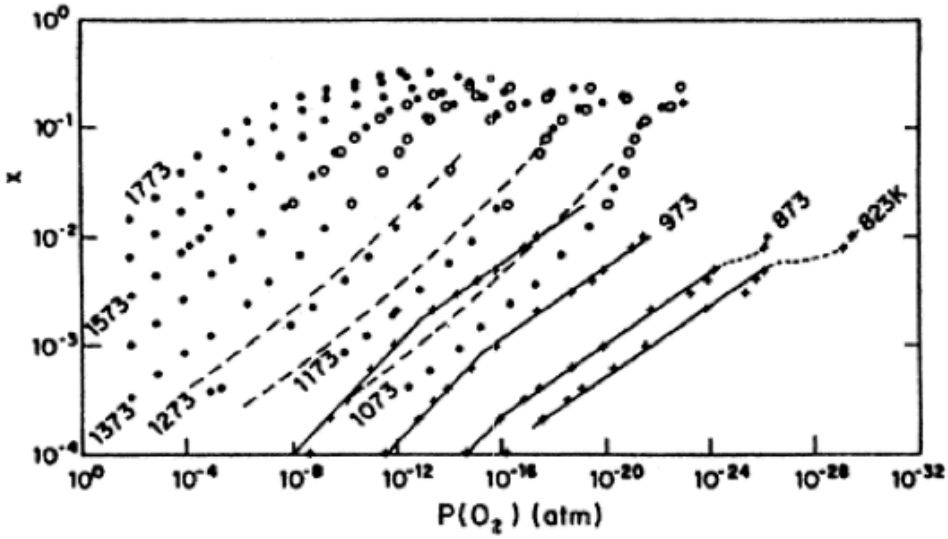

Figure 1.15.[67] Measure of "x" term (*i.e.* oxygen content) in CeO_{2-x} as a function of $P(O_2)$ at different temperatures.

As stated above, ceria also displays variable electron conductivity properties. Ruloph *et al.*[67,122] found that the electronic conductivity was proportional to $P_{O2}^{0.18}$ at 1260 K and Blumenthal, among other researchers,[67,123-125] confirmed that electronic conduction takes place via a "polaron hopping mechanism." Polarons represent not only the electron, but an accompanying electric field distortion and "hopping" is meant to emphasize that the polarons localize on a Ce center[119,126] reducing Ce^{4+} to Ce^{3+}, as opposed to moving through a delocalized band structure.

Electronic conductivity can be further enhanced by forming a cermet with copper.[47,56] The Cu-CeO_{2-x} cermet is especially useful in hydrocarbon fuel utilization, as first demonstrated by Gorte *et al.*[49] Unlike Ni, Cu does not catalyze carbon deposition so coking is not an issue,[43,49,127] while the CeO_{2-x} can easily electrochemically oxidize the hydrocarbon because of its high OSC.

1.2.2 Solid Oxide Electrolyzer Cells

To make H_2 a viable fuel or commodity chemical, it must be produced cleanly and cheaply. Currently, most H_2 is produced via steam reforming which results in using non-renewable fuels and emitting CO_2. Electrolyzer cells (ECs), which are FCs run in reverse, can provide clean and pure H_2. Figure 1.16 shows water electrolysis (*i.e.* water splitting or electroreduction) at an SOEC cathode with the evolution of $O_{2(g)}$ at the anode (OER). The half reactions are thus the reverse of the SOFC:

$$2O^{2-}_{(lat)} \longrightarrow O_{2(g)} + 4e^- \qquad \textbf{(R1.6} \text{ anode reaction, OER)}$$

$$2H_2O_{(g)} + 4e^- \longrightarrow 2H_{2(g)} + 2O^{2-}_{(lat)} \qquad \textbf{(R1.7} \text{ cathode reaction, water electrolysis)}$$

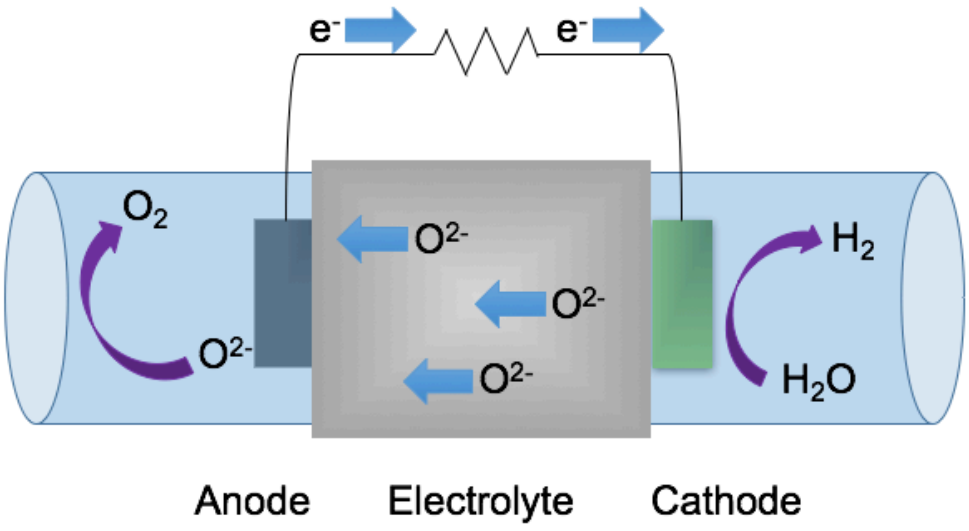

Figure 1.16. A schematic of a simple SOEC splitting H_2O into H_2. The splitting of H_2O via reduction yields H_2 gas and O^{2-} ions which travel to the anode where O_2 gas is evolved through OER.

ECs, especially SOECs, can produce H_2 from water electrolysis with high efficiency (potentially over 95 %),[128,129] especially since they can utilize waste heat from energy sources[128] in the electrolysis process (described in thermodynamics below). In contrast, making H_2 from fossil fuels is a process with only 60 – 85% efficiency.[130]

The high efficiency of the SOEC can be better understood by considering the thermodynamics of operation. The high temperature improves the kinetics of the reactions and decreases the electrical energy demand as can be seen in Figure 1.17.[131] While the endothermicity of water (or CO_2) splitting increases with temperature, the portion of that energy that is supplied by electrical means (ΔG) decreases and the waste heat ($T\Delta S$) that is produced during operation increases and can be utilized for overcoming the endothermicity of the reaction.[128,132-134] This can be more clearly seen by rearranging the terms from Eq. 1.1:

$$\Delta H = \Delta G + T\Delta S = w_{el,\,max} + T\Delta S \qquad \textbf{(Eq. 1.6)}$$

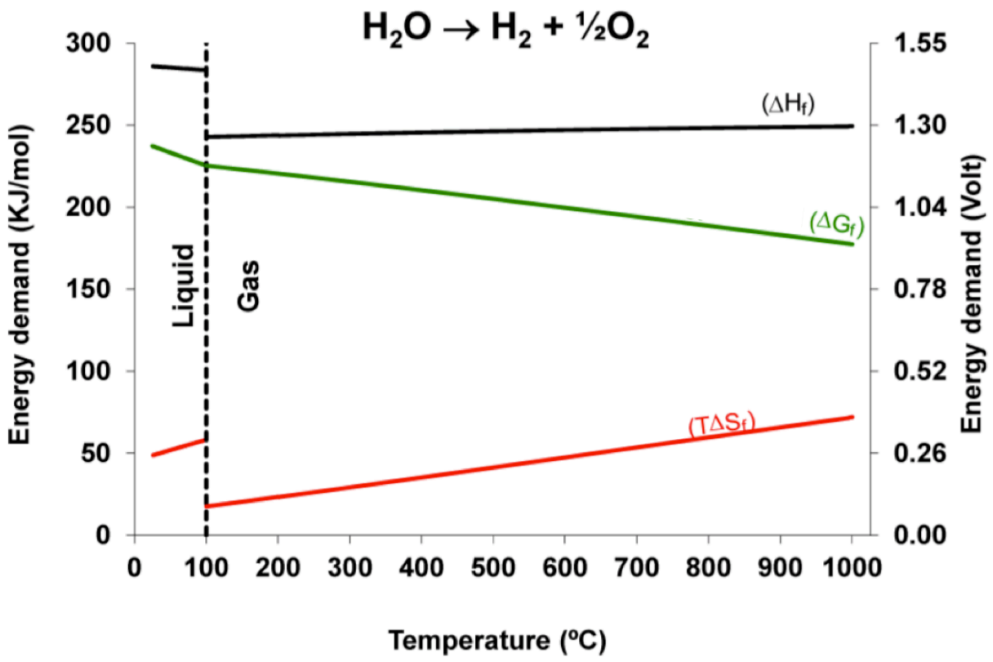

Figure 1.17.[131] Energy demand vs. temperature of steam electrolysis. The total energy demand (black) is the enthalpy of reaction which is the sum of electrical energy demand (green), which is the Gibbs free energy, and heat demand (red), which is the waste heat from entropic processes.

As T increases, the consumption of electrical energy is reduced, and electrolysis becomes more efficient. This can also be represented via the Nernst Equation:

$$E = E^{o} - \frac{RT}{4F}\ln\left(\frac{p^{2}_{H_2O,cathode}\,p_{O_2,anode}}{p^{2}_{H_2,cathode}}\right) \qquad \textbf{(Eq. 1.7)}$$

As can be seen in Eq. 1.7, an increase in temperature will lower the potential required to drive the electrolysis.

1.3 Oxygen Reactions

The following section focuses on fundamental studies and mysteries surrounding ORR and OER, particularly on LSM. While the exact mechanism of these reactions remain unknown, a simplistic, theoretical model on a mixed metal-oxide electrode is:

$$O_{2(g)} + 2V_o + 4e^- \rightleftharpoons 2O^{2-}_{(lat)} \quad \textbf{(R1.8)}$$

where V_o represents an oxygen vacancy in the electrode lattice. When the SOC operates as an SOFC (*i.e.* in the spontaneous direction), ORR (forward reaction) is promoted on LSM, while operating in SOEC mode (non-spontaneous direction) promotes OER (reverse reaction). The oxygen vacancy differentiates this from ORR/OER on a pure metal (*e.g.* Pt, see R1.1). Given that the electrons are conducted via the oxidation and reduction of the transition metals, R1.8 can be adapted specifically for LSM:

$$O_{2(g)} + 2V_o + 4Mn^{3+}_{(lat)} \rightleftharpoons 2O^{2-}_{(lat)} + 4Mn^{4+}_{(lat)} \quad \textbf{(R1.9)}$$

in which $O_{2(g)}$ is reduced by Mn^{3+}, and the oxide ions are incorporated into the oxygen vacancies, either within the LSM or the electrolyte lattice (if a TPB is present), forming $O^{2-}_{(lat)}$. A picture of this process is shown in Figure 1.18. It must be stressed that the figure depicts an idealized surface that is identical to the bulk structure. In reality, the surface is very different, especially at high temperature, and

even more so in the far-from-equilibrium conditions induced by operation. Understanding the surface chemistry is crucial for unraveling the mysteries that surround ORR and OER and is the focus of this dissertation.

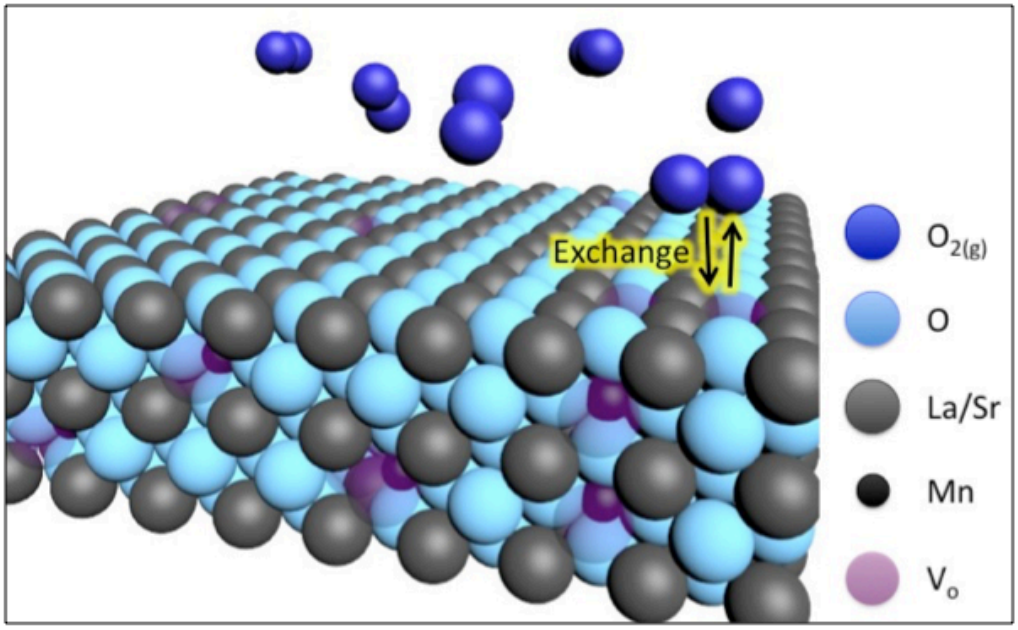

Figure 1.18. Oxygen reduction and evolution on an idealized $La_{1-x}Sr_xMnO_{3\pm\delta}$ (LSM) surface. The LSM lattice consists of La and Sr ions (grey), Mn ions (black), and oxide ions (light blue). Oxygen vacancies (V_o, purple) may be present as well. In oxygen reduction, O_2 gas molecules (dark blue) are dissociated and reduced via the at the surface into two separate oxide ions. If oxygen vacancies are present, the oxide ions may be incorporated into the lattice.

1.3.1 ORR

The ORR was first successfully conducted on a porous Pt cathode,[73] a material that has since been studied extensively.[74,75] Several findings on Pt have influenced the understanding of cathodes toward ORR in general. Through impedance experiments, Mitterdorfer and Gaukler found that ORR was co-limited on the Pt cathode surface by O adsorption and surface diffusion.[135,136] The surface nature of ORR on Pt provided evidence that the active region was restricted to the

area near the TPB, a behavior found in other cathodes.[21] However as previously stated, Pt is not commercially viable so that interest has shifted toward mixed-metal oxides, notable ones including LSM and LSC.

As stated previously, the majority of research on these materials concerning ORR has either consisted of *ex situ* characterizations or electrochemical performance-based *in operando* studies which provide limited insight regarding the fundamental chemistry involved in ORR. Some critical *in situ/operando* studies include mass spectrometry (MS) in conjunction with temperature programmed and oxygen isotopic exchange experiments,[2,39,40] conducted on LSM and LSCF by Wachsman *et al.* A simple two-step mechanism was proposed[2] consisting of dissociative adsorption and lattice incorporation steps to describe ORR:

$O_{2(g)} + 2S \rightleftharpoons 2O_{(ads)}$ (**E1.1** dissociative adsorption)

$2O_{(ads)} + 2V_o + 4e^- \rightleftharpoons 2O^{2-}_{(lattice)} + 2S$ (**E1.2** lattice incorporation)

where S is a vacant surface site and the two reactions sum up to give R1.8. The studies found that LSM was rate-limited by the incorporation step while LSCF was limited by dissociative adsorption. Shao Horn *et al.*[137] probed the surface of LSC thin films with AP-XPS. Under a cathodic bias, Sr segregation was observed on the surface in the form of SrO that decreased the number of active sites by differing degrees, based on crystal plane and Sr doping levels. Mogensen *et al.*[138] studied LSM with electrochemical performance measurements and showed that increasing the length of the TPB increased ORR activity and that resistive (Zr, La)-rich phases

at the cathode/electrolyte interface could be decreased by increasing the Mn content.

While these experiments and others have shown facets of the mechanisms at work in ORR, some key aspects remain elusive and are described below.

1.3.1.1 Nature of the LSM surface in operating conditions:

The nature of a LSM surface is very different from the bulk structure, especially at the high temperatures required for operation. One major difference may be found in the Mn oxidation state. There are disagreements in the literature regarding the surface oxidation state of Mn. Decorse *et al.*[139] used *ex situ* XPS and thermogravimetric analysis (TGA) to show that Mn is more oxidized at the surface, which is expected, given that the surface is exposed to the oxygen environment. However, Li *et al.*[140] conducted *ex situ* electron energy loss spectroscopy (EELS) and XPS experiments on a cross section of an LSM films and found greater reduction at the surface. Lee *et al.*'s[141] first principles calculations showed that V_o formation, which is linked to the reduction of Mn as seen in R1.9, is easier at the surface. Additional studies by Fister *et al.*[142] also hypothesized that a greater amount of oxygen vacancies should exist at the surface given strontium surface segregation.

Sr segregation at the surface is a well-known phenomenon in LSM materials that has been shown to increase with decreasing O_2 pressure[142] and increasing temperature.[143] The driving force behind the segregation is under debate, but is generally considered to be due to both electrostatic interactions and lattice strain. The electrostatic contribution is from a positive space-charge layer forming at the

surface which is neutralized by lower valent Sr^{2+} ions replacing La^{3+}.[144] The lattice strain influence is due to a larger ionic radius in Sr^{2+} compared to La^{3+} so that the Sr ions are driven to the surface where elastic strain is mitigated.[83] Yildiz *et al.'s*[145] XPS experiments on differently strained LSM surfaces support this theory. Enrichment of Sr in the lattice can further result in an extrusion of Sr from the LSM to form SrO particles above the electrode[17,146] which are thought to passivate the surface and lower surface kinetics.[17]

In a broader sense there is a mystery in any perovskite material regarding the surface state. Surface cation ratios between two A-site cation ratios (*e.g.* La:Sr), two B-site cations (*e.g.* Co:Fe in LSCF), or A-site and B-site cations (*e.g.* La:Mn in LSM) are not well-predicted by *ex situ* bulk characterizations (*e.g.* X-ray powder diffraction). Furthermore, gradients in these ratios with surface depth or the mechanisms behind cation segregation (*e.g.* SrO) are unknown. The oxidation state of the transition metals and charge distribution under OCV and operation are largely unknown, as well. Comparing the differences between the two conditions can shed much light on the nature of ORR on a cathode surface.

1.3.1.2 LSM activation

A well-known phenomenon in LSM operation is known as the "activation effect" in which the electrode performance increases rapidly (signified by decreased polarization losses and associated resistances) during cathodic polarization.[83,147-149] The origin of this effect is not clear. Some studies have focused on structural changes, such as the work of Jiang *et al.*,[150,151] which found the formation of well-defined particles with clear grain boundaries after cathodic

bias. Kuznecov *et al*[152]. discovered that nanopores at the LSM/electrolyte interface had developed after three hours of cathodic polarization.

The quintessential work of Wang and Jiang[17] compared the electrochemical performance of two different LSM electrodes, one of which had undergone an acid-etching treatment. The un-etched electrode demonstrated standard behavior under cathodic bias (Figure 1.19A) where a significant drop in polarization resistance was observed within a few minutes of polarization. The acid-etched LSM showed a significantly lower initial resistance (Figure 1.19B) and a much less dramatic activation over time. That surface etching would decrease initial resistances by such a large margin supported the premise that passivating surface species such as segregated SrO particles—which were cleaned off by acid etching—are responsible for the initial high resistances. The authors concluded that the cathodic bias is somehow removing these surface species, presumably by reincorporating them.

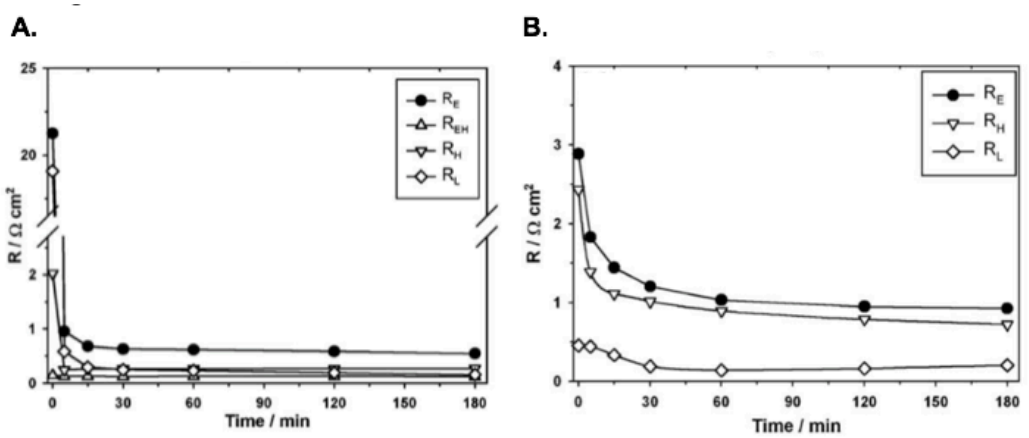

Figure 1.19.[17] Resistances over time under cathodic bias of (A) a freshly prepared LSM electrode and (B) a LSM electrode that had undergone acid-etching treatment prior to polarization. The different resistances are defined as the electrode polarization resistance (R_E), which is the sum of three separate resistances: oxygen surface exchange (R_L), oxide ion transfer at LSM/YSZ interface (R_H), and a charge transfer process (R_{EH}).

While these experiments were highly regarded, they are ultimately based on *ex situ* characterizations. Huber *et al.*[153] shed more light on this work by conducting *in operando* XPS on LSM thin films on a YSZ electrolyte and saw not only the disappearance of SrO, but Sr in the LSM lattice under cathodic bias. However, the experiment was conducted in vacuum conditions (1 nbar of O_2 pressure). Furthermore, Backhaus-Ricoult *et al.*[154,155] conducted several *in operando* XPS studies on a similar cell in the same conditions and witnessed a cathodically-induced *increase* in Sr, and attributed the activation effect to a spread of Mn beyond the LSM/YSZ interface which allows for a more direct incorporation mechanism into the YSZ electrolyte.[155]

In summary, LSM electrodes typically demonstrate a significant improvement in performance over time when cathodically biased. This improvement is known as the activation effect and is potentially due to morphology and structural changes or the removal of passivating surface species such as SrO. While some *in operando* spectroscopic research showed that surface strontium is removed by a cathodic bias, other research has shown the opposite effect, and the exact mechanism of activation remains a mystery.

1.3.1.3 Conductivity of LSM

LSM has long been thought to be an electronic conductor under typical cathode conditions, meaning ORR follows a "surface path" and all electrochemical activity occurs at the TPB (lack of ionic conductivity precludes oxide ion incorporation into the bulk of LSM, see **Figure 1.7**).[43,72] An AFM study conducted by Jiang *et al.*[156] supports this hypothesis as different features were observed before

and after cathodic (and anodic) polarization specifically at the LSM/YSZ interface, indicating that ORR (and OER) only occur at the TPB.

However, some studies refute this notion. Van Heuveln *et al.*[157,158] separated the effects of electrode surface area from the TPB, and found no obvious correlation between electrochemical activity and TPB length. The authors acknowledge that discrepancies can be due to processing and operating history highlighting how difficult it can be to create an overarching "rule" for LSM conductivity. Mizusaki *et al.*[159] found an inverse correlation between LSM thickness and electrochemical performance, even though thickness of the electrode should not have a significant effect on activity if the bulk path can be ignored. Fleig *et al.*[20,160] conducted studies on circular thin films of LSM and found that the bulk path can outcompete the surface path despite low O conductivity. Their studies found that a larger electrode diameter (*i.e.* surface area) lowered the polarization resistance (Figure 1.20)[20] indicating that not all activity could be occurring at the edge, as an increased surface area would only lead to higher electrochemical activity if part of the interior region of the LSM was active. Hammouche *et al.*[161,162] found a distinct change in the behavior of LSM (marked by a significant jump in current) at cathodic overpotentials larger than a critical value (-150 mV to -500 mV vs. air). The researchers attributed the increase in current to a change in operating regimes. At high cathodic polarization, the LSM is reduced with a concurrent formation of oxygen vacancies allowing for facile transportation of O^{2-} and allowing for a bulk path to be followed, while at lower potential LSM behaves as an electronic conductor, as most studies support.

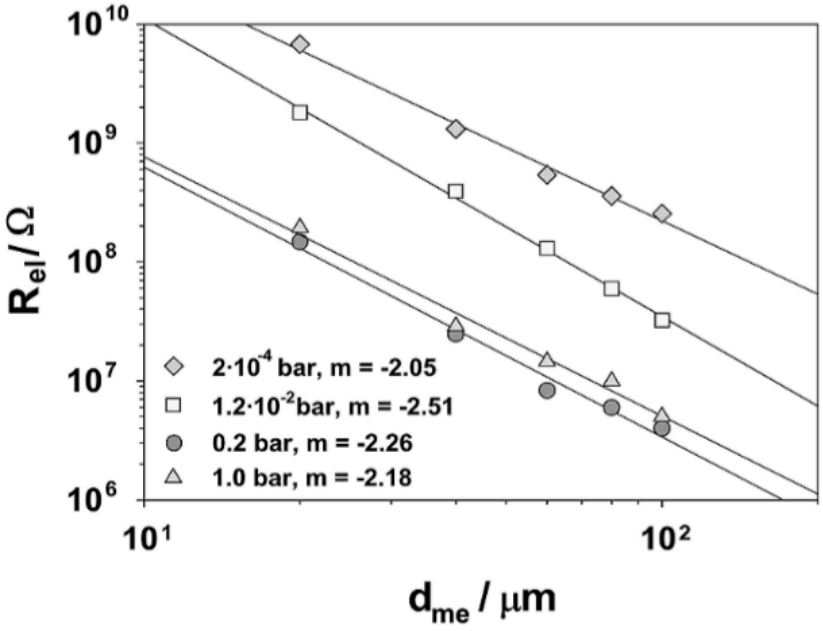

Figure 1.20.[20] Polarization resistance (R_{el}) vs. diameter of the metal oxide electrode (d_{me}) at various O_2 partial pressures.

1.3.2 OER

When a SOC is operated as an SOEC, *i.e.* in the non-spontaneous direction, the electrode on the oxygen side functions as an anode promoting OER. As in a SOFC, the most commonly used electrode at the oxygen side is LSM-based,[163-167] however, OER is far less studied relative to ORR, which has led to a greater paucity of information regarding OER chemistry.

LSM materials are generally thought to not promote OER as well as ORR as evidenced by Eguchi *et al.'s*[168] experiments on a LSM anode-based cell. Marina *et al.*[169] found LSM electrodes suffered greater polarization losses when running in EC mode compared to FC mode. Models developed by Svensson *et al.*[170] predict Tafel-like behavior under cathodic bias, but limiting currents under anodic bias.

Some studies show contrasting results, though. O'Brien *et al.*[171] found little difference in resistances in either operation mode, and while Mogensen *et al.*[172] did observe a decrease in performance in a LSM anode-based SOEC, they attributed it to diffusion slowness at the cathode side, rather than the LSM.

Chen *et al.'s*[173] studies in which LSM electrodes were operated in both directions (cathode and anode) found LSM to be less suitable as an anode due to a deactivation effect observed within 2 hours of anodic biasing. Jiang *et al.*[17] also found a deactivation under anodic bias within 3 hours, and Gorte *et al.*[22] found that a "cathodically-activated" cell (see Section 1.3.1.2), reverted to a near pre-activated state under anodic bias.

However, Liang *et al.*[174] found an initial activation effect under anodic bias similar to that observed for cathodic bias, although the effect's origin is not necessarily the same. Yildiz *et al.*[175] observed the activation effect on LSM thin film anodes, and using *in operando* X-ray absorption spectroscopy (XAS) and X-ray reflectivity techniques, found changes in the concentration and electronic state of La at the LSM/air interface. This work, which presently appears to be the only *in operando* X-ray experiment conducted on OER in the literature, indicates that La may play a beneficially active role in the oxygen chemisorption and charge transfer processes. Chen *et al.*[176] studied a LSM/YSZ composite and found an activation effect initially, but after ~30 hours of operation a deactivation effect was observed (Figure 1.21). The long-term deactivation was attributed to delamination of the electrode, a well-known consequence of anodic bias on LSM.[160,176-179]

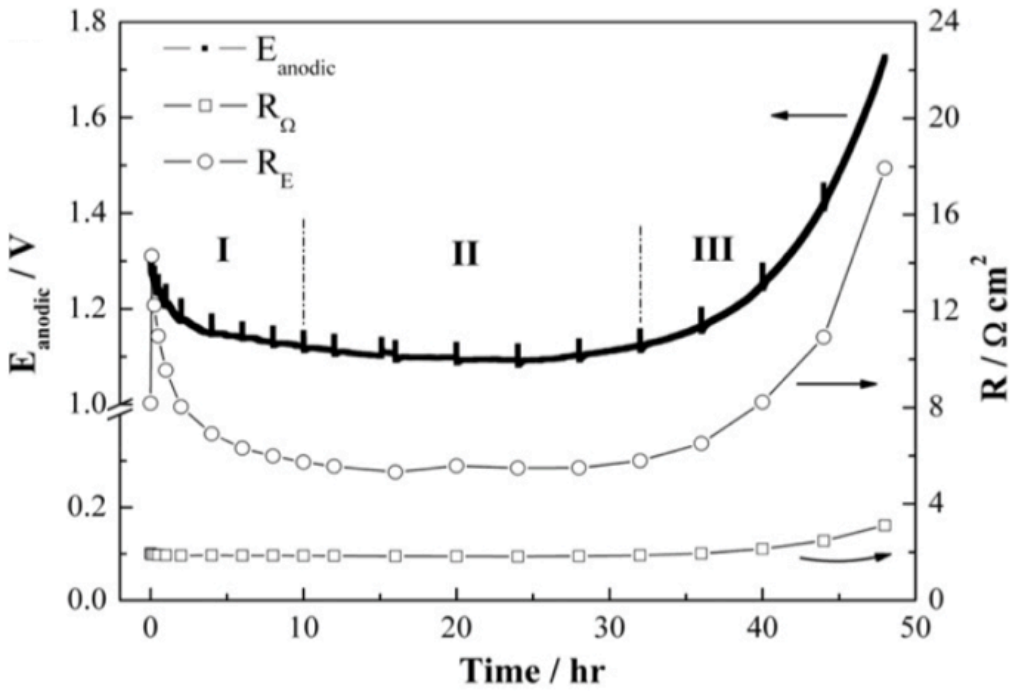

Figure 1.21.[176] Measure of resistances (right axis) over time under an anodic bias.

1.4 *In Operando* Spectroscopic Techniques:

The use of *in operando* spectroscopic techniques has provided new insight into heterogeneous catalytic processes occurring on surfaces in far-from-equilibrium and compositionally distinct states. This far-from-equilibrium state is particularly difficult to study, especially at elevated temperatures, since one needs a surface-sensitive probe that can be employed during an electrochemical process.

Vayenas *et al.* first proposed the use of *in operando* XPS[180] to study electrocatalytic systems so that local surface potentials and chemical states could be measured during electrochemical processing. However, traditional XPS requires ultra-high vacuum (UHV) conditions, whereas active SOCs require the presence of reactive gases. Recent advances in differentially pumped electrostatic lens detectors coupled with synchrotron-based XPS systems[181,182] have alleviated these

incompatibilities allowing for XPS in near ambient conditions (~several Torr of gas pressure) while simultaneously heating and polarizing the cell. We and others have exploited this technology to study *in operando* surface chemistry of high temperature fuel cells, electrolysis cells and other electrocatalytic systems.[23,25-28,183-185]

A useful complementary *in operando* X-ray based technique that can be utilized at a synchrotron light source is X-ray absorption spectroscopy (XAS) which can allow for both surface and bulk characterization of a material's properties including, electronic structure and coordination environments.

Another *in operando* technology employed by us and others is a near infrared (NIR) imaging camera[30-38] to monitor processes in an operating SOC via changes in the temperature or optical properties of a material. The advantage of this technique is that it is relatively inexpensive and accessible in comparison to the above technologies.

In this section the principles and considerations behind XPS, XAS, and NIR imaging, with a focus on XPS theory that is relevant to this work, are described.

1.4.1 XPS

1.4.1.1 General Principles

XPS is a powerful surface characterization technique, typically probing 6 ~ 10 nm into a material, to determine features such as, atomic ratios, surface speciation, and oxidation states (see Section 1.4.1.7). In XPS, a sample is irradiated with "soft" X-rays (energies of 100 ~ 3000 eV), and photoelectrons are ejected provided the X-ray energy is strong enough to overcome the binding energy (BE)

of the electron. By measuring the kinetic energy (KE) of the escaping photoelectrons, the BE can be determined via the photoelectric effect:

$$h\nu = BE + KE \quad \textbf{(Eq. 1.8)}$$

where hν is the energy of the incident X-ray photon. BE values convey substantial chemical and electronic information about the sample, as described further in this Section. In reality, the Eq. 1.8 is complicated by extra experimental terms as detailed in Section 1.4.1.2. The process for photoelectron ejection from a solid material is shown in Figure 1.22. On the left side, full shells of core electrons are presented while the occupied and unoccupied valence states are represented by bands of indiscrete energy states. The highest occupied level is marked by the fermi level (E_F) while the vacuum level (E_{vac}) represents the energy at which the electron leaves the solid. A 1s electron absorbs an X-ray and is ejected leaving behind a vacancy known as a core-hole.

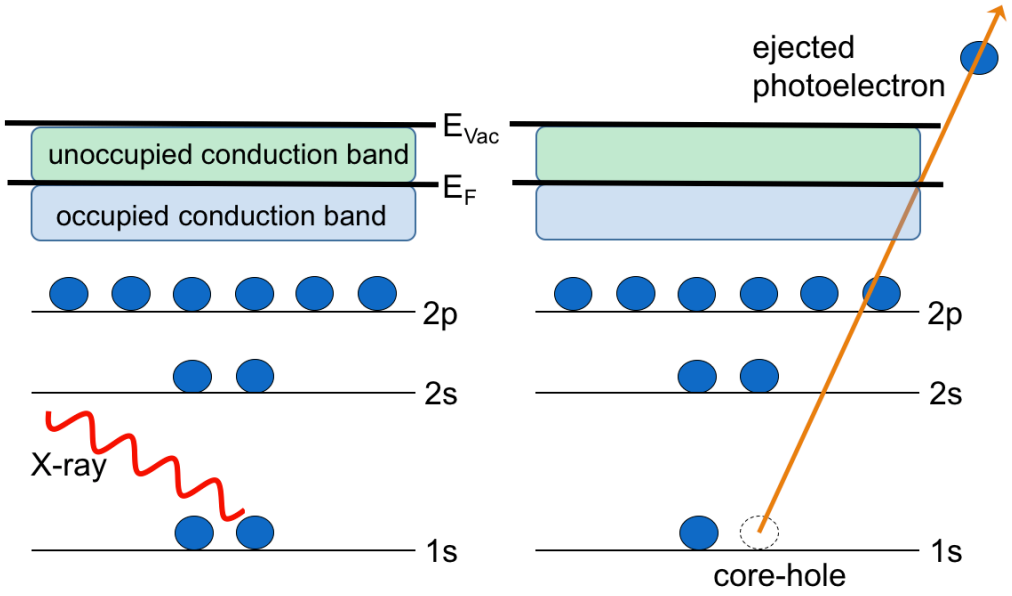

Figure 1.22. A schematic of the photoelectron ejection process for a 1s electron.

The detector counts the number of emitted photoelectrons at each KE. After calculating the BE via Eq. 1.8, photoemission spectra are generated, like those shown in Figure 1.23. These BEs are characteristic for each atom under specific conditions. For example, the BE of a 1s electron in $C_{(s)}$ atom is ~284.8 eV[186] whereas in $O_{(s)}$ atom it is ~529.4 eV.[187]

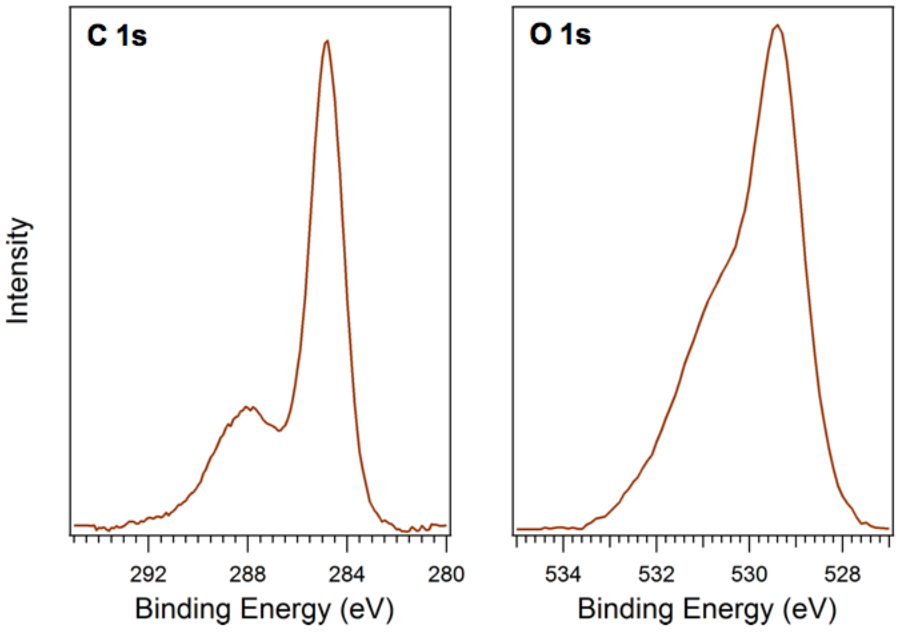

Figure 1.23. Representative XPS spectra of C 1s (left) and O 1s (right). Intensity (arbitrary units) is plotted against the binding energy of the electrons.

The spectra in Figure 1.23A and B are named, C 1s and O 1s, respectively, in accordance with the electron studied. The spectra not only identify the existence of C and O on the surface, but also that more than one C and O species are present, as indicated by the complex peak shapes.

1.4.1.2 Experimental Considerations

X-Ray Sources: There are two primary sources of X-rays: "conventional sources" and "synchrotron light-based sources." In this section only conventional sources are discussed, while synchrotron sources are discussed in Section 1.4.1.8.

In a conventional source, X-rays are typically produced by striking either an Al or Mg target with high energy electrons which have been accelerated by a 10-100 kV voltage.[188] These electrons eject other electrons from the source material causing relaxation processes within the material that produce X-rays of a quantized

energy. The strongest X-rays produced by Al and Mg have energies of 1486.6 eV and 1253.6 eV, respectively, and are known as the Kα X-rays.

Ultra-High Vacuum: The inelastic mean free path (IMFP), *i.e.* the average distance between inelastic collisions, is very small for photoelectrons and thus the chamber must be kept at UHV[189] because gas will interact with the photoelectrons resulting in them not reaching the detector. For this reason, XPS is typically only used to study solids, as liquids tend to have too high a vapor pressure.

Work Function: The work function (Φ) of a solid is the energy difference between the fermi level and the vacuum level. In a solid, the BE is referenced to the E_F, thus the photoelectron's KE as calculated by Eq. 1.8 requires the addition of the workfunction term:

$$KE_{samp} = h\nu - (BE + \Phi_{samp}) \qquad \textbf{(Eq. 1.9)}$$

where the subscript "samp" refers to the property with respect to the sample material. The left side of

Figure **1.24** shows a visual representation of Eq. 1.9. However, the KE of the electron from the sample will not be the same as that detected by the analyzer (KE_{spec}) due to the analyzer having its own workfunction (Φ_{spec}), where "spec" stands for spectrometer. If the solid is a good electronic conductor and well-connected to the grounded spectrometer, the fermi levels will align (see

Figure **1.24**) and the (KE_{spec} + Φ_{spec}) term will be equal to (KE_{samp} + Φ_{samp}). Thus, Eq. 1.9 can be manipulated as:

$$BE = h\nu - (KE_{spec} + \Phi_{spec}) \qquad \textbf{(Eq. 1.10)}$$

Eq. 1.10 is the more relevant equation for the calculation of BE. From here on, the "spec" subscript will be assumed for KE and Φ, while BE is taken to be from the sample's perspective.

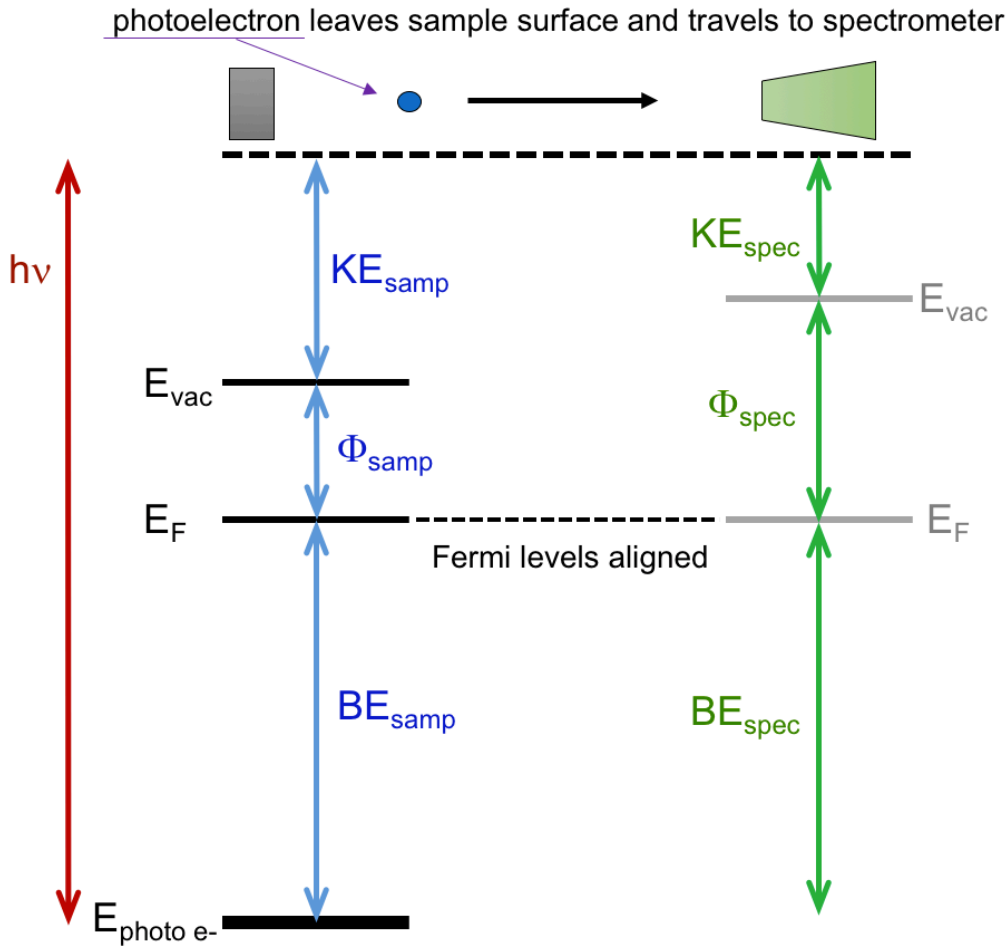

Figure 1.24. A schematic of the energy levels involved in the detection process. On the far left side is the photon energy magnitude, hν. The energy is divided into three parts for the photoelectron with respect to the sample energy levels shown on the left side. The first component overcomes the BE which is the difference between the sample fermi level (E_F) and the energy level that the photoelectron is ejected from ($E_{photo\ e^-}$). The second component overcomes the workfunction of the sample (Φ_{samp}), *i.e.* the difference between E_{vac} and E_F. The rest of the photon energy is converted into KE. Once free of the sample, the photoelectron is captured by the spectrometer and "descends" to the spectrometer's fermi level which is in alignment with the sample fermi level, provided the sample is electronically conductive and in good contact with the instrument. It can visually be seen that the KE and workfunction of the spectrometer when summed up and subtracted from the X-ray energy will give the same BE value as that from the sample's perspective.

Charging: If the sample is electronically insulating, it will not be effectively grounded to the spectrophotometer and as electrons are ejected from the sample, electrons will not be able to "replenish" the surface and a positive charge will build up. This positive charge will cause the fermi levels of the sample and spectrometer to become misaligned (see Figure 1.25) and the calculated BE will increase by the amount of charging (Ψ) on the surface (1 V of charging raises the calculated BE by 1 eV). Thus, to calculate the true BE of an electron, Eq. 1.10 becomes:

$$BE = h\nu - (KE + \Phi + \Psi) \qquad \textbf{(Eq. 1.11)}$$

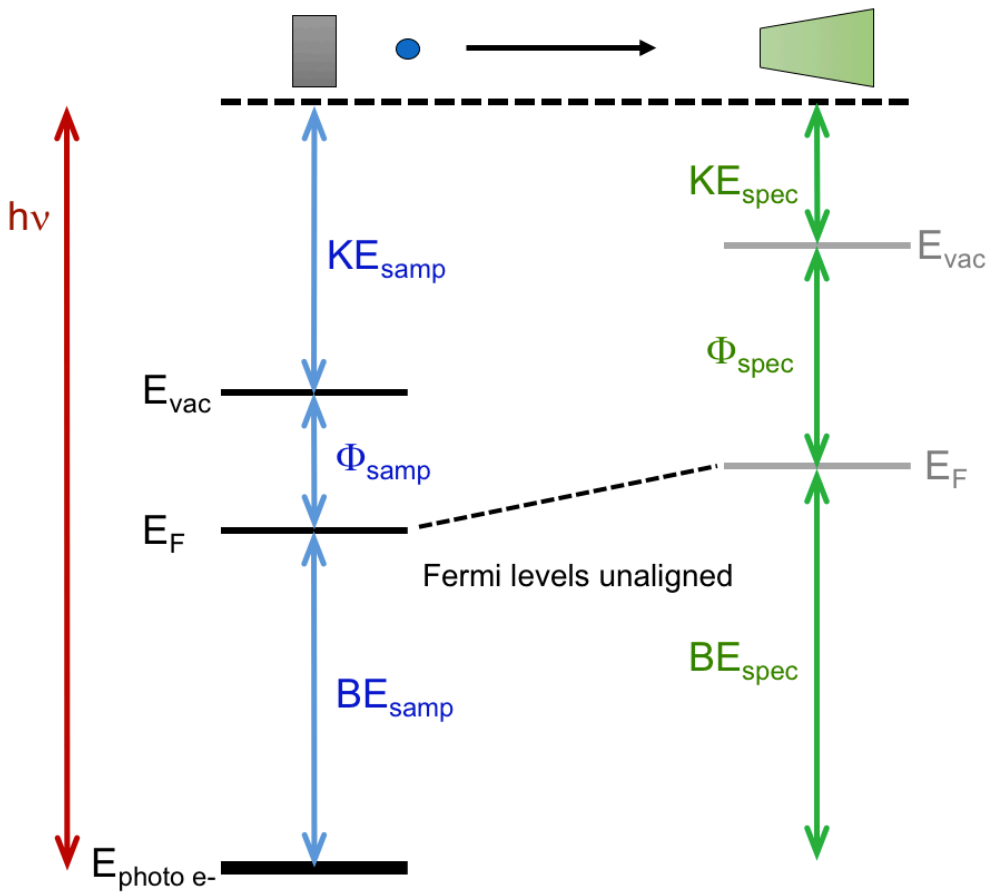

Figure 1.25. A schematic of the energy levels involved in the detection process when sample charging is present. The fermi levels are no longer aligned and so the measured BE from the spectrometer (BE_{spec}) is greater than the true BE (BE_{samp}).

Calibration: Rather than attempt to calculate the values of Φ and Ψ, XPS spectra are typically calibrated to a well-known peak, either a metal in contact with the surface or the C 1s peak. The C 1s peak is useful because all materials have a surface layer of adventitious graphitic carbon from the atmosphere and the C 1s peak is very well known for graphitic carbon (284.8 eV).[186] For example, if the C 1s peak is measured to be 5 eV higher than 284.8 eV, than all XPS peaks will be calibrated by -5 eV to find their true BE.

1.4.1.3 Peak Shape and Intensity Influences

Several sample factors will influence the intensity and shape of a photoelectron peak. The intensity is related to the amount of a species present, the photoelectron's photoionization cross section, and its IMFP in the solid material.

Photoionization Cross Section: The cross section of an electron represents the probability per unit area per unit time that a photon will be absorbed by an atom and eject a photoelectron. Cross sections are different for every core electron in every atom and generally become larger as the energy of the photon approaches the BE of the electron.

IMFP: The IMFP measures the average distance that a photoelectron can travel through a solid material without experiencing an inelastic collision. The IMFP is determined by both the KE of the outgoing electron and the material that the photoelectron is moving through. A general trend of IMFP vs. KE on average in a solid material is shown in Figure 1.26.[190] Above ~50 eV, the IMFP increases with KE, because a higher KE electron has less chance of interaction with other atoms. Below ~50 eV, the IMFP increases with lower KE because it has less energy available for interaction with other atoms. Because an electron has a larger chance of interaction with the solid as it originates from deeper into the material, the intensity of detected electrons decays exponentially with depth:

$$\frac{I(d)}{I_o} = 1 - e^{-(\frac{d}{\lambda})} \qquad \textbf{(Eq. 1.12)}$$

where I_o is the total signal intensity of the photoelectrons, I(d) is the intensity at any given depth, d is depth, and λ is the IMFP. Eq. 1.12 can show that 95% of a signal comes from a depth of 3λ.

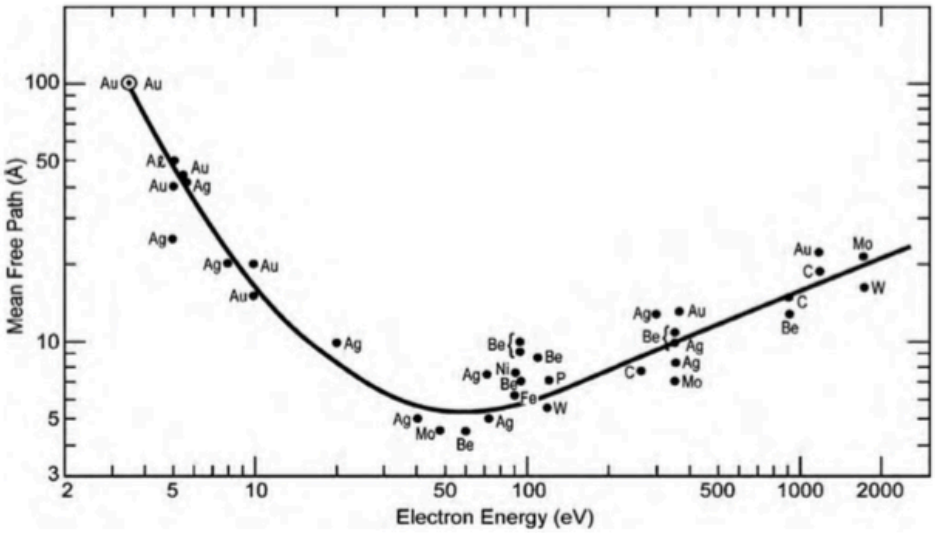

Figure 1.26.[190] The inelastic mean free path (IMFP) at different electron KEs in various solid materials. A line is fit through the data giving a general idea of how IMFP varies with KE in a solid.

Peak Shape: The width of the peak is defined by its full width half maximum (FWHM). A peak is typically a mix of Gaussian and Lorentzian line shapes as shown in the Zr 3d spectrum acquired from a YSZ surface (Figure 1.27, left). The significance and labeling of the two peaks is described in Section 1.4.1.5. In electronically conductive metals, there is usually an asymmetry associated with peaks (see Figure 1.27, Pt 4f spectrum) that evolves from the photoelectrons transferring energy to valence electrons and exciting them to the conduction band of indiscrete energy states. To properly fit asymmetric peak shapes, parameters that modify the Gaussian-Lorentzian peak must be taken into account.

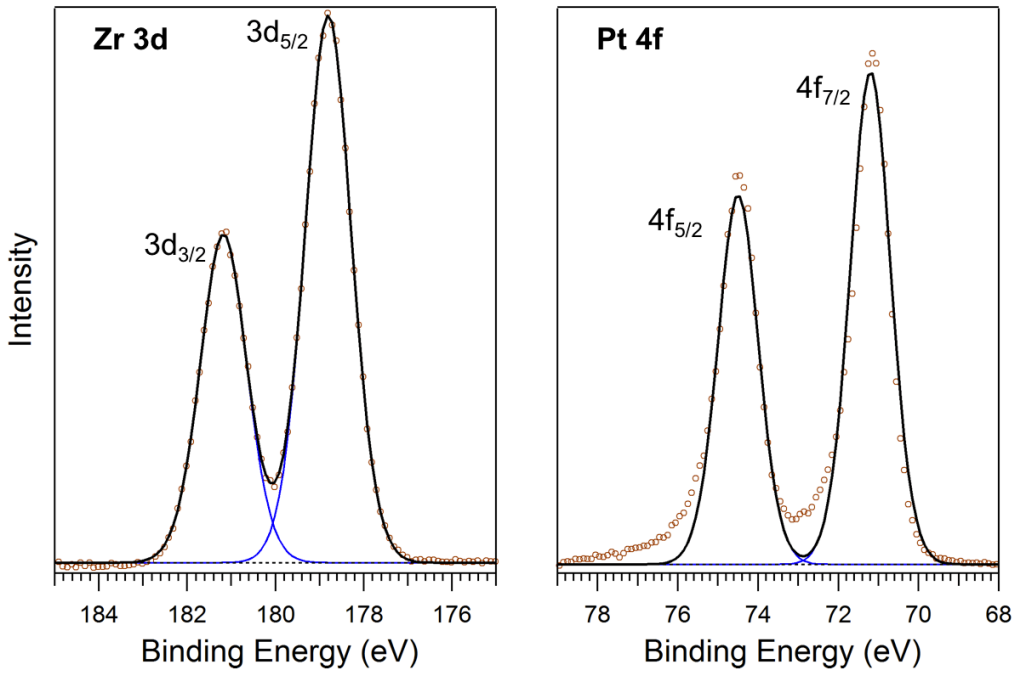

Figure 1.27. (Left) Sample Zr 3d spectrum in which the spectrum (brown) are fit with two peaks of Guassian-Lorentzian mix 70:30 (blue), giving a very well fitting envelope (black). (Right) Pt 4f spectrum in using two peaks of the same mix. It can clearly be seen that this does not provide a good fit because the asymmetry of the two peaks in the actual spectrum are not accounted for.

1.4.1.4 Electronic State Influences on Binding Energy

Binding Energy and Relaxation Energies: In this section, characteristics that influence the BE of an electron that are intrinsic to the electronic state of an atom (*i.e.* not spectrometer work function or charging) are discussed. The BE is defined as the difference between the energy of the atom after and before ionization of the photoelectron (Eq. 1.13):

$$BE = E(z^{+}) - E(z) \qquad \textbf{(Eq. 1.13)}$$

where the $E(z^+)$ is a higher energy (*i.e.* less negative) state than the E(z) state, causing BE to be expressed as a positive value. According to Koopman's Theorem, the BE can be approximated by the Hartree-Fock calculation,[191] which is the calculated energy of an electron based on the difference between the orbital energy and E_{vac} (or E_F of a solid) under the assumption that all other electrons are "frozen," *i.e.* they have no response to electronic perturbations. In reality, when an electron is ejected, other electrons in the atom will screen the outgoing electron causing the $E(z^+)$ state to be more relaxed (*i.e.* more negative than in the frozen orbital approximation), thus the effective BE of the photoelectron is *smaller* than assumed from the Hartree-Fock approximation. This screening process is called, "intra-atomic relaxation" and the BE can be expressed in terms of:

$$BE = -\varepsilon_F - R_a \qquad \textbf{(Eq. 1.14)}$$

where ε_F is the energy from a Hartree-Fock calculation and R_a is the intra-atomic relaxation energy, *i.e.* the energy gained by screening within the atom. The ε_F term is inherently negative, so it must be multiplied by -1 so that BE is a positive quantity.

If the atom of interest does not exist independently but is instead part of a solid, two more considerations will be taken into account, a modification to ε_F which accounts for a free atom entering a solid (ΔE_e) and the extra-atomic relaxation energy (R_{ea}). R_{ea} is a further screening of the photoelectron by electrons in the neighboring atoms. Thus for a solid Eq. 1.14 is further modified:

$$BE = -\varepsilon_F + \Delta E_e - R_a - R_{ea} \quad \textbf{(Eq. 1.15)}$$

Extra-atomic relaxation will occur for a non-free atom in any state, however the magnitude of R_{ea} will decrease (and so BE will increase) with less interaction between neighboring atoms. Thus the BE of an atom in different phases tends to be ranked as: $BE_{(s)} < BE_{(l)} < BE_{(g,\ molecule)} < BE_{(g,\ free\ atom)}$.[191] Furthermore, within a solid phase, R_{ea} will also decrease when the atom is under-coordinated tending to result in higher BEs at the very surface of a material.

Oxidation state: The oxidation state of an atom will typically change the BE of a photoelectron so that the electrons of a more oxidized species will have a higher BE. This can be justified from basic ionization energy considerations, *i.e.* a more oxidized atom has a greater effective nuclear charge even when acting on the core electrons.

Electronegativity: When an atom is coordinated to a more electronegative atom, the BE will tend to shift higher energies for two reasons. The first reason is much the same as in oxidation state considerations, if the oxidation number increases due to electron density being pulled away by a more electronegative neighbor, the effective nuclear charge of the atom will increase. Second, a more electronegative neighbor is less polarizable so that its electrons will be less effective at screening an outgoing photoelectron through the extra-atomic relaxation process.

1.4.1.5 Photoelectron Spectra: Additional Features

Often, an XPS spectrum will be complicated by extra peaks that are not related to different species, but are due to "initial and final state effects." These effects are related to an atom's electronic structure either before photoemission (initial state) or after (final state). Four of the most prevalent effects are listed here: spin-orbit coupling, multiplet splitting, shake up/down satellites, and plasmons.

Spin-orbit Coupling: Spin-orbit coupling arises from a coupling between an electron's internal angular momentum (*i.e.* spin) represented by the quantum number, s, and the orbital angular momentum, l. The sum or difference between these quantum numbers gives a new quantum number, j, which is equal to $| l \pm s |$ where the addition of the two terms represents a parallel configuration and the subtraction gives an anti-parallel configuration, each of which gives rise to a peak at different BE. These effects may be seen in the Zr 3d spectrum above (Figure 1.27) in which the parallel electron ($j = |2 + ½| = 5/2$) is observed at 178.1 eV and the anti-parallel electron ($j = |2 - ½| = 3/2$) is found at 181.2 eV.

Several aspects of the spectrum are noteworthy. First is the energy splitting between the parallel electronic state, which is found at a lower BE than the anti-parallel state. The lower BE in the parallel state is due to an energetically unfavorable alignment of magnetic moments. The difference in energy between these two peaks is mostly fixed for a specific atom and may only have minor changes depending on the environment. The splitting will increase with the nuclear charge, Z. Second, the parallel state is larger than the anti-parallel state by a relation known as the "branching ratio." The branching ratio is described by:

$$\frac{\mathrm{I}_{\mathrm{parallel}}}{\mathrm{I}_{\mathrm{anti-parallel}}} = \frac{2j_{\mathrm{parallel}} + 1}{2j_{\mathrm{anti-parallel}} + 1} \qquad \textbf{(Eq. 1.16)}$$

where I is the peak intensity. Thus, the ratio of the $3d_{5/2}$ peak intensity to the $3d_{3/2}$ is: $\left[\frac{2(5/2)+1}{2(3/2)+1}\right]$, or 3:2. Third, the two peaks must have the same FWHM value.

Finally, it is worth noting that if the photoelectron is from an s orbital, there is no orbital angular momentum to couple to, so that spin-orbit splitting is not observed.

Multiplet Splitting: Multiplet splitting, or spin-spin coupling, is a final-state effect typically observed in transition metals. Multiplet splitting occurs after a core electron is ejected leaving an unpaired core electron. The spin of the unpaired core electron couples with the spin of unpaired d-electrons to give different energy states corresponding to a final spin parallel or anti-parallel arrangement.[192-197] For example, a Mn^{2+} ion has an electron configuration of, [$3s^2$, $3p^6$, $3d^5$], with a spin state of ^6S (Figure 1.28). If a 3s core electron is ejected, two possible final spin states result, [$3s^1$, $3p^6$, $3d^5$], ^7S (parallel arrangement) and [$3s^1$, $3p^6$, $3d^5$], ^5S (anti-parallel arrangement). These two states appear in an XPS spectrum as two different peaks, as shown in Figure 1.29.

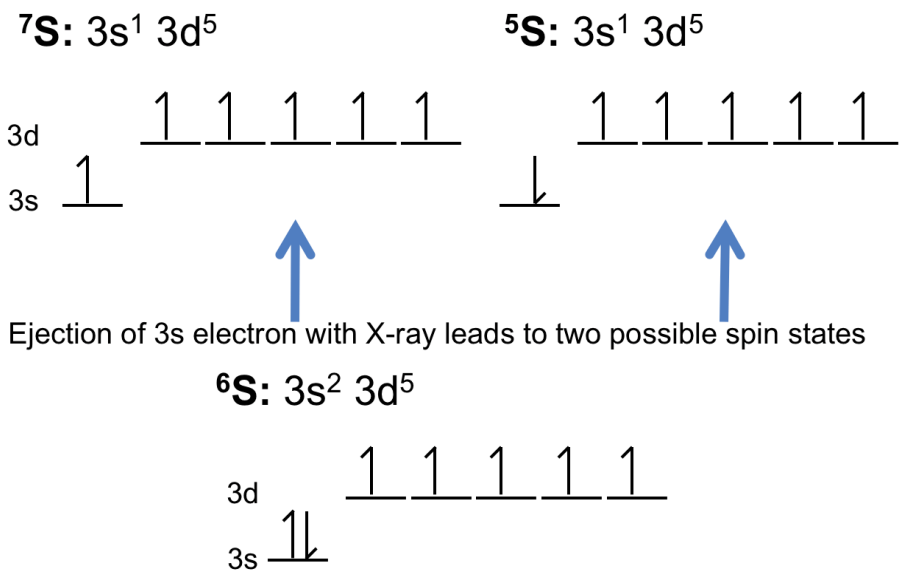

Figure 1.28. Electron levels of different spin-states in a Mn^{2+} ion. Without X-ray bombardment, the Mn^{2+} ion (bottom) has two electrons in the 3s electron and five electrons occupying the 3d orbitals, resulting in a spin state of ^{6}S. Upon ejection of a 3s electron with an X-ray, two spin states develop, one in which the remaining 3s electron is parallel to the spins of the 3d electrons (^{7}S, top left), and one in which the remaining 3s electron is anti-parallel to the spins of the 3d electrons (^{5}S, top right).

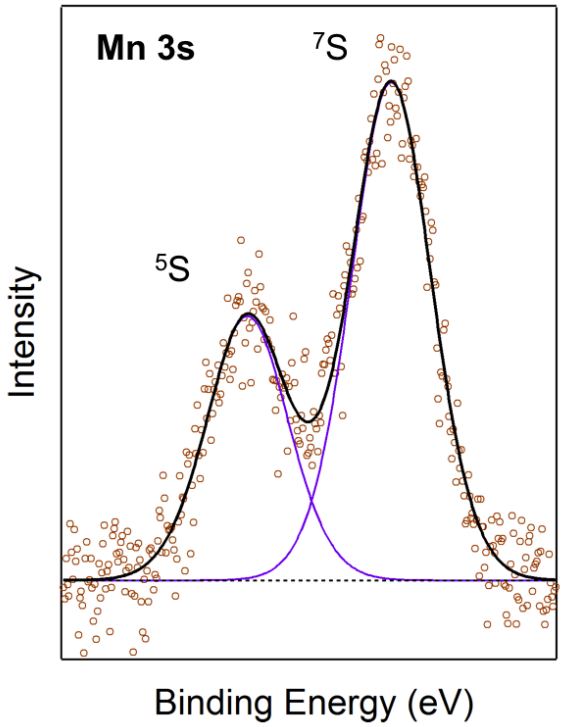

Figure 1.29. Mn 3s spectrum of a Mn^{2+}state. Spin-spin coupling (*i.e.* multiplet splitting) is observed resulting in a parallel ^{7}S state (high intensity) and anti-parallel ^{5}S state (low intensity).

Shake Up/Down Satellites: Shake up and shake down satellites are final state effects that result from a transfer of energy from the outgoing photoelectron to a valence electron, exciting that second electron to either an unoccupied valence state (shake up) or ejecting it entirely (shake down). In either case, the energy transferred to the second electron reduces the KE of the photoelectron creating a satellite structure at an apparent higher BE as per Eq. 1.11. A schematic of the shake up and shake down processes is shown in Figure 1.30 and examples of these peaks may be seen in Figure 1.31.[198] These peaks may also be classified as "charge transfer satellites."

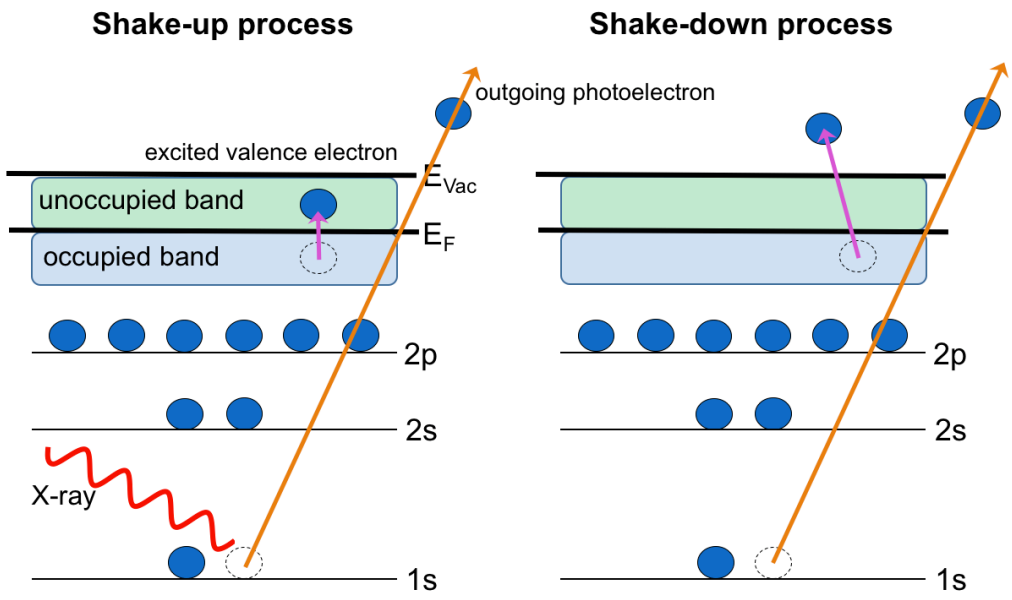

Figure 1.30. (Left) Schematic of the shake-up process. The outgoing photoelectron transfers some energy to excite a valence electron into the unoccupied conduction band, lowering the KE of the photoelectron. (Right) The transferred energy to the valence electron is ejected from the solid in a shake-down process.

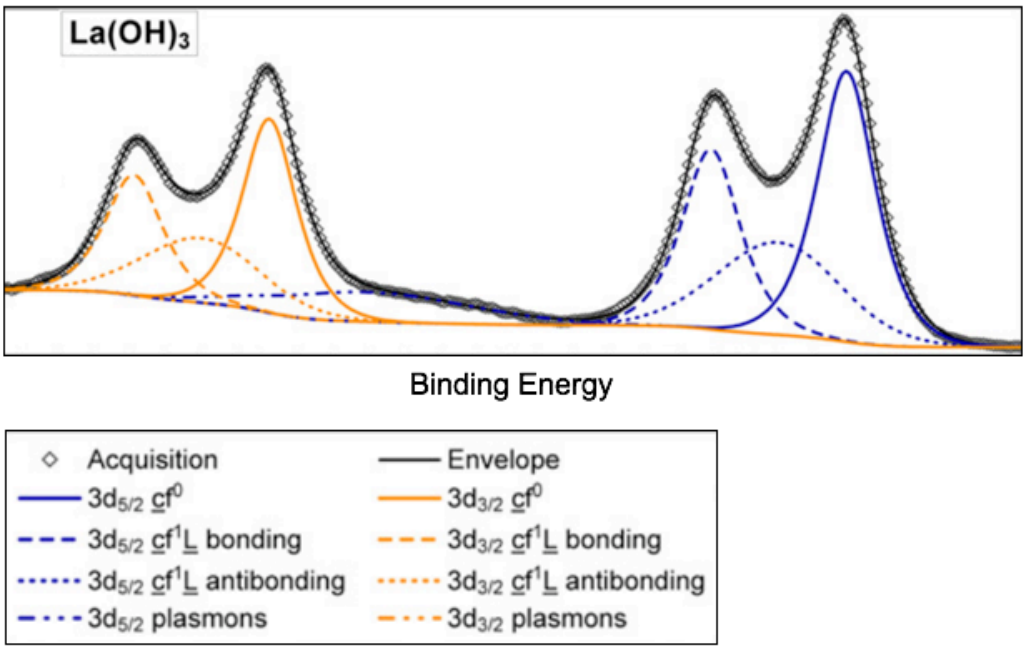

Figure 1.31. La 3d spectrum for $La(OH)_3$, adapted from Ref. 198. Spin-orbit coupling, charge transfer satellites, and plasmons are all present in the spectra. The spin-orbit doublet from the $3d_{5/2}$ (blue) and $3d_{3/2}$ (black) are in solid lines. Two charge transfer satellites are observed for each 3d electron due to a transfer of energy to excite a valence electron into an unoccupied bonding or antibonding orbital in the OH ligand. Finally, each 3d electron excites one plasmon.

Plasmons: Plasmons are a final state effect similar to charge transfer satellites except the outgoing photoelectron transfers a portion of its KE by inducing an oscillation in the electrons of a metal giving rise to a peak at an apparent higher BE. Examples of these peaks may be seen in Figure 1.31.

1.4.1.6 Auger Electrons

Principles: Auger electrons are a type of secondary electron (*i.e.* electrons emitted as a consequence of photoelectron ejection). The process is shown in Figure 1.32. Photoelectron emission leaves behind a "core hole," and an electron from a higher energy level relaxes to fill that hole. The relaxation results in the emission of an X-ray (fluorescence) of energy equal to the difference between the two energy levels and this X-ray is absorbed by another electron in the atom, ejecting it by photoelectric effect principles, leaving behind a two core-hole state.

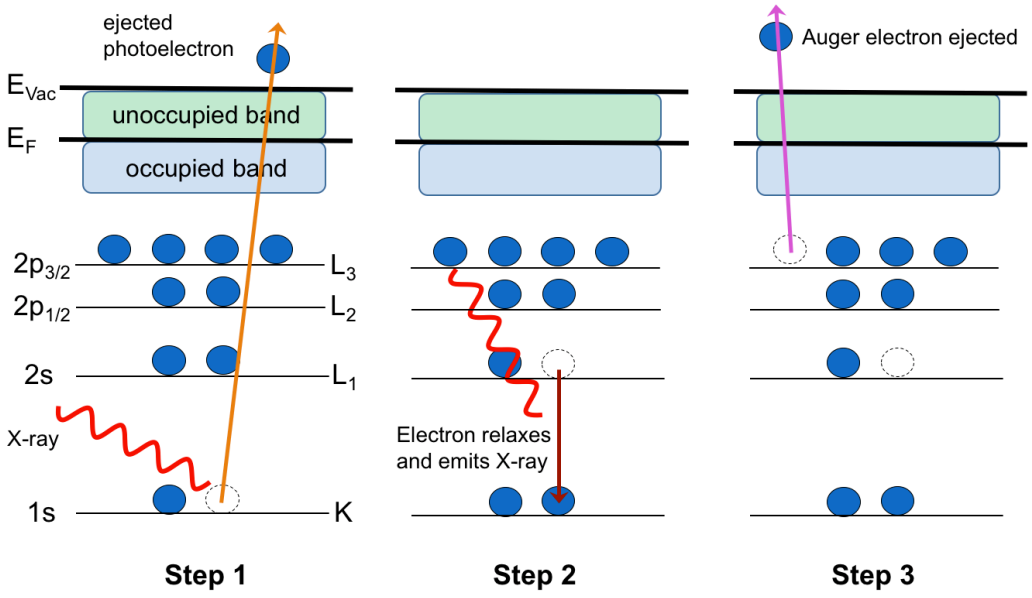

Figure 1.32. Schematic of the Auger emission process. The 2p energy level has been split into two to account for spin-orbit splitting. On the right of the energy levels are the spectroscopic terms for the orbitals. In Step 1, the standard photoelectron ejection happens from the K shell. In Step 2, an electron relaxes from the L_1 subshell and emits an X-ray which is absorbed by a secondary electron in the L_3 subshell. In Step 3, the secondary electron is ejected as an Auger electron.

Naming and Calculating Kinetic Energies of Auger Electrons: Auger electrons are named from the spectroscopic notation. In spectroscopic notation, the energy level of an electron is described by the term, X_y, where X denotes the principle quantum number and y denotes the quantum number, *j* (see Section 1.4.1.5), as shown in Table 1.1.

Sometimes, when the electron of interest is from the valence shell, the term V will be used for the X_y term.

Table 1.1. A list of the names of common orbitals according to Spectroscopic Notation.

X_y	**s** (y = 1)	$\mathbf{p_{1/2}}$ (y = 2)	$\mathbf{p_{3/2}}$ (y = 3)	$\mathbf{d_{3/2}}$(y = 4)	$\mathbf{d_{5/2}}$ (y = 5)
n = 1 (X = K)	K	---	---	---	---
n = 2 (X = L)	L_1	L_2	L_3	---	---
n = 3 (X = M)	M_1	M_2	M_3	M_4	M_5
n = 4 (X = N)	N_1	N_2	N_3	N_4	N_5

Going down a column the principle quantum number, n, increases and the X term increases alphabetically. Going across a row, the orbital and corresponding *j* quantum number change in order of decreasing BE and the y term increases.

An Auger electron is named by the three electrons involved in the process. The Auger electron emitted in Figure 1.32 would be named, KL_1L_3. The first term, K, indicates that the initial photoelectron is ejected from the K shell (1s), the second term, L_1, signifies that the relaxing electron is from the L_1 subshell (2s), and the third term, L_3, refers to the Auger electron that is ejected from the L_3 state ($2p_{3/2}$).

The energy of this Auger electron can be approximated according to the formula:

$$KE_{(\text{Auger e-})} = (BE_{\text{photo e-}} - BE_{\text{relaxing e-}}) - BE_{\text{Auger e-}} \qquad \textbf{(Eq. 1.17)}$$

where the $(BE_{\text{photo e-}} - BE_{\text{relaxing e-}})$ term gives the energy of the fluorescent X-ray which is subsequently absorbed by the auger electron, ejecting it, provided the X-ray is high enough energy to overcome the BE of the auger. Because the KE of the Auger electron is determined only by the BE of electronic states within the atom, KEs of Auger electrons are not influenced by the energy of incident X-rays.

Often for simplicities sake, Auger electrons are grouped together by a general term such as KLL, which encompasses all the possible Auger electrons that result from those shells (*e.g.* there will be peaks of two different energies corresponding to KL_1L_1 compared to KL_1L_2). Thus Auger spectra are complicated and widespread due to the multitude of Auger electron energies. An O KLL (or KVV since L represents the valence shell) spectrum is shown in Figure 1.33.[189]

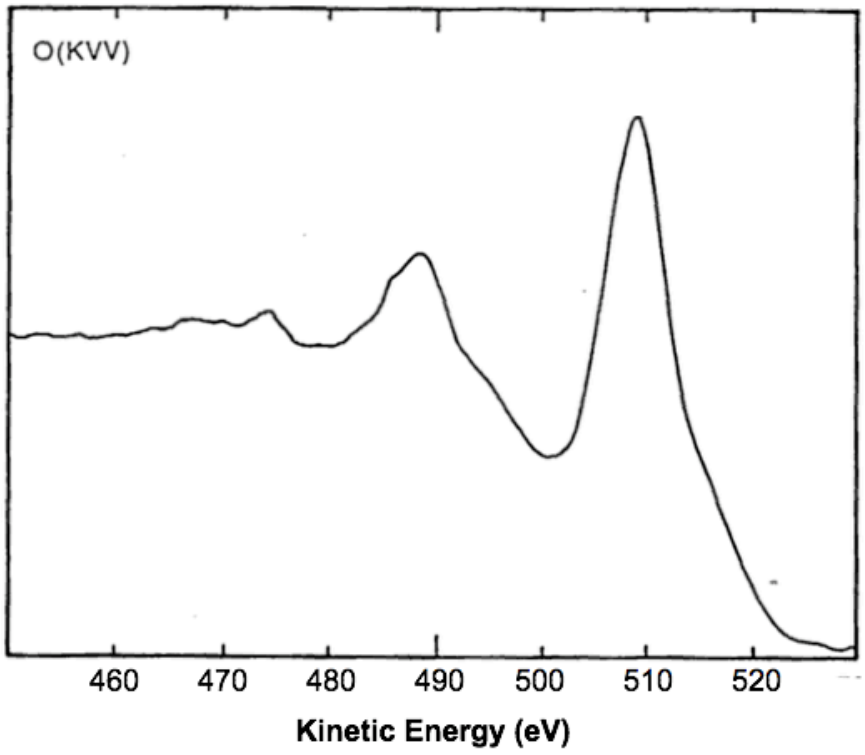

Figure 1.33.[189] Spectrum of the O KVV range of Auger electrons. In the resource the spectrum was taken from, V was used in place of L emphasizing that L is the valence shell.

1.4.1.7 Surface Information:

Aside from identifying which atoms are present on a surface, XPS can be used to determine, oxidation states, atomic ratios, surface speciation, or local surface potentials. Basic principles behind each are described in this section.

Oxidation states: In the simplest situation, shifts in BE can be used to determine changes in oxidation state as described in Section 1.4.1.4. Sometimes the situation is more complicated and other methods, more specific to the atom of interest, must be used (*e.g.* Mn or Ce). These methods are described further in the dissertation when relevant.

Atomic Ratios: The ratio between two different species can be calculated by comparing the intensity of a photoelectron peak (typically the largest) from each of atom with some correctional factors[189]:

$$\frac{n_1}{n_2} = \frac{\left(\frac{I}{f\theta\gamma AT\sigma\lambda}\right)_1}{\left(\frac{I}{f\theta\gamma AT\sigma\lambda}\right)_2} \qquad \textbf{(Eq. 1.18)}$$

where the subscripts 1 and 2 indicate the two types of species, n is the number of atoms/cm^3, I is the intensity of the peaks, f is the X-ray flux, θ is related to the angular efficiency of the instrument, γ is the efficiency of the photoelectric process for forming photoelectrons, A is the area of the sample under study, T is the detection efficiency for the electrons, σ is the photoionization cross section, and λ is the IMFP. The "fθγATσλ" term is typically grouped together as a single quantity, "s," where s is called the "sensitivity factor."

In Eq. 1.18, most of the terms in the sensitivity factor terms will be constant and cancel out between the two atoms. The two primary correctional factors are the cross section and IMFP which are unique to each photoelectron at any given photon energy.

Surface Speciation: Species that migrate to or form at the surface will typically have a higher BE than in the bulk. The higher BE can largely be understood in terms of the extra-atomic relaxation energy (Section 1.4.1.4). Because species near the terminal-surface layer (*i.e.* the top of the surface) are not as well-coordinated as those deeper in the surface, the screening effect from neighboring atoms is not as great and the BE appears higher. Furthermore, the valence band of the under-coordinated atoms narrows producing a different charge distribution (and potential) in the upper surface.[199]

Surface Potentials: The potential at any given point on an operating electrochemical cell surface can be calculated by exploiting the charging effect described in Section 1.4.1.2. When a bias is applied on a SOC, the voltage will drop across the cell from one electrode to the other and the voltage accumulated at any given spot on the surface will shift the BE of all photoelectron peaks in the same manner as when a charge builds up on an electronically insulated surface.[24-27,180] For example, if a Au electrode was scanned under OCV conditions, the distinct Au 4f peaks would appear at 84.0 eV and 87.6 eV. However, if a +1.5 V bias is applied, the peaks would shift by +1.5 eV (see Figure 1.34).

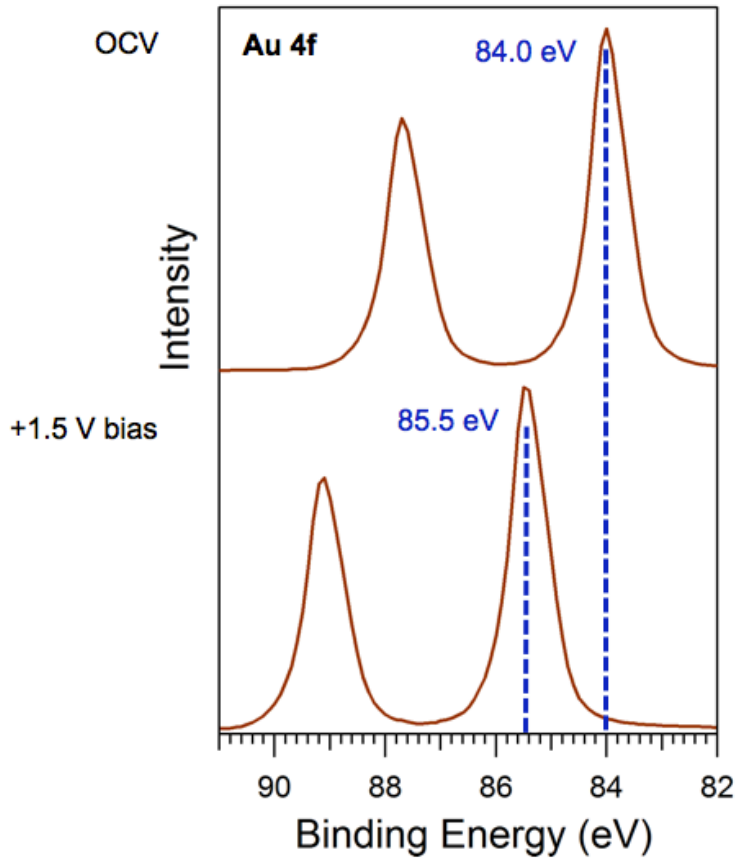

Figure 1.34. Au 4f peaks of a Au sample under OCV (top) and +1.5 V bias (bottom) in which the peaks have shifted by +1.5 eV BE.

A very simple relation can thus be made between surface potential (*i.e.* "local voltage") and the shift in BE of photoelectric peaks between OCV and biased conditions:

$$V_L = BE_{bias} - BE_{OCV} \quad \textbf{(Eq. 1.19)}$$

where V_L is the local voltage in units of V, and BE is in units of eV.

By measuring the BE of photoelectric peaks along an electrochemical cell in OCV and biased conditions, XPS can be used as a non-contact method of

measuring local surface potentials, polarization losses (and associated resistances), and regions of electrochemical activity. For example, the Eichhorn group utilized this method in AP-XPS studies on a single-sided SOC using ceria and Pt electrodes on a YSZ electrolyte in an H_2O/H_2 atmosphere. The potential map generated at +1.2 V polarization may be seen in Figure 1.35.[26] In this cell, the Pt electrode is biased while the ceria (with a Au current collector) is grounded. The potential map (in red) shows that the Pt electrode surface "feels" the full 1.2 V bias applied up to the YSZ interface where there is a sharp drop indicating that all electrochemical activity occurs at the TPB (as predicted by previous electrochemical performance research,[21] but never spectroscopically seen before). A linear voltage drop is observed along the YSZ in agreement with the ohmic losses from oxide ion conduction (see Figure 1.11). At the ceria electrode a voltage drop is observed, but it is *not* sharp or at the TPB, but is gradual and extends radially away from the Au current collector, indicating that the region of active electrode material extends over several hundred microns and that a "bulk path" mechanism is followed, in agreement with ceria being a MIEC electrode (see Figure 1.7). Eventually the potential drops to 0, because the ceria/Au electrode is grounded.

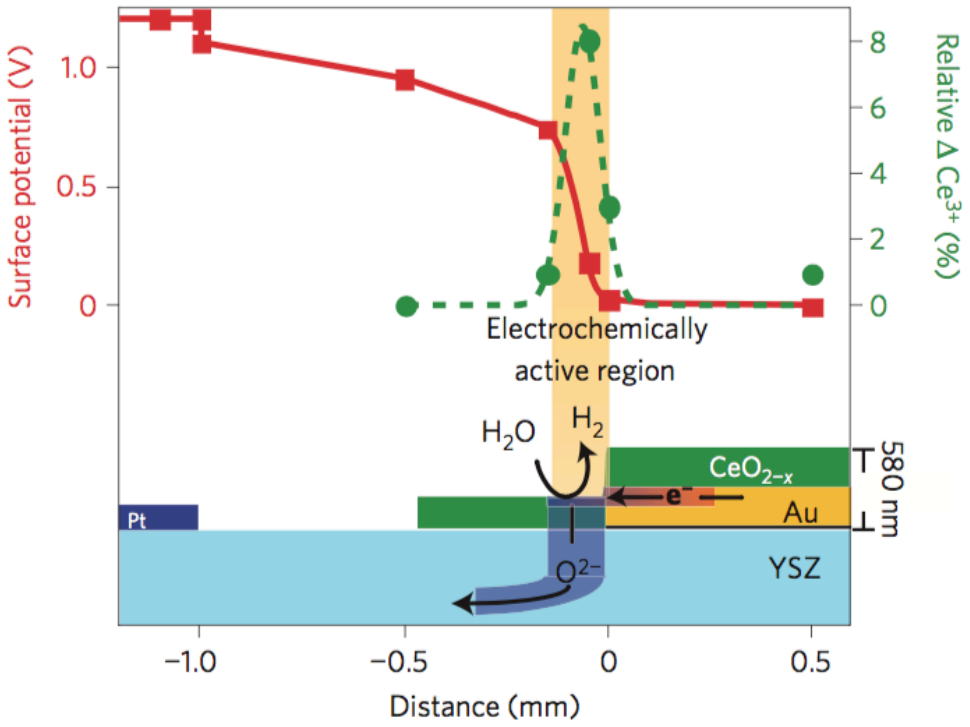

Figure 1.35.[26] Surface potential (left axis, red) measured at different points of an operating SOC.

1.4.1.8 AP-XPS at the Advanced Light Source

The surface information that can be extracted by XPS is valuable for understanding processes that occur in operating SOC, but conventional XPS units require UHV conditions to operate, and are typically not compatible with the high operating temperatures.

The Advanced Light Source (ALS) allows for performance of *in operando* AP-XPS studies at more realistic temperatures. A combination of two technologies allow for these studies, the synchrotron-based radiation source which yields X-ray brightness of roughly 6~11 orders of magnitude higher than conventional XPS units[200] and the differentially pumped electrostatic lens detector, both of which will be described in this section.

***Synchrotron Radiation Source*:** the light source at ALS is a third generation synchrotron. A schematic of the facility maybe viewed in Figure 1.36.[200] The production of radiation consists of four steps. The first step is to accelerate electrons produced from a heated barium aluminate cathode through a linear accelerator (LINAC).[201] The second step is to inject the accelerated electrons into the "booster synchrotron." The third step is to accelerate the electrons by increasing the strength of a magnetic field which directs the particles around the booster ring until they have reached 99% the speed of light. The final step is to release the particles into the "storage ring," another synchrotron. In the storage ring, magnetic fields are used to continuously radially direct and accelerate the electrons. The acceleration produces radiation of a broad wavelength spectrum. This radiation (typically X-rays) can be directed into a "beamline" that connects to an instrument. The beamline is equipped with a monochromator that controls the specific energy of photons used.

The flux of X-ray photons that make it through the monochromator will vary based on the photon energy selected, but at any given energy, the flux is still much higher than in a conventional X-ray source. Because orders of magnitude more X-rays are bombarding the sample, and subsequently orders of magnitude more photoelectrons escape, it becomes possible to detect electrons in non-UHV conditions.

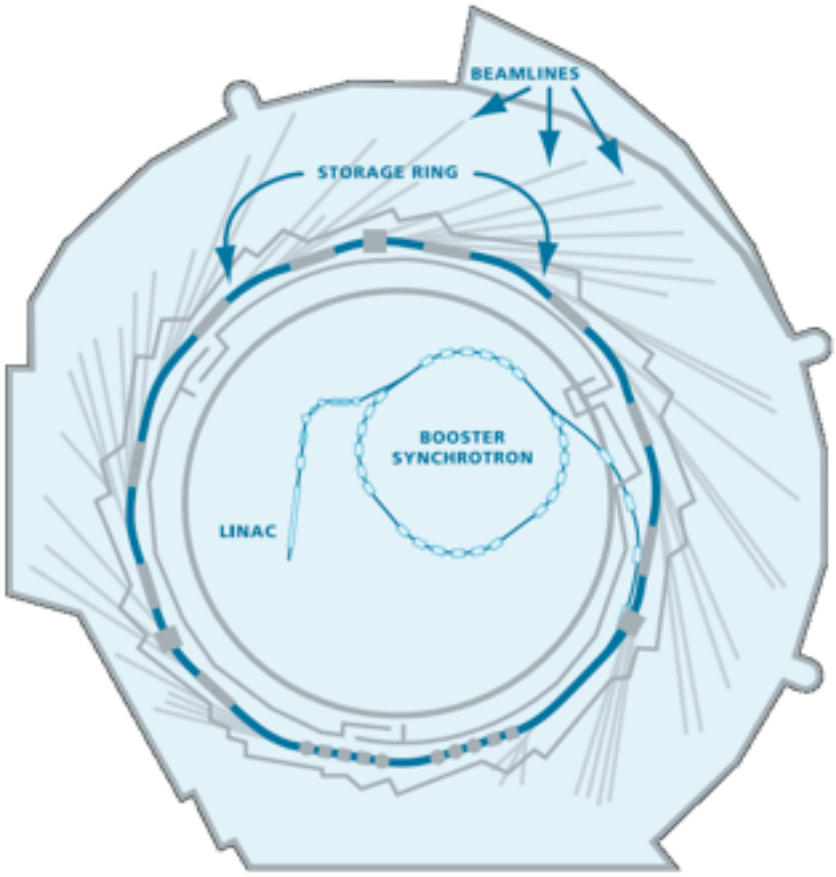

Figure 1.36.[200] Schematic of the ALS synchrotron facility.

Differentially Pumped Electrostatic Lens System: The detector used at ALS allows for the capture of photoelectrons, even when the sample is in a gaseous environment, due to differential pumping and close proximity to the sample surface. A schematic of the lens system is shown in Figure 1.37.[202] In this system, photoelectrons emitted from the sample travel through a series of stages at different levels of vacuum (so that the analyzer is at UHV) as the apertures between each stage become smaller. Lenses between different stages are used to refocus the electrons to allow for these smaller apertures. The first aperture of the system is

placed at a distance from the sample that is determined by the first aperture size typically on the range of 0.1–1.0 mm.

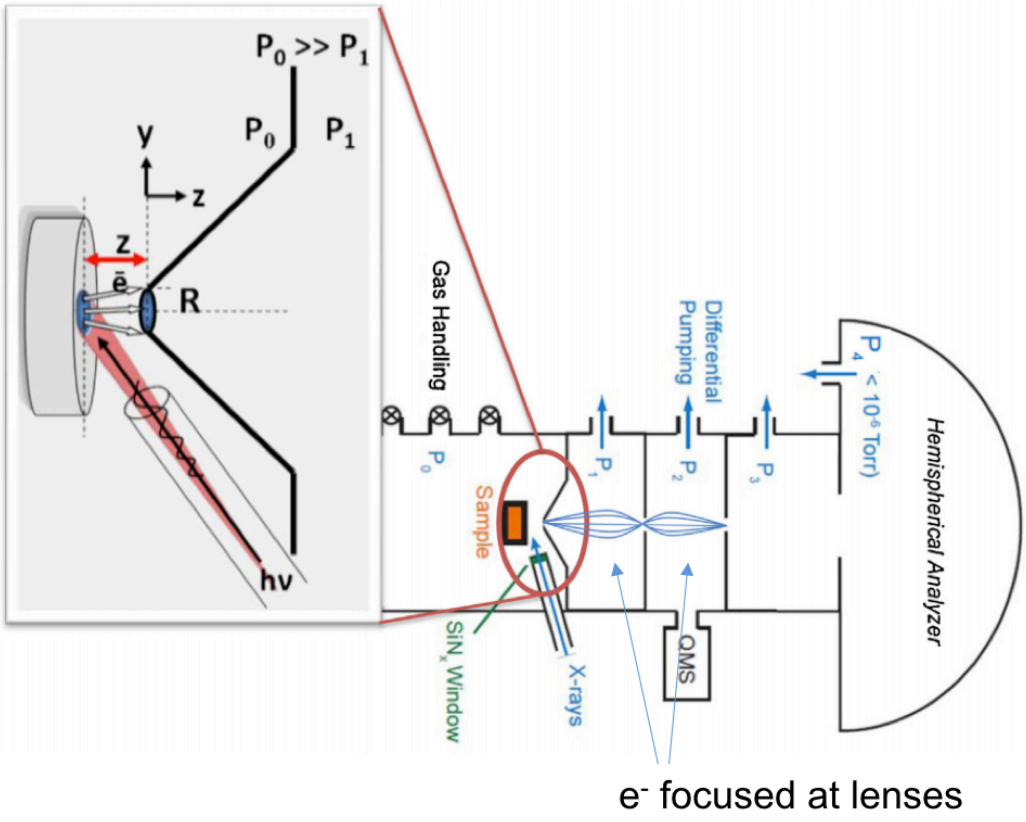

Figure 1.37.[202] Schematic of the differentially pumped electrostatic lens system.

The high flux of photoelectrons from the high synchrotron X-ray production in combination with this differential pumping system is what allows for a reasonable signal, even in environments in the Torr range of pressure.

Depth Profiling: While the primary advantage of the synchrotron is the high intensity of X-rays, another useful feature is found in the wide range of X-ray photon energies that can be accessed. Whereas a conventional unit typically only provides two photon energies (see Section 1.4.1.2), a synchrotron source gives a

spectrum. The spectrum of available energies gives very precise control over a photoelectron's outgoing KE which in turn allows for control over the electron's IMFP (as described in Section 1.4.1.3), which can be directly correlated to the depth of the emitting atom. While depth probing can be accomplished with a conventional unit, the method involves altering the angle of the sample so that photoelectrons are ultimately emitted from shallower depths. Depending on experimental goals (*e.g.* measuring multiple photoelectrons at the same depth), depth profiling in this manner can be more complicated than simply changing a photon energy, as allowed by a synchrotron radiation source.

1.4.2 X-ray Absorption Spectroscopy

1.4.2.1 General Principles

X-ray absorption spectroscopy (XAS) has some similarities to XPS, but a key difference is that it measures the absorption of X-rays rather than ejected electrons. This distinction allows for different information to be acquired such as what electron excitations occur within the atom (electronic structure details), interactions with other atoms as the electron escapes (lattice structure details), and information regarding the bulk and surface of a material.

The technique involves scanning over a range of photon energies lower and higher than the energy needed to eject the electron from the solid (E_{vac}), and measuring the intensity of absorbed X-rays at any given photon energy. Because the technique relies on a spectrum of energies, it can *only* be conducted at a synchrotron light source (see Section 1.4.1.8). XAS scans are divided into two distinct regions, the region within the ~50 eV of the studied electron's BE, called

the "near edge X-ray absorption fine structure" (NEXAFS), and the region beyond that called, "extended X-ray absorption fine structure" (EXAFS). The NEXAFS region primarily gives electronic structure details while the EXAFS region gives structural information. The NEXAFS region was of particular interest in this work, and will be the focus of this section.

Figure 1.38[203] shows a Mn K edge NEXAFS spectrum of three different Mn compounds. For simplicity, the $Mn(II)(acac)_2(H_2O)_2$ spectrum (red) will be the focus of this discussion. In XAS studies, the spectroscopic terms detailed in Table 1.1 are used, thus the Mn K edge follows excitations and ejection of a Mn 1s electron. At ~6544 eV, the photon is just energetic enough to overcome the 1s electron BE, *i.e.* the energy required to excite the electron to the fermi level (first unoccupied energy state), NOT eject the electron from the atom. The lowest unoccupied states are in the narrow 3d band, however, because an s-to-d transition (process 1 in Figure 1.38) is forbidden by the selection rule, $\Delta l \pm 1$, the transition has a very low probability of occurring (allowed by hybridization of d and p states) and only a small intensity change is observed in the "Pre-edge" region. At photon energies of ~6546 eV (process 2), 1s electrons can be excited to the 4p band above which the electron enters the continuum. This transition is allowed and shows a high intensity of X-ray absorption, and this region is known as the "Edge region." At ~6554 eV, the E_{vac} level is accessed, and the electron is ejected (process 3). The intensity begins to decrease with increasing photon energy because the photoionization cross section decreases as the difference between hν and BE increases.

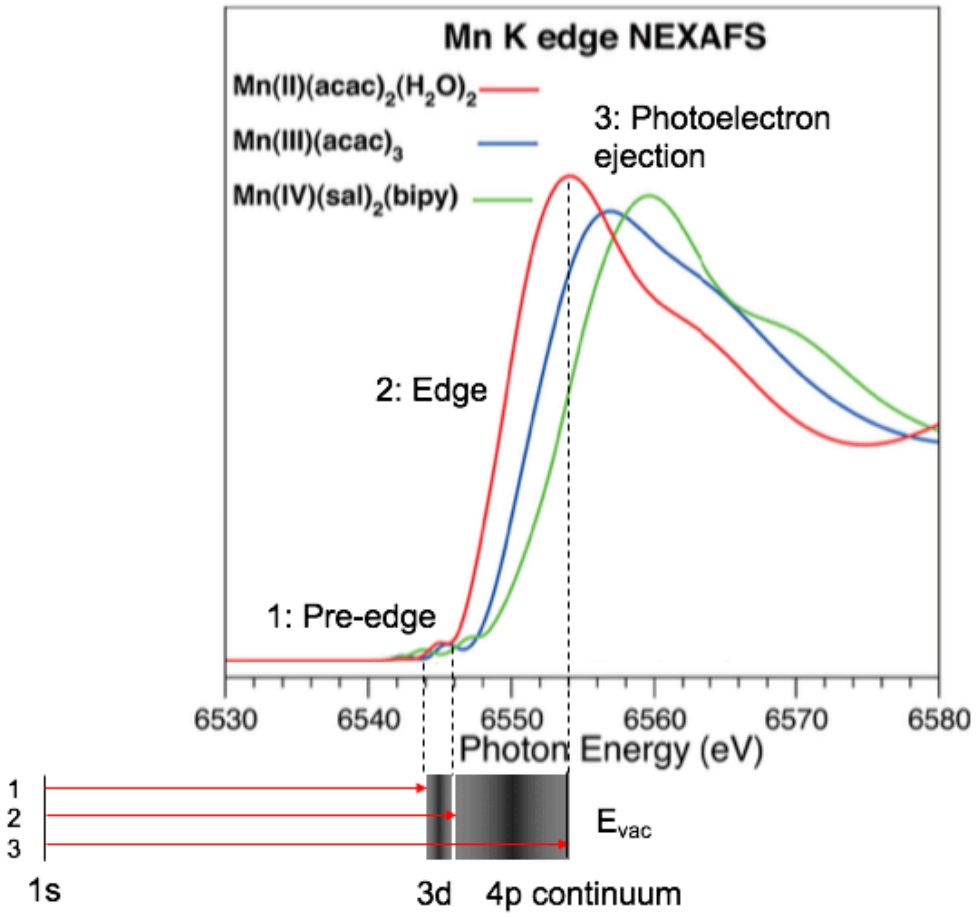

Figure 1.38. Mn K Edge NEXAFS spectra for three Mn compounds adapted from Ref. 203. Three distinct regions are observed and correlate with the 1s electron excitations shown in the lower inlay.

Theoretically, the edge is defined as the energy at which the "Edge region" begins. Experimentally the edge (E_o) is measured as the point where the first derivative reaches maximum value in the region. Oxidation state information can be acquired by monitoring shifts in the edge to higher energy when the atom is oxidized. This phenomenon can be observed in Figure 1.38 where the Mn oxidation state increases between the compounds and the corresponding edges increase in

energy, similar to an XPS spectra. For more complex NEXAFS spectra, sometimes a large change in oxidation state (> ±1) will change the entire spectrum shape, which is another way to monitor changes.

1.4.2.2 Detection Methods

There are three primary detection methods used in XAS, each of which probes a different depth of the material. In order of increasing surface sensitivity, they are: transmission, fluorescence, and electron yield-based methods.

***Transmission Detection*:** transmission detection is a "photon-in, photon-out" detection method in which the intensity of X-rays that pass through the entire sample are measured. The method can only be used with thin foils but gives information on the entire material bulk. The degree of absorption can be understood via Beer's Law:

$$I(t) = I_o e^{-\mu t} \qquad \textbf{(Eq. 1.20)}$$

where I(t) is the X-ray intensity that makes it through the sample, I_o is the original intensity, μ is the absorption coefficient at the X-ray energy, and t is the sample thickness.

Fluorescence Detection: Fluorescence detection does not measure the incident X-rays hitting the sample, but fluorescent X-rays emitted as a *consequence* of X-ray absorption. As detailed in Section 1.4.1.6, when an atom absorbs an incoming photon and an electron is excited or ejected, relaxation processes will occur emitting fluorescent X-rays. These X-rays may excite another electron

resulting in Auger electron emission, or the X-rays leave the system and can be detected. The greater the degree of incident X-ray absorption, the greater the degree of fluorescent emissions, and the higher the fluorescence intensity detected. Because the method is based on measuring X-rays which can escape from greater depths than photoelectrons, fluorescence NEXAFS is considered a bulk probe on the order of hundreds of nm.[204,205]

***Electron Yield*:** Like fluorescence, electron yield is an indirect method of measuring absorption of incident X-rays. As stated above, the fluorescent X-rays from relaxation processes may eject Auger electrons. Some of these Auger electrons will leave the system without loss of energy (*i.e.* any collisions are elastic), but many leave after experiencing inelastic collisions – possibly ejecting electrons of yet another KE. Consequently, as more incident X-rays are being absorbed and more auger electrons are being emitted, an increase of electrons of energies ranging from zero up to the KE of the original Auger electron will be detected (see Figure 1.39). Measuring the increase of all ejected electrons is called, "total electron yield" (TEY). Secondary electrons that have lost a specific amount of energy from inelastic scattering can also be measured in which case the detection is called, "partial electron yield" (PEY). PEY data collection provides greater confidence in the source of the absorption signal as the photons that strike the sample will likely eject other photoelectrons and Auger electrons in addition to the core electron of interest—all of which will be detected in TEY mode. However, PEY does require a more complicated experimental set-up (*e.g.* a detector which can selectively measure electrons of a particular energy).[206]

The work in this dissertation (Chapter 5) utilized PEY detection methods and the information depth was on the order of nanometers (because it is based on electron IMFP).

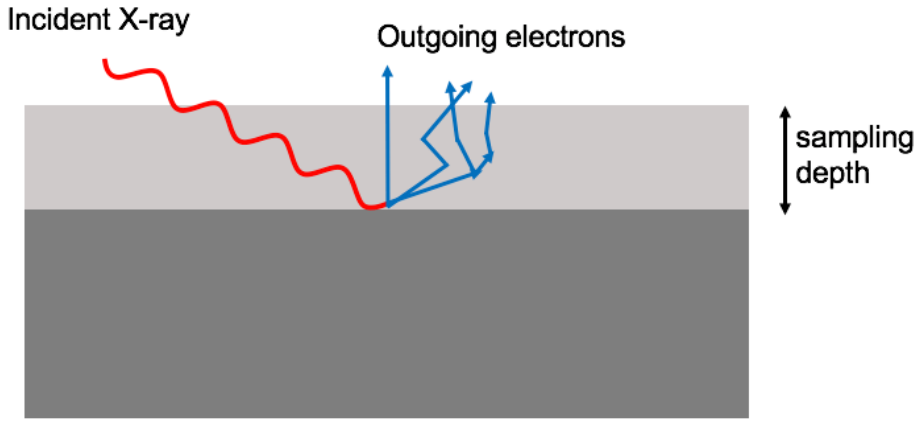

Figure 1.39. A schematic of outgoing secondary electron (*i.e.* not a photoelectron) emission as a consequence of X-ray absorption. An X-ray is absorbed releasing Auger electrons, some of with make it out of the sample surface with no loss of energy, some experience inelastic collisions, ejecting other electrons as well, all of which are detected.

1.4.3 Near Infrared Imaging

1.4.3.1 Theoretical Principles

Near infrared (NIR) imaging, or thermal imaging, is a bulk analysis technique typically used for measuring the temperature of a system and can monitor processes *in situ* and *in operando* by tracking temperature changes in a system from associated thermodynamics. As will be described below, changes in a material's optical properties can also be tracked by this method although this is not as typical.

The technique is based on blackbody radiation theory. The intensity of NIR radiation (photons of wavelength ~700 to 1400 nm) emitted by an object is

measured, and will be different at any given temperature (see Figure 1.40).[207] By using blackbody radiation curves, the temperature of an object can be calculated.

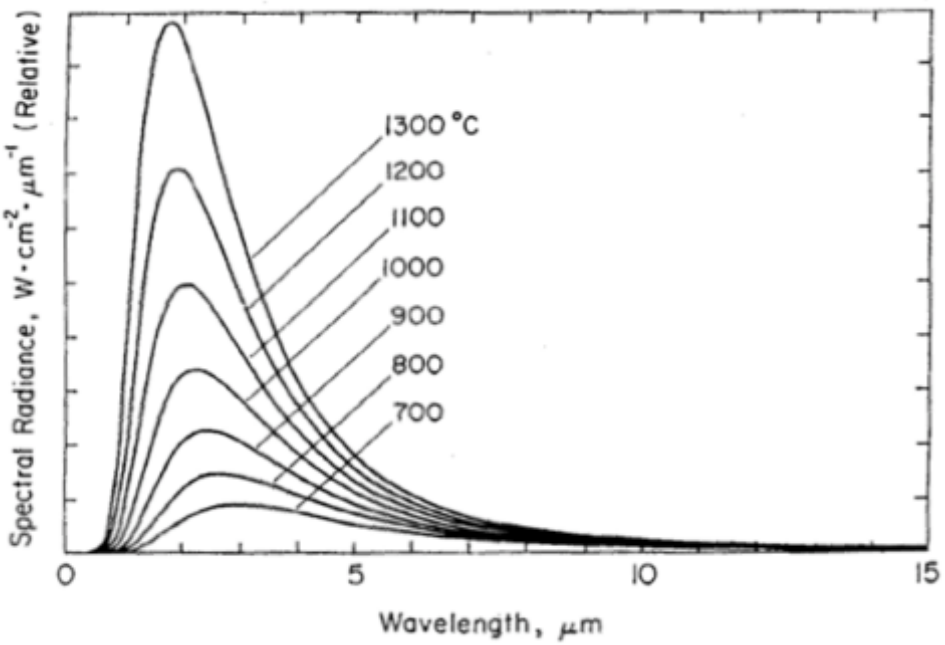

Figure 1.40.[207] Radiation levels as a function of wavelength at different temperatures at which IR radiation is the dominant radiation.

However, on most materials, the temperature reading will be incorrect because they do not behave as blackbodies. A blackbody is an object which absorbs all radiation and emits it at the same intensities:

$$1 = A \qquad \textbf{(Eq. 1.21)}$$

where A is the "absorbance" of a material, *i.e.* the fraction of incident radiation that is absorbed, which in the case of a blackbody is 100%. Any photon absorbed will be emitted (in random directions), thus Eq. 1.21 can be expressed as:

$$1 = \varepsilon \quad \textbf{(Eq. 1.22)}$$

where ε is the "emissivity" of an object, *i.e.* the fraction of how photons that are absorbed and re-emitted by a material. On a non-blackbody, not all of the incident radiation is absorbed/re-emitted. Some is transmitted through the material and some is reflected. For a non-blackbody, Eq. 1.22 must be modified to:

$$1 = \varepsilon + T + R \quad \textbf{(Eq. 1.23)}$$

where T is the fraction of radiation transmitted ("transmittance") and R is the "reflectivity" of the material (fraction of light reflected). The R and T properties will lead to detected intensities of NIR radiation that are not in agreement with the values known for a blackbody, and the calculated temperature of an object will be incorrect. However, as most *in operando* NIR imaging studies are concerned with changes in temperature or NIR radiation intensities, determining an accurate temperature value is not necessary.

1.4.3.2 *In Operando* NIR Intensity Measurements

Historically, this technique has been used to monitor processes on a SOC by tracking temperature changes from thermodynamics associated with those processes.[30-37] For example, researchers at the Naval Research Lab (NRL) studied hydrocarbon cracking on a Ni/YSZ anode[31] as shown in Figure 1.41. The left image shows a NIR intensity image (with intensity to temperature calibrations on the right side) of the Ni/YSZ material in a H_2 atmosphere. The temperatures of different parts

of sample *appear* different because of differences in emissivity and reflectivity values as explained above (the materials are opaque and transmission is ignored). When $H_{2(g)}$ was replaced with $CH_3OH_{(g)}$, the temperature decreased as a result of endothermic hydrocarbon cracking.

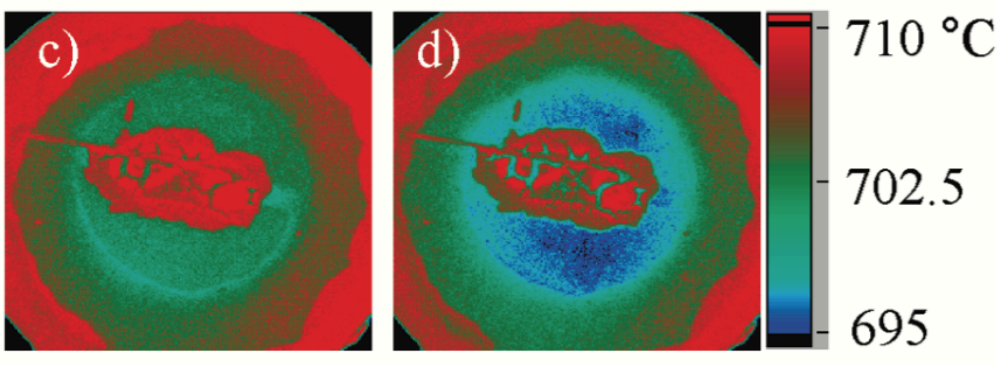

Figure 1.41.[31] Temperature profiles (*i.e.* NIR intensity maps) of a Ni/YSZ material exposed to $H_{2(g)}$ (left) and $CH_3OH_{(g)}$ (right) which causes endothermic hydrocarbon cracking to occur.

While NIR imaging is commonly associated with temperature monitoring, it can also be used to track variations in a material's optical properties from changes in the material itself. For instance, when ceria is reduced, its optical properties change[38,208,209] so that the measured NIR intensity decreases giving the appearance that the sample is decreasing in temperature. This concept will be explored in greater detail in Chapter 4, which focuses on NIR *in operando* studies.

1.5 Scope of Dissertation

This dissertation provides details on the protocols developed for *in operando* research and the results from these studies on SOCs. Extracting mechanistic information from investigating SOCs is important for the rational design of future cells.

The work described involves close collaboration with research groups run by Dr. Hendrik Bluhm and Dr. Ethan Crumlin at the Advanced Light Source and the research group run by Dr. Jefferey Owrutsky at the Naval Research Laboratory. Collaborations with Dr. Eric Wachsman and Dr. Ichiro Takeuchi at the University of Maryland, College Park, have been integral toward this work as well. Some of the results have been or will be published, as follows:

1. Aaron Geller, Angelique Jarry, Yi Yu, Luning Wang, Xiaohong Zhang, Yangang Liang, Noah Masika, Ichiro Takeuchi, Hendrik Bluhm, Ethan Crumlin, Bryan Eichhorn, "*In Operando* Heterogeneous Electrocatalytic Studies of Oxygen Reduction and Evolution on Lanthanum Strontium Manganite Electrodes" *In preparation.*

2. Yi-Lin Huang, Christopher Pellegrinelli, Aaron Geller, Sz-Chian Liou, Angelique Jarry, Luning Wang, Yi Yu, Hendrik Bluhm, Ethan Crumlin, Bryan W. Eichhorn, Eric D. Wachsman, "Direct Observation of Enhanced Water and Carbon Dioxide Reactivity on Multivalent Metal Oxides and Their Composites" *Submitted.*

3. Aaron Geller, Michael Pomfret, Daniel A. Steinhurst, Yi Yu, Zhi Liu, Jeffrey C. Owrutsky, Bryan W. Eichhorn, "Operando Tracking of Electrochemical Activity in Solid Oxide Electrochemical Cells By Using Near Infrared Imaging" *ChemElectroChem.*, **2015**, *2*, 1527.

4. Yi Yu, Baohua Mao, Aaron Geller, Rui Chang, Karen Gaskell, Zhi Liu, Bryan W. Eichhorn, "CO2 Activation and Carbonate Intermediates: An

Operando AP-XPS Study of CO2 Electrolysis Reactions on Solid Oxide Electrochemical Cells" *Phys. Chem. Chem. Phys*., **2014**, *16*, 11633.

5. Yi Yu, Aaron Geller, Baohua Mao, Rui Chang, Zhi Liu, Bryan W. Eichhorn, "Carbon Deposits and Pt/YSZ Overpotentials in CO/CO2 Solid Oxide Electrochemical Cells" *ECS Trans*. **2013**, *57*, 3119.

Chapters 2 and 3 detail AP-XPS studies on a symmetrical cell consisting of two LSM electrodes which allowed for simultaneous studies of ORR and OER. Chapter 2 focuses on analysis details for obtaining information on Sr segregation, LSM surface compositions, Mn oxidation state, and surface potentials, and the results regarding ORR promotion. Chapter 3 describes OER findings.

Furthermore, Chapter 3 summarizes AP-XPS thermal studies of LSM and LSM/YSZ composites in different atmospheres to correlate surface information on oxygen vacancies with bulk information regarding oxygen exchange acquired by the Wachsman group.

Chapter 4 describes the use of NIR imaging to monitor water electrolysis on a ceria-based SOC with realistic operating temperatures, pressures, and cell design. The work correlates bulk analysis results on electrochemical ceria reduction in plausible conditions, to results collected from previous AP-XPS model, surface studies.

Chapter 5 details attempts to develop a method for quantifying the oxidation state of cobalt with XPS by measuring a quantity known as the Auger parameter.

Chapter 6 will summarize the findings of Chapters 2-5 and provide an outlook for future research.

2 *In Operando* Studies of Oxygen Reduction on Lanthanum Strontium Manganite Electrodes

2.1 Introduction

Lanthanum strontium manganite ($La_{1-x}Sr_xMnO_{3\pm\delta}$, LSM) is a perovskite material and is one of the most commonly used cathodes for electrochemical promotion of the oxygen reduction reaction (ORR) in solid oxide electrochemical cells (SOCs). LSM has proven favorable because of its electrocatalytic ability for ORR, stability in SOC operating conditions, and suitable thermal expansion coefficient match with yttria-stabilized zirconia ($(ZrO_2)_{1-x}(Y_2O_3)_x$, YSZ), the most common SOC electrolyte.[44,56,79-81] ORR is of particular importance in SOC operation as it is often the rate-limiting process in overall cell function.[1-5] However, the fundamental chemistry behind ORR on a LSM surface is not well-understood, despite the importance and simplicity of the reaction.

ORR is ultimately the reduction of oxygen molecules into oxide ions. On LSM, ORR is typically thought to occur by the following global process (in the forward direction):

$$O_{2(g)} + 2V_o + 4Mn^{3+}_{(lattice)} \rightleftharpoons 2O^{2-}_{(lattice)} + 4Mn^{4+}_{(lattice)} \qquad \textbf{(R2.1)}$$

where V_o represents an oxygen vacancy in the lattice, and $O^{2-}_{(lattice)}$ and $Mn^{3+/4+}_{(lattice)}$ represent oxide and Mn ions in the lattice, respectively. In a simple mechanism proposed by Wachsman *et al.*,[2,39,40] given below, $O_{2(g)}$ is thought to adsorb to the LSM surface and dissociate into two O atoms. Electrons are subsequently

transferred to O from $2Mn^{3+}$ to give O^{2-} ions and $2Mn^{4+}$. The O^{2-} ion is then incorporated into any available oxygen vacancies. If an anodic bias is applied to LSM, the reverse reaction, oxygen evolution reaction (OER), is promoted. The above process can be described with two steps:

$$O_{2(g)} + 2S \rightleftharpoons 2O_{(ads)} \quad \text{(dissociative adsorption, } \mathbf{E2.1}\text{)}$$

$$2O_{(ads)} + 4Mn^{3+}{}_{(lattice)} + 2V_o \rightleftharpoons 2O_{lattice}{}^{2-} + 4Mn^{4+} + 2S \quad \text{(lattice incorporation, } \mathbf{E2.2}\text{)}$$

where S represents a vacant surface site and $O_{(ads)}$ represents oxygen adsorbed on the LSM surface.

Wachsman *et al.*[39-41] used isotope exchange experiments to show that ORR is rate-limited by incorporation of oxide ions into the lattice on LSM. These thermal studies (*i.e.* non-electrochemical) on oxygen exchange with the LSM bulk material yielded important details regarding the ORR mechanism, however, there is a still a paucity of information regarding the state of the LSM cathode *surface* in operating conditions (*in situ*), let alone during operation (*in operando*). For example, surface ratios between the A-site cations (*i.e.* La:Sr) and gradients in these ratios, are not well-predicted by bulk stoichiometry. This ratio difference is largely due to segregation of Sr from the bulk to the surface, so that there is a relative enrichment in Sr atoms at the LSM surface compared to the bulk.

Sr segregation is a well-known phenomenon in LSM (and other Sr-doped perovskites)[17,28,142-146,183,210,211] that has been shown to increase with lower O_2 pressure[142] and increasing temperature.[143] The driving force behind the segregation

is still under investigation, but is generally considered to be due to both electrostatic interactions and lattice strain.[83,144,145] Enrichment of Sr in the lattice surface can further result in an extrusion of Sr to form SrO particles on the surface of the electrode.[17,146] This extrusion of Sr will alter the La:Sr ratio in the LSM surface even further. Additionally, these SrO particles may have repercussions on LSM performance as the particles may act as a "passivating layer" that blocks active surface sites for ORR promotion, resulting in sluggish kinetics.[17]

It is possible that these passivating SrO particles are removed by a short-term application of cathodic bias. It is well-documented that LSM cathode performance increases rapidly during initial stages of cathodic polarization.[17,83,148,149,158] This phenomenon, known as the "activation effect," does not have a clear origin, but a common theory holds that cathodic bias results in the removal of passivating surface species such as SrO. Supporting data was largely provided by Jiang *et al.*[17] who showed that a LSM cathode that was etched with HCl (i.e. SrO surface removal) exhibited an initial electrochemical performance that was close to that of an un-etched LSM electrode, post-activation. The conclusion of these studies was that the activation effect is the result of removal or reincorporation of passivating surface species under cathodic bias. This conclusion was supported by *in operando* X-ray photoelectron spectroscopy (XPS) studies conducted by Huber *et al.*[153] on LSM thin films in ~vacuum conditions (750 nTorr O_2). Huber observed that not only did SrO particles disappear upon cathodic bias, but Sr within the LSM surface lattice did, as well. However, Backhaus *et al.*[154,155] conducted *in operando* XPS studies in similar conditions, and saw an increase in

Sr at the surface upon cathodic bias. Crumlin *et al.*[28] engaged in similar work in "near ambient pressure" (~760 mTorr O_2) on lanthanum strontium cobaltite electrodes and found Sr segregation was promoted by cathodic polarization as well.

In addition to surface stoichiometry, charge distributions at the surface (*i.e.* Mn oxidation states), during ORR remain largely unquantified. Reduction of Mn is associated with the generation of oxygen vacancies, which promote the incorporation of oxygen into LSM.

LSM is typically thought to behave as an electronic conductor, where the electrons presumably transport via Mn centers (thereby reducing Mn), and as an ionic insulator. These properties require all electrochemical activity to occur at the triple phase boundary (TPB), *i.e.* where gas, electrode, and electrolyte meet.[43,72,156] A full explanation of electronic conductor behavior is given in Section 1.2.1.3 (Figure 1.7). Briefly, due to the very low ionic conductivity in LSM, ORR must take place at the electrode/electrolyte interface (which are both exposed to O_2 gas) so that electrons reduce the oxygen into O^{2-} which can then be incorporated into oxygen vacancies in the *electrolyte*, which is more suitable for incorporating and conducting oxide ions than LSM.

Some research refutes the belief that LSM strictly behaves as an electronic conductor, though.[99,157,158,162,212] For example, Fleig *et al.*[20,160] conducted studies on circular thin films of LSM and found that electrochemical performance increased with increasing electrode diameter. This result indicated that not all activity could be occurring at the edge, as an increased surface area would only lead to higher electrochemical activity if part of the interior region of the LSM was active.

The goals of our research are to address the above phenomena and questions regarding the LSM surface and ORR mechanism. We determine the cation ratios between La and Sr, the extent of SrO extrusion out of the LSM electrode, and how these factors change when the electrode is in operation (*i.e*. we determine if SrO is removed by a cathodic bias as some research suggests). We address the oxidation state of surface Mn, and how it changes under cathodic polarization. We identify the regions of electrochemical activity and whether LSM is a more active electrocatalyst for ORR than OER, which is a controversial topic as well (see Chapters 1 and 3).[168-171,213]

To accomplish these goals, we use ambient pressure XPS (AP-XPS) to monitor a symmetrical LSM-based SOC (*i.e.* both the cathode and anode were LSM) surface, *in operando*, in an O_2 environment at temperatures ranging from 500 to 700 ^{o}C. This chapter focuses on the cathodic polarization results. We show that Sr extrudes onto the surface in the form of SrO, and that this extrusion is augmented reversibly by the application of cathodic bias. Additionally, the surface Mn oxidation state is lower than the bulk stoichiometry predicts, and is further reduced during cathodic operation. Lastly, by mapping the surface potentials across the cell, we find that ORR and OER only occur at the electrode/electrolyte interface (*i.e.* the TPB), and that the measured resistance to electrochemical activity is lower for ORR than OER.

2.2 Experimental Information

2.2.1 Experimental Procedures

2.2.1.1 Cell Fabrication

A schematic representation of the symmetrical SOCs used in this study is shown in Figure 2.1. The single-sided cells were fabricated on 10 mm x 5 mm x 1 mm, single-side polished YSZ (8 mol% Y_2O_3) single crystal electrolytes with 111-orientation (*MTI Corporation*). Two 100 nm thick LSM electrodes (3.5 mm x 3.5 mm, l x w) were deposited on the same side by using pulsed laser deposition (PLD) with a 1 mm gap in between them. The LSM stoichiometry was, $(La_{0.8}Sr_{0.2})_{0.95}MnO_{3\pm\partial}$, and the deposition was carried out in 100 mTorr O_2 at 740 ^oC with a fixed laser energy and pulse rate of 25 mJ and 5 Hz, respectively.[214] The LSM/YSZ interface, which is the TPB (when the SOC is exposed to gas), is indicated in the bottom portion of Figure 2.1 by a blue circle.

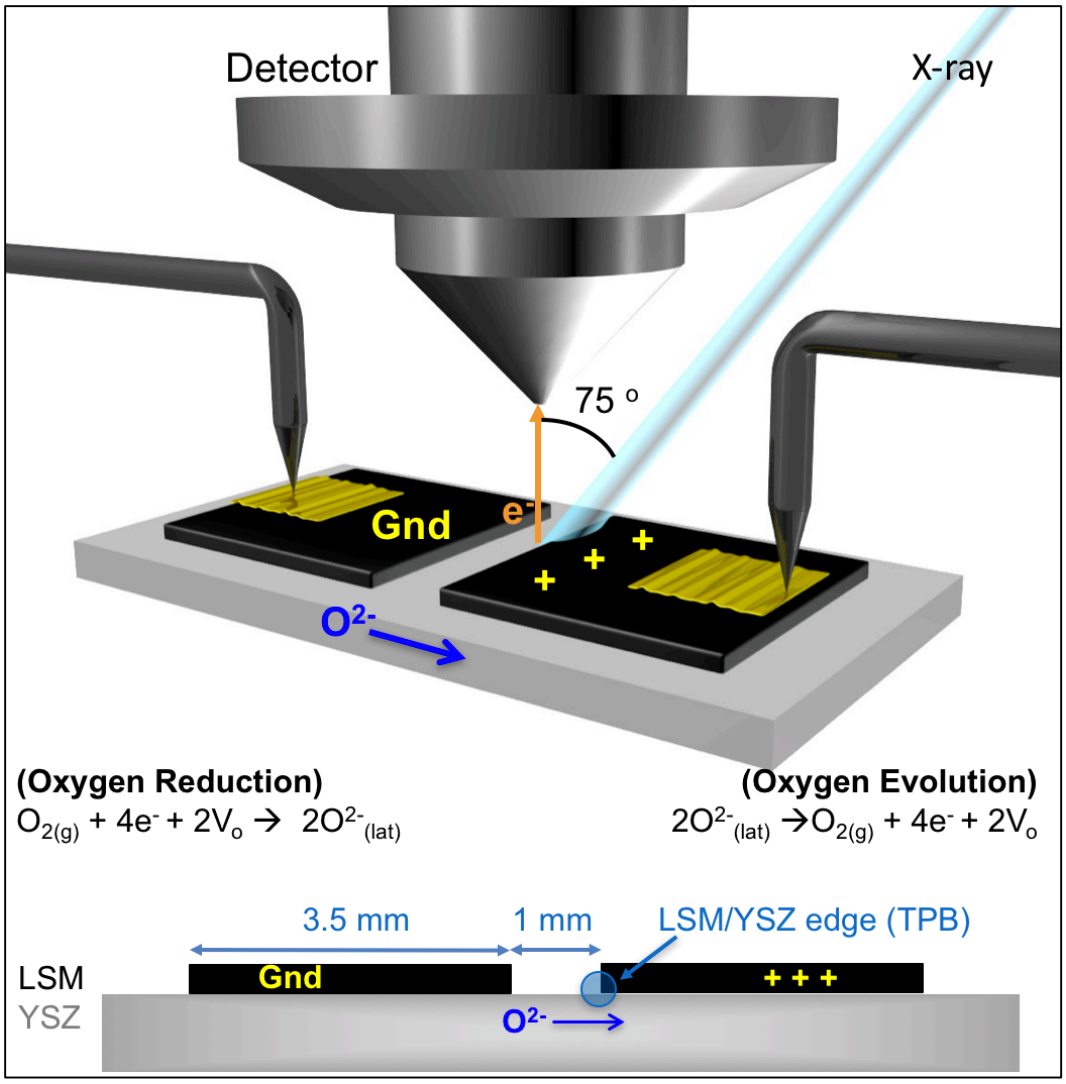

Figure 2.1. (Above) schematic of the symmetric LSM/YSZ cell and the experimental set up. Two 100 nm thick LSM electrodes separated by 1 mm are deposited on a YSZ electrolyte. Au foils are placed on top of each electrode for electrical contact with the leads which connect to a potentiostat. One electrode is anodically biased while the other electrode (cathode) is grounded. X-rays strike the sample at 75° with respect to surface normal and electrons are ejected perpendicular to the surface. (Below) a lateral depiction of the cell and electrochemical process. The LSM/YSZ edge (*i.e.* the TPB) is circled in blue.

2.2.1.2 Experimental Set-Up

Cells were exposed to ~200 mTorr of O_2 at temperatures of 530 ^oC, 620 ^oC, or 680 ^oC depending on the experiment. The temperature was determined by using a thermocouple and measuring the bulk resistance (R_B) value by impedance spectroscopy. The ionic conductivity of YSZ exhibits Arrhenius behavior[215,216] so that its bulk resistance (*i.e.* resistance to ionic transport) is directly related to temperature and a calibration curve between temperature and R_B can be determined. Electrical contacts were made by placing Au foils on top of each electrode, and holding them in place with spring-loaded Au-Pd coated tungsten tips, which also served to hold the sample to the ceramic heater. The cell was connected in a 2-electrode configuration in which the working electrode (WE) was grounded and a positive bias was applied to the counter electrode (CE) through the use of a BioLogic SP-300 potentiostat. Thus the CE functioned as the anode (OER) and the grounded WE behaved as the cathode (ORR), as shown in Figure 2.1.

Cells typically were operated in two cycles, each consisting of recording XPS data at open circuit voltage (OCV) and under polarization (+1.5 V) so that a cell would be studied in the following conditions: $OCV_{cycle\ 1}$, 1.5 $V_{cycle\ 1}$, $OCV_{cycle\ 2}$, and 1.5 $V_{cycle\ 2}$.

Electrical impedance spectroscopy (EIS) tests were recorded at OCV before and after an experiment. Impedance spectra and settings may be found in SI section 2.6.1.

2.2.1.3 AP-XPS Measurements

AP-XPS experiments were performed at the Advanced Light Source (ALS) at the Lawrence Berkeley National Lab (LBNL). Two beamlines, 9.3.2 and 11.0.2, were used for different experiments.

Beamline 9.3.2 delivers X-rays of photon energies between 200 – 900 eV at maximum fluxes of ~10^{11} photons/s. The spot size of the beam is elliptical with diameters of ~0.5 mm and ~1.0 mm. The beamline is also equipped with a 2D area detector that allows spatial resolution of XPS scans into 20 micron increments along a line scan. On this beamline we were able to operate at a maximum temperature of ~530 ^{o}C.

Beamline 11.0.2 gave access to a greater range of photon energies (90 – 2000 eV), higher fluxes (~10^{12} photons/s), and a narrower spot size (50 ~ 200 μm diameter depending on photon energies). We were also able to achieve temperatures of over 600 ^{o}C.

At both beamlines, the samples were oriented so that the X-ray beam strikes the sample at incident angle of 75^{o} and the electron emission angle is 0^{o} with respect to the surface normal, as shown in Figure 2.1. The XPS spectra collected were Sr 3d, La 4d, La 3d, Mn 3s, and Zr 3d. The spectra were analyzed with the CasaXPS program and the details of these spectra are given in the following section.

2.2.2 XPS Spectra: Collection Details and Fitting Parameters

The La 4d and Sr 3d scans were taken at photon energies of 345 eV, 490 eV, and 900 eV for different depths of surface probing (see Section 1.4.1.8). La 3d scans were taken at photon energies of 1085 eV and 1230 eV to eject electrons at

the same kinetic energy (KE) as the La 4d electrons at photon energies of 345 eV and 490 eV. These energies allowed us to probe the same depth of the LSM surface with two different La signatures to establish better confidence in our measurements. We could not achieve reliable signal-to-noise for La 3d at the same depth as the La 4d 900 eV due to poor X-ray flux at that photon energy (1640 eV).

For Mn 3s scans, only two energies were used; 490 eV and 900 eV. For Zr 3d, only a photon energy of 490 eV was used.

All spectra were fit with a Shirley background. The Sr 3d, La 4d, and La 3d XPS spectra are complicated and some of the fitting parameters we needed for the peaks are not well-established. Thus, some fitting parameters were determined empirically, by using the following general procedure (specific details for fitting each XPS spectra are given further below).

We took all of the OCV scans collected on a cell for the spectrum of interest, introduced the peaks that we knew to be present, and implemented any constraints that are well-established (*e.g.* the branching ratio and FWHM constraints between spin-orbit doublets, see Section 1.4.1.5). We then found all the values of interest (*e.g.* BE, FWHM, area) between the OCV spectra and averaged them, which determined the constraint. For example, when interested in the position splitting between the $3d_{5/2}$ and $3d_{3/2}$ peaks in the Sr species, we looked at the twelve OCV spectra acquired on a particular cell. We found that the average binding energies (BEs) of the $3d_{5/2}$ and $3d_{3/2}$ peaks were 136.84 eV and 138.60 eV, respectively, giving a difference of 1.76 eV. Thus when we analyzed the data, a BE splitting of 1.76 eV was imposed between the two peaks.

At OCV it is assumed that each electrode will display the same parameters since the cell is symmetrical allowing us to double the amount of data. Furthermore, because the cells were typically cycled, we used OCV data from multiple cycles to build further confidence in the consistency between values.

We applied these constraints to any other samples studied, to ensure that all cells had spectra fit with the same parameters and to also show that these constraints worked well, universally.

2.2.2.1 Sr 3d

Because there are two Sr species associated with LSM, Sr in the LSM lattice ($Sr_{lattice}$) and Sr species that reside on top of the surface (which we attribute to SrO),[153,183,217] the Sr 3d spectrum exhibits four peaks. The fitting parameters for the four peaks are given in Table 2.1. The two peaks pertaining to the $Sr_{lattice}$ doublet are labeled peaks A and B, corresponding to the $3d_{5/2}$ and $3d_{3/2}$ peaks, respectively. The $3d_{5/2}$ and $3d_{3/2}$ peaks corresponding to SrO are labeled peaks C and D, respectively.

Table 2.1. Sr 3d peak constraints.

	$Sr_{lattice}$ doublet		**SrO doublet**	
Peak	Peak A	Peak B	Peak C	Peak D
Area (cps)	---	A * 0.666	---	C * 0.666
FWHM	---	A * 1	A * 1.685	C * 1
Position (eV)	---	A + 1.76	---	C + 1.81

The constraints for area, FWHM, and position (rows) are found for each peak (columns). "---" means that no constraint was needed.

To determine the constraints, OCV scans at each photon energy (345 eV, 490 eV, 900 eV) were used. First a Shirley background was used and peaks were fit with a Gaussian Lorentzian mix of 70:30. Two doublets were fit with the expected area and FWHM constraints (see Section 1.4.1.5). While the peaks within each doublet have an equal FWHM, the FWHM between $Sr_{lattice}$ and SrO peaks are not necessarily equal.

To determine the energy splitting (*i.e.* position constraint) for each doublet, the BE of each peak in each OCV spectra was averaged. The average position of A was found to be 136.84 eV and peak B was on average at 138.60 eV. The splitting constraint is thus 1.76 eV, *i.e.* the difference between the two. A similar procedure was used to find a splitting of 1.81 eV between peaks C and D. These splitting values are within ~5% of measurements made on standard Sr materials.[217] A FWHM constraint between the two Sr species was determined from the average ratio of $FWHM_{peak\ C}$: $FWHM_{peak\ A}$ (=1.69). No area constraints between the $Sr_{lattice}$ and SrO were used because the relative amounts of $Sr_{lattice}$ and SrO change in different conditions.

The raw data for each OCV scan used in the constraint determinations may be found in SI Table 2.2.

The $Sr_{lattice}$ $3d_{5/2}$ peak (peak A) was calibrated to 132.0 eV in agreement with the Sr 3d assignments on LSM made by Decorse *et al.*[217]

2.2.2.2 La 4d

The La 4d spectrum involved four peaks, La $4d_{5/2}$ (peak A), La $4d_{3/2}$ (peak B), a peak encompassing charge-transfer satellites (peak C), and a Si 2p peak from

a surface SiO_2 contaminant (peak D). The fitting parameters are shown in Table 2.2.

Table 2.2. La 4d and Si 2p peak constraints.

	La			Si
Peak	Peak A ($4d_{5/2}$)	Peak B ($4d_{3/2}$)	Peak C (sats)	Peak D (2p)
Area (cps)	---	A * 0.666	A * 1.96	---
FWHM	---	A * 1	A * 2.77	A * 1.11
Position (eV)	---	A + 3.27	A + 2.70	---

The constraints for area, FWHM, and position (rows) are found for each peak (columns). "---" means that no constraint was needed.

We first determined the position, area and FWHM constraints for the three La 4d peaks. We used the OCV data collected at photon energy of 900 eV, because at these energies, we penetrate deep enough into the surface that the Si 2p peak from surface contamination is negligible. A Shirley background was used and peaks corresponding to the La 4d doublet were fit with a Gaussian-Lorentzian mix of 70:30, and standard spin-orbit constraints on the FWHM and area were used. For peak C, an asymmetric peak was fit in accordance with Mullica *et al.*[218]

To determine the position constraints between the three peaks, the difference between the average BE values of each peak was used (see SI Table 2.3 for the raw OCV data). Peaks B and C were respectively found to be 3.27 eV and 2.70 eV higher than peak A. The average area and FHWM ratio between peak C and peak A were found and the constraints were determined to be:

$$Area_{peak\ C} = 1.96\ (Area_{peak\ A}) \text{ and } FWHM_{peak\ C} = 2.77\ (FWHM_{peak\ A})$$

Because SiO_2 is expected to change in concentration and charge differently as a surface species, no area or position constraints were applied to the Si 2p peak (peak D). However, we determined a FWHM constraint relative to peak A by looking at the OCV scans of each electrode and cycle at photon energies of 345 and 490 eV where the Si 2p peak was prominent. First the three peaks corresponding to La 4d were fit with the constraints determined above. A fourth peak for the Si 2p was then fit (peak D) with a Gaussian-Lorentzian mix of 70:30. The ratio between $FWHM_{peak\ D}$: $FWHM_{peak\ A}$ was determined for each spectra (see SI Table 2.4 for the raw OCV data).

The La 4d data calibrated by the $Sr_{lattice}$ $3d_{5/2}$ peak at 132.0 eV.

2.2.2.3 La 3d

The La 3d spectrum involved two major regions corresponding to the $3d_{5/2}$ and $3d_{3/2}$ electrons and two accompanying charge-transfer satellite peaks for each region. Only the $3d_{5/2}$ region was analyzed and the constraints may be viewed in Table 2.3. The main $3d_{5/2}$ peak is labeled peak A and the charge-transfer satellites from excitation are labeled B and C.

Table 2.3. La 3d peak constraints.

	La $3d_{5/2}$ Region		
Peak	Peak A ($3d_{5/2}$)	Peak B (satellite 1)	Peak C (satellite 2)
Area (cps)	---	A * 2.38	A * 2.38
FWHM	---	A * 1.55	A * 2.10
Position (eV)	---	A + 4.58	A + 1.20

The constraints for area, FWHM, and position (rows) are found for each peak (columns). No constraints were used for Peak A, because B and C were constrained relative to it.

We used the OCV scans at photon energy of 1230 eV to determine constraints (the first time we ran an experiment with La 3d spectra, this was the only photon energy that we used). A Shirley background was used and three peaks were fit with a Gaussian-Lorentzian mix of 70:30. The two satellite peaks (peaks B and C) were set to have equal areas based on Sunding *et al.'s*[198] work.

To determine the remaining constraints on peak B and C, the same basic method as outlined for Sr 3d and La 4d was used. The average position, FWHM, and area of B and C relative to A were determined, and we based our constraints on that. For example, the average difference in BE for peaks B and A was equal to 841.49 eV – 836.91 eV leading to a splitting of 4.58 eV.

The raw data for each OCV scan used may be found in SI Table 2.5.

2.2.2.4 Mn 3s and Zr 3d XPS Spectra

The Mn 3s spectrum exhibits two peaks due to multiplet splitting (see Section 1.4.1.5),[192-197] unlike a typical XPS spectrum of an s orbital electron. The peaks were fit with a Gaussian Lorentzian mix of 70:30. Because there is no specific branching ratio for the two peaks,[219] no constraints were used.

The Zr 3d spectrum consists only of the expected spin-orbit pair of $3d_{5/2}$ and $3d_{3/2}$ electrons so that standard spin-orbit coupling parameters could be used (the energy splitting was equal to 2.3 eV).

2.2.3 Calculations from XPS Data

2.2.3.1 Calculating La:$Sr_{lattice}$ Atomic Ratios

To calculate the La:$Sr_{lattice}$ ratio we use the following equation:

$$\frac{\mathrm{La}}{\mathrm{Sr_{lattice}}} = \frac{\left(\frac{\mathrm{I}}{\mathrm{f\theta\gamma AT\sigma\lambda}}\right)_{\mathrm{La\ 4d}}}{\left(\frac{\mathrm{I}}{\mathrm{f\theta\gamma AT\sigma\lambda}}\right)_{\mathrm{Sr\ 3d\ lattice}}} \quad \textbf{(Eq. 2.1)}$$

where "I" represents the sum intensity of relative peaks in the spectra and the term "fθγATσλ" represents the "sensitivity factor." The symbol and calculation details are described in Section 1.4.1.7. The fθγAT values will cancel out because these are instrumental factors and are equal between the La 4d and Sr 3d scans. The remaining quantities, σ (photoionization cross section) and λ (inelastic mean free path, IMFP) are unique to each species and Eq. 2.1 simplifies to:

$$\frac{\mathrm{La}}{\mathrm{Sr_{lattice}}} = \frac{\left(\frac{\mathrm{I}}{\mathrm{\sigma\lambda}}\right)_{\mathrm{La\ 4d}}}{\left(\frac{\mathrm{I}}{\mathrm{\sigma\lambda}}\right)_{\mathrm{Sr\ 3d\ lattice}}} \quad \textbf{(Eq. 2.2)}$$

The values of the cross sections and IMFP may be found in SI Section 2.6.3.

2.2.3.2 Calculating SrO Thickness

The *average* thickness of the SrO surface species can be quantified with the following equation,[220,221] which is used to calculate the thickness of a metal oxide surface layer:

$$\mathrm{Thickness} = \lambda_{\mathrm{surf}}\cos\theta\ln\left[1 + \frac{\left(\frac{\mathrm{I_{surf}}}{\mathrm{S_{surf}}}\right)}{\left(\frac{\mathrm{I_{lattice}}}{\mathrm{S_{lattice}}}\right)}\right] \quad \textbf{(Eq. 2.3)}$$

where λ_{surf} is the IMFP of the surface layer, θ is the photoelectron emission angle with respect to the surface normal, "s" represents the sensitivity factor (given in Eq. 2.1) of the relevant species, and "I" represents the intensity of the species under

study. The same sensitivity factor terms that were cancelled out in Eq. 2.1 may be cancelled for the same reasons as outlined previously. Furthermore, the cross section of the Sr 3d electrons is material independent, so that it can also be removed from the sensitivity factor. Finally, θ is equal to 0^{o}, thus Eq. 2.3 is simplified to:

$$\text{Thickness}_{\text{SrO}} = \lambda_{\text{SrO}} \ln\left[1 + \frac{\left(\frac{I_{\text{SrO}}}{\lambda_{\text{SrO}}}\right)}{\left(\frac{I_{\text{Sr lattice}}}{\lambda_{\text{Sr lattice}}}\right)}\right] \quad \textbf{(Eq. 2.4)}$$

The IMFP of SrO at each photon energy may be found in SI 2.6.3. It is important to note that this thickness assumes a homogenously thick SrO layer and a homogenous density of Sr atoms in the lattice, neither of which is likely the case. Thus the thickness measurement is a more qualitative measurement of how the SrO layer changes and represents the *average* thickness of SrO in the region scanned.

2.2.3.3 Mn Oxidation State Calculations

Mn 3s spectra exhibit two peaks from multiplet splitting (described in Section 1.4.1.5 and Section 2.3.3) and the energy difference between the two peaks is directly related to the oxidation state of Mn.[193] Galakhov *et al.*[193] studied numerous Mn samples of different oxidation states and developed a curve relating oxidation state and energy splitting. The following linear relationship can be extracted from their work:

$$\text{Mn Oxidation state} = -\frac{\Delta E}{0.9} + 8.89 \quad \textbf{(Eq. 2.5)}$$

where ΔE is the difference between the two peaks in units of eV.

2.3 Results

2.3.1 LSM surface composition at OCV

AP-XPS experiments were conducted to measure the surface composition at high temperature (620 ^{o}C) and in an O_2 environment (200 mTorr). The bulk stoichiometry predicts a 4:1 ratio between La and Sr in our LSM samples ($(La_{0.8}Sr_{0.2})_{0.95}MnO_{3\pm\partial}$). However, even at OCV (before any electrochemistry), we observe that the surface La:Sr ratio is higher than the 4:1, although the bulk ratio is approached as we probe deeper into the surface. We measure the surface composition by recording Sr 3d and La 4d XPS data and applying Eq. 2.2 (see Section 2.2.3.1). Spectra were collected using three photon energies to probe different depths of the surface (see Section 1.4.1.8): 345 eV, 490 eV, and 900 eV, which give information depths of, ~2.0 nm, ~2.7 nm, and ~4.5 nm, respectively.

Figure 2.2 shows representative Sr 3d spectra recorded at OCV in 200 mTorr O_2, at 620 ^{o}C. In each spectrum, two distinct spin-orbit doublets are observed. As previously stated it is well known that two species of Sr are found in LSM, the Sr in the lattice ($Sr_{lattice}$) and SrO that resides on top of the electrode.

The low BE doublet (green) represents $Sr_{lattice}$ and the high BE doublet (yellow) represents the SrO that forms a surface layer on top of the LSM, as evidenced by its change in intensity relative to the $Sr_{lattice}$ at different photon energies (*e.g.* it is most intense at the most surface sensitive energy). While the SrO surface species' BE is similar to those of $Sr(OH)_2$ or $SrCO_3$, these compounds are not stable in O_2 only environments at T > 500 ^{o}C. In addition, we see no evidence of carbonate formation in the C 1s XPS studies.

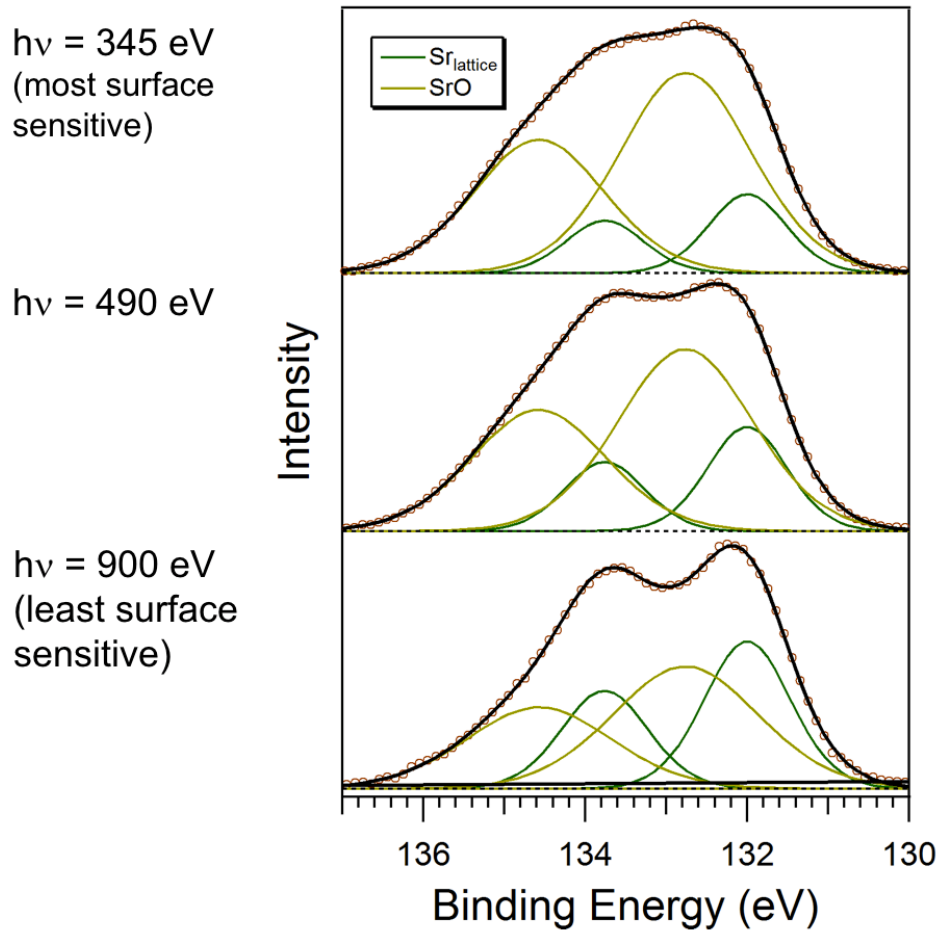

Figure 2.2. Sr 3d spectra taken under OCV at three photon energies: 345 eV (top), 490 eV (middle), and 900 eV (bottom). The $Sr_{lattice}$ and SrO species are represented by the green and yellow doublets, respectively.

Figure 2.3 shows representative La 4d spectra taken at OCV in 620 ^{o}C with the same photon energies used for Sr 3d. The La 4d spectrum is known to be complicated due to the presence of charge-transfer satellites.[198,218,222] The expected spin-orbit doublet (red) is fit with an additional third peak (blue) that encapsulates the other associated auxiliary peaks, as established by Mullica *et al*.[218] For the

information of interest (atomic ratios, surface potentials), a more complicated fitting is not necessary.

Lastly, a peak corresponding to 2p photoelectrons of a surface SiO_2 species (BE = 101.5, grey) is observed. SiO_2 is a ubiquitous contaminant of YSZ and previous studies have shown it to migrate to the surface under high temperature.[27,154] The energy splitting from spin-orbit coupling of a Si 2p electron is too small to be resolved. The increase in its relative intensity at lower, more surface sensitive photon energies, is commensurate with it being a surface species.

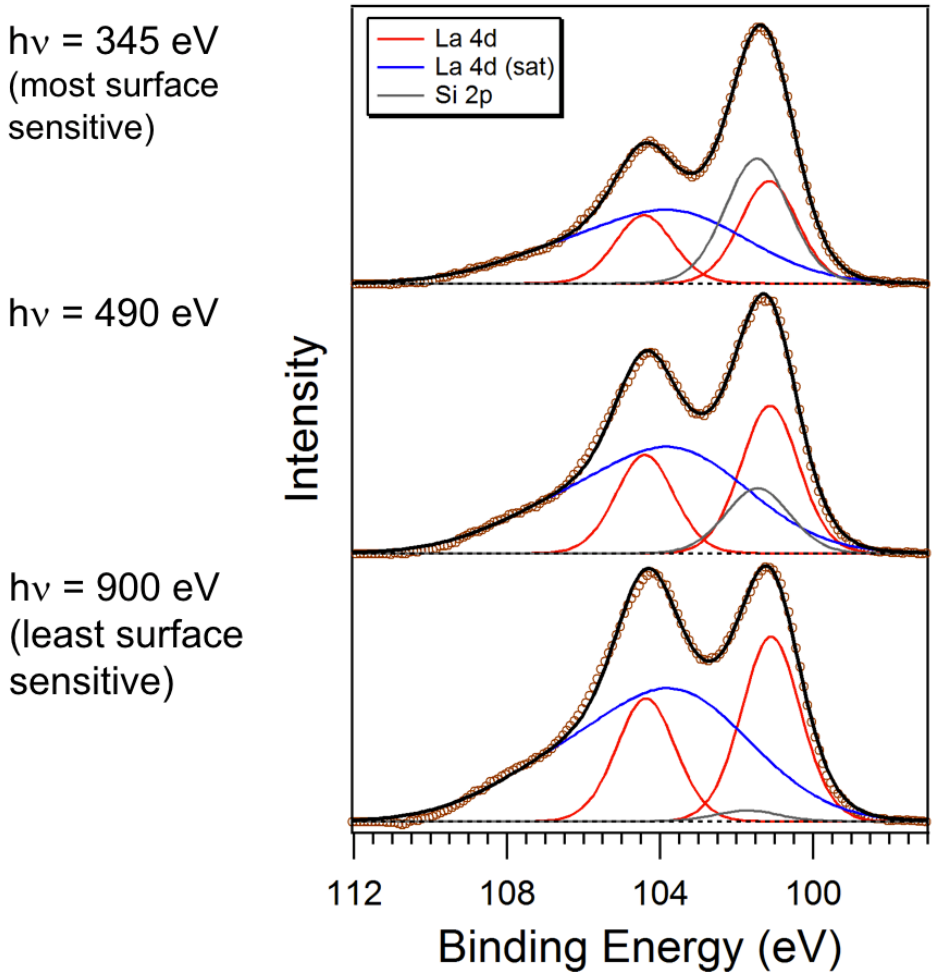

Figure 2.3. La 4d spectra recorded under OCV at three photon energies: 345 eV (top), 490 eV (middle), and 900 eV (bottom). The main 4d peaks (5/2 and 3/2) are represented by the red peaks, while the charge transfer satellites are represented by the asymmetric blue peak. The Si 2p peak from a SiO_2 impurity is shown in grey.

Figure 2.4 shows the $La:Sr_{lattice}$ ratio at 620 ^{o}C during $OCV_{Cycle\ 1}$ (*i.e.* before any bias was applied). The ratio is calculated at each photon energy (345 eV, 490 eV, and 900 eV) and approaches the expected value of 4 (indicated by the dotted purple line) as we probe deeper into the surface. The higher $La:Sr_{lattice}$ ratio observed at more surface sensitive energies is attributed $Sr_{lattice}$ depletion in the surface. The depletion of the $Sr_{lattice}$ is very likely due to extrusion as SrO.

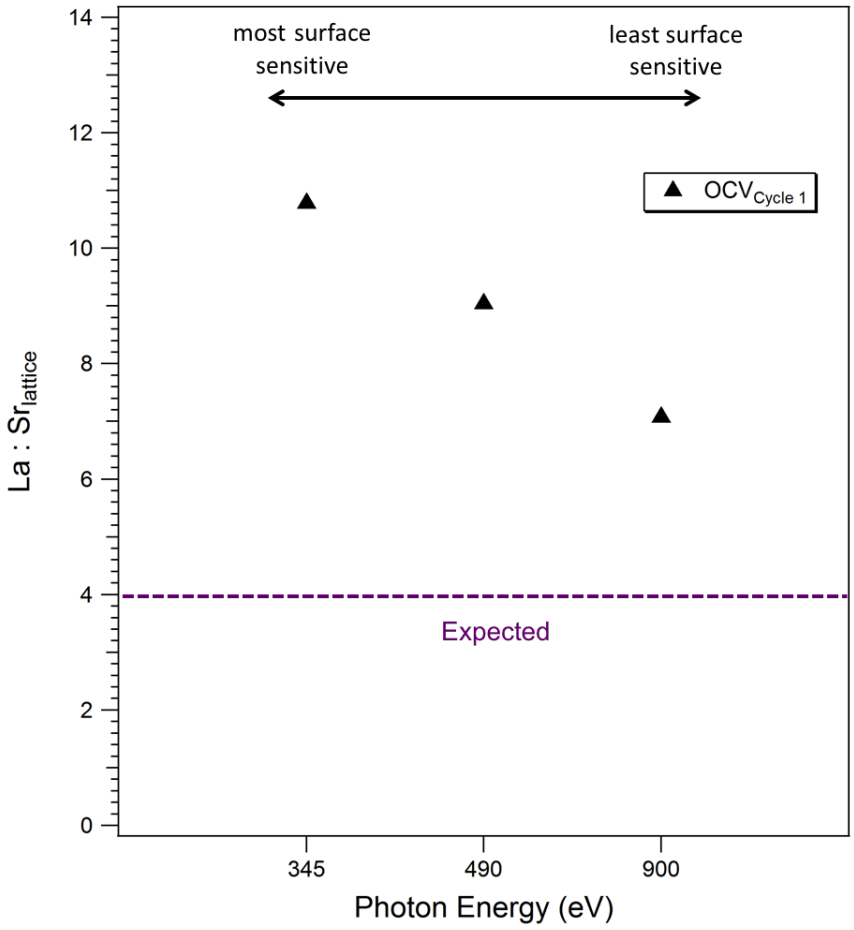

Figure 2.4. La:$Sr_{lattice}$ values at different photon energies (345 eV, 490 eV, and 900 eV). The expected value of 4, based on the bulk stoichiometry of the material, is indicated by the dotted purple line.

2.3.2 SrO Growth and Electrode Composition Changes with ORR

At 620 ^{o}C and under cathodic bias, LSM will further extrude Sr from the lattice onto the surface in a partially reversible process.

Sr 3d XPS data were collected at 620 ^{o}C on LSM, ~200 μm behind the LSM/YSZ interface over two cycles of switching between OCV and bias. The scans recorded at 900 eV are shown in Figure 2.5, and the 345 eV and 490 eV data are given in SI Figure 2.2. The relative amount of SrO (high BE doublet) increases under bias (1.5 V_{Cycle1}), decreases when the cell is returned to OCV (OCV_{Cycle2}), and increases again upon reapplication of the bias (1.5 V_{Cycle2}). The spectra are calibrated so that the $Sr_{lattice}$ $3d_{5/2}$ peak is located at 132.0 eV.

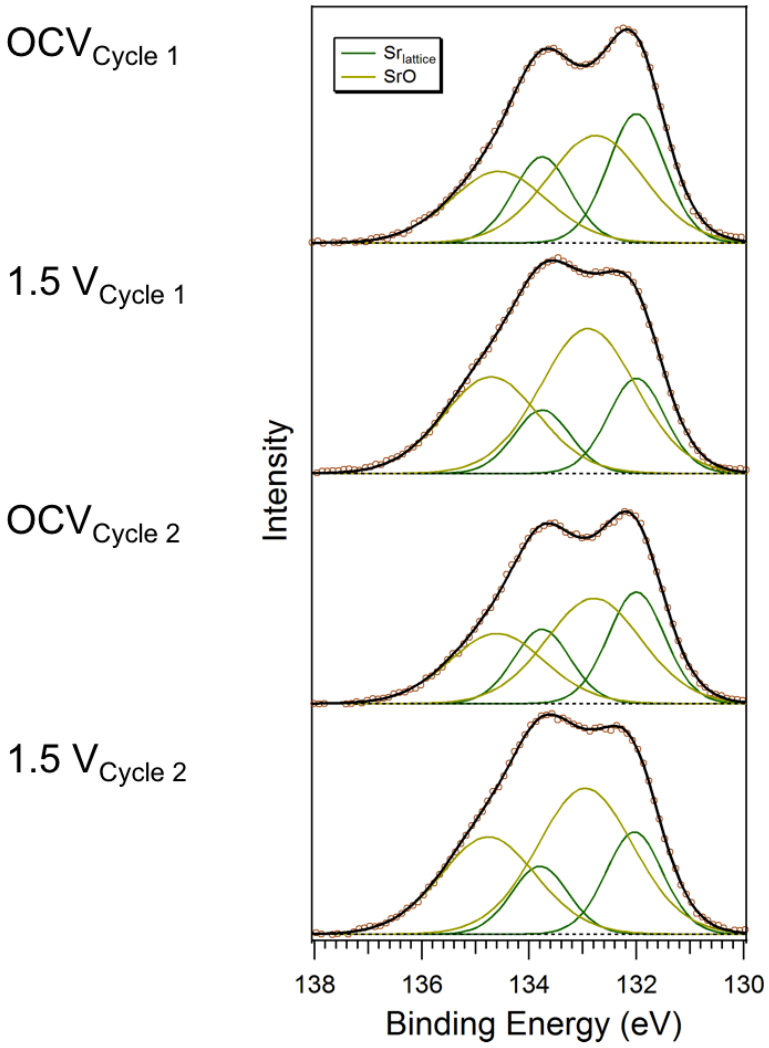

Figure 2.5. Sr 3d spectra recorded at a photon energy of 900 eV, 200 microns behind the LSM/YSZ interface at 620 ^{o}C and 200 mTorr O_2. From top-to-bottom the spectra correspond to cycles between OCV and 1.5 V bias. The green and yellow doublets represent the $Sr_{lattice}$ and the SrO species, respectively (a slight shift in the peaks is observed under bias due to local surface potentials).

The thickness of SrO was calculated with Eq. 2.4 and is shown in Figure 2.6 for each condition (OCV or biased) at different photon energies. The thickness increases between OCV_{cycle1} (black, closed) and 1.5 V_{cycle1} (red, closed). When the bias is removed (OCV_{cycle2}, black, open) the thickness drops to *near* the previous

OCV value, but increases again upon further polarization (1.5 $V_{cycle2,}$ red, closed). These results indicate that at least in early cycles, there is a partially reversible SrO growth that is cathodically induced.

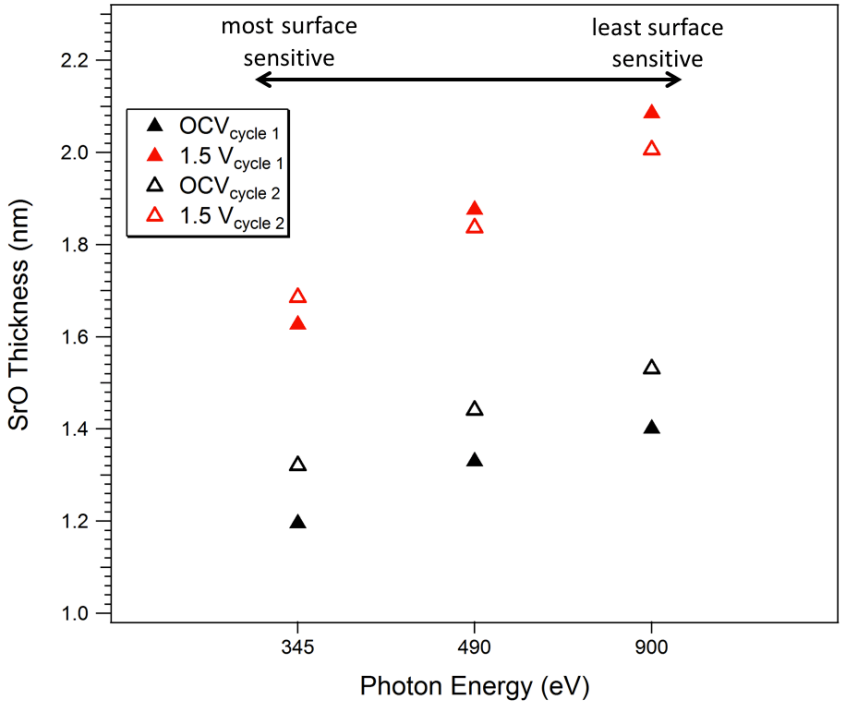

Figure 2.6. SrO thickness values calculated from Sr 3d XPS spectra collected 200 microns behind the LSM/YSZ interface at 620 ^{o}C. Three different photon energies were used to probe different depths of the surface, 345 eV, 490 eV, and 900 eV. The black and red symbols represent OCV and biased conditions, respectively. The cycle is indicated by a closed symbol (Cycle 1) or open symbol (Cycle 2).

In principle, the calculated thickness of SrO should remain constant regardless of which depth of LSM we probe, but we see a seemingly systematic increase in calculated thickness with higher photon energy. Several factors may explain this increase including, the relatively low, and thus, error prone signal of $Sr_{lattice}$ at more surface sensitive energies, or a difference in the X-ray beam

diameter (*i.e.* scanning area) at different photon energies. Regardless of which photon energy is studied, the same trend is observed.

As the SrO increases under cathodic polarization, $Sr_{lattice}$ is depleted as evidenced by an increased La:$Sr_{lattice}$ ratio at more surface sensitive energies, shown in Figure 2.7. We do not attribute the change in the ratio to La concentration changes as the absolute La intensity remains relatively stable compared to that of $Sr_{lattice}$ during the experiment. At less surface sensitive energies, the La:$Sr_{lattice}$ ratio approaches the expected bulk values, confirming that depletion of Sr in the LSM occurs in the near surface region.

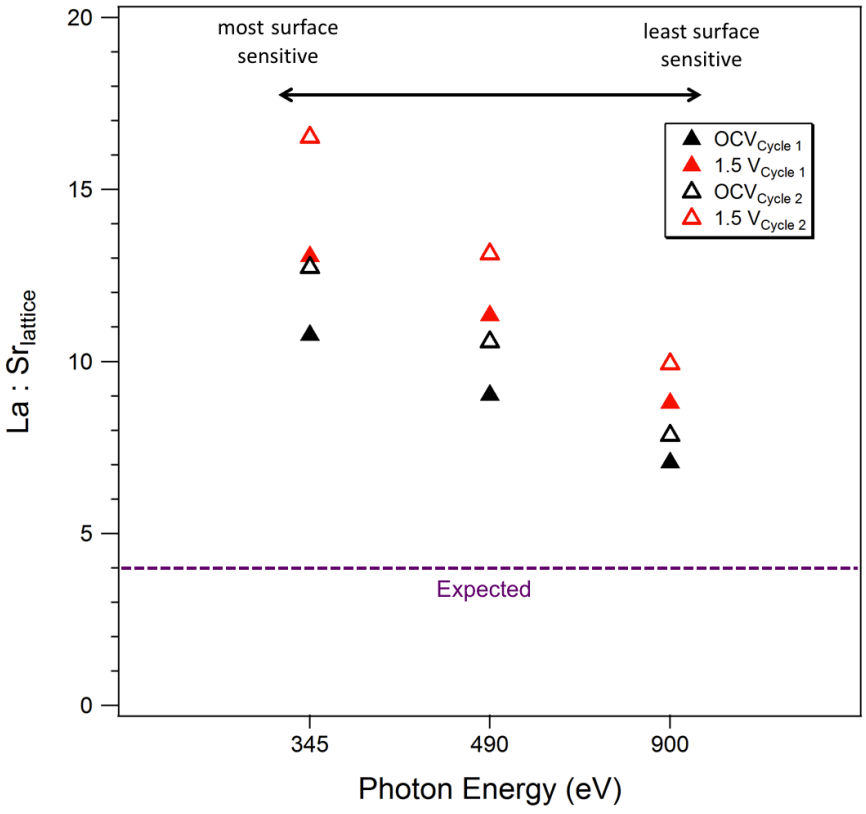

Figure 2.7. La:$Sr_{lattice}$ values calculated from La 4d and Sr 3d data collected on LSM, ~200 microns behind the LSM/YSZ interface at 620 °C. The symbols and photon energies are the same as in Figure 2.6.

In addition to our depth profiling experiments, we monitored electrochemical surface processes at 530 ^{o}C using a 2D area detector, which allowed us to spatially resolve a Sr 3d line scan from the LSM/YSZ interface to ~400 microns behind that interface. However, each line scan could only collect reliable data over a range of ~370 microns, necessitating data collection over two different regions of the electrode, in order to cover the entire region of interest. The Sr 3d data was collected with 490 eV photons. Despite the lower temperature, SrO growth is also induced by cathodic polarization, although the SrO thickness is not uniform across the electrode.

Figure 2.8 shows the calculated SrO thickness under different conditions (same color code as Figure 2.6) as a function of position in which 0 mm demarcates the LSM/YSZ interface. The two different line scans used are signified by the direction of the triangle markers, with overlap around -0.05 mm. While the thickness observed at OCV during cycle 2 is more scattered compared to the first cycle, both OCV cycles exhibit lower SrO thicknesses compared to each polarized condition.

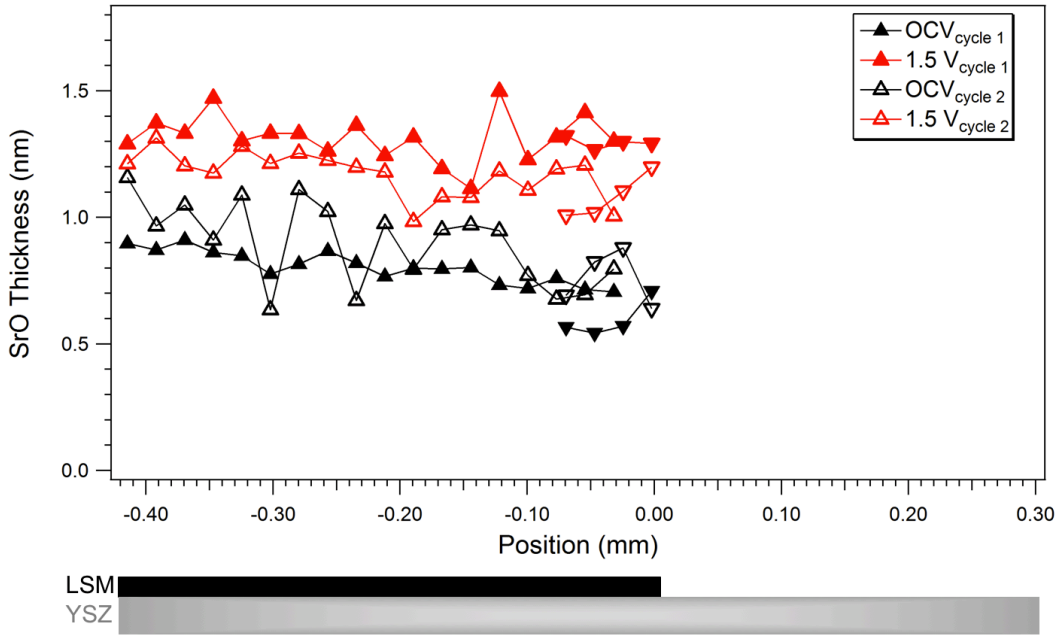

Figure 2.8. A plot of SrO thickness as a function of position along the LSM electrode at 530 ^{o}C with the same color code as Figure 2.6. The LSM/YSZ interface is demarcated by 0 mm. Two separate sets of data, denoted by the direction of the triangles, were recorded. A lateral schematic of the electrode on the YSZ electrolyte is provided at the bottom for position clarification.

2.3.3 Mn Oxidation States

The Mn oxidation state varies with P_{O_2}, surface chemistry, and polarization. When a positive bias is applied to the CE in the presence of O_2 gas, oxide ions are driven through the YSZ toward the CE and the following electrochemical reactions are promoted on each electrode (depicted in Figure 2.1):

Left (WE): $O_{2(g)} + 4Mn^{3+} + 2V_o \rightleftharpoons 2O^{2-}_{(lattice)} + 4Mn^{4+}$ (**R2.2** cathode, ORR)

Right (CE): $2O^{2-}_{(lattice)} + 4Mn^{4+} \rightleftharpoons O_{2(g)} + 4Mn^{3+} + 2V_o$ (**R2.3** anode, OER)

where the "forward-weighted" equilibrium arrows emphasize the far-from-equilibrium conditions that the LSM electrodes experience.

The Mn oxidation state can be measured by collecting Mn 3s XPS spectra as described below. We recorded Mn 3s data under two cycles of OCV and 1.5 V bias at 530 ^{o}C. Data was collected once more at OCV (cycle 3) and then the cell was heated to 680 ^{o}C where one more cycle (cycle 4) was performed.

It is well-established that Mn 3s spectra (see Figure 2.9) exhibit two peaks as a result of multiplet splitting,[192-197] which occurs in transition metals when the spin of the remaining unpaired 3s electron couples with the spin of unpaired 3d electrons (described further in Section 1.4.1.5). The energy splitting between the peaks is oxidation state dependent,[193,223] with a larger splitting observed on more reduced Mn species. This larger splitting is due to a greater degree of spin-spin coupling when there are more unpaired d electrons present. From the energy splitting, the oxidation state of Mn can be calculated by Eq. 2.5 (see Section 2.2.3.3).[193] Figure 2.9 shows the Mn 3s spectra collected at 900 eV during the first OCV condition ($OCV_{Cycle1\text{-}530\ C}$) and reducing polarization at 680 ^{o}C (1.5 $V_{Cycle\ 4\text{-}680\ C}$), which gave the largest variance in oxidation state. Because our primary interest is in the splitting of the peaks and not the absolute BEs, the low BE peak is fixed at 0 eV. Mn 3s spectra collected with 490 eV photons are shown in SI Figure 2.3.

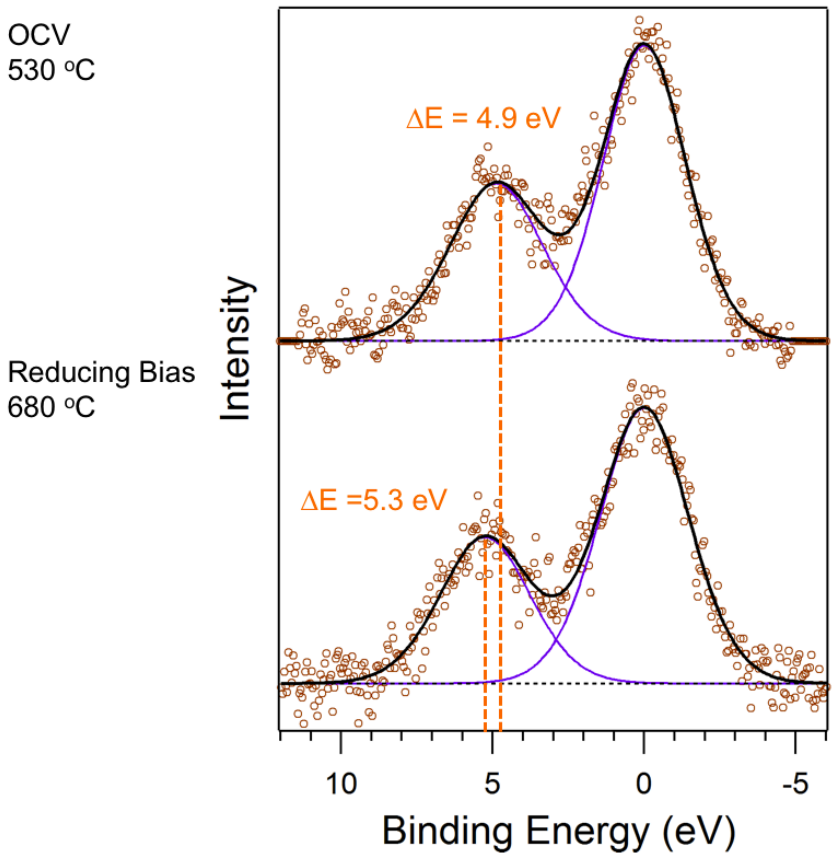

Figure 2.9. Representative Mn 3s spectra taken at a photon energy of 900 eV under two conditions: OCV at 530 °C (top) and a reducing bias at 680 °C (bottom). Two peaks are observed due to multiplet splitting. The low BE peak is set to 0 eV.

Figure 2.10 displays the Mn oxidation state in each condition determined from two photon energies, 490 eV and 900 eV. Scans were recorded ~200 μm behind the LSM/YSZ interface and both energies show the same trends in oxidation state changes. At 530 °C, Mn is less reduced in all three OCV conditions (black) than under the two polarizations (red). At 680 °C, Mn is more reduced at both OCV and 1.5 V applied bias, relative to the same conditions at 530 °C. The greater degree of reduction at higher temperatures is consistent with expectations with P_{O_2} phase behavior as described by Mizusaki *et al.*[14] The reproducible change in oxidation

state validates both the experimental method and the fact that electrochemical reduction is reversible.

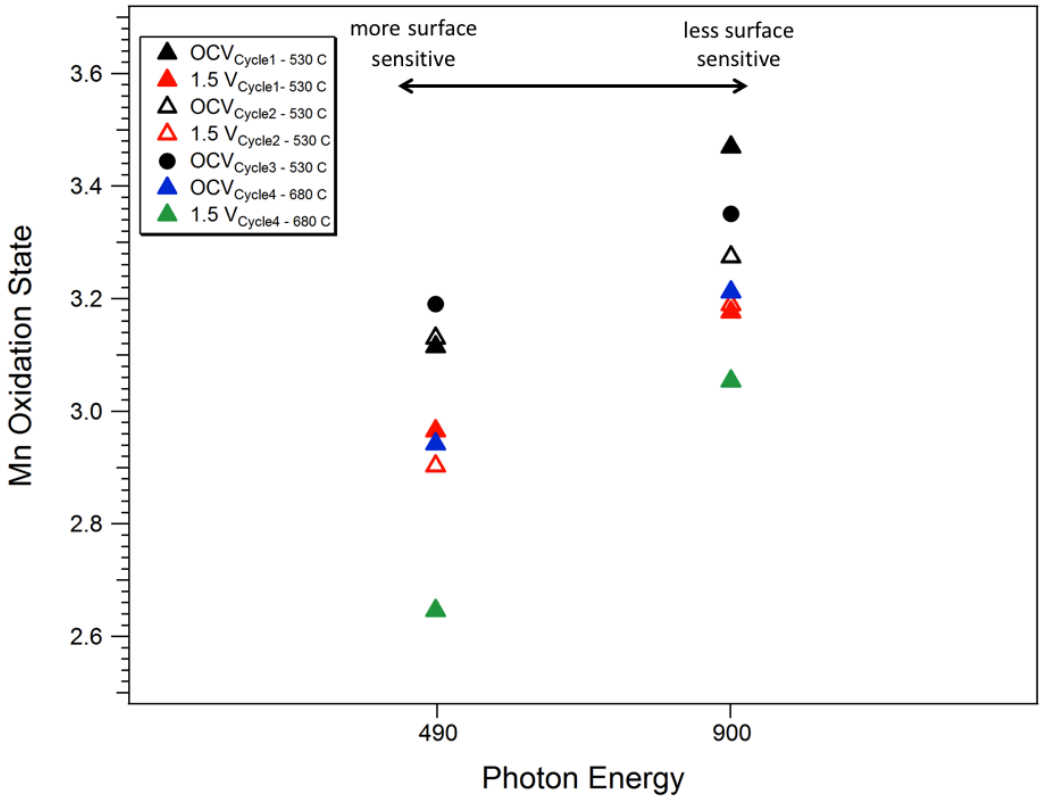

Figure 2.10. Mn oxidation states calculated from Mn 3s XPS data collected on LSM, ~200 microns behind the LSM/YSZ interface at 490 eV and 900 eV photon energies. The black and red symbols represent OCV and biased conditions, respectively, at 530 ^{o}C. The cycle is indicated by a closed symbol (Cycle 1), open symbol (Cycle 2), or a circle (Cycle 3). The 680 ^{o}C data at OCV (blue) and 1.5 V bias (green) are also given.

The data show that Mn is more reduced toward the surface and at higher temperature, which is explored below (Section 2.4.1). Regardless of which depth we study, reduction is induced by cathodic bias. We further investigated Mn reduction by using the 2D area detector to spatially resolve the Mn oxidation state in a line along the LSM electrode with a photon energy of 490 eV. The lower plot in Figure 2.11 shows the Mn oxidation state as a function of position over one cycle.

The oxidation state is relatively constant over OCV (black) with an average of ~3.3, while a ~3.0 average is found upon biasing (red). We also show at the top (in blue) that the difference between the two conditions, *i.e.* the extent of reduction, is ~constant. Points at which no polarized reduction is observed already exhibit relatively reduced Mn states at OCV.

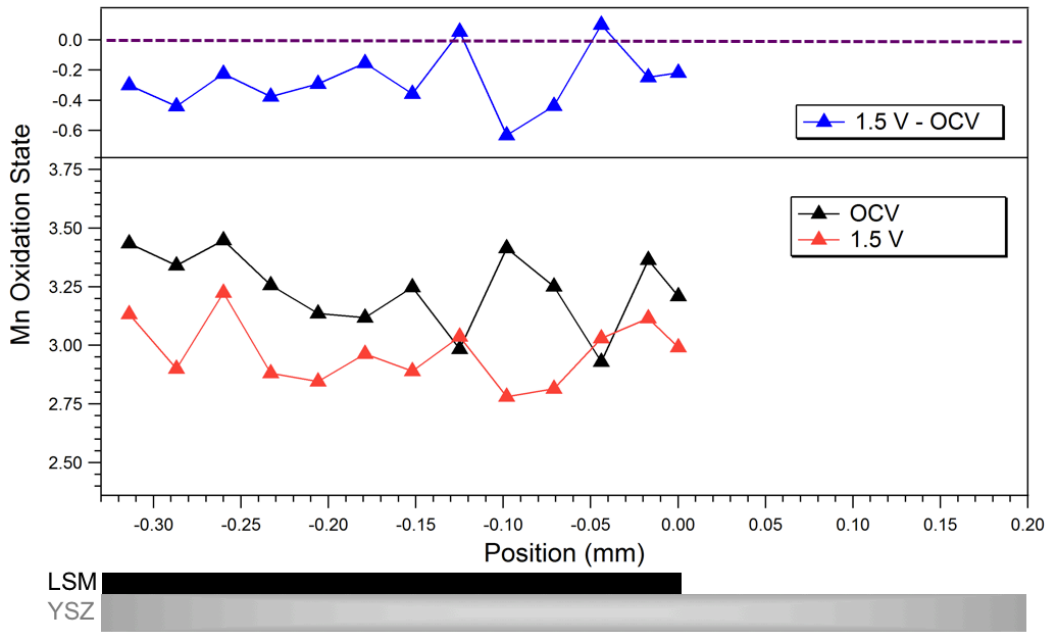

Figure 2.11. The lower plot shows the Mn oxidation state as a function of position along the LSM electrode at 530 ^{o}C in 200 mTorr O_2. The black and red symbols represent OCV and biased conditions, respectively. The top plot in blue shows the difference between the oxidation state under bias and OCV. A lateral schematic of the electrode on the YSZ electrolyte is provided at the bottom for position clarification.

2.3.4 Surface Potential Maps

We mapped the surface potentials across the SOC at 530 ^{o}C and found that all electrochemical activity on LSM occurs at the LSM/YSZ interface. On a cell such as ours, we expect three primary processes to take place (see Figure 2.1): electron transfer between the Au foils to LSM, oxide ion conduction through the

YSZ, and electrochemical reactions on LSM (ORR and OER). Measuring surface potential drops across the cell indicates where the above processes occur, and what the resistances to those processes are. These resistances can be approximated using Ohm's Law (V = iR), where V is the drop in local surface potentials built up on the surface from polarization.

2.3.4.1 Calculating Local Surface Potentials

The details of measuring surface potential (V_L) are provided in Section 1.4.1.7. To briefly recap, we exploit the phenomenon that a surface potential will shift the BE of all photoelectrons according to the equation:

$$V_L = BE_{bias} - BE_{OCV} \quad \text{(Eq. 2.6)}$$

where V_L is in units of V and BE is in units of eV.

The potentials were measured by tracking BE shifts in the Zr 3d peaks on YSZ and the La 4d and Sr 3d peaks on LSM. A representative Zr 3d XPS spectrum is shown in Figure 2.12.

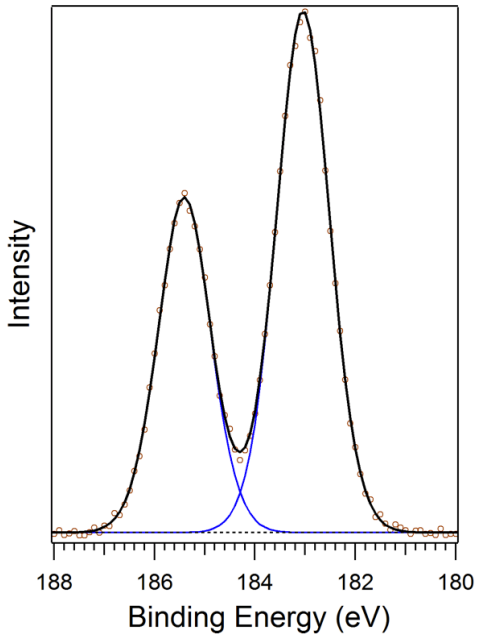

Figure 2.12. Representative Zr 3d spectrum recorded at 490 eV.

2.3.4.2 Probing Local Potentials Across the SOC

The surface potential was measured from one electrode to the other by utilizing the 2D area detector and photons of 490 eV. Figure 2.13 shows the surface potential vs. position when a +1.5 V bias is applied to the anode (OER) at 530 ^{o}C. The positions, 0.0 mm and 1.0 mm, mark the LSM/YSZ interfaces at the cathode and anode, respectively. The potentials measured on LSM were determined from the surface SrO species (yellow) and the two lattice species, La (red) and $Sr_{lattice}$ (green). The potentials on YSZ are based on Zr (blue).

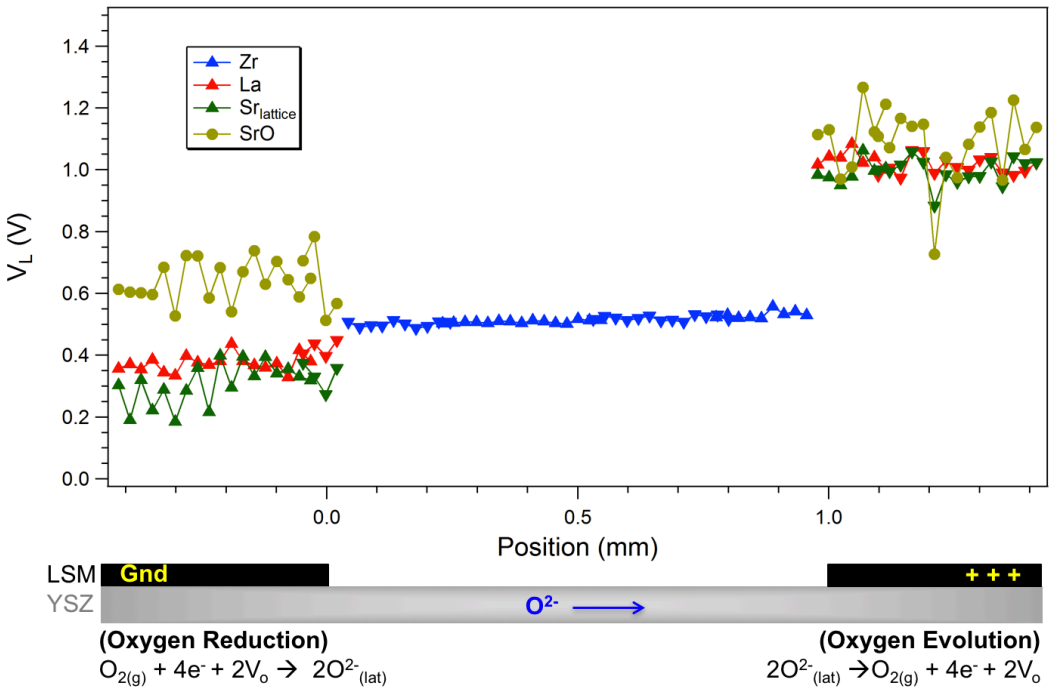

Figure 2.13. A plot of local surface potentials vs. position across the SOC at 530 °C. The LSM/YSZ interfaces are demarcated by 0.0 and 1.0 mm for the cathode (left) and anode (right), respectively. Measured potentials on LSM correspond to La (red), $Sr_{lattice}$ (green), and SrO (yellow). Potentials on YSZ are from Zr (blue). A lateral schematic of the electrode on the YSZ electrolyte is provided at the bottom for position identification.

Applying a 1.5 V bias to the anode and grounding the cathode necessitates a 1.5 V potential drop from anode to cathode. There are three primary regions of potential drops across the cell: at the Au foil/LSM interfaces of each electrode, across the YSZ electrolyte (ohmic iR drop), and at the LSM/YSZ interfaces of each electrode. These regions are discussed individually, below.

Because the LSM electrode is connected to the potentiostat through physically compressed Au foils (see Figure 2.1), there is a ~0.35 V potential drop (overpotential) at the Au/LSM interface. This overpotential most likely represents the electrical resistance across the Au/LSM interface resulting from imperfect

contacts. Thus, we observe that on the anode (right) the local potential is not at the expected 1.5 V value, nor is the grounded cathode (left) at 0 V. Other experiments (not shown) confirm that these potentials are only found on the Au foils.

Across the YSZ, a linear drop from 0.55 V to 0.5 V is observed between the anode and cathode interfaces. The bulk resistance (R_B) can be evaluated from the linear voltage drop across the YSZ between the right and left LSM edges ($V_{L(Zr\ right)}$ - $V_{L(Zr\ left)} \approx 0.05$ V). The current was 310 μA, thus from Ohm's Law we calculate R_B as ~200 Ω which is not in agreement with the ~1600 Ω reading we found from our EIS tests (SI Figure 2.1). However, 200 Ω is the R_B value across 1 mm of YSZ, *i.e.* the distance between electrode edges. The distance between the electrode *contacts* (*i.e.* the tips shown in Figure 2.1), which is the more relevant distance for ionic conductivity, is 8.5 mm. Because R_B scales with distance we can multiply 200 Ω / 1 mm by the 8.5 mm to determine the R_B from contact-to-contact. This value, 1700 Ω, is in much better agreement with the EIS results.

Across the anode (right LSM), we observe a relatively constant potential up to the LSM/YSZ interface regardless of which species we monitor, and the three species exhibit average V_L readings in close agreement of, ~1.1 V (SrO), ~1.0 V (La), and ~1.0 V ($Sr_{lattice}$). At the anode LSM/YSZ interface, a potential drop (associated with OER) is observed. At the cathode edge, another sharp potential drop (associated with ORR) is observed. As seen on the anode, each species displays a relatively constant surface potential across the LSM cathode. However, these voltages are not in agreement with each other showing average values of, ~0.6 V (SrO), ~0.4 V (La), and ~0.3 V ($Sr_{lattice}$).

The potential separation observed between SrO, La, and $Sr_{lattice}$ species on the cathode side is a phenomenon observed on multiple cells (more examples below), supporting that it is not a random measurement error. The cause of this separation is attributed primarily to a capacitive effect between the LSM surface and electronically insulating, poorly connected SrO species, as further explored in the Discussion Section.

2.3.4.3 Probing Local Potentials at Different Depths and Temperatures

We conducted depth profiling experiments on a different cell at 530 ^{o}C to see how the potential separation phenomenon varies as a function of depth from the electrode surface. The potential mapping experiments described above made use of the 2D area detector at beamline 9.3.2 so that we could measure surface potentials laterally across the SOC. However, because only one photon energy was used (490 eV), all of the potential measurements were acquired from only one depth on the LSM electrodes (~2.7 nm into the surface). At beamline 11.0.2, we had access to higher photon energies and utilized three different energies: 345 eV, 490 eV, and 900 eV, which probed depths of ~2.0 nm, ~2.7 nm depth, and ~4.5 nm, respectively. Thus we were able to measure surface potentials at different depths of the surface. No area detector was used, so that spectra were collected at one point on each LSM electrode, ~200 microns behind the LSM/YSZ interface.

At beamline 11.0.2, photon energies of 1085 eV and 1230 eV were accessible, which allow for the ejection of La 3d photoelectrons at the same KE as La 4d photoelectrons at photon energies of 345 eV and 490 eV. In other words, we

could acquire the same depth information with the La 3d data as the La 4d data recorded at 345 eV and 490 eV, and then corroborate results.

Representative La 3d spectra collected under OCV conditions at 530 ^{o}C are shown in Figure 2.14. The La 3d spectra are complicated by similar issues as the La 4d spectra. In addition to the $3d_{5/2}$ and $3d_{3/2}$ peaks (at 838.2 eV and 855.2 eV, respectively), satellite peaks and plasmons exist, the nature and identification of which are very controversial.[198,218,222,224] Because of these complications, the fitting method developed by Sunding *et al.*[198] was employed to simplify the analysis. This method assumes that the "$3d_{5/2}$ region" consists of a single $3d_{5/2}$ peak (red) with two satellites (blue). To measure surface potentials, it was only necessary to fit the peaks in the "$3d_{5/2}$ region", and track the shifts in those peaks.

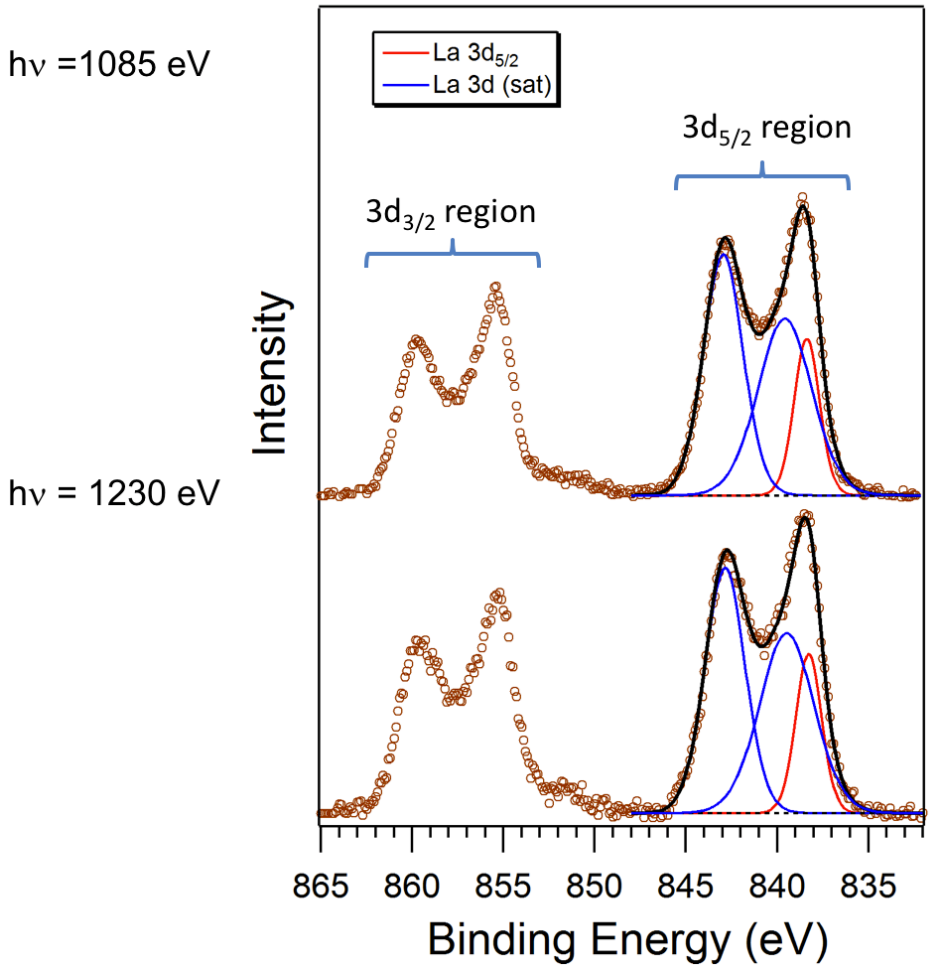

Figure 2.14. La 3d spectra taken under OCV at photon energies of 1085 eV (top) and 1230 eV (bottom). The regions of peaks that surround the $3d_{5/2}$ and $3d_{3/2}$ peaks are labeled with only the $3d_{5/2}$ region fitted. The main $3d_{5/2}$ is represented by the red peak and the satellites are represented by the blue peaks.

Figure 2.15 shows the local voltages measured with each photon energy, at ~200 microns behind the LSM/YSZ interface of the two electrodes. V_L measurements from La 3d (open red triangles) agree well with the La 4d measurements. As in Figure 2.13, the three species display no significant potential measurement differences on the anode, while a clear division is present on the cathode. This separation is constant within the depths that we probed. The

~constant $V_L(SrO)$ values between the three photon energies provides confidence in our measurements, as a surface layer should display the same potential regardless of what depth of the LSM lattice we profile.

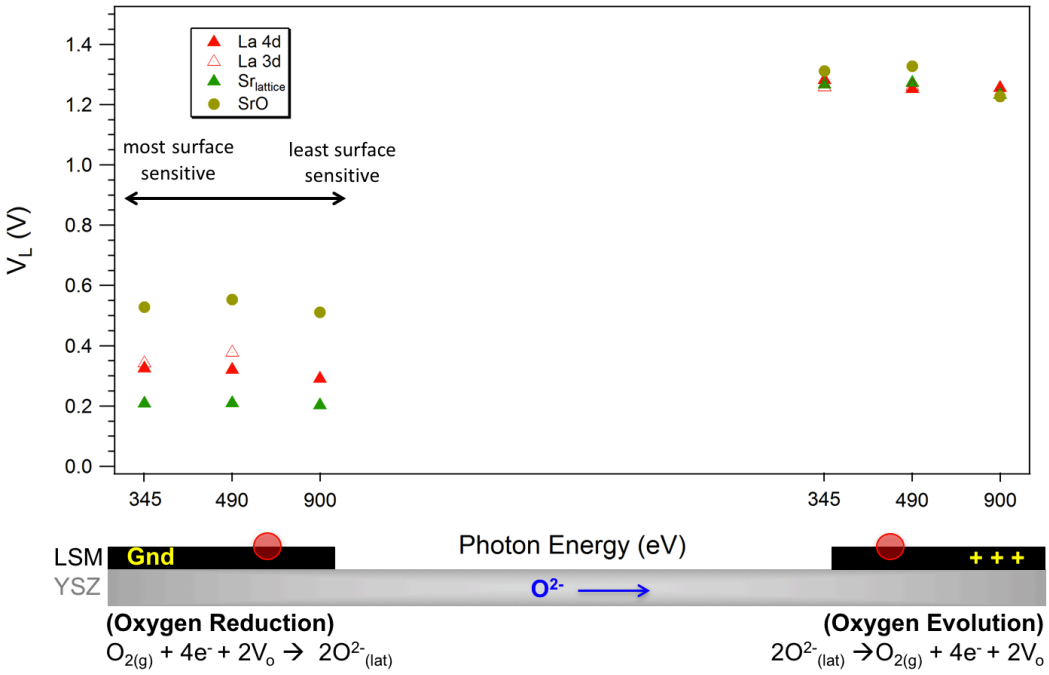

Figure 2.15. Local surface potentials calculated at different depths using photon energies of 345 eV, 490 eV, and 900 eV for La 4d and Sr 3d scans. Energies of 1085 eV and 1230 eV were used for La 3d to probe the same depth as the 345 eV and 490 eV data. Scans were taken ~200 microns behind the LSM/YSZ interface on each electrode at 530 ^{o}C. La potentials are shown in red and measured using both La 4d (closed) and La 3d (open) spectra. $Sr_{lattice}$ and SrO potentials are represented by green and yellow symbols, respectively.

We then increased the temperature to 680 ^{o}C and observed that the nature of the cathode potential separation had changed (Figure 2.16), indicating that potential distributions on the LSM cathode are more complicated and vary with temperature. At lower temperature (530 ^{o}C), we observe the following trend in surface potentials: $V_L(SrO) > V_L(La) > V_L(Sr_{lattice})$. At higher temperature (680 ^{o}C),

the measured $V_L(Sr_{lattice})$ is greater than $V_L(La)$ at more surface sensitive photon energies. The reversal of potentials with temperature is likely due to surface restructuring as discussed Section 2.4.4. At less surface sensitive photon energies, the local potentials of $Sr_{lattice}$ and La converge. The $V_L(SrO)$ floats at either temperature due to a capacitive charging effect, as will be discussed in Section 2.4.4. This higher temperature, cathode surface potential behavior was observed on a different cell, as well (see SI 2.8.2).

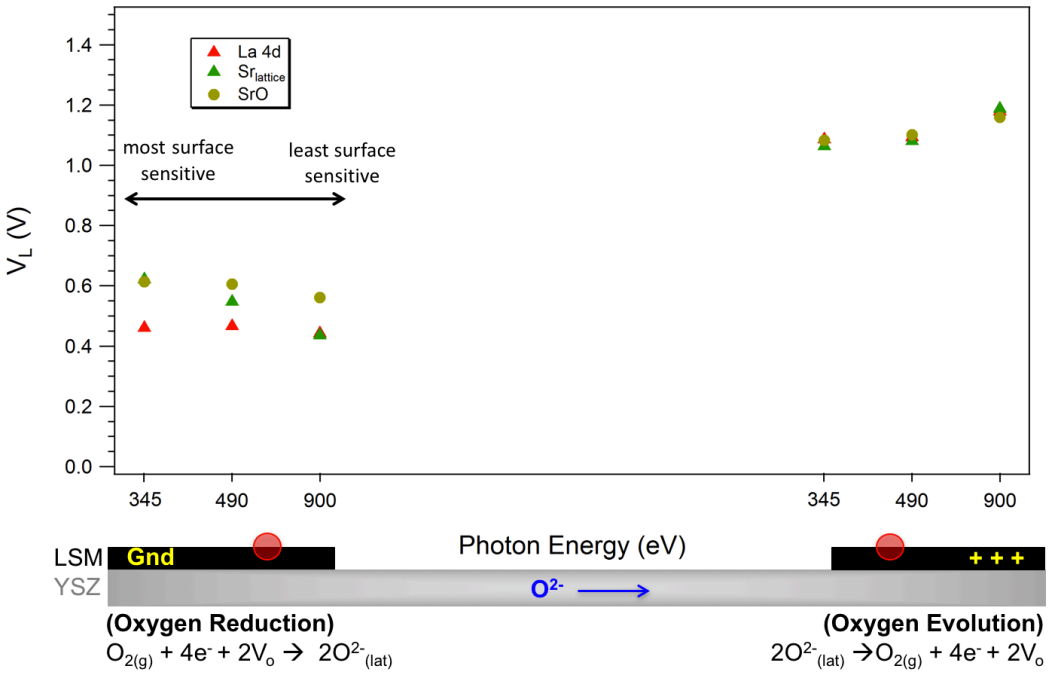

Figure 2.16. Local surface potentials calculated at different depths using photon energies of 345 eV, 490 eV, and 900 eV. Scans were recorded at a single location (red spot) ~200 microns behind the LSM/YSZ interface on each electrode at 680 ^{o}C in 200 mTorr. La potentials are shown in red, while $Sr_{lattice}$ and SrO potentials are represented by green and yellow symbols, respectively.

2.4 Discussion

As stated previously, a simple two-step process has been proposed for ORR on LSM,[2,39,40,225,226] and is re-written below. The first step is dissociative adsorption

of $O_{2(g)}$ (E2.1) and the second step involves incorporation of O into the lattice (E2.2). Wachsman *et al.*[2,39,40] conducted thermal, isotopic exchange experiments and showed that E2.2 is rate-limiting, assuming this mechanism. Under cathodic bias an additional third step, representing the polarization-induced reduction of Mn, must be taken into account (E2.3). The mechanism is thus:

$$O_{2(g)} + 2S \rightleftharpoons 2O_{(ads)} \quad \textbf{(E2.1)}$$

$$2O_{(ads)} + 4Mn^{3+}{}_{(lattice)} + 2V_o \rightleftharpoons 2O_{lattice}{}^{2-} + 4Mn^{4+} + 2S \quad \textbf{(E2.2)}$$

$$Mn^{4+} + e^- \rightleftharpoons Mn^{3+} \quad \textbf{(E2.3)}$$

where S represents a vacant surface site and $O_{(ads)}$ represents oxygen adsorbed on the LSM surface. The forward-weighted equilibrium arrows are used to emphasize the far-from-equilibrium conditions when the SOC is in operation. Our studies have shown Mn oxidation states lower than 3+ (Figure 2.10 and Figure 2.11) implying that the Mn centers are not always reduced from 4+ to 3+.

Reduction of Mn is more accurately described by itinerant (*i.e.* delocalized) electron conduction,[227,228] rather than localization of electrons on specific Mn centers. Itinerant conduction is evidenced by the Mn 3s spectra (Figure 2.9) where we observe only *one* doublet of spin-spin coupled peaks. In XPS, when ions of two distinct oxidation states exist (as in a localized electron conduction mechanism), each oxidation state generates a distinct spectrum. For example, when ceria (CeO_{2-x}) is reduced, electrons will localize on specific Ce centers reducing them from Ce^{4+} to Ce^{3+}. The two distinct oxidation states exhibit two distinct XPS spectra, *both of*

which are observed when a mix of the two states is present.[26,27] If LSM displayed this type of behavior, the Mn 3s spectra would exhibit multiple doublets of spin-spin coupling peaks, each representing distinct oxidation states (*e.g.* Mn^{4+}, Mn^{3+}, and Mn^{2+}). This behavior is not observed in our spectra, indicating an itinerant electron conduction mechanism.

When OER is electrochemically-promoted, E2.1 – E2.3 are reversed.

2.4.1 Surface Mn Oxidation States and Sr Segregation

Sr segregation to a LSM surface is a well-established phenomenon, the driving forces of which are typically attributed to electrostatic interactions or lattice strain from size mismatch between the A-site cations,[83,144,145] inducing segregation of the larger A-site cations (Sr).

Our findings show that under OCV conditions, the LSM surface is Sr-enriched, but in the form of SrO lying *on top* of the surface. Evidence that SrO is on top (and not well-connected to the LSM) is provided when the LSM is biased, and we observe a floating surface potential on SrO (Section 2.3.4), as will be discussed further in Section 2.4.4. The Sr that remains in the surface lattice is relatively depleted compared to the bulk. Mn is also reduced toward the upper surface of the material and the oxidation state is further reduced by increasing the temperature (Figure 2.10).

Enhanced Mn reduction at the surface is surprising, given the surface exposure to the O_2 atmosphere. The more reduced surface is in agreement with the *ex-situ* EELS studies conducted by Li *et al.*[140] and isotopic exchange tests of Yi-lin *et al.*[229] Surface reduction of Mn likely originates from minor structural

transformations of the perovskite, *i.e.* formation of Ruddlesden-Popper (RP) or oxygen-deficient phases as described below.

The RP phase, $A_{n+1}B_nO_{3n+1}$, as represented in Figure 2.17, is a stacking of "n" ABO_3 perovskite layers with inserted AO layers along the c-axis. In Figure 2.17, a standard LSM perovskite unit cell, with no cation or oxygen vacancies, is shown on the left. The A-site ion is represented by a mixture of La and Sr to indicate the expected 4:1 ratio. This ratio results in a Mn oxidation state of, [3+x]+, where "x" represents the Sr content (*i.e.* 0.2). A RP phase unit cell in which "n = 1," *i.e.* $(La_{0.8}Sr_{0.2})_2MnO_4$, is shown on the right side of the figure. In this unit cell the Mn oxidation state is calculated as, [2(1+x)]+, thus Mn has been reduced from 3.2+ to 2.4+. If the excess AO phases are relatively Sr-enriched, the Mn oxidation state will be higher than 2.4+. Formation of surface RP phases have been previously observed in *ex situ* studies on LSM[230] and similar perovskites (*e.g.* strontium titanates)[210,231-233]

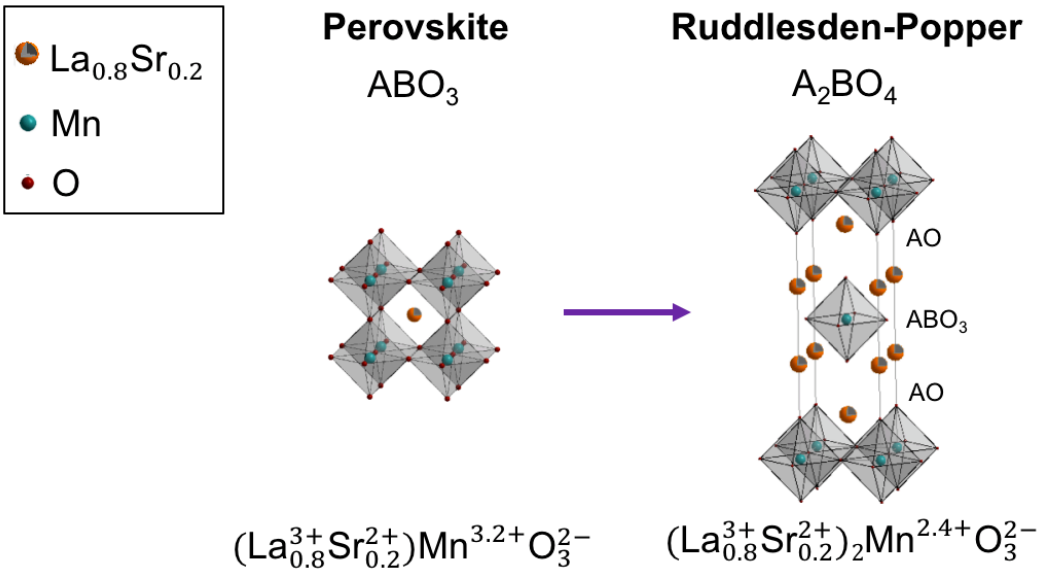

Figure 2.17.[234] A standard perovskite unit cell with no vacancies is shown on the left. The A-site is represented by a "mixed ion," $La_{0.8}Sr_{0.2}$, in orange/grey, oxide ions are in red and Mn ions are in blue with an oxidation state of [3+x]+, where "x" is the Sr content (0.2). The Mn are octahedrally coordinated and the A-site cations are 12-fold coordinated by oxide ions. On the right is a "n=1" RP phase (A_2BO_4) unit cell, containing excess AO layers in which the A site is 9-fold coordinated by oxide ions. The Mn oxidation state in the RP phase is [2(1+x)]+.

Oxygen-deficient phases can be obtained via reversible topotactic reduction of the stoichiometric ABO_3 perovskite, leading to the $ABO_{2.5}$ Brownmillerite-type structure, as shown in Figure 2.18. The figure uses the same symbols as in Figure 2.17, and shows the perovskite lattice on the left. The center of the figure shows oxygen vacancies being introduced and ordered along the [110] direction, forming intermediate phases of, $ABO_{3-\partial}$, in which "∂" represents the oxygen vacancy content. These vacancies are associated with a reduction in B-site ion (Mn) coordination, along with reduction of the B-site ion valence state. In LSM, Mn is reduced by 2∂ and the oxidation state is calculated as, [3+x-2∂]+, where "x" still represents the Sr^{2+} content. A Brownmillerite phase is shown on the right of the

figure with the formula, $La_{0.8}Sr_{0.2}MnO_{2.5}$ (Mn oxidation state is 2.2+). Brownmillerite phases can be described as BO_6 octahedral layers sandwiched between BO_4 tetrahedral chains. While a bulk Brownmillerite phase is likely not formed, oxygen vacancy formation at perovskite *surfaces* has been shown to be more facile.[141,235,236]

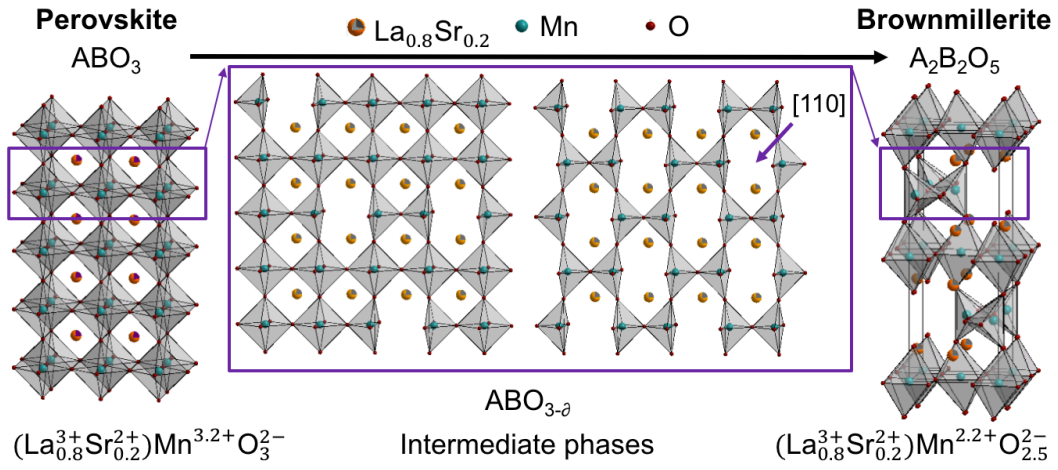

Figure 2.18.[234] A perovskite lattice (left) with no vacancies in which the A-site ions ($La_{0.8}Sr_{0.2}$) are in orange/grey, the Mn ions are in blue and are octahedrally coordinated by oxide ions in red. Proceeding to the right are intermediate phases with oxygen vacancies introduced along the [110] direction to different degrees. On the right is a Brownmillerite lattice, with the Mn in either an octahedral or a tetrahedral oxygen environment. The oxidation state may be described by, [3+x-2∂]+, where "x" represents Sr content (0.2) and "∂" represents oxygen vacancies (0.5 for the Brownmillerite phase).

A synergistic effect of Sr segregation, and formation of RP and oxygen-deficient phases at the surface is a plausible reason for surface Mn reduction. A postulated representation of the structure resulting from this theory is shown in Figure 2.19. The perovskite phase with oxygen vacancies, as in the intermediate phases displayed in Figure 2.18, is found in the lower surface region. The ratio

between La (grey spheres) and Sr (orange spheres) is larger than 4:1, meaning that Sr content is depleted in this surface region relative to the bulk. In the upper surface, an A_2BO_4 RP phase enriched in Sr from segregation is depicted. However, in temperature or under cathodic bias, Sr further extrudes from the upper surface to form SrO islands.[210,211] Thus the stoichiometry of the depicted upper surface is, $(La_{1-x}Sr_{x-y})_2MnO_{4-2y-\partial}$, in which "x" represents the initial Sr content before SrO extrusion and "y" represents the degree of SrO extrusion. The final oxidation state of Mn in this region can be described as, $[2(1+x-\partial)]+$, while the underlying perovskite is still described by $[3+x-2\partial]+$. While we assume that Sr is enriched in the upper surface RP phase due to the aforementioned lattice strain, enough Sr must be extruded as SrO so that the overall LSM surface is Sr-depleted, as indicated by Figure 2.4.

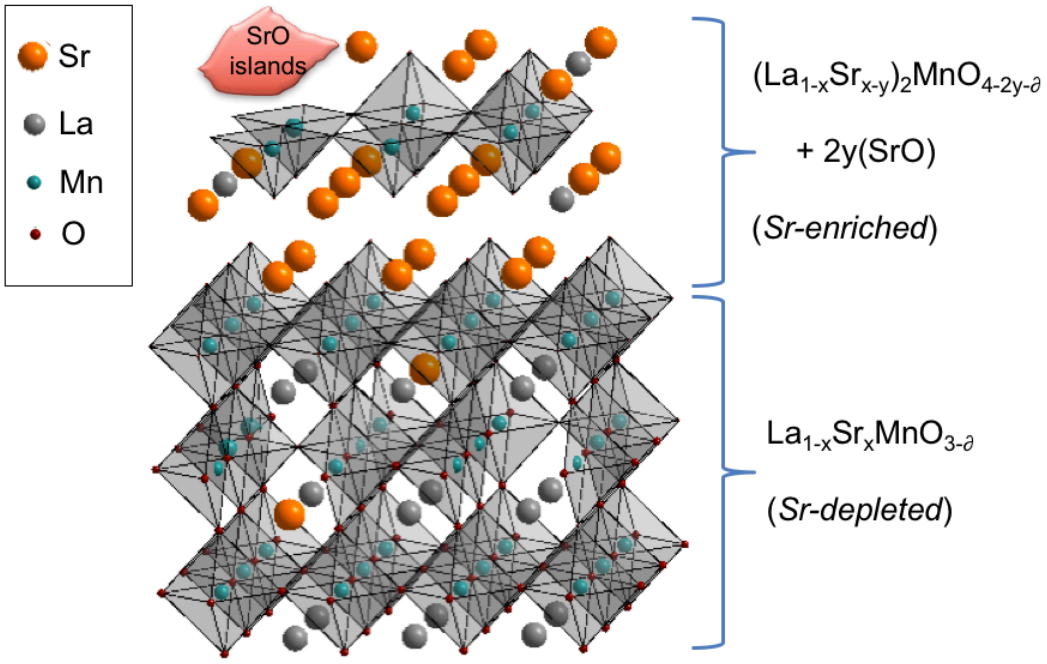

Figure 2.19.[234] Hypothetical, simple representation of the atomic distributions in the LSM surface. The lower surface is depicted as an oxygen-deficient intermediate phase between the full perovskite and Brownmillerite phase. La ions (grey spheres) and Sr ions (orange spheres) are found with a relative Sr depletion compared to the bulk stoichiometry (*i.e.* $La:Sr_{lattice} > 4$). Oxygen vacancies are present and represented by "∂." At the upper layer of the surface, a RP phase forms which primarily consists of Sr^{2+} ions in the A-site that have segregated to the surface. These Sr^{2+} ions may further extrude on top of the LSM surface as SrO islands leaving the upper surface layer with a stoichiometry of $(La_{1-x}Sr_{x-y})_2MnO_{4-2y-\partial}$, where "x" represents the initial Sr content before SrO extrusion and "y" represents the extent of SrO extrusion.

Because the increased Sr content in the RP phase may increase the Mn oxidation state, the larger driving force in Mn surface reduction is likely oxygen vacancy formation. Vacancy formation is further augmented by an increase in temperature, in agreement with the thermogravimetric and coulometric titration bulk studies of Mizusuki *et al.*[14] and Decorse *et al.*[139]

2.4.2 Cathodically-Induced SrO Extrusion

Cathodic bias induces a partially reversible growth in SrO on top of the entire LSM electrode, and appears to be concurrent with the reduction of Mn (*i.e.* increased oxygen vacancies). As shown in Section 2.3.3, Mn is reduced under cathodic bias whereas in Chapter 3 (Section 3.3.1) we will show that Mn is oxidized under anodic bias. However, SrO does not exhibit appreciable growth under anodic polarization, indicating that oxygen vacancies are correlated with SrO extrusion. This augmented SrO extrusion may be due to a growing instability of Sr as oxygen vacancies form and Sr becomes increasingly under-coordinated. By entering the fully coordinated, highly stable SrO rock-salt phase, the instability is mitigated.

The cathodic polarization increases the average SrO thickness on the electrode surface (Figure 2.8) which implies that active sites might be blocked. However, the electrochemical performance of the cell does not decline, but remains relatively stable at constant bias (~1% change over 2 hours). Our data is in agreement with the *in operando* XPS studies on LSM conducted Backhaus-Ricoult[154,155] who also saw an enrichment in Sr under cathodic bias, although it is unclear if this enrichment was in the form of $Sr_{lattice}$ or SrO. However, the data is contrasted with the findings of Huber *et al.,*[153] who saw a depletion of both SrO *and* $Sr_{lattice}$ with a concurrent improvement in electrochemical performance. Both Backhaus' and Huber's work were conducted in significantly different conditions (750 nTorr O_2) than ours (200 mTorr O_2), though.

Our results do not necessarily contradict the premise that the removal of passivating SrO species is the cause for cathodic activation. While the LSM did not exhibit a removal of SrO under bias, the large improvements in electrochemical performance typically seen in over a short time were not observed either. The discrepancy between results of SrO extrusion or reincorporation (as observed in some other works) into the LSM lattice under cathodic bias bears more investigation, but may be due to different operating conditions in our studies.

2.4.3 Electrochemically Active Regions and Charge Transfer Resistances

While LSM is generally regarded as an electronic conductor, there are some contradictory findings. Both our spatially resolved Mn oxidation state and surface potential measurements (Figure 2.11 and Figure 2.13) provide what we believe to be the first AP-XPS evidence that LSM behaves as a primarily electronic conductor

material, under the conditions studied, as described below. Furthermore, our potential map supports that LSM is superior for electrochemically promoting ORR than OER.

Figure 2.20 gives a simple depiction of how the ORR mechanism would occur on an electronic conductor (top) and a mixed ionic/electronic conductor (MIEC, bottom). When a cathodic bias is applied to an electronic conductor, as LSM is in our experiments, electrons flow into the LSM and travel through the *entire* electrode by reducing Mn centers from their equilibrium (*i.e.* OCV) oxidation states (E2.3). Mn reduction is observed across the entire electrode region scanned in Figure 2.11 (~300 μm behind the LSM/YSZ interface up to the interface). Additionally, scans over 1 mm away from the interface (SI Figure 2.5) show that the Mn is reduced further away from the region depicted in Figure 2.11, further indicating that LSM is reduced everywhere.

In the proposed mechanism, the reduced Mn will transfer electrons to surface adsorbed oxygen atoms via E2.2, reducing them to oxide ions. This step occurs at the LSM/YSZ interface (*i.e.* the TPB) in an electronic conductor, as YSZ has a significantly greater ability for incorporating the oxide ion than LSM. The surface potential map shown in Figure 2.13 supports the electronic conduction path, as the potential only drops at the LSM/YSZ interface. The potential drop is a marker of where electrochemical activity occurs, signifying that the path of least resistance for ORR (and OER) is at the TPB.

Electronic Conductor
(surface path)

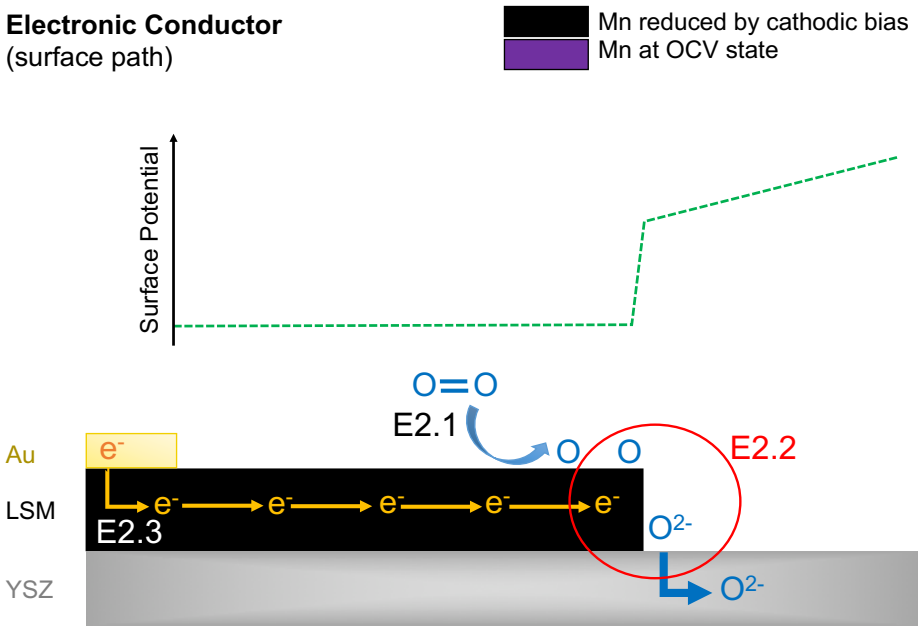

Mixed Ionic/Electronic Conductor
(bulk path)

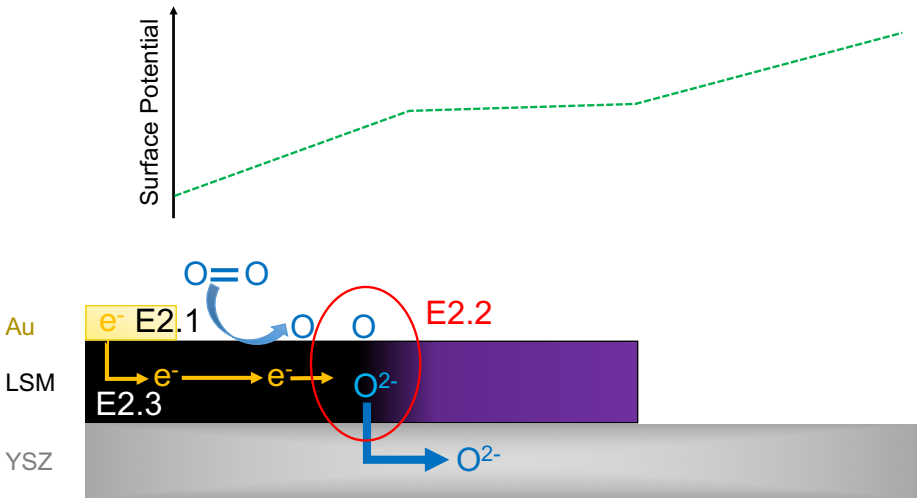

Figure 2.20. Schematics for the three mechanistic steps for (Top) electronic conduction and (Bottom) MIEC conduction. In the electronic conduction path electrons flow into the LSM from the Au reducing Mn (E2.3). The electrons travel to the LSM/YSZ interface (TPB) thereby reducing the entire LSM electrode (represented by black coloring). On the surface of the LSM, $O_{2(g)}$ adsorbs and dissociates (E2.1) and at the TPB, electrons are able to reduce the O species into O^{2-} ions which can be incorporated into the YSZ electrolyte via oxygen vacancies (E2.2). The potential map shape is provided above (dotted green line) showing a sharp drop at the interface where all electrochemical activity is occurring. In the MIEC scheme the three steps are the same except E2.2 is able to occur on the LSM itself, not just at the TPB. As such, electrons are utilized in E2.2 as they flow into LSM and, in an extreme case as depicted, are used up before they reach the interface. In this case, some of the Mn oxidation states remain at OCV values (purple). Because activity occurs as early as the point of electron insertion, a potential drop over the entire active region would be observed, rather than just a sharp drop at the TPB.

For a MIEC electrode, surface reactions such as E2.2 do not require a TPB site as the electrode has sufficient ionic conductivity to directly incorporate the oxide ion (Figure 2.20, bottom). Therefore, as electrons flow into the electrode under bias, they are consumed by surface reactions (E2.2) before they reached the end of the electrode. This phenomenon has been seen in our previous work on the MIEC material, ceria.[26] If LSM was not behaving as a pure electronic conductor, Mn oxidation states beyond this "active region" would not show a clear deviation from their OCV value (as depicted in the MIEC path). This situation is not in agreement with our data. Furthermore, because electrochemical activity is able to occur on the electrode itself, the potential drop should be closer to the electrode contacts and would likely be extended over a region of the electrode, which is not what we observe in our work.

The potential drops at the LSM/YSZ interfaces of the symmetrical cell demonstrate that LSM is a better electrocatalyst for ORR than OER under our conditions. Table 2.4 shows the measured voltage drop, current, and resistance (approximated from Ohm's Law, V = iR) between the LSM and YSZ on each side with respect to the surface potential evaluated from La and $Sr_{lattice}$. Even though the potentials do not match on the cathode side, regardless of which we use in evaluation, the R_{ct} is significantly lower than on the anode side.

Table 2.4. Measured potential drops for the LSM/YSZ interfaces for cathode and anode sides.

i (μA)	Component	Potential Drop (V)	R (Ω)
310	Anode (OER)	$V_{L(La)} - V_{L(Zr)} = 0.45$	~1450
		$V_{L(Sr\ lattice)} - V_{L(Zr)} = 0.45$	~1450
	Cathode (ORR)	$V_{L(Zr)} - V_{L(La)} = 0.10$	~325
		$V_{L(Zr)} - V_{L(Sr\ lattice)} = 0.20$	~650
	Electrolyte	$V_{L(Zr\ right)} - V_{L(Zr\ left)} = 0.05$	~200

The drops are calculated by taking the difference between the V_L of Zr and La or $Sr_{lattice}$, and the corresponding resistance is calculated from $V_L = iR$. The potential drop and resistance from the right interface (anode) to the left interface (cathode) along the electrolyte is also determined.

2.4.4 Potential Separation

We observe a separation in measured surface potentials on the cathode, in which SrO exhibits a potential that is always higher than the lattice species, and sometimes, the YSZ electrolyte. A temperature dependent separation between $Sr_{lattice}$ and La potentials is observed as well. Regardless of the cause of the surface potential separation, our main conclusion remains unaffected. The major potential

drops associated with ORR and OER occur at the LSM/YSZ interface, and the drop (and associated resistance) corresponding to ORR is lower than that for OER.

We believe that because of the electronically insulating properties of SrO,[210,211] SrO is not electronically well-connected to the LSM electrode, creating a capacitive effect. In the cathode surface potential measurements at 530 ^{o}C (Figure 2.13), we observe a divide between the calculated local voltages of SrO, La, and $Sr_{lattice}$, in which the SrO displays the highest value, while $Sr_{lattice}$ displays the lowest. This divide increases with larger bias (see SI Section 2.6.7.1) and does not appear to vary appreciably with depth (Figure 2.15).

This capacitive effect places a positive charge on the SrO and a negative charge on the LSM upper surface layer (see Figure 2.19) The positive charge increases the measured SrO BE_{bias} *in addition* to the increase caused by the local potential (see SI Section 2.6.7.2 for further details). The artificial charging increase in the BE_{bias} measurement accounts for the calculated V_L(SrO) being higher than the calculated V_L(YSZ) value, given that the potential should *drop* at the grounded LSM (as it does for the lattice components). That the SrO is not well-connected to the LSM surface is supported by scanning tunneling microscopy measurements on strontium titanate perovskites made by Chen *et al.*,[210,211] which found a wide bandgap (~4.2 eV) on surface SrO. The wide bandgap is consistent with electronically insulating islands on top of the perovskite, as opposed to RP phases that are well-connected to the surface and exhibit a bandgap of ~1.0 eV, in those materials.[210,211]

As the SrO experiences a positive charging effect, the LSM surface experiences an excess of negative charge build-up that negatively shifts the measured BE_{bias} values of species at the upper surface (SI Section 2.6.7.2). In our RP phase assumption, the upper surface is relatively enriched in $Sr_{lattice}$ (Figure 2.19) so that the $BE_{bias}(Sr_{lattice})$ is modified by this negative charging effect by a more significant degree than the La centers, which are concentrated in the lower regions of the surface. The $V_L(Sr_{lattice})$ values likely do not change appreciably with depth because the negative charging of the $Sr_{lattice}$ species in the upper surface dominates over the depleted $Sr_{lattice}$ species in the lower surface. In turn, because La is concentrated in these lower layers, the measured La potentials are mostly unaffected by the capacitor charging and do not vary appreciably with depth either.

At temperatures between 600 - 700 ^{o}C, the calculated potentials of La and SrO display similar behavior as at 530 ^{o}C, but the $V_L(Sr_{lattice})$ varies with depth. The calculated $V_L(Sr_{lattice})$ matches the $V_L(SrO)$ at more surface sensitive energies, but matches the $V_L(La)$ value at deeper surface probing (Figure 2.16 and SI Figure 2.4). We attribute this behavioral change to changes in the surface at higher temperature. It is possible that at higher temperatures, as more oxygen vacancies are formed and more Sr extrudes out the surface as SrO, the RP phase becomes less prominent. As the $Sr_{lattice}$ depletes further, the charging effect on the $Sr_{lattice}$ relative to the La becomes less significant, hence we do not see a relatively lower surface potential on $Sr_{lattice}$.

Other possibilities include an increase in under-coordinated $Sr_{lattice}$ centers, which dominate the upper surface layers, as greater SrO extrusion occurs. Lower

coordination would decrease the extra-atomic relaxation energy (see Section 1.4.1.4 for more details), which in turn would increase the measured $BE_{bias}(Sr_{lattice})$, and thus the calculated $V_L(Sr_{lattice})$, at more surface sensitive energies.

2.5 Conclusion

We conducted *in operando* AP-XPS studies on a LSM symmetrical cell to monitor electrode composition changes, surface speciation, Mn oxidation states, and surface potentials, as one LSM electrode functioned as a cathode and the other as an anode. At OCV, Mn is reduced toward the upper region of the surface, presumably from the formation of oxygen-deficient RP and Brownmillerite phases. Sr is likely enriched in the RP phase, but is then depleted via SrO extrusion. A cathodic bias induces further reduction of Mn and extrusion of SrO, and our spatially-resolved XPS measurements show that these phenomena occur throughout the LSM surface.

We also spatially-resolved local surface potentials across the SOC and found that all electrochemical activity, signified by a voltage drop, occurs at the electrode/electrolyte interface on both the cathode and anode sides. Because the voltage drop occurs at the electrode/electrolyte interface, and Mn is reduced relative to its OCV value on the entire LSM surface under cathodic bias, we are able to provide what we believe is the first *in operando* spectroscopic evidence that LSM behaves as an electronic conductor. The measured potentials on the LSM cathode displayed different values attributed to a capacitive effect between the LSM surface and poorly, electronically connected SrO islands on top of the electrode. Furthermore, a smaller potential drop was observed on the cathode side compared

to the anode side, signifying that there is lower resistance, and therefore superior activity, for ORR in comparison to OER on LSM.

2.6 Supporting Information

2.6.1 Impedance Spectra

SI Figure 2.1 shows EIS scans taken at each operating temperature: 530 ^{o}C (red), 620 ^{o}C (blue), and 680 ^{o}C (green). The scans were taken at 0 V vs. OCV with a sin wave amplitude of 10.0 mV. Settings which varied between temperatures may be found in SI Table 2.1, along with corresponding R_B values (measured at the high frequency intercept). The R_B value can be directly correlated with the temperature of the sample. The spectrum at 530 ^{o}C is noisy which is attributed to relatively low operating temperatures for LSM making our R_B a large estimate.

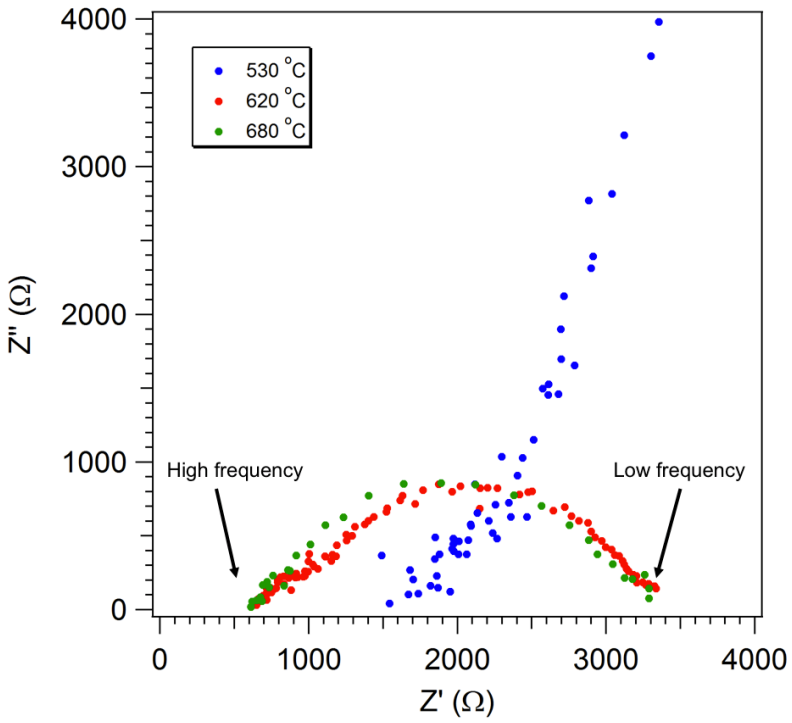

SI Figure 2.1. Impedance spectra taken at the three studied temperatures 530 ^{o}C (red), 620 ^{o}C (blue), and 680 ^{o}C (green).

SI Table 2.1. EIS settings taken at 0V vs. OCV with logarithmic values between low and high frequency. The sin wave amplitude was 10.0 mV.

TC (^{o}C)	High Frequency (kHz)	Low Frequency (mHz)	R_B (Ω)
530	5.000	100.000	1600 ± 200
620	5.000	100.000	640 ± 20
680	100.000	20.000	580 ± 20

2.6.2 Determining XPS Spectra Constraints: Raw Data

2.6.2.1 Sr 3d Constraints

Two doublets were fit for $Sr_{lattice}$ (peaks A and B) and SrO (peaks C and D) species. The raw OCV data from two cycles on each LSM electrode for determining the Sr 3d fitting parameters given in Table 2.1. are shown in SI Table 2.2**.**

SI Table 2.2. Sr 3d OCV values for determining peak constraints.

Cycle / Electrode	hν (eV)	Pos A (eV)	Pos B (eV)	Pos C (eV)	Pos D (eV)	FWHM A	FWHM C
Cycle 1 / Cathode	345	136.84	138.61	137.63	139.47	1.20	1.89
	490	136.84	138.61	137.60	139.41	1.15	1.96
	900	136.75	138.51	137.45	139.28	1.22	2.14
Cycle 2 / Cathode	345	136.85	138.62	137.65	139.47	1.16	1.89
	490	136.86	138.62	137.68	139.49	1.20	1.93
	900	136.77	138.55	137.53	139.31	1.21	2.12
Cycle 1 / Anode	345	136.89	138.64	137.67	139.50	1.21	1.90
	490	136.88	138.65	137.65	139.47	1.19	1.98
	900	136.83	138.59	137.57	139.38	1.23	2.13
Cycle 2 / Anode	345	136.88	138.63	137.75	139.56	1.17	1.92
	490	136.85	138.62	137.71	139.53	1.14	2.02
	900	136.78	138.56	137.57	139.38	1.20	2.17
Average	**---**	**136.84**	**138.60**	**137.62**	**139.44**	**1.19**	**2.00**

The first column states the OCV cycle and electrode that the spectra were taken from while the second column states the photon energy used. The other columns give the relevant values for determining constraints between different peaks. The peaks A and B represent the $3d_{5/2}$ and $3d_{3/2}$ peaks for $Sr_{lattice}$, respectively, and peaks C and D represent the $3d_{5/2}$ and $3d_{3/2}$ peaks for SrO, respectively. The bottom row shows the average value of each column. Constraints already present in the fitting at the time this data was analyzed were the area and FWHM constraints on peaks B and D seen in Table 2.1.

2.6.2.2 La 4d Constraints

Three La 4d peaks were fit, $4d_{5/2}$ and $4d_{3/2}$ (peaks A and B, respectively), and a peak encompassing charge-transfer satellites (peak C). A fourth peak was eventually fit to account for the Si 2p peak (peak D) from a SiO_2 contaminant. The raw OCV data from two cycles on each LSM electrode used for determining the La 4d peak fitting parameters given in Table 2.2 are shown in SI Table 2.3.

SI Table 2.3. La 4d OCV values for determining peak constraints.

Cycle / Electrode	hν (eV)	Pos A (eV)	Pos B (eV)	Pos C (eV)	FWHM A	FWHM C	Area A (cps)	Area C (cps)
Cycle 1 / Cathode	900	105.89	109.13	108.61	1.80	5.4145	70965	143603
Cycle 1 / Anode	900	105.98	109.20	108.66	1.88	5.0764	70886	130412
Cycle 2 / Cathode	900	105.90	109.17	108.55	1.83	5.0243	66633	136773
Cycle 2 / Anode	900	105.87	109.20	108.62	1.91	5.0235	73381	142066
Average	**---**	105.91	109.18	108.61	1.85	5.13	70467	138214

The first column states the OCV cycle and electrode that the spectra were taken from while the second column states the photon energy used. The other columns give the relevant values for determining constraints between peaks A, B, and C. The peaks A and B represent the $4d_{5/2}$ and $4d_{3/2}$ peaks of La, respectively, and peak C encompasses the charge transfer satellites. The bottom row shows the average value of each column. Constraints already present in the fitting at the time this data was analyzed were the area and FWHM constraints on peak B as seen in Table 2.2.

The raw OCV data used to determine the Si 2p (peak D) FWHM relative to peak A are found in SI Table 2.4. The data used were acquired over two cycles of OCV scans on the cathode and one cycle of OCV scans on the anode. The second anode cycle was neglected for reasons described below.

SI Table 2.4. La 4d and Si 2p OCV values for determining peak constraints.

Cycle / Electrode	hν (eV)	FWHM A	FWHM D
Cycle 1 / Cathode	345	1.77	1.97
	490	1.77	2.02
Cycle 1 / Anode	345	1.81	1.89
	490	1.82	1.88
Cycle 2 / Cathode	345	1.77	2.11
	490	1.80	2.09
Average	**---**	1.79	1.99

The first column states the OCV cycle and electrode that the spectra were taken from while the second column states the photon energy used. The other columns give the relevant values for determining constraints between peaks A and D. Peak A represents the $4d_{5/2}$ of La while peak D represents the 2p peak of Si. The bottom row shows the average value of each column. Constraints already present in the fitting at the time this data was analyzed were the constraints on peaks B and C as seen in Table 2.2.

2.6.2.3 Determining La 3d Constraints

Three peaks were fit in the $3d_{5/2}$ region of the La 3d XPS spectra. A peak corresponding to the $3d_{5/2}$ photoelectron (peak A) and two charge-transfer satellites (peaks B and C). To determine the constraints between the peaks, OCV data collected on each electrode over two cycles was used and is given in SI Table 2.5.

SI Table 2.5. La 3d OCV values for determining peak constraints.

Cycle / Electrode	Pos A (eV)	Pos B (eV)	Pos C (eV)	FWHM A	FWHM B	FWHM C	Area A (cps)	Area B (cps)	Area C (cps)
Cycle 1 / Cathode	836.95	841.53	838.13	1.66	3.51	2.64	9532	24150	24150
Cycle 1 / Anode	836.95	841.53	838.13	1.66	3.51	2.64	9532	24150	24150
Cycle 2 / Cathode	836.88	841.45	838.10	1.71	3.59	2.56	10825	24322	24322
Cycle 2 / Anode	836.88	841.45	838.10	1.71	3.59	2.56	10825	24322	24322
Average	836.91	841.49	838.11	1.68	3.55	2.60	10178	24236	24236

The first column states the OCV cycle and electrode that the spectra were taken from while the second column states the photon energy used. The other columns give the relevant values for determining constraints between peaks A, B, and C. Peak A represents the $3d_{5/2}$ peak and peaks B and C represent charge transfer satellites. The bottom row shows the average value of each column. Constraints already present in the fitting at the time this data was analyzed were the equal areas between peaks B and C.

2.6.3 Cross Sections and IMFPs

Cross sections and IMFPs for La 4d and Sr 3d in LSM are given in SI Table 2.6 and were determined from the works of Yeh and Lindau[237] and the NIST Electron Effective Attenuation-Length Database,[238] respectively. The IMFPs of Sr 3d electrons in SrO are in SI Table 2.7.

SI Table 2.6.[237,238] List of cross sections and IMFPs at different photon energies for La 4d and Sr 3d electrons in the LSM material**.**

Photoelectron	hν (eV)	Cross Section	IMFP (nm)
La 4d	345	1.00	0.696
	490	0.78	0.923
	900	0.30	1.523
Sr 3d	345	3.35	0.645
	490	1.70	0.874
	900	0.34	1.478

SI Table 2.7.[238] List of IMFPs at different photon energies for La 4d and Sr 3d electrons in SrO.

Photoelectron	hν (eV)	IMFP (nm)
Sr 3d	345	0.804
	490	1.111
	900	1.909

2.6.4 Auxiliary Spectra

2.6.4.1 Sr 3d Scans Taken Over Two Cycles at 345 eV and 490 eV

SI Figure 2.2 shows the Sr 3d spectra taken under the same conditions as in Figure 2.5 at photon energies of 345 eV and 490 eV (SI Figure 2.2A and B, respectively). It can be observed at each energy that the intensity of SrO relative to Sr increases under cathodic bias, but decreases when reverting to OCV indicating that SrO growth is induced by cathodic bias, but is partially reversible, in agreement with the 900 eV data reported in Section 2.3.2.

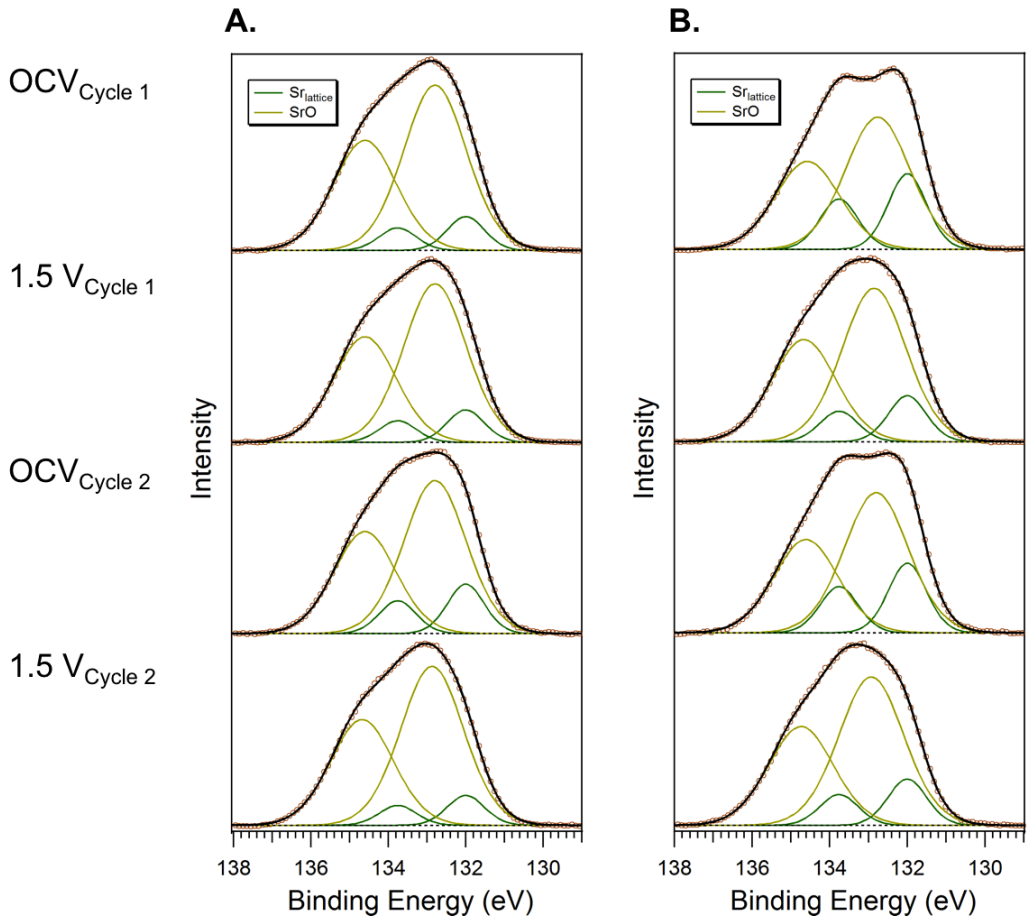

SI Figure 2.2. Sr 3d spectra collected at photon energies of 345 eV (A) and 490 eV (B), ~200 microns behind the LSM/YSZ interface at 620 ^{o}C, between two cycles of OCV and 1.5 V bias. The green and yellow doublets represent the $Sr_{lattice}$ and the SrO species, respectively. A slight shift in the peaks is observed under bias due to local surface potentials.

2.6.4.2 Mn 3s Spectra taken at 490 eV under OCV and Bias

SI Figure 2.3 shows the Mn 3s taken under the same conditions as in Figure 2.9. Compared to that figure, we observe a larger ΔE between the peaks at either condition than in the deeper 900 eV scans. Furthermore, reduction is promoted by bias and higher temperatures.

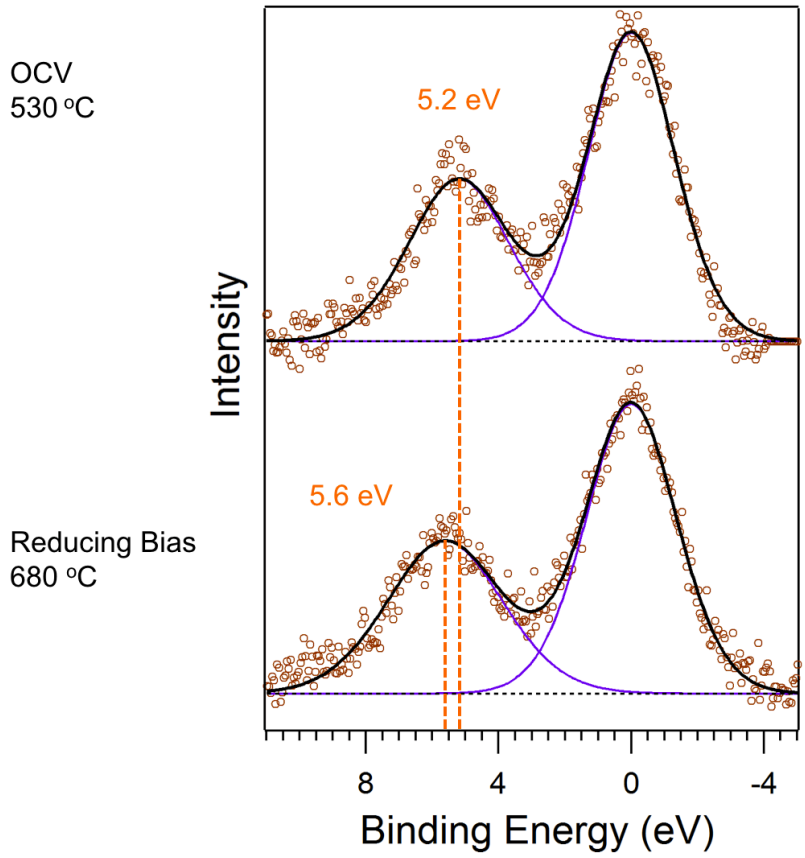

SI Figure 2.3. Mn 3s spectra taken at a photon energy of 490 eV under two conditions: OCV at 530 °C (top) and a reducing bias at 680 °C (bottom). A larger ΔE, commensurate with more reduced Mn, is observed at higher T with cathodic bias. The low BE peak is calibrated to 0 eV.

2.6.5 Surface Potentials with Depth at ~620 °C

A similar experiment was conducted as that shown in Figure 2.16, but at 620 °C, which was still a significantly higher temperature than our 530 °C studies. The difference was enough to induce the same switch in local potential separation as seen in Figure 2.16, in which the SrO and La exhibit ~constant V_L with depth, but the $Sr_{lattice}$ varies. At the most surface sensitive energy it is near equal to the SrO while toward the bulk, it is near equal to La. This reproducibility builds

confidence that the higher temperature regime results in different $Sr_{lattice}$ behavior with regards to measured potential.

In this experiment, we only collected La 3d scans at a photon energy of 1230 eV, allowing the kinetic energy (depth) to be the same as La 4d electrons at 490 eV.

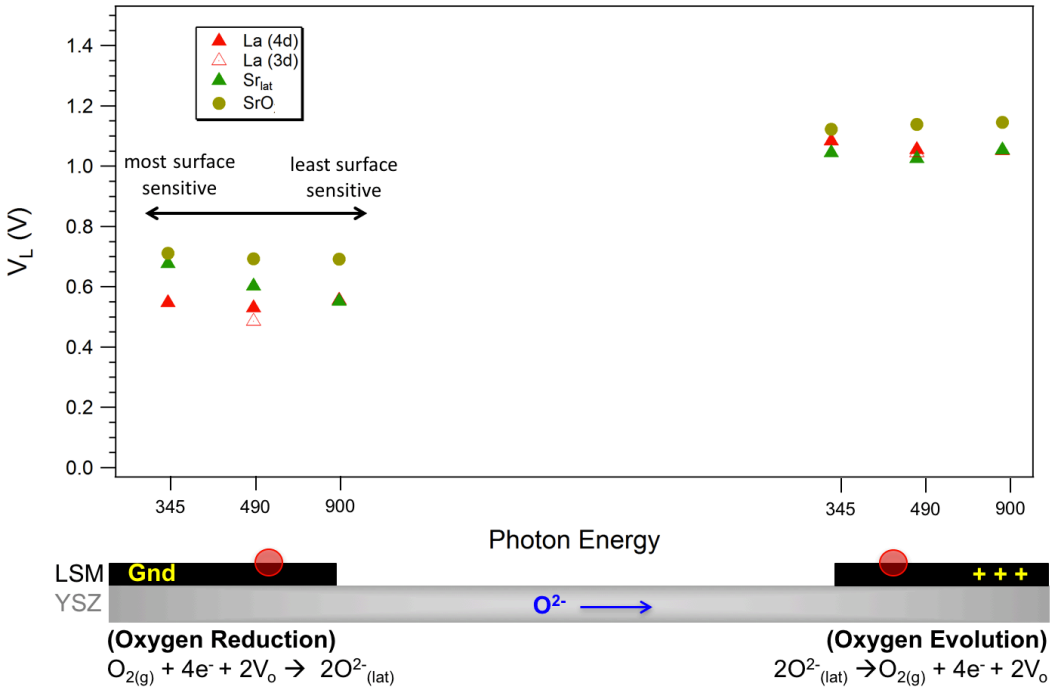

SI Figure 2.4. Local surface potentials measured in the same manner as in Figure 2.16, but at 620 °C. As in Figure 2.16, this cell showed a potential separation on the ORR side with SrO at the highest potential, while La is ~constant with depth, but the $Sr_{lattice}$ varies with depth.

2.6.6 Mn Reduction Across the LSM Cathode Surface

SI Figure 2.5 lower plot shows the Mn oxidation state along the electrode from the LSM/YSZ interface to 1.25 mm behind the interface. The spectra were collected at OCV (black) and 1.5 V bias (red) at four different points in the cell (no area detector was used). The temperature was in the range of 500 ~ 550 °C. The difference between biased and OCV states is shown in the top plot (blue) and shows

the extent of reduction. As can be seen, this difference is relatively constant up to the edge, where no clear reduction is observed. This lack of reduction could be related to ORR kinetics at the TPB, where Mn^{3+} is transferring electrons to oxygen and converting back to Mn^{4+}, but it could also be due to the weaker signal found at the edge where only part of the scanning window includes LSM. Furthermore, at the interface, there are likely a fair amount of LSM islands from the deposition which would not be electrically connected to the electrode and would not have a lower oxidation state from polarization.

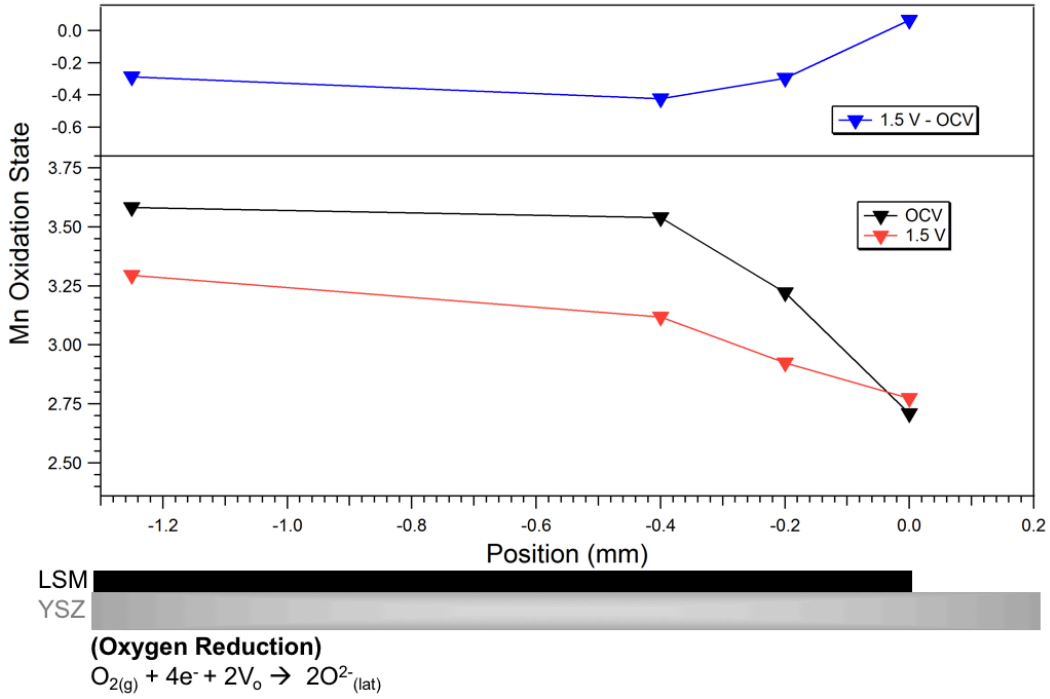

SI Figure 2.5. Mn oxidation state (lower plot) as a function of position along the LSM electrode at 500 ~ 550 ^{o}C in 200 mTorr O_2. The black and red symbols represent OCV and 1.5 V biased conditions, respectively. The top plot in blue shows the difference between the oxidation state under bias and OCV and effectively shows the extent of reduction along the electrode. The LSM/YSZ interface is found at 0 mm. A lateral schematic of the electrode on the YSZ electrolyte is provided at the bottom for position clarification.

For this experiment, we used a different potentiostat and program that did not allow for impedance tests. Furthermore, no thermocouple was attached to the sample, so that our temperature estimate is based on currents drawn at comparable levels to the cells run at 530 ^{o}C in the main body of the chapter.

2.6.7 SrO Capacitive Effect under Cathodic Bias

2.6.7.1 Potential Map and Sr 3d spectrum at Very High Polarization

The cell shown in Figure 2.13 was polarized at 5.0 V and the resulting potential map is shown in SI Figure 2.6. The separation of local potentials between the three species on the cathode side is larger while the local potentials on the anode side are still relatively close to one another. The growing separation of $V_{L(SrO)}$ from $V_{L(Sr\ lattice)}$ with bias is clearly visible in the Sr 3d XPS spectra as can be seen in SI Figure 2.7 which shows three different conditions (from bottom to top): OCV, 1.5 V bias, and 5.0 V bias. To emphasize the growing distance between the $Sr_{lattice}$ and SrO doublets, with potential, the $Sr_{lattice}$ $3d_{5/2}$ peak has been calibrated to 132.0 eV, removing the surface potential induced BE shift. At 1.5 V, the SrO BE is still higher than in the OCV condition and this effect increases at 5.0 V. This extra shift is attributed to positive charging from a capacitive effect, as detailed below.

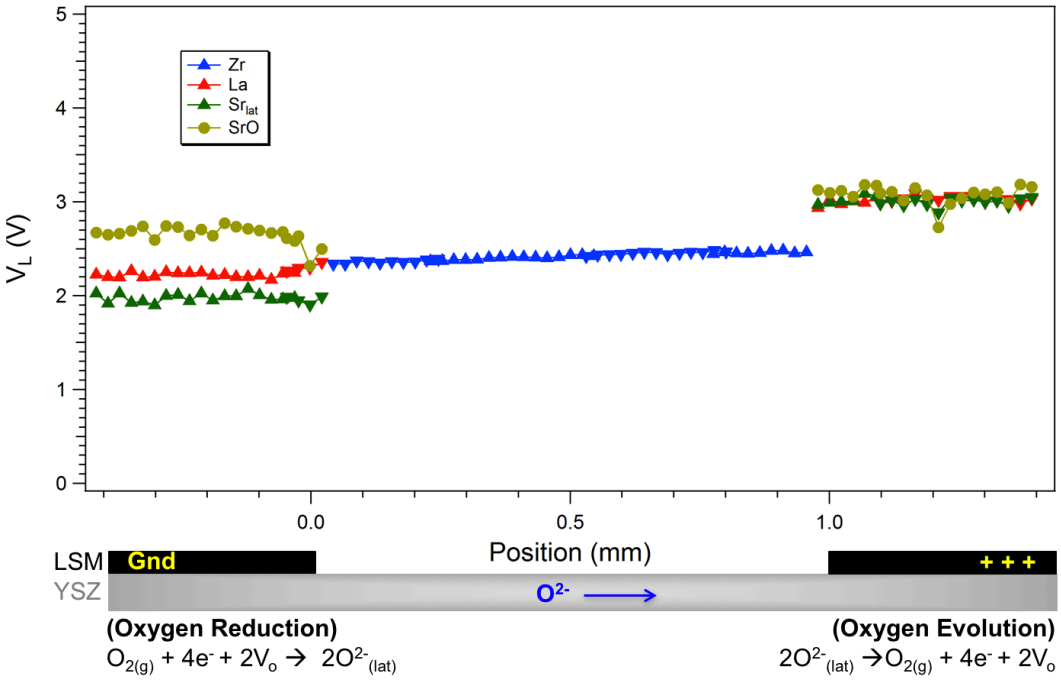

SI Figure 2.6. Local surface potentials as a function of position along the LSM electrode at 530 ^{o}C in 200 mTorr O_2. The map is read in the same manner as in Figure 2.13. The potential on each electrode is still relatively constant, but on the cathode side, the measured potentials for SrO, La, and $Sr_{lattice}$ show a greater separation than at 1.5 V.

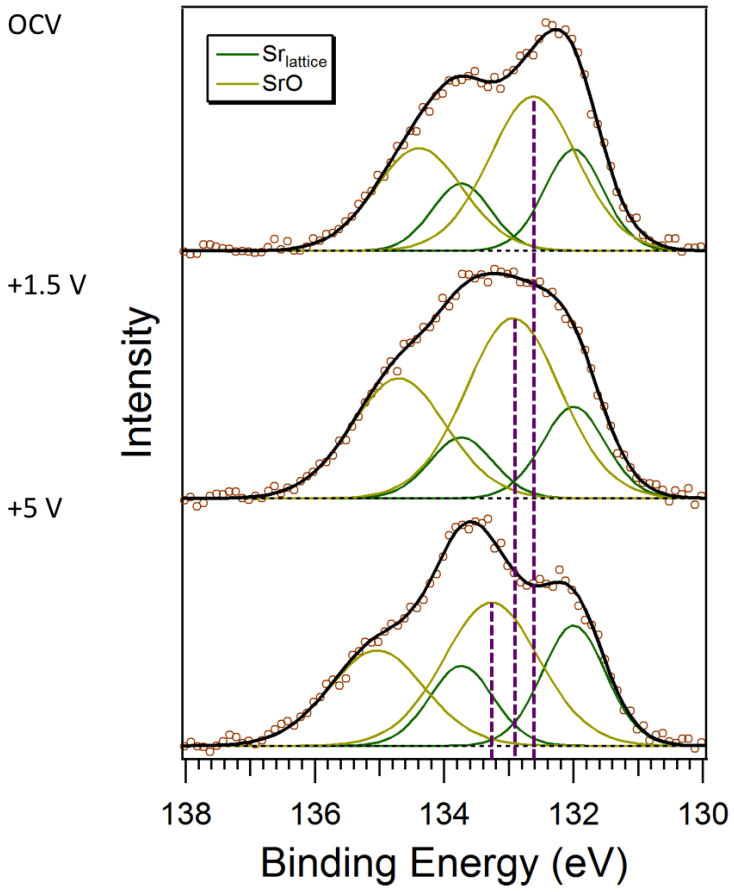

SI Figure 2.7. Sr 3d spectra taken at a photon energy of 490 eV in 200 mTorr O_2 at 530 ^{o}C, for OCV, 1.5 V, and 5.0 V at the same spot (~400 µm behind the LSM/YSZ interface). The green and yellow doublets represent the $Sr_{lattice}$ and the SrO species, respectively. The spectra were calibrated so that the $Sr_{lattice}$ $3d_{5/2}$ peak is located at 132.0 eV to remove the local surface potential effects, and it can be seen that with increasing bias the SrO doublet moves further away from its OCV position.

2.6.7.2 BE Shifts Induced by Capacitive Charging

The positive charge on the SrO will shift the calculated V_L value to higher-than-true values. To demonstrate this shift, we consider that the measured BE value under bias will be equal to the BE under OCV shifted by both the local potential and positive charging:

$$BE_{bias} = BE_{OCV} + V_{L\ true} + C$$

where $V_{L\ true}$ represents the actual surface potential and "C" represents the charging caused by the poorly, electronically-connected SrO acting as the positive end of a capacitor. Rearranging the equation and recognizing that $BE_{bias} - BE_{OCV}$ will equal the local surface potential that we calculate ($V_{L\ calculated}$), we have:

$$V_{L\ calculated} = V_{L\ true} + C$$

Because the "C" value is positive, the capacitive effect increases the calculated V_L from true. A similar logic can be applied to the $Sr_{lattice}$ that exists in the RP phase at the upper surface of LSM, except "C" is negative, causing the V_L calculated to be lower than true.

3 Oxygen Evolution on LSM Electrodes and Surface Oxygen Vacancy Formation on LSM and LSM/YSZ Composite Materials

3.1 Introduction

This chapter provides details on two different ambient pressure X-ray photoelectron spectroscopy (AP-XPS) experiments involving lanthanum strontium manganite ($La_{1-x}Sr_xMnO_{3\pm\partial}$, LSM). The first set of experiments pertain to electrochemical LSM studies on the oxygen evolution reaction (OER). These studies were concurrent with the oxygen reduction reaction (ORR) research presented in Chapter 2, which was based on a symmetrical cell. However, Chapter 2 focuses on the ORR reaction when LSM behaves as a cathode, while this Chapter concentrates on the OER process, where LSM is an anode.

The second set of experiments involves the study of both, a pure LSM material and composite materials of LSM combined with yttria-stabilized zirconia (LSM/YSZ) exposed to different gas environments and temperatures to monitor differences in surface chemistry. These studies were part of a collaboration with the Wachsman group at the University of Maryland.

3.1.1 LSM and OER

Solid oxide electrolyzer cells (SOECs) are a potentially clean and cost-effective tool to produce either hydrogen through the electrolysis of H_2O, or syngas (H_2/CO mix) through co-electrolysis of H_2O and CO_2.[131,132,213,239] H_2 itself can be utilized directly as a fuel in a solid oxide fuel cell (SOFC) or, as part of a syngas mixture, be used to generate synthetic hydrocarbon fuels via the Fischer-Tropsch process.[131,132,178,213,239] H_2 is also of use for industrial purposes for producing

ammonia via the Haber-Bosch process,[10] or aldehydes,[11] acids,[240] and ketones[12] via carbonylation.

While several electrolysis technologies have been developed, such as alkaline and proton-exchange membranes electrolyzers, SOECs are potentially the most efficient,[128,241,242] reaching efficiencies of $\geq 95\%$.[131] This is due to the high operating temperatures of the SOEC compared to the other devices, which allows for a lower electrical energy input toward the endothermic electrolysis reaction as more energy is provided by thermal energy.[128,132-134]

LSM and LSM-based composite materials are the most commonly used anodes in SOECs,[163-167] even though they are more often associated with SOFCs as cathode materials due to their superior promotion of ORR[168-170,173,243] (although there are some conflicting results on the supposed superior ORR activity[171,213]). As such, there are fewer fundamental studies regarding the use of LSM as an anode. Furthermore, the bulk of *in operando* research has focused on electrochemical performance or modeling tests.[244-248] There has been little spectroscopic investigation of important phenomena such as, the activation effect from anodic polarization, surface changes, and the controversially lower activity toward OER.

Eguchi[168] found that LSM was less electrocatalytically active for OER relative to ORR—a finding supported by Svensson *et al.*'s modeling studies[170] and Marina *et al.*'s electrochemical tests,[169] who both asserted that the lower performance was due to a filling of oxygen vacancies (*i.e.* more oxidized Mn). However, both O'Brien *et al*[171]. and Mogensen *et al.*[213] found little-to-no difference in LSM anodic performance in their impedance and voltammetry tests. Yildiz *et*

al.[175] conducted *in operando* X-ray reflectivity and X-ray absorption spectroscopy studies on LSM anodes and found polarization-induced changes in the concentration and electronic state of La, which they believe to be a contributing cause for the activation effect observed in LSM anodes.

To the best of our knowledge, Yildiz's study is the only *in operando* X-ray research conducted on LSM anodes. We describe here the use of *in operando* AP-XPS to interrogate the LSM surface during OER promotion in 200 mTorr O_2, at temperatures ranging from 500 ^{o}C to 700 ^{o}C. We address whether the degree of SrO extrusion is augmented or diminished upon application of an anodic bias, and show that insubstantial changes occur relative to when a cathodic bias is applied. We also show that anodic polarization induces an increase in surface Mn oxidation states. Finally, by measuring surface potentials under bias, we identify that under our experimental conditions, OER only occurs at the three phase boundary (TPB), and LSM is a less active electrocatalyst for OER than ORR.

3.1.2 LSM Oxygen Exchange and Surface Oxygen Vacancy Concentrations

Wachsman *et al.* have provided great insight into understanding the mechanisms behind ORR. Our collaborative experiments are designed to further advance their extensive *in situ* mass spectrometry (MS) bulk studies on mixed metal oxides with our *in situ* surface AP-XPS studies. Their experiments employed ^{18}O-enriched oxygen gas with MS analysis to monitor oxygen exchange in these oxides and elucidate mechanistic information regarding their catalytic activity for promoting ORR.[2,39,40,42,249] Among the materials studied were LSM and a LSM/YSZ composite. LSM/YSZ composites are known to exhibit greater ORR

activity than pure LSM.[250-255] However, most studies on the two materials have been electrochemical in nature (*e.g.* determining polarization resistance from impedance measurements) and give little indication of the chemical processes in one material compared to another. Wachsman *et al*.'s recent exchange experiments were able to extract *chemical* information regarding these two materials' reactivity with oxygen in different environments[42,249] (O_2 and common impurities in air, H_2O and CO_2).

The experiments involved saturating the LSM and LSM/YSZ composite with ^{18}O and exposing them to individual or combinations of the gases listed above (containing the standard ^{16}O isotope) at different temperatures and pressures, as shown in Figure 3.1.[249] Figure 3.1A shows the LSM (left) and LSM/YSZ (right) in a O_2/CO_2 environment (10:1 pressure ratio) at different P_{O2} values and temperatures. Figure 3.1B conveys the same information in a O_2/D_2O (4:1 pressure ratio) environment. For any given oxygen partial pressure, the temperature at which an ^{18}O signal is observed (*e.g.* a mass of 48, indicating $C^{18}O_{2(g)}$ is produced from the material) would signify the onset of oxygen exchange between the material and the atmosphere. This exchange is a measurement of the material's activity for dissociative adsorption or lattice incorporation, according to a proposed two-step reaction scheme (see Section 1.3.1). Among the findings was a significantly higher activity toward oxygen exchange in the LSM/YSZ composite compared to LSM. For example, in the O_2/CO_2 environment at $P_{O2} \sim 0.01$ atm, the LSM/YSZ exchanges oxygen with the atmosphere at a rate of $\sim 2 * 10^{-7}$ mol/(m^2*s) (green

intensity) at a temperature of ~200 °C while LSM does not exhibit comparable oxygen exchange until the temperature is increased to ~800 °C.

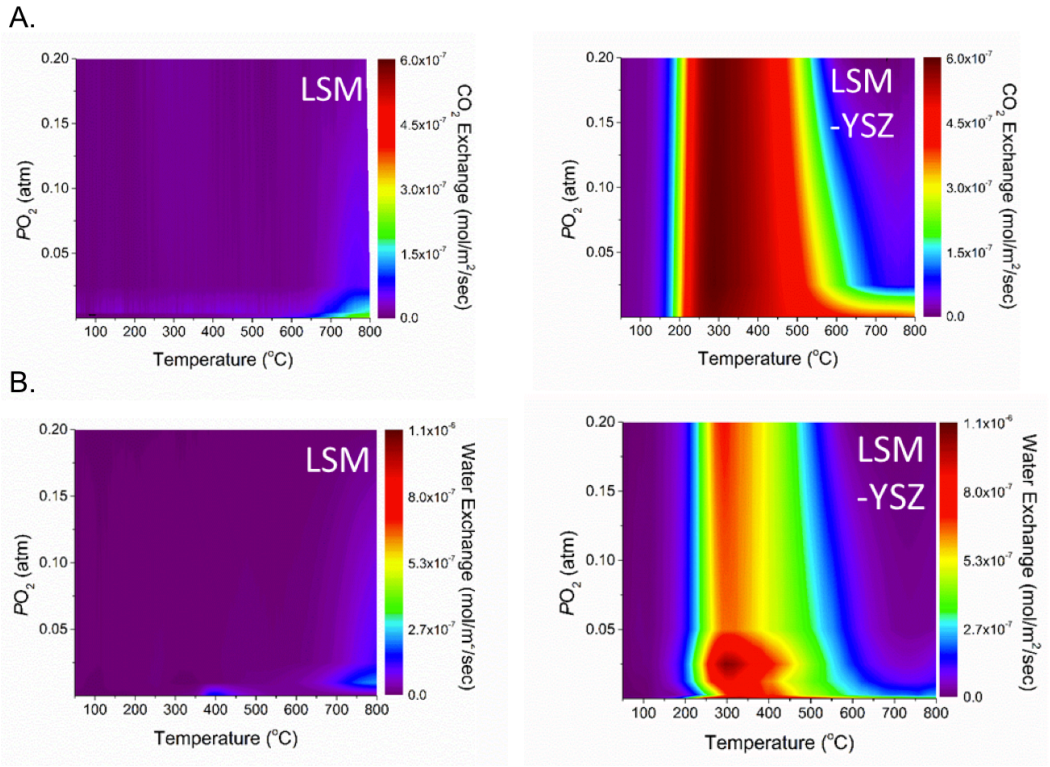

Figure 3.1.[249] (A) CO_2 and (B) water (D_2O) isotope exchange as a function of temperature and P_{O2} on LSM (left) and LSM-YSZ (right). The pressure ratio of O_2 : D_2O and O_2 : CO_2 was 4:1 and 10:1, respectively. To the right of each plot is an intensity calibration curve for determining how much exchange is occurring on the material at a given temperature and P_{O2}.

Our goal is to explore the surface activity and elucidate a more detailed answer on why the composite would show such enhanced activity. We exposed LSM and LSM/YSZ to similar gases and temperatures at the Advanced Light Source (ALS) and monitored surface chemical changes with AP-XPS. In any condition, the LSM/YSZ composite showed a greater extent of Mn reduction than the pure material, suggesting a larger concentration of oxygen vacancies (see

Section 1.3, R1.9) which may enhance the ability of the material to exchange oxygen at the surface.[256]

3.2 Experimental Information

For the electrochemical OER studies presented in this chapter, all experimental information, including cell fabrication, APXPS/electrochemical set-up, and collected spectra may be found in the Experimental Information section of Chapter 2 (Section 2.2.1). Briefly, symmetrical cells of 100 nm LSM electrode thin films on a YSZ electrolyte were operated in 200 mTorr O_2 at either 530 ^oC, 620 ^oC, or 680 ^oC, depending on the cell and experiment. The cells were typically cycled twice between open circuit voltage (OCV) and a 1.5 V bias. With respect to the electrode of interest in this chapter, the bias was anodic.

The experimental information regarding oxygen exchange surface studies on LSM and the LSM/YSZ composite are provided in the remainder of this section.

3.2.1 Sample Synthesis and Characterization

LSM and LSM-YSZ (1:1 wt ratio) pads were dropcoated onto a single-side polished YSZ single crystal with 111-orientation (*MTI Corporation*). Both the YSZ in the composite and the single crystal substrate were 8 mol % yttria. The sample was heated to an intermediate temperature of 400 ^oC for 1 hour followed by heating at 1200 ^oC for 2 hours. Both heating and cooling rates were 2 ^oC/min.

Ex situ XPS studies on the LSM and LSM/YSZ composite were obtained with a Kratos Axis 165 X-ray photoelectron spectrometer with a monochromated Aluminum kα X-ray source (hν = 1486.6 eV).

3.2.2 AP-XPS Experiments

AP-XPS experiments were performed at beamline 11.0.2 at ALS.

Five different gas atmospheres were used in the experiments:

Table 3.1. The different gas atmospheres and pressures used in thermal redox experiments.

Atmosphere	Pressure (mTorr)
O_2	200
H_2O	50
O_2 and H_2O	200 and 50, respectively
CO_2	200
O_2 and CO_2	200 and 200

In each environment, spectra were collected at three temperatures, 400 ^oC, 500 ^oC, and 600 ^oC.

The sample was oriented at X-ray incident angle of 75^o and the electron emission angle was 0^o with respect to the sample normal. Mn 3s spectra were collected at a photon energy of 490 eV and were analyzed with the CasaXPS program. A full description of Mn 3s spectra and fitting methods may be found in Section 2.2.2.4. Calculation details for determining the Mn oxidation state from the spectra are detailed in Section 2.2.3.3. The standard deviation of the average Mn oxidation state between the fifteen conditions listed above was determined by the standard calculation:

$$SD = \sqrt{\frac{\Sigma|x - \bar{x}|^2}{n}}$$

where "x" is the Mn oxidation state in any given condition, "$\bar{x}$" is the average Mn oxidation state between all 15 conditions, and "n" is the number of conditions (15).

3.3 Results and Discussion

3.3.1 LSM OER Studies

These data were taken concurrently with the ORR data in Chapter 2 (Section 2.3). We have shown in Section 2.3.4.2 that there is a larger potential drop (*i.e.* polarization resistance) when LSM behaves as an anode of a symmetrical cell and that the drop occurs at the LSM/YSZ interface, indicating that OER activity is constrained to the triple phase boundary (TPB). To the best of our knowledge, this was the first spectroscopic evidence that LSM behaves as a primarily electronic conductor anode with lower electrocatalytic ability toward OER than ORR.

3.3.1.1 LSM Anodic Oxidation

In this experiment, a cell was subjected to two cycles at 530 ^{o}C between OCV and 1.5 V and was brought under OCV a third time. The cell was then heated to 680 ^{o}C and operated in one more cycle (cycle 4). The oxidation state was calculated from the Mn 3s XPS spectra (see Section 2.2.3.3) and representative spectra are found in SI Figure 3.1.

Figure 3.2 shows the Mn oxidation state results from two photon energies, 490 eV and 900 eV. Spectra were collected ~200 μm behind the LSM/YSZ interface. At 530 ^{o}C, the OCV conditions are shown in black while the two polarizations are in red. At 680 ^{o}C the OCV and polarized conditions are given in blue and green, respectively.

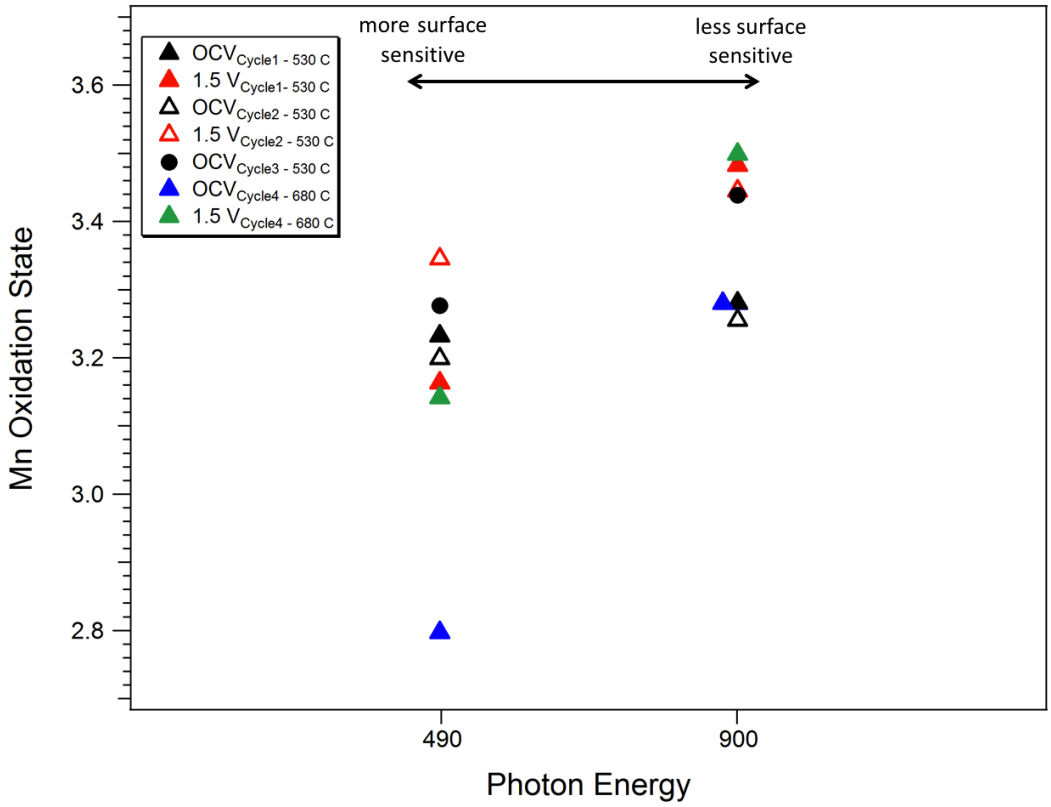

Figure 3.2. Mn oxidation states calculated on LSM at 530 °C, ~200 microns behind the LSM/YSZ interface. Photon energies of 490 eV and 900 eV were used. The black and red symbols represent OCV and biased conditions, respectively. The cycle is indicated by a closed symbol (cycle 1), open symbol (cycle 2) or a circle (cycle 3). The temperature was increased to 680 °C and the cell was cycled between OCV (blue) and 1.5 V bias (green).

As explained in Section 1.4.1.8, higher photon energies allow for deeper probing into the surface. As on the cathode side (Figure 2.10), the Mn is generally more reduced at the more surface sensitive energy (490 eV), especially at higher temperature where the OCV oxidation state is reduced compared to 530 °C.

At 680 °C (cycle 4), an anodic polarization results in a clear oxidation at each photon energy between the OCV (blue) and polarized (green) conditions. At 530 °C, the changes in oxidation state are not as obvious, although the

measurements at each photon energy generally support that the oxidation state is raised upon anodic polarization (red symbols), and lowered upon removal of the bias (OCV, black symbols). The first cycle and second cycles at 530 ^{o}C are indicated by closed and open triangular symbols, respectively, while the third OCV condition is represented by a circle.

We also studied the electrode at 530 ^{o}C using the 2D area detector at a photon energy of 490 eV. The lower plot in Figure 3.3 shows the Mn oxidation state as a function of position over one cycle from ~0.16 mm behind the interface to the edge (marked by 0 mm). Two line scans (signified by direction of the triangle symbols) with overlap at -0.05 mm were used. The oxidation state is relatively constant over OCV (black) with an average of ~3.4 while a ~3.6 average is found upon biasing (red). We also show at the top of the chart (in blue) the difference between the two conditions which represents the degree of oxidation across the electrode.

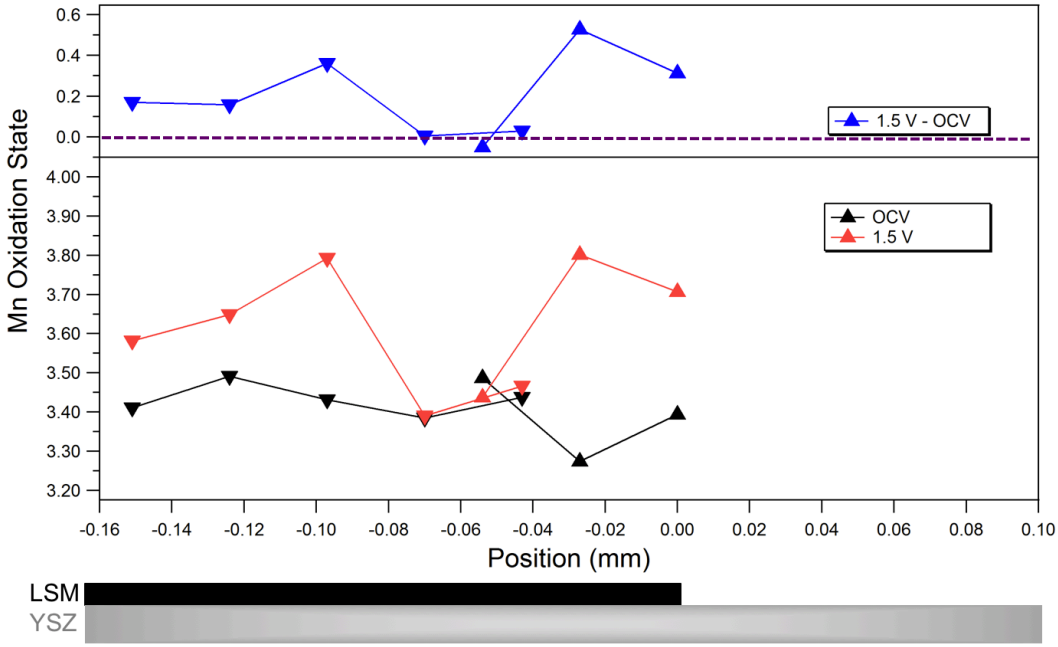

Figure 3.3. The lower plot shows the Mn oxidation state as a function of position at 530 ^{o}C. The black and red symbols represent OCV and biased conditions, respectively. The top plot in blue shows the difference between the oxidation state under bias and OCV and the mostly positive values along the electrode indicates that oxidation is occurring throughout the LSM region scanned up to the LSM/YSZ interface, demarcated by 0 mm. Data from two line scans was used with an overlap at -0.05 mm. A lateral schematic of the electrode on the YSZ electrolyte is provided at the bottom for position clarification.

As on the cathode side, the anode shows relatively stable oxidation up to the edge, yielding further spectroscopic evidence that LSM behaves primarily as an electronic conductor material (see Section 2.4.3 for further discussion). The oxidation and larger potential drop (compared to ORR) observed in our OER studies support the modeling work of Svensson[170] and ambient pressure, high temperature (650 – 850 ^{o}C) electrochemical performance studies of Marina,[169] who found greater polarization losses observed when LSM behaves as an anode instead of a cathode, and attributed these greater losses to a decrease in oxygen vacancies.

3.3.1.2 SrO Changes

Surface extrusion of Sr from the LSM lattice ($Sr_{lattice}$) onto the LSM surface as SrO is not nearly as distinct under an anodic bias, relative to under a cathodic bias. Our LSM cathode studies show a distinguishable and partially reversible extrusion of Sr upon polarization (Section 2.3.2), likely correlated with oxygen vacancy formation (*i.e.* Mn reduction). However, our studies on SrO formation under oxidizing polarization are more ambiguous, further implicating the importance of forming oxygen vacancies for SrO extrusion to occur.

Figure 3.4A shows changes in SrO thickness at 620 ^{o}C determined by recording Sr 3d XPS spectra ~200 microns behind the LSM/YSZ interface at three different photon energies, 345 eV, 490 eV, and 900 eV, between two cycles of OCV (black) and a 1.5 V anodic bias (red). Closed symbols and open symbols correlate with cycle 1 and cycle 2, respectively. Representative Sr 3d spectra may be found in SI Figure 3.2 and a detailed explanation of the spectra and thickness calculations may be found in Sections 2.2.2.1 and 2.2.3.2, respectively. In principle, the measured SrO thickness should not change at different depths, but some variation is observed (discussed in Section 2.3.2). Furthermore, the trend in SrO changes over the two cycles is not consistent between the three energies used.

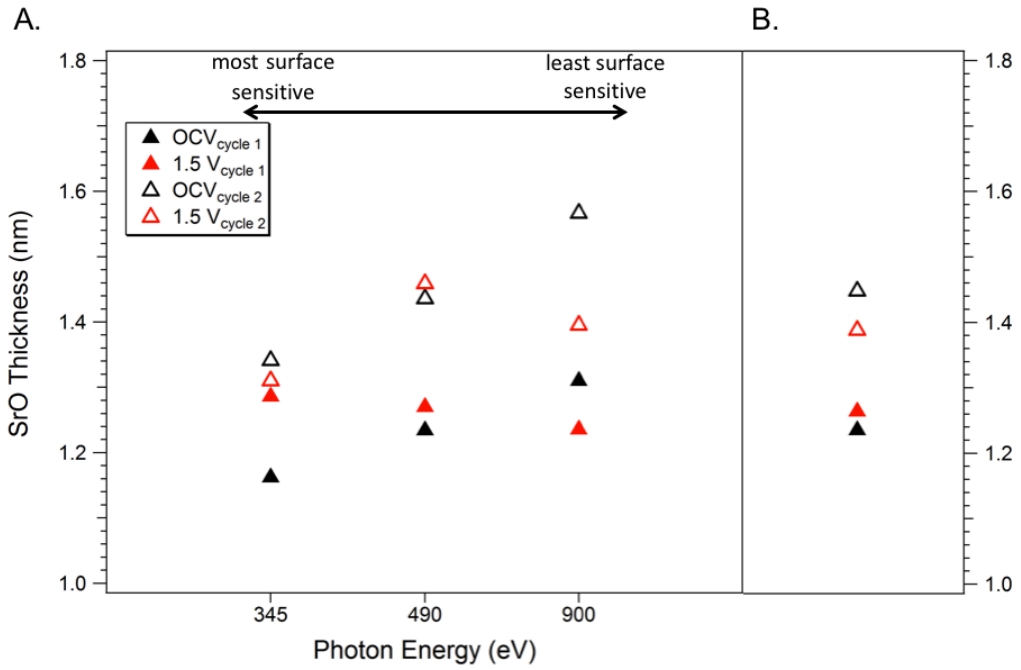

Figure 3.4. (A) SrO thickness values calculated from Sr 3d spectra collected 200 microns behind the LSM/YSZ interface at 620 ^{o}C. Three different photon energies were used, 345 eV, 490 eV, and 900 eV. The black and red symbols represent OCV and biased conditions, respectively while closed symbols and open symbols represent cycles 1 and 2, respectively. (B) The SrO thickness at each condition from averaging the three different photon energy measurements.

Given the inconsistency, the data from each photon energy were averaged and can be seen in Figure 3.4B. Referencing the average values, there seems to be insignificant segregation of SrO under polarization in cycle 1. When the bias is turned off, there is some SrO growth at OCV and upon repolarization, the SrO changes very little indicating that this may be an irreversible growth.

It is unclear if the SrO extrusion observed at OCV_{cycle2} was induced by removing polarization, or if the SrO segregation under anodic conditions is slow and had continued to take place after we had finished taking Sr 3d scans on the anode. We also note that these changes in SrO thickness are not nearly as significant

as those taking place on the cathode side which were roughly growing from ~1.3 nm to ~1.8 nm. Furthermore, all three photon energies agreed on the extent of segregation under bias and reincorporation at OCV (see Figure 2.6). On the anode side, the average growth is ~0.2 nm, and not all data sets agree.

We also conducted studies at 530 ^{o}C using a 2D area detector, and the results may be seen in Figure 3.5. The figure shows SrO thickness measurements as a function of position over two cycles. The color and symbol meaning is the same as in Figure 3.4, and 0.00 mm demarcates the LSM/YSZ interface (the lower inlay is for position clarification). Two different line scans were used, with overlap around -0.10 mm. The photon energy used to collect Sr 3d spectra was 490 eV.

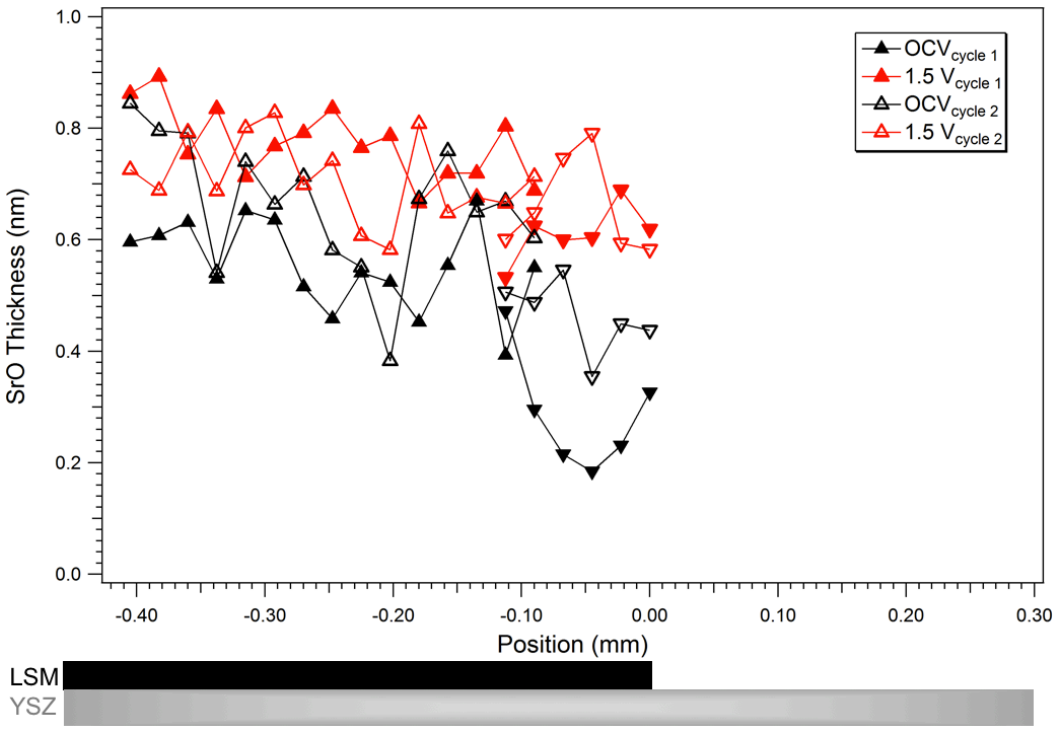

Figure 3.5. A plot of SrO thickness as a function of position at 530 ^{o}C. The black and red symbols represent OCV and biased conditions, respectively. The cycle is indicated by a closed symbol (cycle 1) or open symbol (cycle 2). To accumulate the data two line scans, denoted by the direction of the triangles, were taken with sufficient overlap. A lateral schematic of the electrode on the YSZ electrolyte is provided at the bottom for position clarification and the LSM/YSZ interface is demarcated by 0.00 mm.

While the polarized SrO thicknesses are larger than under OCV conditions, these increases (0.1~0.2 nm on average) are not as significant as those experienced on the cathode side, which showed an average increase of 0.4~0.5 nm (Figure 2.8). Furthermore, while it was clear that the polarized SrO thicknesses on the cathode were larger than at OCV (SrO had grown at every point on the LSM under the two polarizations), on the anodic side there is less consistency.

In summary, while there may be changes in SrO thicknesses under anodic bias, at either temperature studied, there is enough inconsistency and insignificant growth in comparison to the cathode side, that SrO changes do not seem particularly commensurate with anodic bias. The lack of appreciable SrO growth with the oxidation (depletion of oxygen vacancies) that we observe in our Mn studies above supports the correlation between oxygen vacancy generation and SrO growth as discussed in Section 2.4.2.

3.3.2 Surface Oxygen Vacancies on LSM and LSM/YSZ

The LSM and LSM/YSZ composite were studied with AP-XPS in atmospheres and temperatures approximating those used in Yi-Lin *et al.*'s isotopic labelling oxygen exchange experiments,[249] to determine the crucial surface differences that allow for the composite material to have more facile O exchange

than the pure LSM (see Figure 3.1). It was determined that the LSM/YSZ composite contains a larger concentration of oxygen vacancies at the surface than pure LSM. Preliminary *ex situ* XPS and electron energy loss spectroscopy (EELS) studies on the materials support this finding. The XPS shows that the Mn oxidation state in the composite material are reduced relative to the pure LSM (see SI Figure 3.3) while the EELS studies show that Mn is more reduced at the LSM/YSZ interface found in the composite materials.[249] Our AP-XPS studies found the greater reduction persists, *in situ*.

Figure 3.6 shows representative Mn 3s spectra of LSM and LSM/YSZ at 500 ^{o}C in a 4:1 O_2/H_2O atmosphere in which the spectra have been calibrated so that the low binding energy (BE) peak is at 0 eV. The Mn oxidation states were calculated from the energy splitting between the two peaks in the same manner as described in Section 2.2.3.3. The Mn oxidation states of the two materials as they were exposed to each environment is shown in Figure 3.7. In all 15 conditions, the LSM/YSZ (red) exhibits greater reduction than the pure LSM (black), where the average oxidation state in the composite is 2.76 and in the LSM is 3.06, with standard deviations of 0.12 and 0.07, respectively. The greater reduction in the composite implies an increase in oxygen vacancies to compensate the lower charges on Mn. This increase in vacancies may explain the greater degree of oxygen exchange in the composite material as there are more active sites available, likely at the LSM/YSZ interfaces.[256] We conducted other *in situ* studies on these materials and found similar results (see SI section 3.5.2).

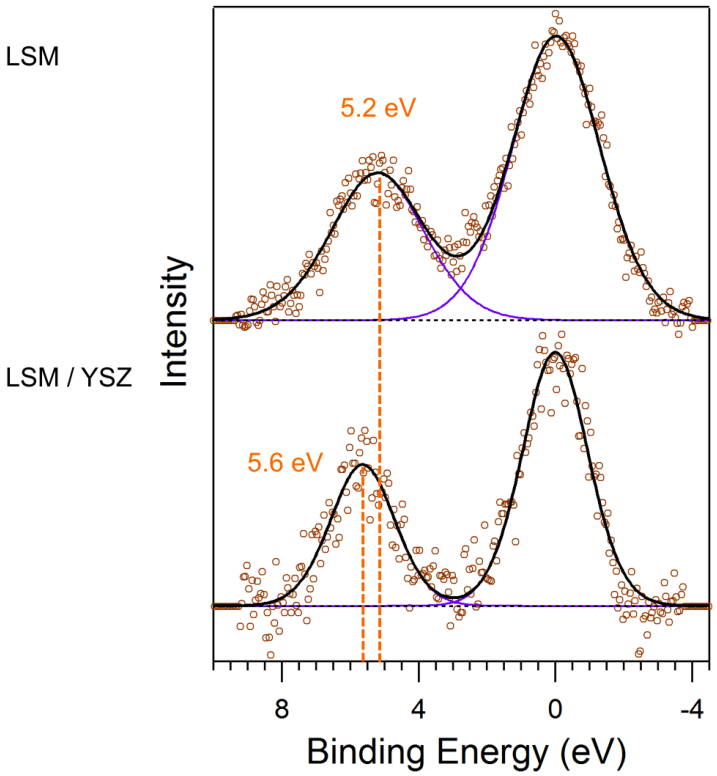

Figure 3.6. Representative Mn 3s data for the pure LSM (top) and LSM/YSZ composite (bottom) in the 4:1 O_2/H_2O atmosphere. The composite shows a greater energy separation between the peaks indicating more reduced Mn.

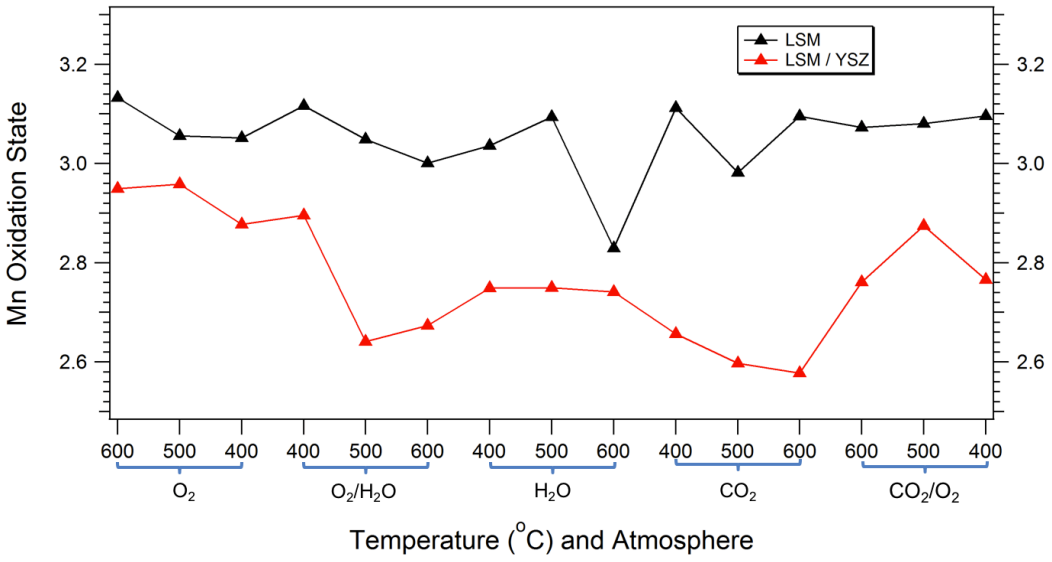

Figure 3.7. Mn oxidation states for the LSM (black) and LSM/YSZ (red) materials as the sample experienced different temperatures and atmospheres in the order that they occurred.

In the *ex situ* XPS studies (SI Figure 3.3), the full width half maximum (FWHM) is nearly the same in both materials, while in the *in situ* studies (Figure 3.6), the LSM shows a broader FWHM than the composite; a phenomenon present in all 15 conditions. It is possible that there is a lower concentration of Mn at the surface relative to the bulk of the composite material. A lower surface Mn concentration in the composite material would imply a lower concentration of under-coordinated surface Mn compared to the pure LSM, thus the composite would exhibit a narrower FWHM (signifying a lower variability in coordination environments). This is supported by the similar FWHMs observed in the 1486.6 eV *ex situ* studies in which a much greater depth (7.0 nm vs. 2.8 nm) of each material is profiled. We also cannot exclude differences in surface composition that result from the *in situ* conditions (*e.g.* formation of RP phases, SrO extrusion).

3.4 Conclusion

We conducted *in operando* AP-XPS experiments on a LSM thin film, electrochemically promoting OER in an oxygen atmosphere. We found that LSM under anodic bias is oxidized up to the LSM/YSZ interface and that the oxidation was concurrent with a lack of significant SrO segregation, implying oxygen vacancies are a key factor in SrO surface extrusion.

We also conducted *in situ* AP-XPS experiments on LSM and LSM/YSZ composite materials in different combinations of O_2, H_2O, and CO_2 atmospheres at high temperatures. These thermal studies demonstrated that the LSM/YSZ composite consistently has a larger concentration of surface oxygen vacancies,

likely promoting the more facile exchange of oxygen observed on the composite relative to LSM in isotopic labeling studies.

3.5 Supporting Information

3.5.1 OER Representative XPS Spectra

3.5.1.1 Mn 3s Spectra

To illustrate the largest difference in oxidation states, SI Figure 3.1 shows the Mn 3s spectra collected at 490 eV during the high temperature 680 ^{o}C OCV condition and oxidizing polarization at 530 ^{o}C (1.5 $V_{680\,C}$), which gave the clearest difference between ΔE values. The low BE peak was fixed at 0 eV and ΔE decreases from 5.5 eV to 5.0 eV when going from OCV to bias, indicating Mn oxidation.

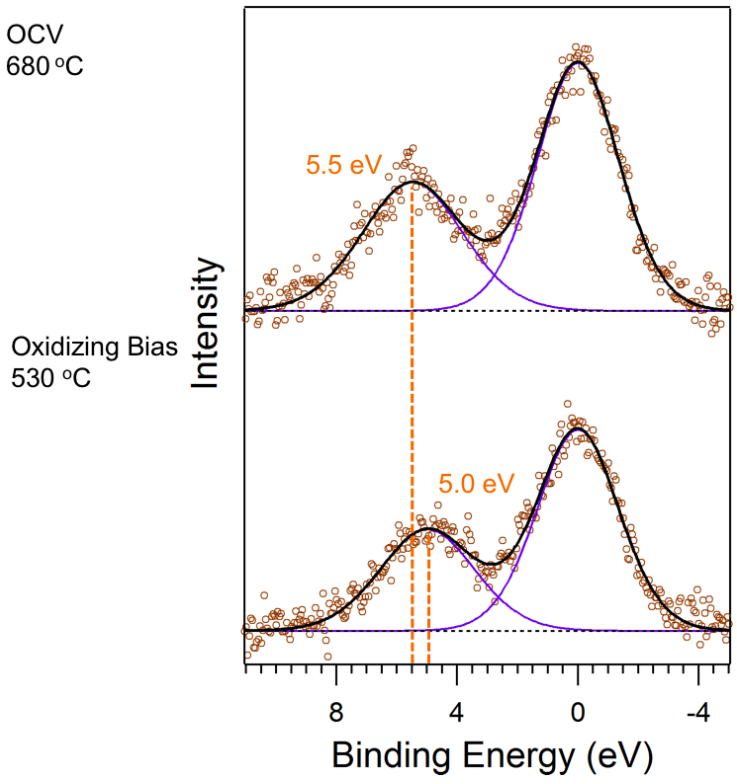

SI Figure 3.1. Mn 3s spectra collected at 490 eV on LSM ~200 microns behind the LSM/YSZ interface under OCV at 680 ^{o}C (top) and 1.5 V oxidizing bias at 530 ^{o}C. The low BE peak was calibrated to 0 eV.

3.5.1.2 Sr 3d spectra

SI Figure 3.2 shows changes in the Sr 3d spectra taken at 490 eV photon energy over two cycles between OCV and anodic bias. The $Sr_{lattice}$ is represented by the green doublet and the SrO by the yellow. Changes in the intensity of SrO relative to $Sr_{lattice}$ are unclear over the experiment.

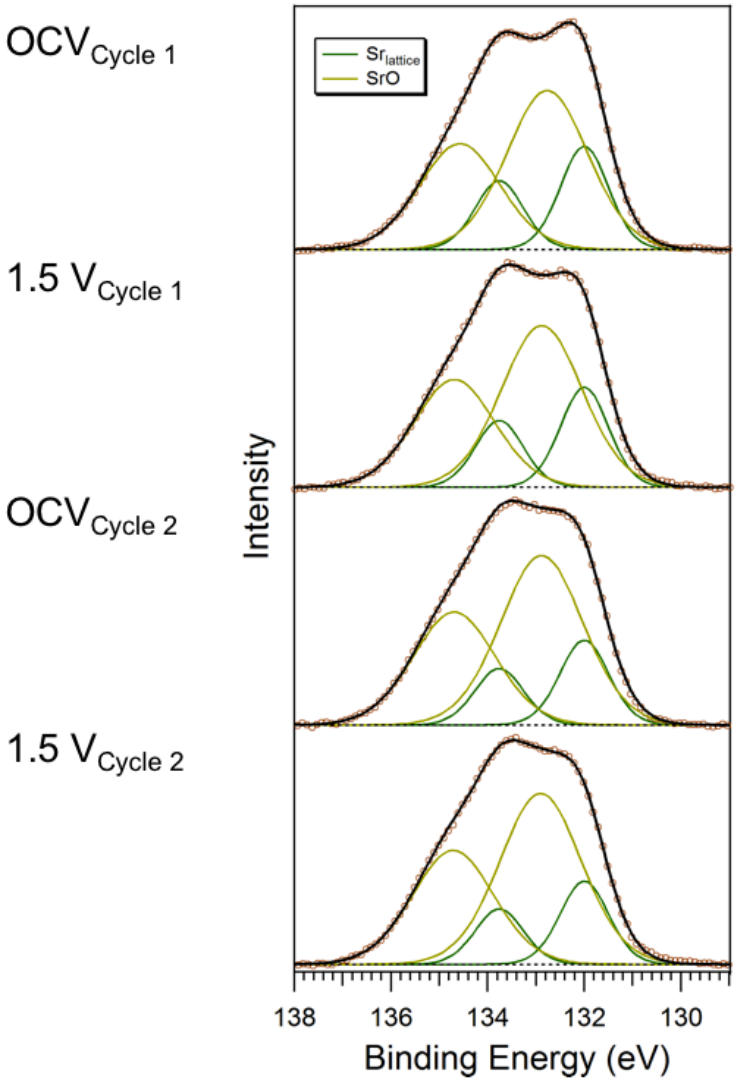

SI Figure 3.2. Sr 3d spectra taken at a photon energy of 490 eV, 200 microns behind the LSM/YSZ interface at 620 ^{o}C. From top to bottom the spectra correspond to cycles between OCV and 1.5 V anodic bias. The green and yellow doublets represent the $Sr_{lattice}$ and the SrO species, respectively.

The $Sr_{lattice}$ $3d_{5/2}$ was calibrated to 132.0 eV in all spectra.[217]

3.5.2 Auxiliary Mn 3s XPS Spectra for Oxygen Exchange Experiments

Mn 3s spectra of the LSM and LSM/YSZ composite may be viewed in SI Figure 3.3. The composite shows a greater energy splitting than the pure LSM signifying greater reduction. Several other *ex situ* XPS characterizations of these materials showed the same results.

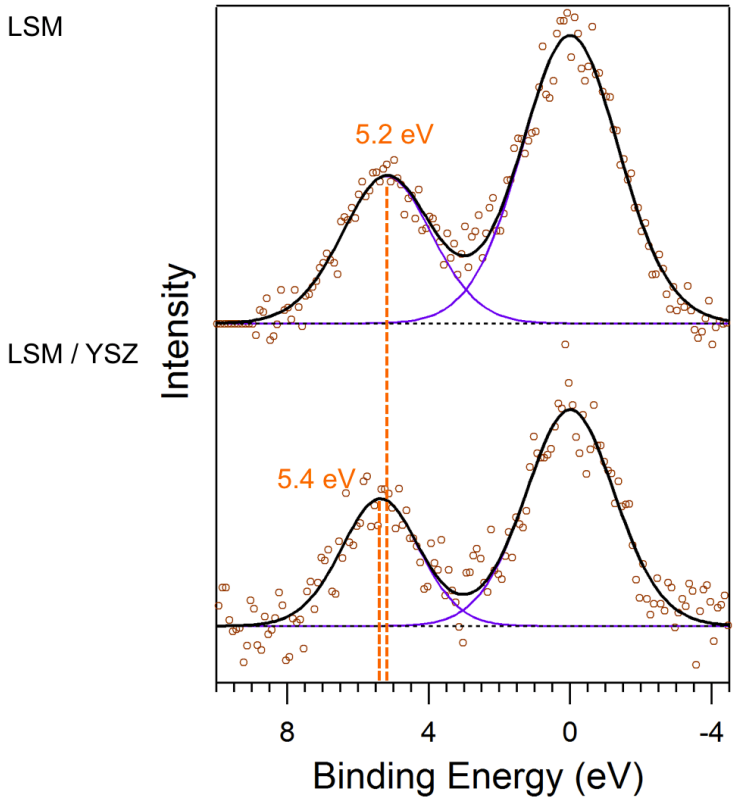

SI Figure 3.3. *Ex situ* Mn 3s on the LSM (top) and LSM/YSZ composite. The low BE peak is calibrated to 0 eV.

A different set of similar AP-XPS experiments were performed on these materials and also showed more reduced Mn in the LSM/YSZ composite compared to the pure material. Representative Mn 3s spectra in a 200 mTorr O_2 and 200 mTorr

CO_2 gas mixture at 400 ^oC are shown in SI Figure 3.4, in which there is a larger ΔE in the composite scans.

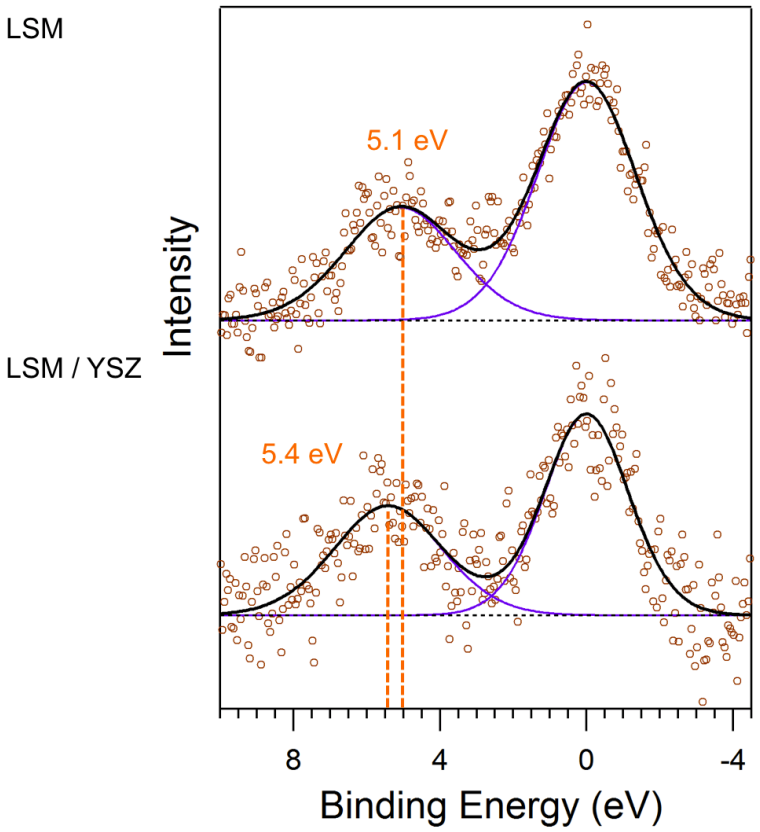

SI Figure 3.4. Representative Mn 3s spectra collected with photons 490 eV on the LSM (top) and LSM/YSZ composite (bottom) in 200 mTorr CO_2 and 200 mTorr O_2 at 400 ^oC. The low BE peak is calibrated to 0 eV.

4 Monitoring Water Electrolysis on Ceria *in Operando* with Near Infrared Imaging

4.1 Introduction

In Chapters 2 and 3, we demonstrated that the *in operando* surface states of electrodes in solid oxide electrochemical cell (SOC) systems can differ significantly from their equilibrium *in situ* states. Surface speciation, local surface potentials, and electrochemically-induced redox can be spatially resolved and quantified through the use of ambient pressure XPS (AP-XPS) experiments.

But while AP-XPS provides unique atomistic insight into operating electrochemical systems, the experiment involves instrumentation that is not easily accessible and typically requires the use of model cells and conditions that only approximate authentic SOC devices (the so called, "pressure-materials gap"). For example, in the electrochemical cells used in the oxidation reduction/evolution reaction (ORR/OER) studies in Chapters 2 and 3, only 200 mTorr of O_2 was used, and while that was not the limit, these AP-XPS systems can still only handle several Torr at most—far from the ambient conditions these devices typically operate in. Furthermore, the cells in the aforementioned studies were fabricated with both electrodes on the same side of the electrolyte for optical access (see Figure 2.1), resulting in oxide ions traveling laterally through the electrolyte. However, in a realistic SOC, the cathode and anode are on opposite sides of the electrolyte (Figure 1.2).

Complementary techniques, such as *in operando* Raman spectroscopy[257-263] and near infrared (NIR) imaging[30-37] are more widely accessible, cost effective, and

allow for more realistic set-ups. However, they provide different spectroscopic information and probe different properties of the electrode (*e.g.* vibrational modes, thermal signatures). In addition, NIR imaging is a bulk probe whereas AP-XPS is a surface characterization tool and the combination can provide complementary information on an operating electrode. A central goal of our research efforts involves connecting the atom-specific mechanistic information gained through our AP-XPS experiments with the more accessible techniques that are easily employed in actual devices in a variety of research laboratories.

We describe here the combination of NIR imaging and AP-XPS in the *in operando* study of water electrolysis on a ceria-based SOC. By reproducing the electrode structure on both model (single sided) and authentic (double sided, two chamber) SOCs, we show that NIR imaging can be used to spatially resolve electrochemically active regions associated with *in operando* changes in ceria oxidation states. The regions of electrochemical activity and electrochemical responses are virtually identical to those observed in the AP-XPS model studies conducted at the Advanced Light Source (ALS),[25-27] which shows that the techniques are truly complementary and that the near ambient pressure conditions of the model studies are representative of the ambient operating conditions. We also show how the NIR imaging technique can be used to monitor cell conditioning, electrode performance, and spatially resolve redox changes on ceria electrodes.

4.2 Experimental Information

4.2.1 Solid Oxide Electrochemical Cell Fabrication

A schematic of the cell design is shown in Figure 4.1 and a full description

of its fabrication is given in the Supporting Information (SI Section 4.5.1.1). A ~1mm thick polycrystalline yttria-stabilized zirconia (YSZ) electrolyte was prepared by pressing 2.825 ± 0.025 g of YSZ (*Tosoh Inc.,* TZ-8YSB, 8 mol % Y_2O_3) into a pellet and sintering it at 1450 ^oC for 3 hours. Two ceria working electrodes (WEs) were prepared via sputter deposition and consisted of 50 nm of alumina (oxide ion blocking layer), followed by 300 nm of Au (current collector), and a 1000 nm thick film of ceria (CeO_{2-x}) which rested on top of Au from 3.8 ± 0.3 mm behind the gold edge and 1.1 ± 0.2 mm in front the edge. A design of the ceria-side of the fuel cell can be seen in Figure 4.1a. A Pt counter electrode (CE) was prepared by applying a Pt paste (*FuelCellMaterials.com*, Lot # 310-118) to the other side of the pellet. The completed fuel cell was sintered at 800 ^oC for 3 hours. Description of operating details are found in Section 4.3.1.

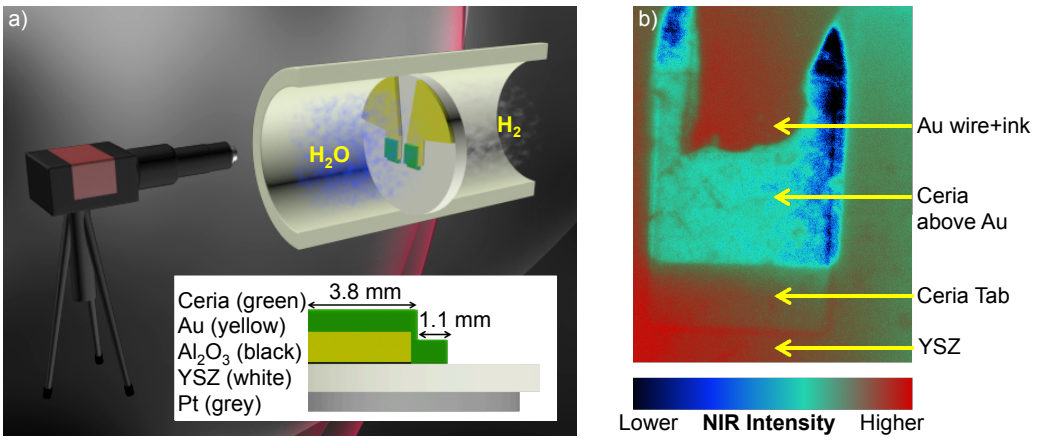

Figure 4.1. (a) a schematic of the experimental set-up. The ceria side of the SOC is shown and a lateral view of the cell is provided in the inlay. For electrochemical water-splitting on ceria, ceria is exposed to $H_2O_{(g)}$, and Pt is exposed to $H_{2(g)}$. NIR data were taken with a Si-charged-coupled device camera. (b) a NIR image of a ceria electrode. Variations in the NIR intensities depend on the NIR optical properties of the materials, morphology and geometry, as well as viewing angle with respect to the camera.

4.2.2 Experimental-Set Up

Gold wires (*Sigma Aldrich*, #265780) were attached to the ceria electrodes with gold paste (BASF #A1644). A platinum-mesh (*Sigma Aldrich* #298093) was attached to the Pt electrode by using Pt paste (*Heraeus* #6082). The SOC was attached, ceria-side out, to a 25.4 mm O.D. alumina tube (*SentroTech,* P/N:STT-0750) with alumina paste (*Aremco Products, Inc.*, #552). A 47.6 mm O.D. alumina tube (*SentroTech,* P/N:STT-1625) surrounded the alumina-supported SOC and a 50.8 mm diameter, 3.175 mm thick sapphire window (*Swiss Jewel Co.*, #W50.00) was attached to one end of the outer alumina tube to contain the reactant and product gases while providing optical access to the ceria side. Gases are introduced to both electrodes and exhausted via 6.4 mm O.D. alumina tubes (*SentroTech,* P/N:STT-0187). The rear of the assembly was sealed with RTV silicone-based paste (*Permatex*, #81878). The assembled SOC manifold was placed inside a tube furnace (*Thermo Scientific*, Lindberg/Blue M, Model # HTF55322A). A K-type thermocouple (*Omega,* P/N: XCIB-K-2-4-10) was positioned on the outside of the larger alumina tube to provide a temperature reference. A schematic of the optically accessible SOC assembly has been published previously[6] and is included in the Supporting Information (SI 4.5.1.2).

4.2.3 NIR Imaging

A Si-charged-coupled device (CCD) camera (*Allied Vision Technologies*, Stingray F504B, 5MP, 2452 pixels width x 2056 pixels height) with an 18 – 108 mm focal length macro zoom lens (*Navitar*, Zoom 7000) and 1.5 X magnifying spacer (*Edmunds Optics*, P/N:54-357) was used to acquire NIR emission images.

An in-house written software program in Labview was used to collect data. A 720 nm long-pass filter (*Hoya*, R72) was used to block emitted and ambient-reflected visible light.

NIR intensities were analyzed and displayed in real time while simultaneously recording and storing the data for post-processing. Spatial resolution was typically 10 microns (camera position dependent) and intensity readings were taken every 3 seconds. A NIR emission image of the ceria electrode is shown in Figure 4.1b. The changes in NIR background are most likely due to the well-recognized effects of "geometric view factors"[1,3] and not due to temperature gradients. Changes in camera angle and surface homogeneity can significantly alter the NIR backgrounds. In addition, there are contributions to the observed intensities from both cell emission and reflection. Furthermore, because NIR imaging is a bulk probe and the ceria electrode is thin, optical effects from the ceria underlayers (Au or YSZ) are observed.

4.2.4 Experimental Procedures

The fuel flows were regulated with mass flow controllers (*Celerity, Inc*., FC-260V-4S) and the temperature inside the furnace was kept at 720 ^{o}C. NIR intensity data on the ceria-side of the SOC was acquired during the procedures detailed. Gas flow rates and pressure calculations are described in Supporting Information (SI 4.5.1.3).

In "Chemical Redox Change Experiments" (Section 4.3.2) with NIR imaging, the ceria side was first allowed to equilibrate in an oxidizing H_2O atmosphere (17.5 Torr). The H_2O was evacuated and a reducing H_2 atmosphere

(304 Torr) was introduced for 10 minutes. The H_2 was then evacuated and the H_2O was reintroduced for 10 minutes.

In "Electrochemical Water-Splitting Experiments," (Sections 4.3.3 and 4.3.4) the ceria side was exposed to 17.5 Torr H_2O, while 17.7 Torr H_2 was introduced to the Pt side in order to achieve a near 1:1 ratio between the H_2O and H_2 fuels. A potentiostat (*Gamry Instruments*, Reference 3000 Potentiostat/Galvanostat/ZRA) was used to perform electrochemical measurements. Typically, a polarization measurement consisted of three steps: first, the cell would be monitored at open circuit voltage (OCV) for 40 seconds. Second, the voltage would be turned on for a minimum of 200 seconds. Lastly, the voltage would be turned off, and the cell would be allowed to rest for 300-600 seconds before applying the next polarization. Linear sweep voltammetry (LSV) and electrochemical impedance spectroscopy (EIS) measurements were made at the beginning and end of each experiment to check cell integrity (SI Figure 4.2). The OCV value was typically between -0.500 ~ -0.750 V.

4.2.5 AP-XPS Experiments

AP-XPS studies were conducted at ALS at the Lawrence Berkeley National Lab, at the beamline 9.3.2 endstation which was equipped with an area detector capable of XPS scans with 16 micron spatial resolution.[182] An SOC, similar to the one used in our NIR imaging studies, was used (fabrication described fully in Ref. 27). The cell was heated to ~700 ^oC and exposed to $H_2O_{(g)}$ (200 mTorr). The $H_2O_{(g)}$ was then evacuated and the cell was exposed to $H_{2(g)}$ (200 mTorr). The sample was oriented so that the X-ray beam struck the sample at incident angle is 75^o and the

electron emission angle was 0^o with respect to the sample normal. XPS spectra were analyzed with the CasaXPS program and a detailed explanation of the fitting procedure can be found in Ref. 27.

4.3 Results and Discussion

4.3.1 Cell Operation

Single-sided SOCs for AP-XPS studies were prepared by sputter depositing ceria and Pt electrodes onto YSZ electrolyte supports. The SOC is designed to separate oxide and electron transport as shown in Figure 4.2a and as discussed below. The single-sided SOC is designed to have both the ceria WE and the Pt CE exposed to the X-ray beam for *in operando* interrogation, necessitating the mixture of H_2O and H_2 gases in the XPS chamber (400 mTorr total pressure). The electrochemistry is driven by applying a potential across the WE and the CE.

A double-sided (two chamber) SOC with a nearly identical ceria electrode geometry was constructed for the NIR experiments; the main difference in the cell design is that the Pt counter electrode was placed on the opposite side of the YSZ electrolyte substrate. The change in electrode locations alters the direction of oxide transport (Figure 4.2b) and allows for each electrode to be exposed to an individual gas, which also facilitates higher gas pressures (760 Torr total pressure on each side).

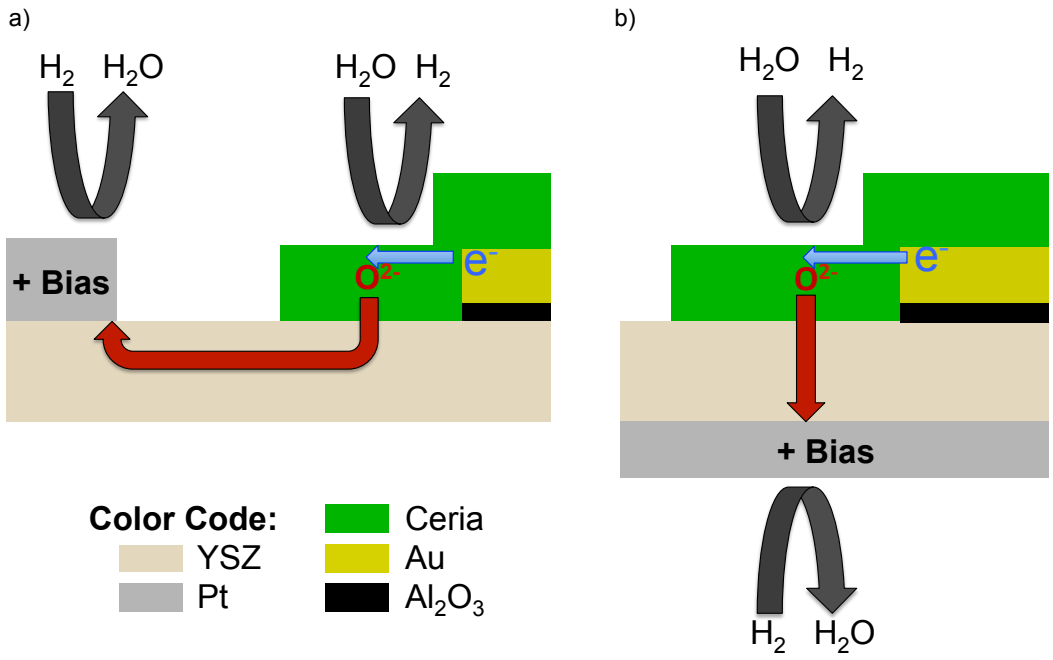

Figure 4.2. (a) Schematic drawing of the SOC used for AP-XPS experiments and the processes that occur when a positive polarization is applied to the Pt electrode. O^{2-} ions are drawn toward Pt where they react with $H_{2(g)}$ by R1, producing electrons and water. On the ceria side, electrons are laterally driven into the ceria via the Au current collector, reducing Ce^{4+} to Ce^{3+} (R2). The reduced ceria then reacts with $H_2O_{(g)}$ via R3 to produce O^{2-} and $H_{2(g)}$. The O^{2-} ions are vertically transported through ceria to YSZ, then laterally through YSZ to Pt, completing the circuit. The Al_2O_3 blocks oxide ions from transport between Au and YSZ. (b) Lateral schematic of the SOC and operational processes that occur in NIR imaging experiments. The processes are very similar to those in the AP-XPS cell, except oxide ions are transported vertically through the electrolyte between the CE and WE and each electrode is exposed to only one gas: ceria (H_2O), Pt (H_2).

The electrochemistry occurring at the CE and WE is summarized by the overall reactions given below and shown in Figure 4.2a. In the AP-XPS experiments, the chamber is filled with H_2O and H_2 gases and a positive bias is applied to the Pt electrode, promoting the following reactions:

$H_{2(g)} + O^{2-}_{(lat)} \rightleftharpoons H_2O_{(g)} + 2e^-$ (**R4.1**) at Pt / YSZ triple phase boundary

$Ce^{4+} + e^- \rightleftharpoons Ce^{3+}$ (**R4.2**) at ceria electrode

$H_2O_{(g)} + 2Ce^{3+} \rightleftharpoons H_{2(g)} + O^{2-}_{(lat)} + 2Ce^{4+}$ (**R4.3**) at ceria electrode

where $O^{2-}_{(lat)}$ is an oxide ion in the ceria lattice. Oxide ions are driven laterally through the YSZ toward Pt where they react with $H_{2(g)}$ by R4.1, producing water and electrons. On the ceria side, electrons are laterally driven into the ceria through the Au current collector, reducing Ce^{4+} to Ce^{3+} (R4.2). The reduced ceria reacts with $H_2O_{(g)}$ via R4.3 to produce O^{2-} and hydrogen in the water electrolysis reaction. The O^{2-} ions are vertically transported through ceria to YSZ, where they move laterally toward Pt, completing the circuit. The alumina (Al_2O_3) blocks oxide ions from traveling between Au and the YSZ. Because the electrons are transported through the reduced ceria to promote R4.3 on the electrode surface, and ceria is a mixed ionic electronic conductor (MIEC), the majority of the electrochemistry occurs in front of the Au current collector rather than at the three phase boundary (see Figure 1.7 and Figure 2.20). The maximum distance traveled by the electrons demarcates the "electrochemically active region," which is the result of a co-limiting process between electron transport and surface reactions.[26] Previous AP-XPS experiments[25-27] showed that the active region extended ~200 microns in front of the Au edge. Furthermore, these experiments showed that the reduction of ceria is a rate-limiting process, resulting in an accumulation of Ce^{3+} centers in this region.

4.3.2 Thermal Redox Studies

In situ AP-XPS shows that significant changes of Ce oxidation states can

be induced by altering the gas composition at 700 °C. As such, we performed AP-XPS experiments as a benchmark for probing the oxidation states of ceria under different chemical reducing/oxidizing environments, either 200 mTorr H_2 or 200 mTorr H_2O at ~700 ^oC. In either atmosphere, the following equilibrium exists between the ceria surface and gas phase:

$$2Ce^{4+} + H_{2(g)} + O^{2-}_{(lat)} \rightleftharpoons 2Ce^{3+} + H_2O_{(g)} \quad \textbf{(R4.4)}$$

there is always Ce^{3+} and Ce^{4+} present at the 700 °C operating temperature. The introduction of hydrogen drives the equilibrium to the right, resulting in an increase in Ce^{3+}. The removal of hydrogen and addition of $H_2O_{(g)}$ drives the equilibrium to the left and decreases the Ce^{3+} concentration. To monitor the Ce oxidation states, Ce *4d* spectra (details in SI Section 4.5.2) were taken in a line scan that encompassed 300 microns of ceria on each side of the Au edge (Figure 4.3). Another line scan was performed further down the ceria electrode, allowing us to image as far as 400 microns in front of the Au edge. The percentage of Ce^{3+} states is substantially higher in a reducing H_2 environment compared to an oxidizing H_2O environment (Figure 4.3), and the difference in Ce^{3+} abundance between the two environments is relatively consistent throughout the surface of the ceria electrode. Subsequent X-ray powder diffraction (XRD) experiments will show that this reduction process represents a bulk reduction of the entire electrode and is not just a surface phenomenon.

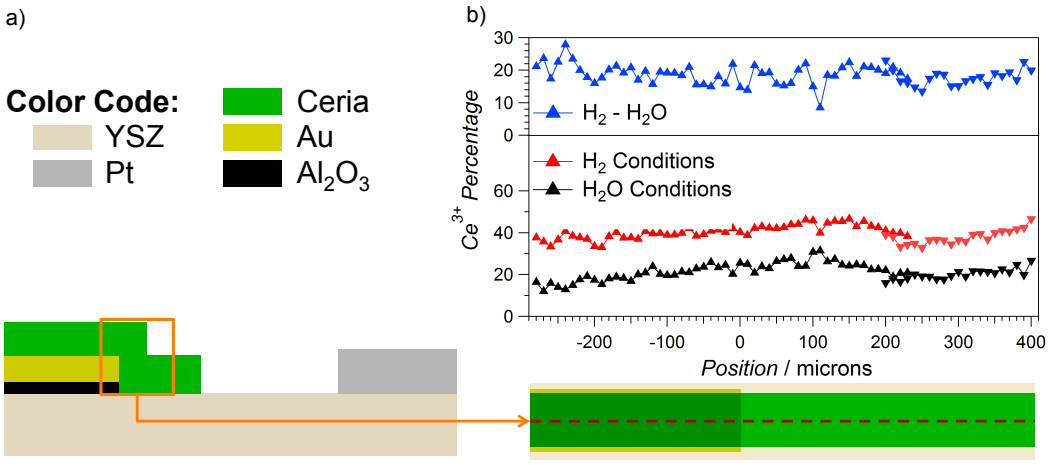

Figure 4.3. (a) A schematic drawing of the SOC design for AP-XPS measurements. (b) Percentage of Ce^{3+} relative to the total Ce as a function of position at 700 ^{o}C. The top plot (blue) shows the difference in % Ce^{3+} between the H_2 and H_2O conditions. The bottom shows the Ce^{3+} percentage in the two environments: 200 mTorr H_2O (black) or 200 mTorr H_2 (red). A top view drawing of the imaged region is provided for position clarification (darker green distinguishes ceria above Au from the light green ceria above YSZ) and the Au edge is defined at 0 microns. The dashed line represents the region of data collection and two different line scans were performed with some overlap at ~200 microns.

In situ/operando NIR imaging reveals the same changes in Ce oxidation states for chemical and electrochemical reduction of the ceria electrode and in addition, operates at atmospheric conditions without the requirement of a single-sided cell. These changes in Ce oxidation state are characterized by changes in ceria emissivity, which are detected in the NIR image, as described in Section 4.3.5. Despite the differences in SOC design and pressures, when water electrolysis is promoted on ceria, a ~200 micron active region is observed in front of the Au edge, consistent with AP-XPS studies described in Section 4.3.1. Furthermore, our NIR imaging camera can view the entire operating electrode at once and can collect full high resolution images in 30 to 60 second intervals, which offers distinct

advantages with respect to characterizing a wide range of conditions and providing kinetic information compared to the A methods.

For the NIR experiments, the ceria electrode was exposed to either H_2O (17.5 Torr) or H_2 (304 Torr) gas to mimic the AP-XPS control experiments. NIR intensities were measured on the entire ceria electrode of the cell and a representative cross-sectional slice (comprising 492 data points) is shown in Figure 4.4. These data represent the average NIR intensities over a 60 second data acquisition period after the ceria had come to equilibrium under each condition, H_2O (black) and H_2 (red). The blue curve shows the difference in NIR intensities of the two conditions. A top view of the imaged portion of the SOC (same color code as depicted in Figure 4.3) is provided for position clarification, as is a NIR image.

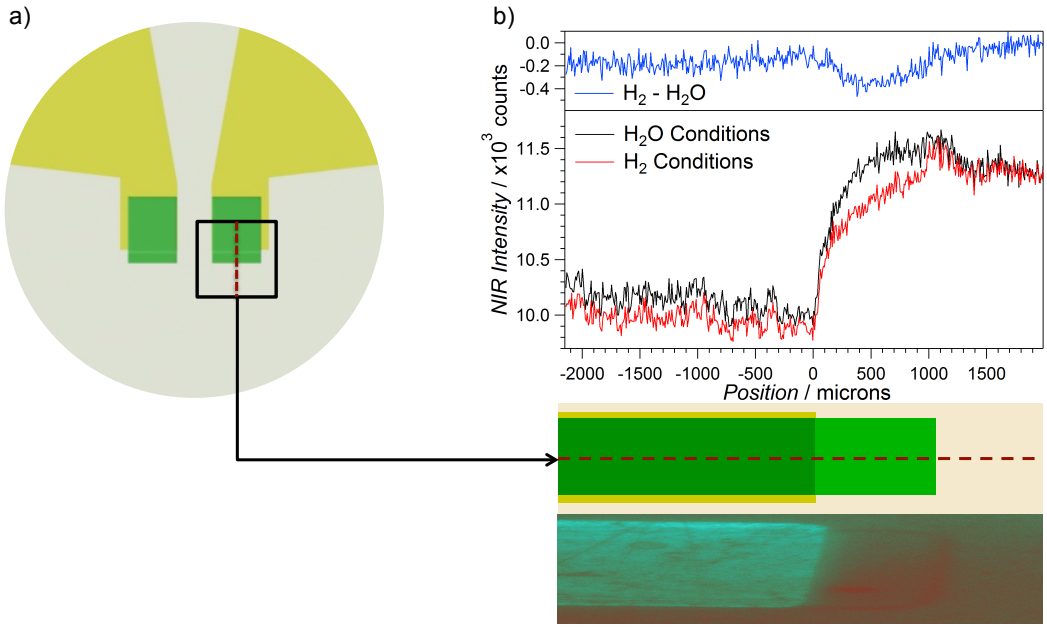

Figure 4.4. (a) Schematic drawings (same color code as Figure 4.2) and NIR image (bottom) of the SOC thermally processed in 17.5 Torr H_2O at 700 °C when the ceria tab was fully oxidized. (b) Plots of the 60-second averaged NIR intensity readings recorded under 17.5 Torr H_2O (black) or 304 Torr H_2 (red) atmospheres at 700 °C. The difference in NIR intensities between H_2 and H_2O conditions is shown in blue.

The emission profile reveals distinct differences between the three regions. Upon changing the gas from H_2O to H_2, the YSZ shows no detectible change in intensity. The ceria deposited on top of the Au current collector exhibits different degrees of emissivity changes compared to ceria deposited on YSZ. Since the AP-XPS control experiments above show that the degree of Ce^{3+} accumulation is the same across the ceria film, regardless of the underlying substrate, these differences are most likely a result of the underlying Au optical properties rather than an indication of differing concentrations of Ce^{3+}. However, we cannot exclude the possibility of slightly different degrees of reduction at the two locations or if there is a deeper (more bulk-like) reduction in the region in front of the Au current collector. Furthermore, the difference in effective oxygen partial pressures, due to the differences in total pressures dictated by the respective experiments, will affect the relative concentrations of Ce^{3+} present on the surface and bulk[184] in the AP-XPS and NIR imaging experiments. Regardless, the NIR intensity changes and the localization of Ce^{3+} occur under similar conditions and in the same locations. As such, NIR imaging can further bridge the gap between near ambient pressure XPS and practical atmospheric pressures. The origins of the NIR emissivity changes are outlined in Section 4.3.5

4.3.3 *In Operando* Water-Splitting on Ceria

In operando NIR imaging of the ceria electrode of the two-chamber cell during electrochemical water-splitting (ceria is exposed to water, Pt to hydrogen, see Figure 4.1a) shows a localized active region of reduced ceria that is very consistent with our AP-XPS measurements.[25-27] In contrast to the AP-XPS experiments, the cells were operated at ~760 Torr pressure, which generated currents more than 50% larger than the AP-XPS cells at the same temperature and similar conditions. Despite these differences, both AP-XPS and NIR experiments show virtually identical electrochemically active regions, marked by an accumulation of Ce^{3+}, that extends ~200 microns in front of the Au edge.

Figure 4.5a shows the AP-XPS results[25] for the single-sided SOC described in Figure 4.2a (see Ref. 25 for details). The percent Ce^{3+} relative to the total Ce concentration is plotted as a function of position in a 200 mTorr H_2O / 200 mTorr H_2 gas mixture under three conditions: +1.2 V (blue), OCV (white), and -1.2 V (red). At 1.2 V applied bias (electrochemical water-splitting on ceria), an increase in Ce^{3+} is observed ~200 microns in front of the Au edge (some reduction was observed behind the edge in this cell as well). The -1.2 V bias promotes hydrogen electroxidation, which does not affect a change in the Ce^{3+} concentration.

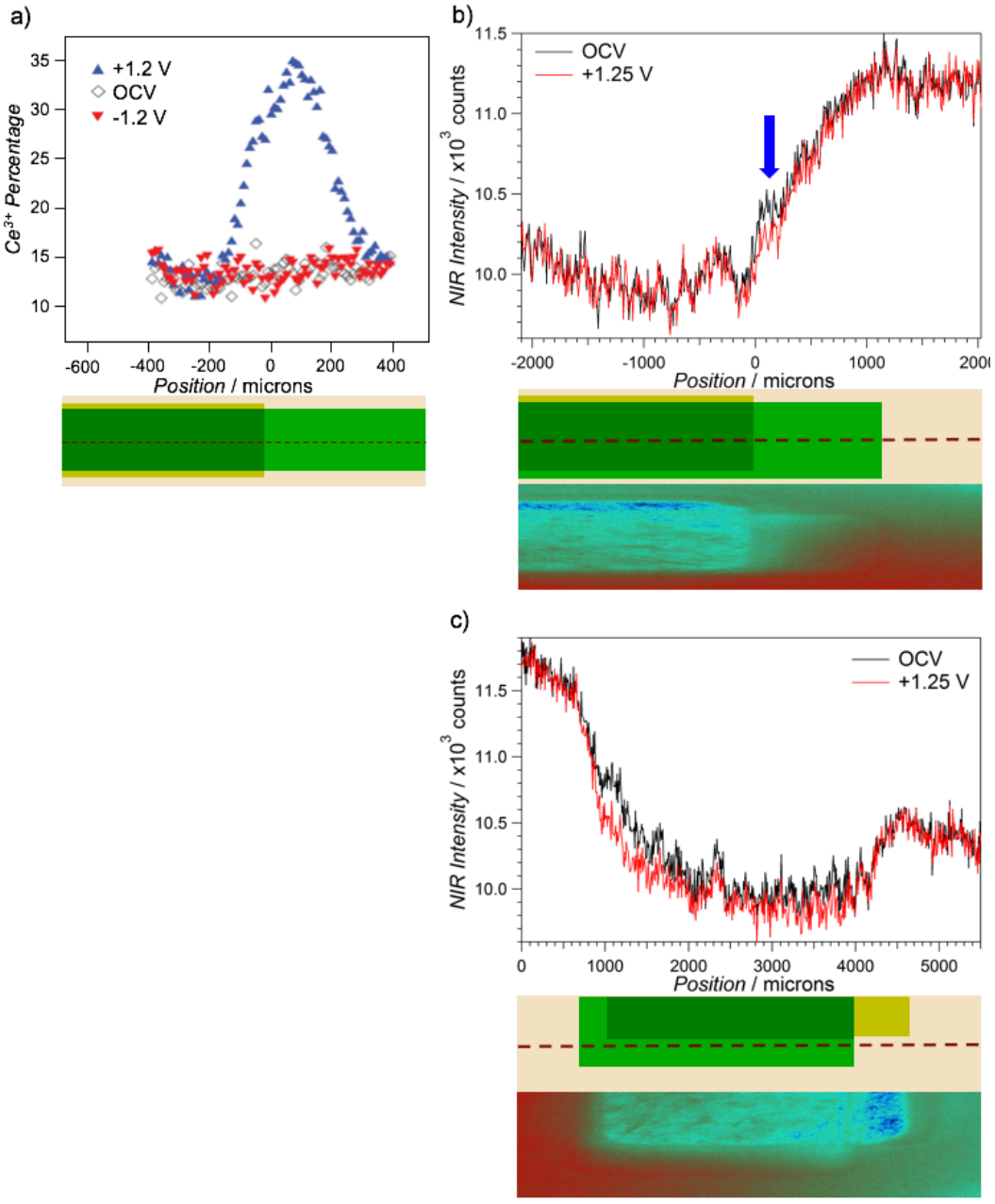
a)
+1.2 V
OCV
-1.2 V
Ce3+ Percentage
Position / microns
b)
OCV
+1.25 V
NIR Intensity / x10^3 counts
Position / microns
c)
OCV
+1.25 V
NIR Intensity / x10^3 counts
Position / microns

Figure 4.5. (a) The percentage of Ce^{3+} relative to the total Ce concentration plotted as a function of position. Data were collected in a 200 mTorr H_2O and 200 mTorr H_2 gas mixture under three conditions: +1.2 V (blue), OCV (white), and -1.2 V (red). The figure is a modified version of a figure from Ref. 25. (b) and (c) 30 second-averaged NIR intensity data at OCV (black) and +1.25 V bias (red). In (b), a profile was analyzed down the middle of the electrode. The active region is indicated by the blue arrow. In (c) data were analyzed across the electrode ~50 microns in front of the Au edge. Beneath the plots are schematic drawings (same color code as Figure 4.3) showing the profiled region (red dashed line). In (a) and (b), the Au edge is marked by 0 microns. In (c), the image is oriented 90 degrees, clockwise, with respect to (b) and the drawing enlarged. Both NIR images were collected at +1.25 V bias.

To observe electrochemical activity, NIR emission data sets were collected on the entire ceria electrode operating at a 1.25 V applied potential on the Pt CE and at OCV. Representative cross sectional slices of processed data from the two voltages are shown in Figure 4.5b. The black curve represents the average NIR intensity over a 30 second data acquisition period at OCV. The red curve represents the average intensity over a 30 second data acquisition period after the 1.25 V potential is applied and the current is stabilized. The two curves are essentially superimposable except in the ~200 micron region of ceria in front of the Au edge where there is a small but significant decrease in NIR intensity. As illustrated in the control AP-XPS experiments, this reduction in NIR intensity signifies a build-up of Ce^{3+}.

To further probe this region of electrochemical activity, a line of emission data was analyzed ~50 microns in front of the Au edge and is shown in Figure 4.5c (the cell picture has been rotated 90 degrees, clockwise). Redox activity is observed along this entire region of ceria while the YSZ regions exhibit no discernible

changes in emissivity. When the applied potential is turned off and the cell returns to OCV, the NIR intensity reverts to its original OCV value (see Figure 4.7), indicating that the phenomenon is reversible and is induced by the applied potential. The results are reproducible and have been replicated on various batches of cells (see SI Section 4.5.3).

4.3.4 *In Operando* Ceria Electrode Conditioning

Because of its speed and versatility, we have found that NIR imaging is an effective tool for evaluating electrode conditioning, *in operando*. During conditioning stages, we observed bias-induced decreases in NIR intensities over the entire ceria region in front of Au (Figure 4.6). After conditioning is complete, reduction is only observed in the expected ~200 micron region, similar to Figure 4.5 indicating that cell has reached optimal performance. For example, operation at 1.00 V for ~3 min results in the disappearance of the extended region and the irreversible localization of activity in the ~200 micron region in front of the Au current collector (Figure 4.7), indicating that the appropriate conditioning had been reached. Once the conditioning process is complete, the localization of activity to the ~200 microns in front of the Au edge is an irreversible transition. In all cases (conditioned or unconditioned), the NIR intensity of ceria returns to its OCV value when the applied bias is turned off. Localization of the active region is accompanied by an increase in current and a decrease in impedance (see SI Figure 4.5), which suggests that this process may be associated with optimizing oxide transport across the ceria-YSZ interface as discussed below. This conditioning process was observed on different cells, although the conditioning time varied and

was cell dependent. However, all cells eventually show localized activity in the ~200 micron region after conditioning is complete (SI Figure 4.6).

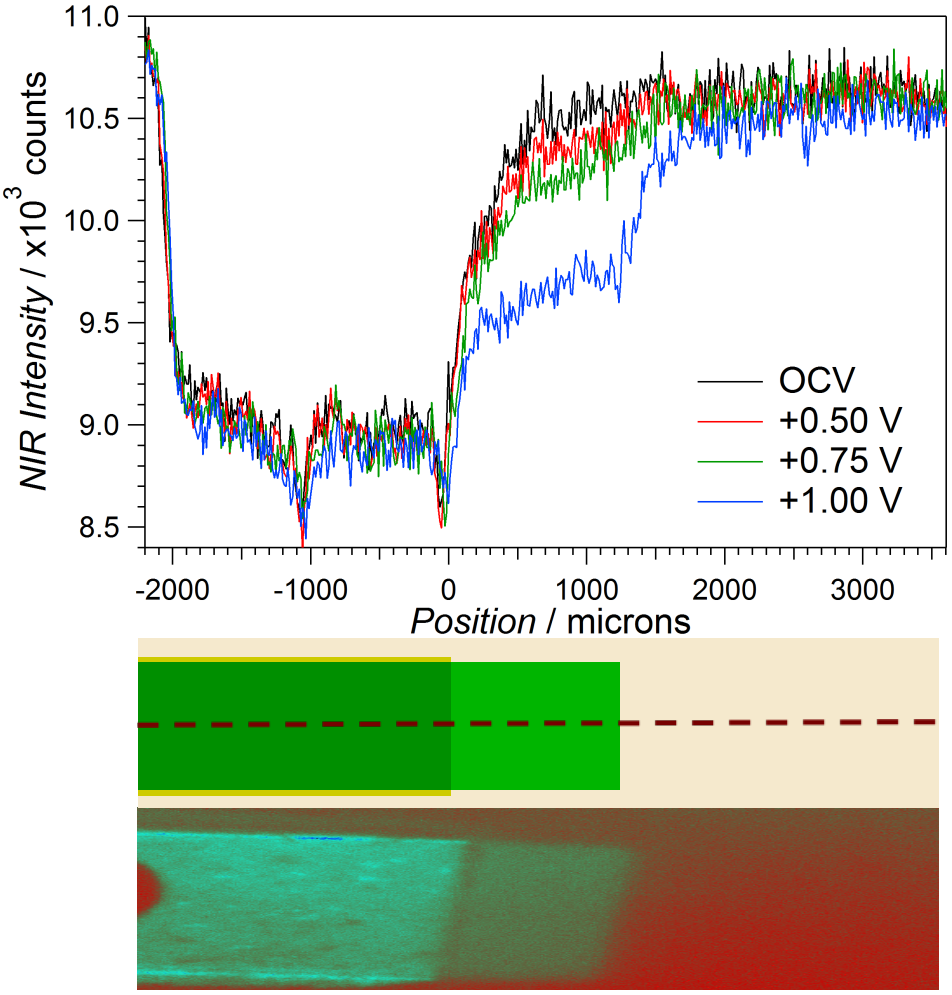

Figure 4.6. 30 second-averaged NIR intensity readings down the middle of the electrode at OCV (black), +0.50 V (red), +0.75 V (green), and +1.00 V (blue) biases. Between each bias, the SOC was kept at OCV and the intensity curves at OCV were essentially identical to the one depicted (pre-0.50 V bias). Beneath the plot is an NIR image collected at +1.00 V and a schematic drawing (same color code as Figure 4.2) showing the profiled region (red dashed line). The Au edge is marked by 0 microns.

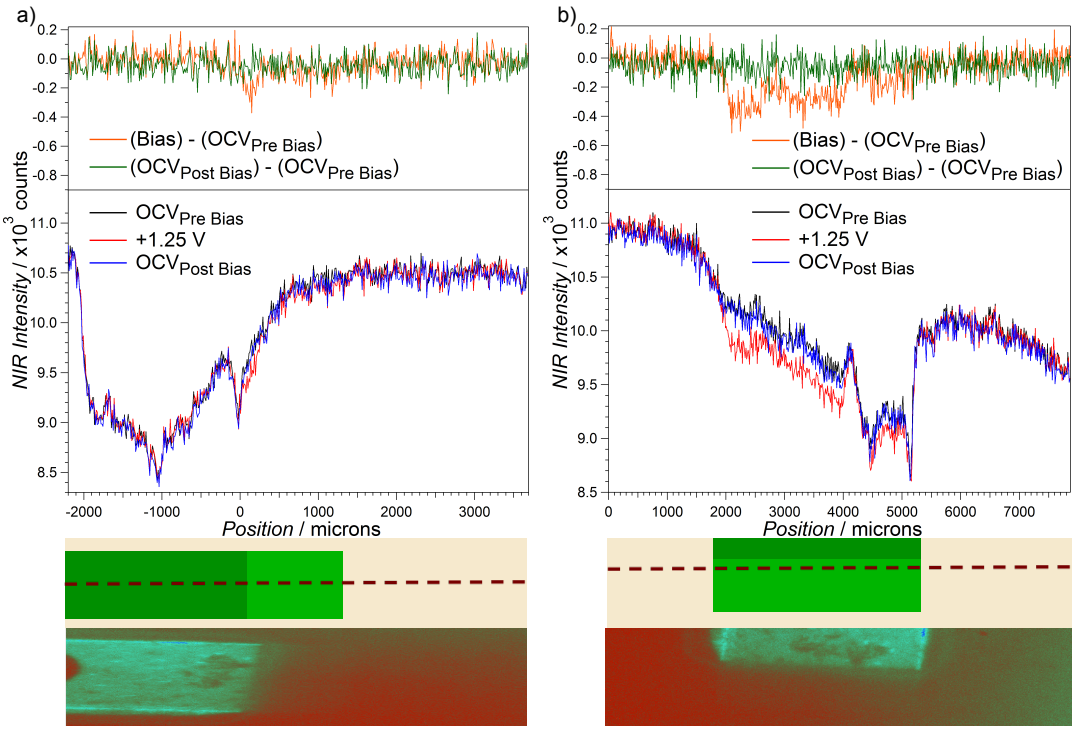

Figure 4.7. a) Plots of 30 second-averaged NIR intensity readings at pre-bias OCV (black), +1.25 V bias (red), and post bias OCV (blue). The top plots show the difference in NIR intensities between +1.25 bias and pre-bias OCV (green) and post-bias OCV and pre-bias OCV conditions (orange). A NIR image recorded at +1.25 V and a schematic drawing of the profiled region are shown below the image. (b) The same image set analyzed across the electrode ~50 microns in front of the Au edge. In (a), the Au edge is marked by 0 microns. In (b), the image is rotated 90 degrees, clockwise, with respect to (a) and the drawing enlarged. An inactive region of the ceria electrode is observed at ~4000 microns where the intensity does not change under bias.

We attribute this conditioning process and the associated localization of electrochemical activity to a change in rate limiting processes on the ceria electrode. As shown in Figure 4.2b, there are three major processes at work on the ceria electrode: lateral electron transport from Au to ceria, surface electrochemical reactions (R4.3), and vertical oxide ion transport from ceria to YSZ. The ~200 micron active region in the conditioned cell is the result of co-limiting processes:

electron transport and surface reactions.[26] The reduction of the entire ceria region in front of the Au suggests that electron transport is not rate-limiting in the pre-conditioned cell. We suggest that oxide transport across the YSZ-ceria interface is rate limiting (or co-limiting) in pre-conditioned cells. This barrier to oxide transport (a charge transfer overpotential) renders electron transport non-limiting in this regime and electron conduction (reduction) occurs across the entire tab (*i.e.* the resistance to electron transport is now less than the charge transfer overpotential). During the conditioning process, the YSZ-ceria interface is annealed and oxide transport becomes more facile and is no longer rate limiting. As a consequence, cell performance improves and electron transport becomes co-limiting, which results in the ~200 micron active region of the cell. This conditioning process is accompanied by a decrease in impedance, presumably due to a decrease in the charge transfer resistance across the ceria – YSZ interface (see SI Figure 4.5).

4.3.5 Changes in Ceria Oxidation states and Optical Properties

The data presented here show that the lateral dimensions of electrochemical activity are quite similar in both the AP-XPS conditions (~ 1 Torr) and the NIR conditions (~760 Torr) in this ceria-based electrochemical system. While we cannot use NIR imaging to directly measure surface concentrations of intermediates such as OH^-, the reversible accumulation of Ce^{3+} in the 200 micron electroactive region observed in the NIR experiments suggests that redox shifts observed in the two different conditions are the same and implies that the same processes are co-limiting: lateral electron transport in the ceria electrode and the water electrolysis

reaction (R4.3).

The control experiments in Section 4.3.2 were used to demonstrate that the NIR experiments probe changes in ceria emissivity and are not associated with temperature changes. It is known from literature[264,265] that H_2 reduces ceria to CeO_{2-x} at elevated temperatures, where x depends on the effective O_2 partial pressure.[184] Our AP-XPS control experiments also show that ceria is uniformly reduced across the electrode surface upon H_2 exposure and is subsequently re-oxidized when exposed to H_2O gas, as expected. When analogous H_2 and H_2O exposures are used in the NIR experiments, we observe a marked decrease in NIR emission from ceria when under a reducing atmosphere (304 Torr H_2) compared to an oxidizing atmosphere (17.5 Torr H_2O) as shown in Figure 4.4.

This decrease in emission is attributed to a change in the optical properties associated with the increase in Ce^{3+} concentration in the ceria. The decrease in emissivity persists well after equilibrium is achieved suggesting that it the emissivity decrease is due to a change in optical properties and not a change in temperature associated with an endothermic chemical reaction. While we cannot exclude small temperature changes, they are likely to be quite small. Although we have observed endothermic cooling associated with thermal reformation, we have never seen any temperature changes associate with Faradaic processes, even when the current densities are many times larger than those studied here.

To further support our claim that we are seeing changes in optical properties rather than temperature, we contrast our results with previous *in situ* NIR thermal imaging experiments conducted by our collaborators at the Naval Research

Laboratory (NRL).[6,266] The studies showed that when hydrocarbon or alcohol fuel is introduced to a Ni/YSZ anode, the electrode surface cools down due to endothermic fuel cracking during cell operation. Also, the extent of heating during electrochemical oxidation was used to determine how much carbon is formed during SOC operation. In these cases, the spatially resolved intensity changes are due to temperature changes, which is confirmed by observing that the effect is reversible; the emission intensity returns to the initial level in the absence of fuel for endothermic cracking (*i.e.* when the system returns to equilibrium), unlike in the control experiments described in our work. Clearly the emissivity changes are equilibrium effects and are not associated with an endothermic process.

The NIR intensity changes are assigned to ceria reduction. Several reports indicate that the appearance of ceria turns from yellow to a darker color (in the visible region) when it is reduced.[26,27) However, the changes we observe in the NIR imaging experiments are not as straightforward to interpret because the optical properties in the region of interest are subtle and the observed intensity changes depend on the experimental geometry.[267] Exposing ceria to reducing conditions has been reported to result in small changes in the bandgap of ceria[208] (at higher energies (>3.5 eV) than those directly pertinent to our emission wavelengths, >720 nm, <1.72 eV). The most pertinent change is an increased index of refraction,[208,209] ~2.2 to 2.7, which is consistent with the reduced emission intensity observed under reducing conditions for ceria.[3,268] The higher index of refraction results in a higher reflectivity and lower emissivity. The lower emissivity reduces the NIR intensity we observe as long as the intensities have a greater contribution from SOC emission

rather than reflection from the surroundings. Strong evidence that the cell emission rather than reflection dominates in our studies is found by recognizing that lower intensities are observed for the regions with bare Au and ceria with Au underneath. If the observed intensities were mostly from reflected radiation, the intensities in these regions would be higher than for the ceria and YSZ regions.

4.4 Conclusion

We demonstrate that combining AP-XPS and NIR imaging yields detailed information on SOCs that extends to true ambient operating conditions. The NIR imaging system represents complementary *in operando* tool to use in the study of SOC electrode materials, such as measurements of active regions and changes in rate-limiting regimes. The simplicity of the method is a distinct advantage over other spectroscopic probes and other *in operando* techniques. The present data shows that NIR imaging is a fast, effective method to track reduction in ceria electrodes by observing a decrease in NIR intensity. Furthermore, the NIR imaging data depicts an electrochemically active region commensurate with that found in the model AP-XPS system. These data simultaneously support the reliability of the AP-XPS models and show that NIR imaging can be used as a complementary technique to elucidate mechanistic details on operating SOCs. In addition, the NIR analysis enabled the measurement of conditioning processes on ceria electrodes that presumably involve changes in rate-limiting processes.

4.5 Supporting Information

4.5.1 SI Auxiliary Experimental Information

4.5.1.1 SOC Fabrication

To prepare the polycrystalline YSZ electrolyte, 2.825 ± 0.025 g of YSZ (*Tosoh Inc.,* TZ-8YSB, 8 mol % Y_2O_3) was weighed out and placed in a coaxial stainless steel die (2.95 ± 0.05 cm inner-diameter). The die was pressurized under five metric tons of pressure for thirty seconds, followed by 10 ~ 10.5 metric tons of pressure for five minutes. The substrate was then sintered in an oven (*MTI corp***,** KSL1700X**)** by heating it from 25 ^{o}C to 1450 ^{o}C at a rate of 1 ^{o}C/min. The temperature remained at 1450 ^{o}C for 3 hours, and was subsequently cooled to 25 ^{o}C at the above heating rate. The final dimensions of the YSZ pellet were 2.3 ± 0.1 cm in diameter and ~1 mm in thickness. Two ceria working electrodes were prepared on one side of the pellet by placing patterned stainless steel shielding masks (*FotoFab*) over the YSZ. An ATC 1800-V (*AJA International, inc.*) sputter deposition unit was used to sputter 50 nm of alumina (oxide ion blocking layer) followed by 300 nm of Au (current collector). The masks were changed, and a *Kurt J. Lesker Co.* PVD75 sputter deposition system was used to sputter a 1000 nm thick film of ceria that rested on top of Au from 3.8 ± 0.3 mm behind the gold edge and then extended 1.1 ± 0.2 mm beyond the edge. To prepare the Pt counter electrode, a Pt paste (*FuelCellMaterials.com*, Lot # 310-118) was applied to the other side of the pellet and allowed to dry. The completed fuel cell was sintered at 800 ^{o}C for 180 minutes using the same starting temperature, heating rate, and oven listed

above.

4.5.1.2 SOC Assembly

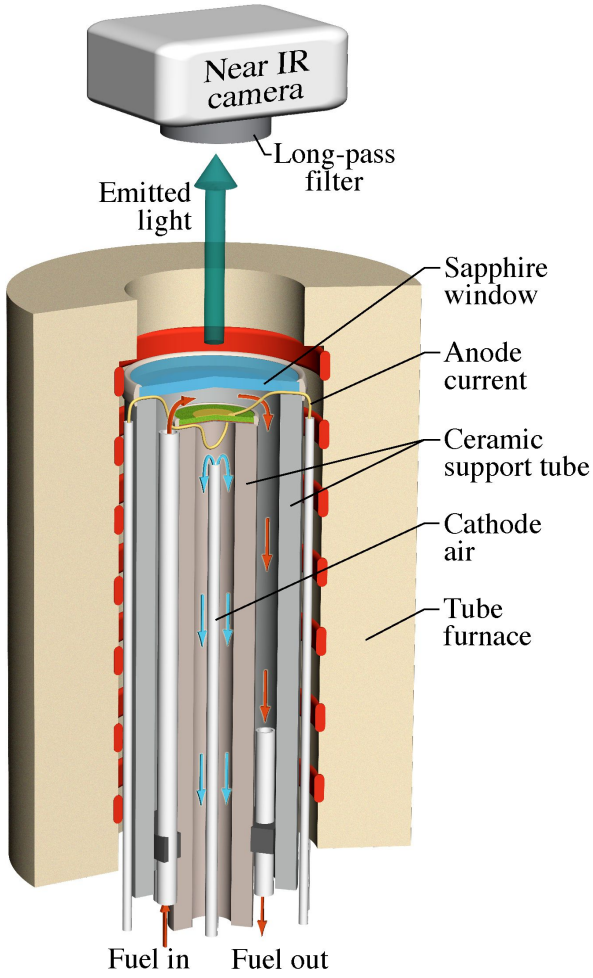

SI Figure 4.1. Schematic of the SOC experimental apparatus for NIR imaging (reprinted from Ref. 6 in original manuscript).

4.5.1.3 Gas Flows to Pressure Conversion for NIR Experiments

Gas Flows:

Ar gas flowed through a water bubbler at 20 ^{o}C resulted in a gas mixture that was 2.3% H_2O.

SI Table 4.1. gas flows for each experiment

Experiment	Ceria Side	Pt Side
Chemical Reduction Experiments	100 sccm H_2 150 sccm Ar	100 sccm Ar
Chemical Oxidation Experiments	150 sccm wet Ar (2.3% H_2O)	100 sccm Ar
Electrochemical Experiments	150 sccm wet Ar (2.3% H_2O)	6.9 sccm H_2 290 sccm Ar

The pressure on each side of the SOC was approximately 760 Torr, so that the partial pressure of a gas on either side of the cell can be calculated as:

$$\left(\frac{\text{Individual Gas Flow Rate}}{\text{Total Gas Flow Rate}}\right) \text{x } 760 \text{ Torr} = \text{Partial Pressure (Torr)}$$

resulting in pressures of:

SI Table 4.2. Gas pressures for each experiment

Experiment	Ceria Side	Pt Side
Chemical Reduction Experiments	304 Torr H_2 456 Torr Ar	760 Torr Ar
Chemical Oxidation Experiments	17.5 Torr H_2O 742.5 Torr Ar	760 Torr Ar
Electrochemical Experiments	17.5 Torr H_2O 742.5 Torr Ar	17.7 Torr H_2 742.3 Torr Ar

4.5.1.4 Electrochemical Characterization

The LSV scans were run between OCV and +1.250 V (bias on the Pt electrode) at a rate of 100 mV s^{-1}. EIS measurements were made at frequencies between 100 kHz and 0.2 Hz, inclusive, at a V_{DC} of 0.100 V vs. OCV and a V_{AC} of 0.050 V.

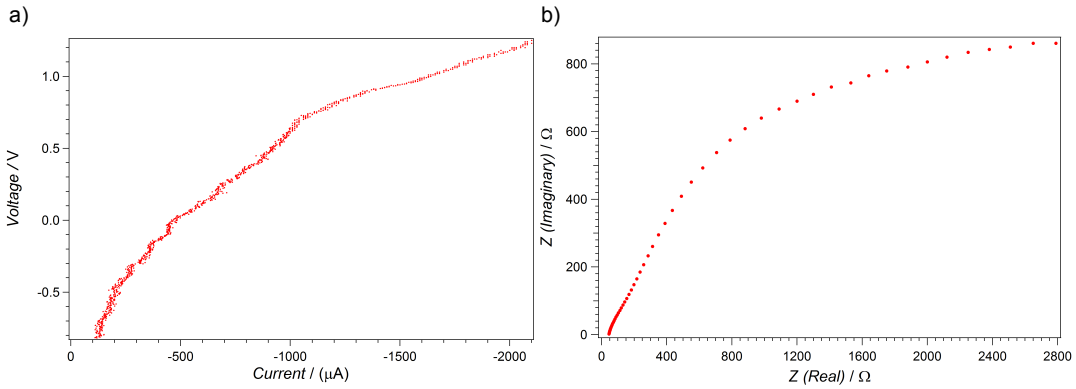

SI Figure 4.2. Representative LSV (A) and EIS (B) scans conducted in the same conditions as the electrochemical water splitting experiments.

4.5.2 XPS: Ce *4d* Spectrum

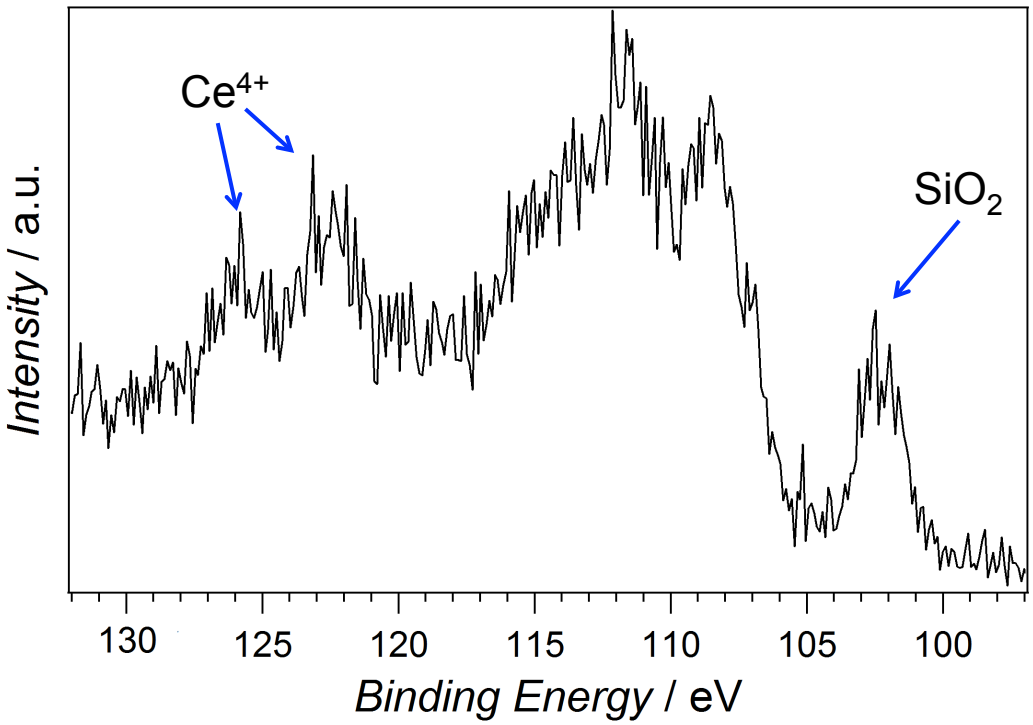

SI Figure 4.3. Representative Ce *4d* XPS spectrum.

Peaks were calibrated by taking a C *1s* spectrum and adjusting the graphitic carbon peak to the accepted binding energy of 284.8 eV.[186] The peak located at 102 eV is a Si *2p* peak, associated with ubiquitous SiO_2. The peaks in the range of 105

– 117 eV are a mix of Ce^{3+} and Ce^{4+}, while the peaks at 122 and 126 eV are specific to Ce^{4+}. See Ref. 27 for more details on background and fitting procedure.

4.5.3 SI Additional Results

4.5.3.1 Water Splitting: Electrochemically Active Region

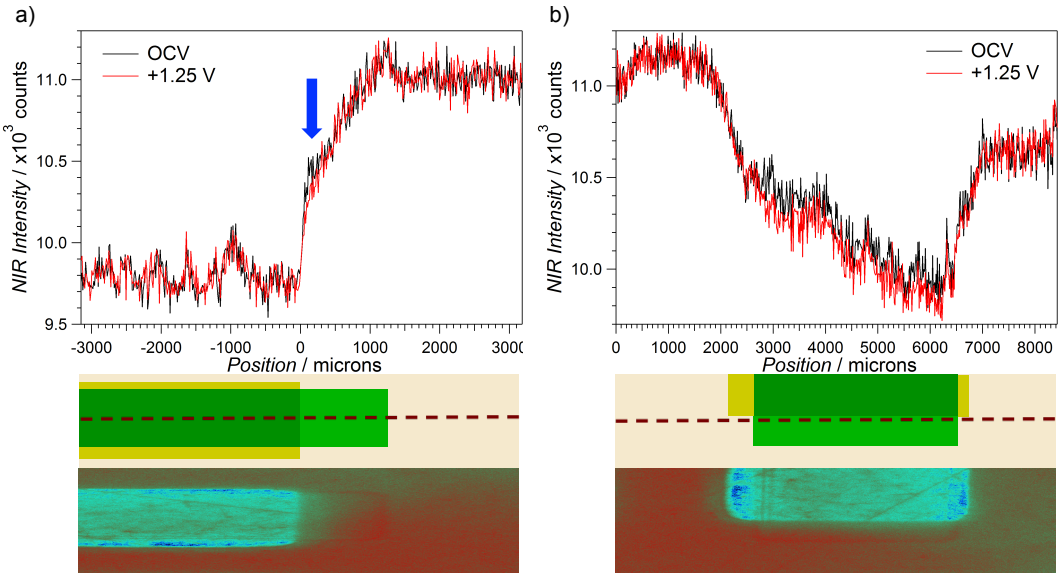

SI Figure 4.4. NIR intensity readings vs. position (a) through the middle of the electrode and (b) across the electrode, ~50 microns in front of the Au edge

30 second-averaged NIR intensity readings at OCV (black) and +1.25 V bias (red). (a) a profile was analyzed down the middle of the electrode. The blue arrow indicates the active region (b) data was analyzed across the electrode ~50 microns in front of the Au edge. Both a NIR image and schematic drawing are provided for position clarification (light green = ceria above YSZ, dark green = ceria above Au current collector, yellow = Au, manila = YSZ). The dashed line indicates the profiled region. In (a), the Au edge is marked by 0 microns. In (b), the image is oriented 90 degrees, clockwise, with respect to (a) and the scaling has changed.

In (a) a decrease in NIR intensity (signifying ceria reduction) under bias can be seen extending ~200 microns in front of the Au edge, while everywhere else shows ~identical NIR intensities under OCV or bias. The profile in (b) shows a marked decrease in NIR intensity along the region of the ceria electrode studied when under bias. This region of lower NIR radiation correlates well with the 200 micron electrochemically active region we have seen in previous AP-XPS studies.

4.5.3.2 Electrochemical Impedance Spectra of Conditioned SOCs

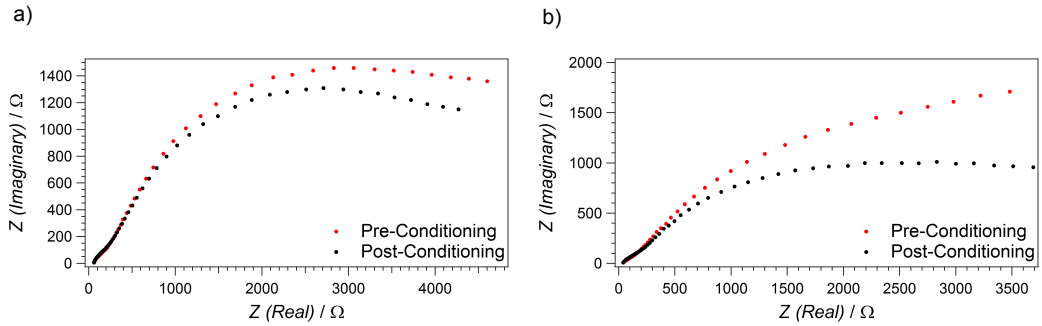

SI Figure 4.5. Impedance measurements for: (a) the SOC from Figures 5 and 6, and (b) the SOC from Figure S4

Pre-conditioned (red) and post-conditioned (black) impedance data for (a) the SOC from Figure 4.6 and Figure 4.7, and (b) the SOC from SI Figure 4.6.

EIS measurements were made at frequencies between 100 kHz and 0.2 Hz, inclusive, at a V_{DC} of 0.100 V vs. OCV and a V_{AC} of 0.050 V. While the impedance is too high for a low frequency intercept to be observed, the spectra show that the post-conditioned cell exhibits a lowered overall impedance.

4.5.3.3 Electrochemical Water Splitting: Electrode Conditioning

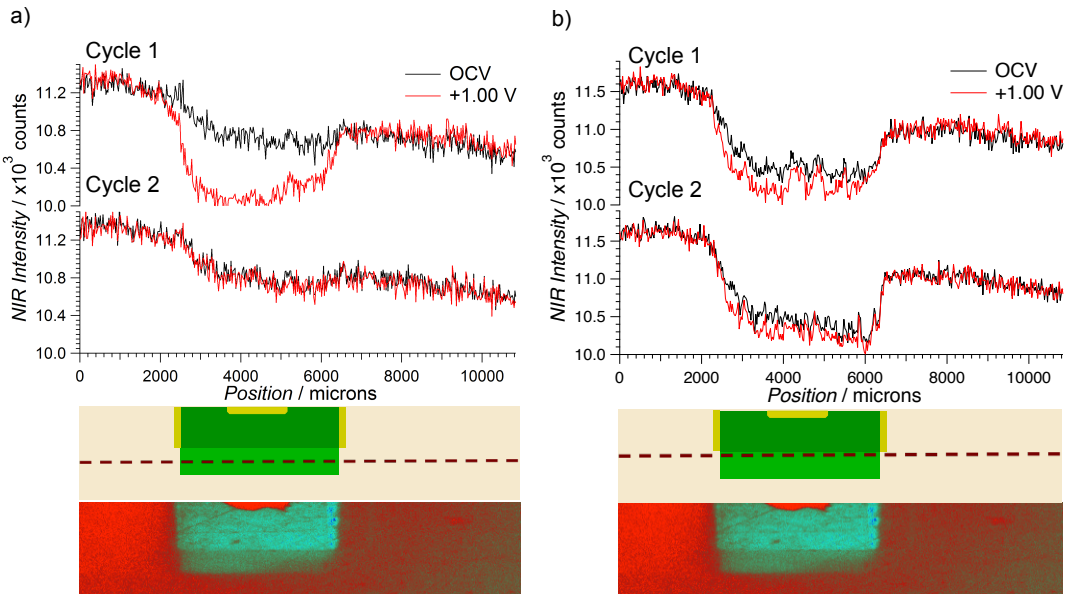

SI Figure 4.6. NIR intensity readings vs. position across the electrode (a) ~670 microns in front of the Au edge and (b) ~50 microns in front of the Au edge.

The cell was polarized at 1.00 V, allowed to rest at OCV for 10 minutes, then polarized at 1.00 V again.

30 second-averaged NIR intensity readings at OCV (black) and +1.00 V bias (red) were taken across the ceria electrode for each cycle in two different regions: (a) ~670 microns in front of the Au edge (b) ~50 microns in front of the Au edge. Both a NIR emission image (from cycle 1 polarization) and schematic (same color-code as SI Figure 4.4) are provided for position clarification. The dashed line indicates the region of profiling.

In (a) a significant decrease in NIR intensity (signifying reduction) along the middle of the ceria electrode can be seen under bias in cycle 1, but not in cycle 2, whereas in (b) the bias-induced reduction of ceria is seen in both cycles. These results show that the extended active region present in cycle 1 has disappeared, and the much shorter, expected active region is found in cycle 2, signifying a change in

rate-limiting regimes. The current measured in cycle 1 was 760 μA whereas the cell drew 900 μA in cycle 2, showing that the cell performed better in the new regime. EIS data in SI Figure 4.5b shows a lowering of impedance in the post-conditioned state.

4.5.3.4 Optical Properties of Oxidized and Reduced Ceria

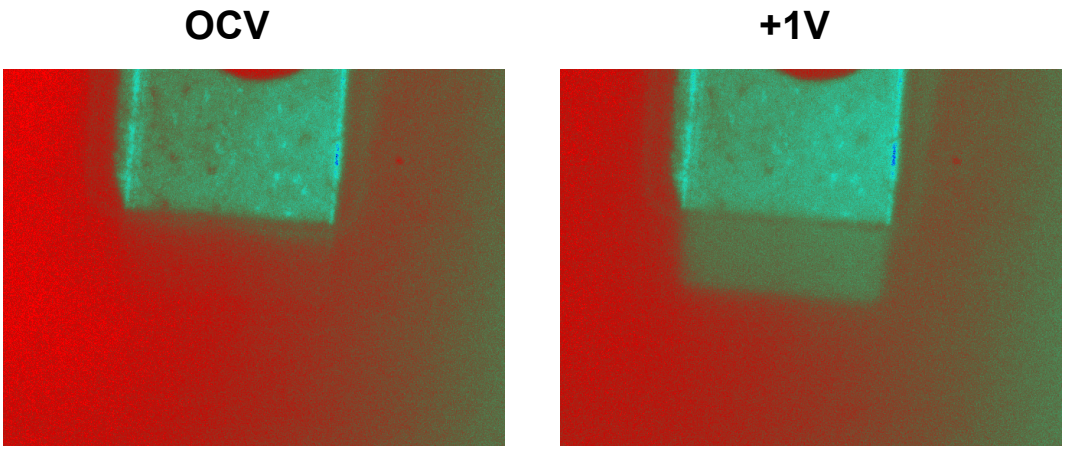

SI Figure 4.7. The preconditioned cell at OCV and +1.0 V illustrating the differences in optical properties of ceria tab when reduced or oxidized.

5 Measuring Cobalt Oxidation states with the Auger Parameter

5.1 Introduction

5.1.1 Cobalt Oxidation States

In operando determination of the Co oxidation state on the surface of operating cobalt-based electrocatalysts such as LSC ($La_{1-x}Sr_xCoO_{3-x}$) is of critical importance for understanding their behavior in SOC operations. There is limited information with regards to measuring changes in Co oxidation state using near edge X-ray absorption fine structure (NEXAFS) spectroscopy,[269-273] but quantification of the oxidation state using X-ray photoelectron spectroscopy (XPS) remains elusive. Standard techniques for measuring the oxidation state of materials such as tracking shifts binding energies (BEs) (Section 1.4.1.7) are not effective. For example, the prominent $2p_{3/2}$ peak,[274,275] exhibits a BE for a Co^{3+} species (780.0 eV) that lies *in between* that of Co^{2+} and Co^0 species (781.0 eV and 778.5 eV, respectively) meaning that there is no clear linear correlation between BE and oxidation state, especially in a mixed valent Co compound. Attempts at deconvolution of the 2p signal into separate peaks corresponding to different oxidation state have been pursued, but reports on peak BE assignments are varied.[276] Chen *et al.*[277] quantified the intensity of a charge-transfer satellite to measure the amount of Co^{2+} in Co-N-C catalysts, however, this satellite only appears when the Co^{2+} is octahedrally-coordinated[188,278,279] and in a high spin state. Further complications in the 2p spectra involve multiplet splitting (see Section 1.4.1.5) *in addition* to the spin-orbit splitting.[280,281]

While measuring the degree of multiplet splitting in a relatively simple Co 3s spectrum may yield oxidation state information similar to Mn 3s studies (see Section 2.2.3.3), this splitting is more difficult to distinguish due to a lower magnetic moment[282] (*e.g.* 4.3-5.2 μ_B in Co^{2+} high-spin vs. 5.6-6.1 μ_B in Mn^{2+} high-spin). Additionally, Van Heide *et al.*[280] note the controversial existence of satellites within the 3s spectra that appear for late transition metals, which further complicate analysis. Even if these issues are resolved, the method is unsuitable for monitoring oxidation state changes in a LSC electrode as the La 4d and Co 3s peaks overlap, rendering it impossible to reliably fit the Co 3s.

However, studies on Co_xSi_y compounds by Zhao *et al.*[283] showed a steady increase in a quantity known as the Auger parameter (AP) with decreasing Co oxidation state. The AP is a quantity defined by Wagner[191] and is fully described in the next section.

5.1.2 The Auger Parameter

The AP was originally defined by Wagner[191] as the difference between the kinetic energy (KE) of an Auger electron and a photoelectron:

$$\alpha = KE_{Auger\ e^-} - KE_{photo\ e^-} \qquad \textbf{(Eq. 5.1)}$$

where α represents the Auger parameter.

The AP can be defined with respect to the KEs of any Auger electron and photoelectron, although it is conventional for the measured photoelectron to be the one that induces the measured Auger electron's emission (see Section 1.4.1.6). For

example, when measuring KLL Auger electrons, which are produced by the ejection of a 1s (K shell) photoelectron, the AP would typically be measured between the KE of the KLL Auger electron and the 1s photoelectron. However, the AP can be unconventionally defined as the KE difference between the KLL Auger electron and a 2s or 2p (L shell) photoelectron, if the 1s photoelectron is difficult to collect data on.

The above definition of the AP can sometimes produce negative values and has since been modified to:

$$\alpha' = KE_{Auger\ e^-} + BE_{photo\ e^-} \quad \textbf{(Eq. 5.2)}$$

where α' is the "modified Auger parameter,"[284] (which AP will refer to from hereon).

The AP is directly related to an atom's environment via the "extra-atomic relaxation" energy (R_{ea}) of an atom so that a change in AP in a solid material represents a change in R_{ea}:

$$\Delta\alpha' = 2\Delta R_{ea} \quad \textbf{(Eq. 5.3)}$$

This relationship is described in greater detail in SI Section 5.5.1.

The R_{ea} (Section 1.4.1.4) represents how well the electrons of neighboring atoms can screen an outgoing photoelectron, which is related to the neighboring atoms' polarizability (more electronegative atoms are less polarizable). For

example, in Zhou's studies on Co_xSi_y compounds,[283] as the amount of relatively electronegative Si neighbors are increased, the oxidation state of Co increases. Furthermore, as Co is surrounded by a greater number of Si atoms, which are more electronegative (*i.e.* less polarizable) than Co, the R_{ea} of Co photoelectrons decrease. The R_{ea} decreases because the neighboring Si electrons cannot screen the outgoing photoelectrons as well as electrons in a less electronegative neighboring atom (*e.g.* other Co atoms). The decrease in R_{ea} results in a direct decrease in the measured Co AP, as Zhou observed. To summarize, it has been demonstrated that if an atom transitions from one electronic state to another (*e.g.* Co metal is reduced), the R_{ea} and associated AP will likely change. This change can be calculated as:

$$\Delta\alpha'_{(\text{ox metal} \rightarrow \text{red metal})} = 2[R_{ea\ \text{red metal}} - R_{ea\ \text{ox metal}}] \qquad \textbf{(Eq. 5.4)}$$

hence measuring the Co AP may provide a key to quantifying Co oxidation state changes, especially given the aforementioned studies by Zhao. Furthermore, studies on Ni, another late transition metal, have shown that Ni oxidation states can be correlated with variations in the AP.[285]

To properly quantify the oxidation state of Co, we developed standards of well-defined composition, containing Co oxidation states between 2^+ and 3.5^+ primarily in both octahedral and tetrahedral environments as these may also affect the AP. X-ray powder diffraction (XRD) and NEXAFS were used for characterization and subsequently the samples were studied with XPS. Additionally, we conducted ambient pressure XPS (AP-XPS) studies in which two

reducible Co perovskites, LSC and $LaCoO_{3-\partial}$, were exposed to different reducing and oxidizing environments to determine *in situ* changes in the Co oxidation state could be correlated to the AP. We found that we cannot make a definitive calibration curve between the AP and oxidation state that encompasses all Co materials because the coordination environment also affects the AP, which precludes oxidation state determination. However, within a single material in which Co is reducible (*e.g.* LSC), the AP may be useful for measuring changes in Co oxidation state as our thermal AP-XPS tests show.

5.2 Experimental Procedures

All compounds were prepared as powders with the exceptions of a $LaCoO_{3-\partial}$ pellet and a LSC thin film (which were used for thermal AP-XPS tests). Each compound, oxidation state, and coordination environment as determined by NEXAFS (SI Section 5.5.2) and references, are listed in **Table 5.1**:

Table 5.1. Cobalt standards and their theoretical Co oxidation states and coordination.

Compound	Oxidation State	Coordination
$Co(OH)_2$	2+	Octahedral
$CoFe_2O_4$	2+	Octahedral[286]
$CoAl_2O_4$	2+	Tetrahedral[287,288]
$CoCr_2O_4$	2+	Tetrahedral[289]
Co_3O_4	2.66+	Tetrahedral (2+) / Octahedral (3+)
$NiCo_2O_4$	3+	Tetrahedral / Octahedral (50:50)[290]
$LaCoO_{3-\partial}$ pellet	3+	Octahedral
LSC ($La_{0.9}Sr_{0.1}CoO_{3-\partial}$)	3.1+	Octahedral
LSC ($La_{0.7}Sr_{0.3}CoO_{3-\partial}$)	3.3+	Octahedral
LSC ($La_{0.5}Sr_{0.5}CoO_{3-\partial}$)	3.5+	Octahedral

For the $LaCoO_3$ and LSC compounds, the oxidation state assumes that the ∂ term in the O is equal to 0.

5.2.1 Sample Syntheses

Co_3O_4, and $Co(OH)_2$ were standards provided by Dr. Yi Yu, and $NiCo_2O_4$ was prepared by an undergraduate researcher, Cody Sherlock, both previous members of the Eichhorn research group. The LSC thin film was deposited onto a yttria-stabilized zirconia (YSZ) single crystal (*MTI Corporation*) via pulsed laser deposition (PLD) by our collaborator, Dr. Xiaohong Zhang (Takeuchi lab). The synthesis details of the remaining compounds are given below.

High temperature heating was conducted in either a KLX1700 box furnace (*MTI Corporation*) or a Thermolyne F21135 tube furnace with the sample in a covered alumina crucible unless otherwise noted. All samples were characterized by XRD.

5.2.1.1 $CoFe_2O_4$

$CoFe_2O_4$ was prepared by the ceramic method. 248.1 mg and 688.8 mg of $Co(NO_3)_2 \bullet 6H_2O$ and $Fe(NO_3)_3 \bullet 9H_2O$, respectively, were grinded together and pre-calcined at 1000 ^oC for 12 hr. The ramp rate (rr) up and down was 2 ^oC/min.

The sample then underwent two cycles of grinding and heating for 24 hr at 1000 ^oC (cycle 1) and 1150 ^oC (cycle 2) with a 2 ^oC/min rr.

5.2.1.2 $CoAl_2O_4$

$CoAl_2O_4$ was prepared by the ceramic method. 115.3 mg Al_2O_3 and 90.7 mg of Co_3O_4 were ground together and the mixture was heated in a tube furnace at 1000 ^oC for 12 hr (2 ^oC/min rr up, natural cooling). The product was reground and heated to 1000 ^oC for 12 hr in the box furnace (rr up and down was 2 ^oC/min).

The sample then underwent two cycles of being ground and heated for 24 hr at 1000 ^{o}C and 1150 ^{o}C (cycle 2) with a 2 ^{o}C/min rr. The product was reground, pressed into a pellet, and heated in the box furnace at 1100 ^{o}C for 24 hr (same rr). Finally, the sample was removed from the oven and reground.

5.2.1.3 $CoCr_2O_4$

$CoCr_2O_4$ was prepared by a sol-gel method adapted from the work of Jasaitis *et al*.[291] 384.8 mg $Co(NO_3)_2 \bullet 6H_2O$ and 1058.2 mg $Cr(NO_3)_2 \bullet 9H_2O$ were placed in 50 mL H_2O at 55~60 ^{o}C. 1 mL ethylene glycol was added and the solution was boiled at 105 ^{o}C. The leftover product was ground and then heated in a tube furnace at 700 ^{o}C for 3 hr with a 3 ^{o}C/min rr up and natural cooling down. The sample was then reground and heated in the tube furnace again at 1000 ^{o}C for 10 hr (same rr).

5.2.1.4 $NiCo_2O_4$

$NiCo2O_4$ was prepared by a co-precipitate method adapted from Klissurski and Uzunova.[292] 1482.9 mg of Na_2CO_3 was dissolved in 10 mL H_2O and the solution was heated to 70 ^{o}C. 331.3 mg of $Ni(NO_3)_2 \bullet 6H_2O$ and 662.6 mg of $Co(NO_3)_2 \bullet 6H_2O$ were then dissolved in a separate 5 mL of water, and then added to the Na_2CO_3 solution. The solution was stirred for 30 minutes, cooled, and then vacuum filtered. The product was washed with hot water 10 times, and then ground into powder. The powder was heated in the box furnace and heated to ~110 ^{o}C for 24 hours at 2 ^{o}C/min rr. The sample was reground, heated to 500 ^{o}C for 24 hours in the box furnace with 3 ^{o}C/min rr.

5.2.1.5 $LaCoO_3$ Pellet

A $LaCoO_3$ pellet was prepared by the ceramic method. 880.7 mg of $La(NO_3)_2 \bullet 6H_2O$ and 591.9 mg $Co(NO_3)_2 \bullet 6H_2O$ were grinded together and the resulting powder was pre-calcined at 1000 ^oC in the box furnace for 12 hr (rr 5 ^oC/min).

The sample then underwent two cycles of being reground, pressed into a pellet, and heated to 1000 ^oC (cycle 1) or 1100 ^oC (cycle 2) for 24 hr using the same rr.

5.2.1.6 LSC ($La_{1-x}Sr_xCoO_{3-\partial}$) samples

LSC materials with different Sr doping levels (indicated by "x' value) were prepared via ceramic method. Starting materials of La_2O_3, $SrCO_3$, and $Co(NO_3)_2 \bullet 6H_2O$ were used in the quantities listed in Table 5.2. The materials were ground together and heated to 800 ^oC in the box furnace for 12 hr with a 5 ^oC/min rr.

The samples then underwent two cycles of being reground and heated to 1100 ^oC for 24 hr at the same rr. The samples were then ground and pressed into a pellet before undergoing the same heating treatment again. The samples were finally ground once more.

Table 5.2. Amounts of starting materials to produce 500.0 mg of LSC at different doping levels.

$La_{1-x}Sr_xCoO_{3-\partial}$	m La_2O_3 (mg)	m $SrCO_3$ (mg)	m $Co(NO_3)_2 \bullet 6H_2O$ (mg)
x = 0.1	304.5	30.7	604.5
x = 0.3	247.5	96.1	631.6
x = 0.5	185.0	167.7	661.0

5.2.2 Instrumentation

5.2.2.1 Conventional Characterization Measurements

Samples were characterized, *ex situ*, at the University of Maryland with XRD and XPS. The XRD instrument used was a Bruker C2 Discover diffractometer equipped with a VÅNTEC-500 detector using monochromatic Cu Kα radiation source running at 40 kV and 40 mA. XPS measurements were obtained with a Kratos Axis 165 X-ray photoelectron spectrometer with a Mg X-ray source (hν = 1253.6 eV).

5.2.2.2 AP-XPS and NEXAFS set up

AP-XPS and NEXAFS experiments were performed at the Advanced Light Source (ALS) at the Lawrence Berkeley National Laboratory, on Beamline 11.0.2. We conducted *ex situ* NEXAFS scans of the Co standards and *in situ* NEXAFS and AP-XPS scans of a $LaCoO_3$ pellet and $La_{0.5}Sr_{0.5}CoO_{3-\partial}$ thin film that was exposed to different oxidizing/reducing environments.

Samples were oriented so that the X-ray beam strikes the sample at an incident angle of 75^o and the electron emission angle is 0^o with respect to the sample normal.

In the *in situ* experiments on $LaCoO_3$, the pellet was scanned in increasingly reducing conditions:

Table 5.3. Conditions that the $LaCoO_3$ pellet was exposed to in AP-XPS experiments.

Condition	Atmosphere	Temperature
1	Ultra high vacuum (UHV)	Room temperature (rt)
2	200 mTorr H_2	rt
3	200 mTorr H_2	200 ^oC
4	200 mTorr H_2	400 ^oC
5	500 mTorr H_2	400 ^oC

Temperatures were measured with a thermocouple.

The LSC film studies involved a different series of steps. Temperature readings are estimated based on calibrations of heater settings against a thermocouple in separate runs.

Table 5.4. Conditions that the LSC thin film was exposed to in AP-XPS experiments.

Condition	Atmosphere	Temperature
1	200 mTorr O_2	400 ± 50 ^oC
2	UHV	100 ± 50 ^oC
3	200 mTorr H_2	400 ± 50 ^oC
4	500 mTorr H_2	500 ± 50 ^oC
5	500 mTorr O_2	500 ± 50 ^oC

5.2.3 XRD Bulk Characterization

XRD characterization of Co standards are shown in Figure 5.1. Diffraction patterns were collected from 1-3 hours depending on the sample, and the background has been subtracted.

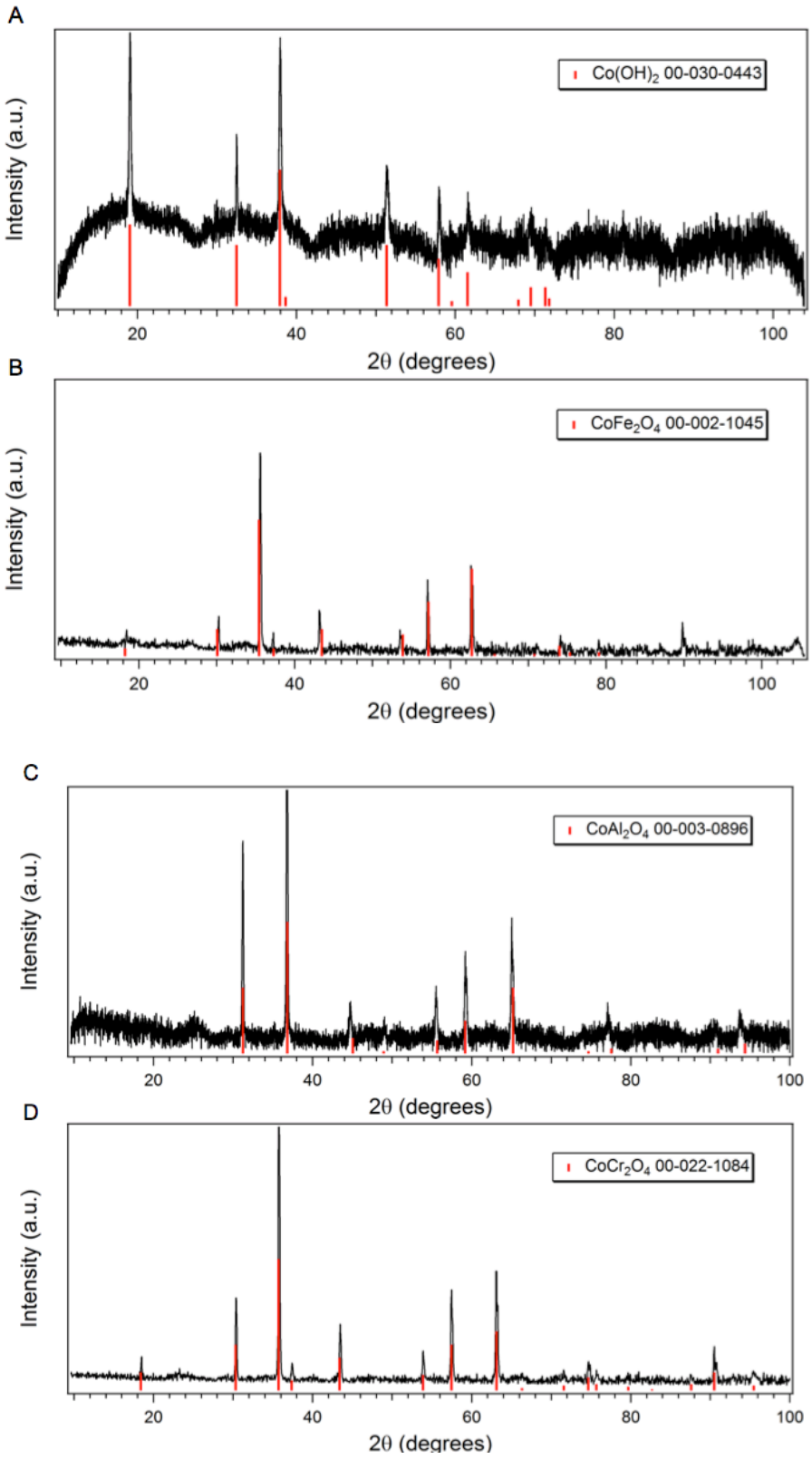
A
Co(OH)2 00-030-0443
Intensity (a.u.)
20
40
60
80
100
2θ (degrees)
B
CoFe2O4 00-002-1045
Intensity (a.u.)
20
40
60
80
100
2θ (degrees)
C
CoAl2O4 00-003-0896
Intensity (a.u.)
20
40
60
80
100
2θ (degrees)
D
CoCr2O4 00-022-1084
Intensity (a.u.)
20
40
60
80
100
2θ (degrees)

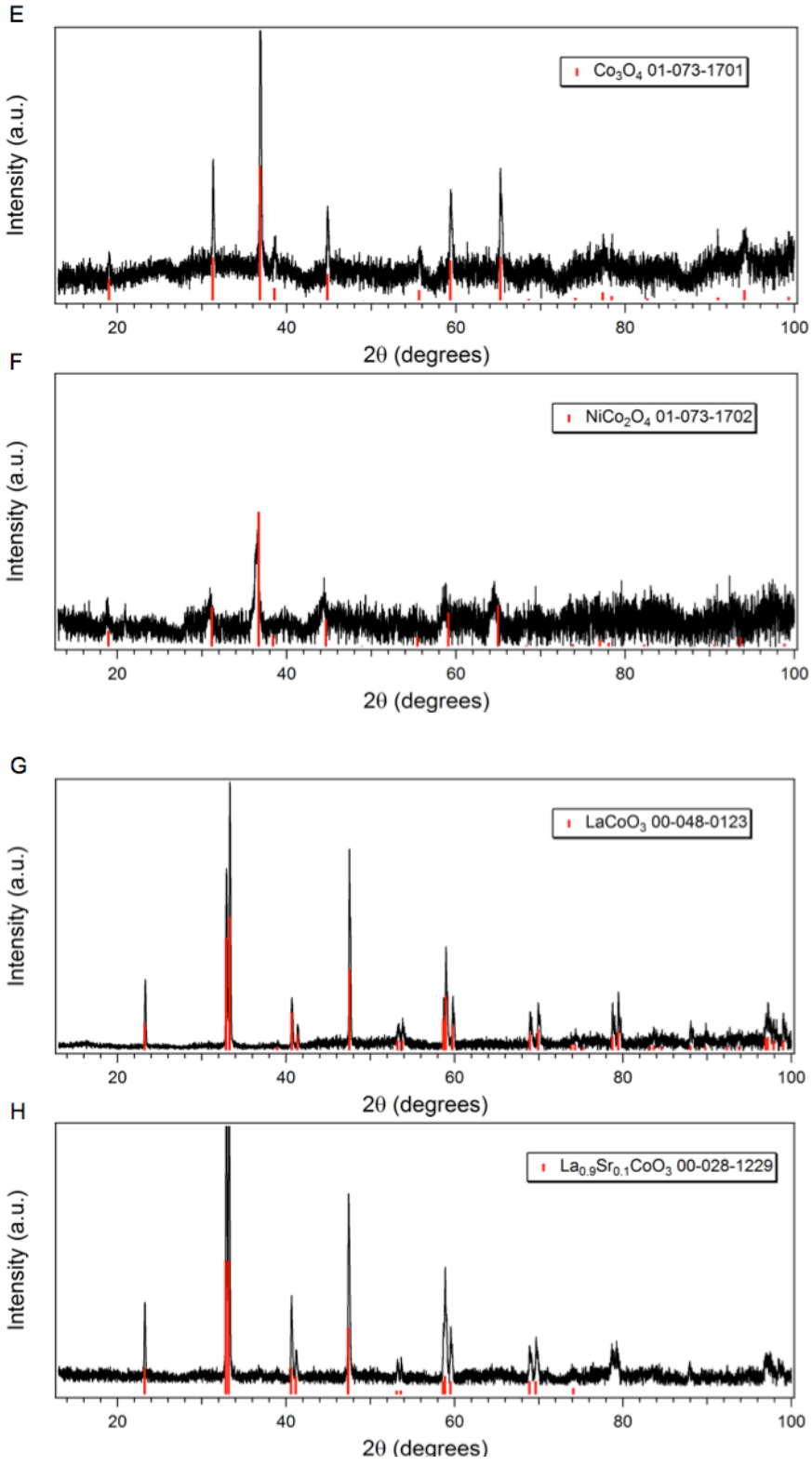
E
Intensity (a.u.)
Co3O4 01-073-1701
20
40
60
80
100
2θ (degrees)
F
Intensity (a.u.)
NiCo2O4 01-073-1702
20
40
60
80
100
2θ (degrees)
G
Intensity (a.u.)
LaCoO3 00-048-0123
20
40
60
80
100
2θ (degrees)
H
Intensity (a.u.)
La0.9Sr0.1CoO3 00-028-1229
20
40
60
80
100
2θ (degrees)

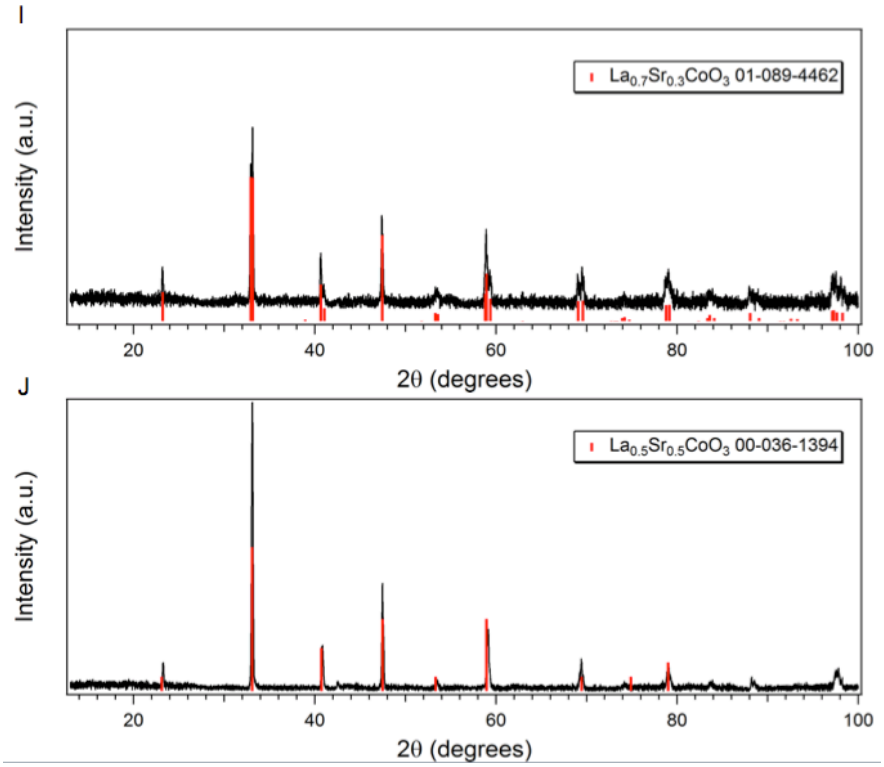

Figure 5.1. XRD of Co standards: (A) $Co(OH)_2$; (B) $CoFe_2O_4$; (C) $CoAl_2O_4$; (D) $CoCr_2O_4$; (E) Co_3O_4 ; (F) $NiCo_2O_4$; (G) $LaCoO_3$; (H) $La_{0.9}Sr_{0.1}CoO_3$; (I) $La_{0.7}Sr_{0.3}CoO_3$; (J) $La_{0.5}Sr_{0.5}CoO_3$

5.2.4 XPS and NEXAFS Spectra Measurements

We measured two different APs between the Co $L_{23}VV$ Auger electron and either the 2p or 3p photoelectron, labeled α'_{2p+LVV} and α'_{3p+LVV}, respectively. While the 2p is the more standard Co core electron to study with XPS, the 3p electron is easier to measure with the photon energies available for our AP-XPS studies. No calibration of the XPS peaks was needed as AP measurements do not require it (the $KE_{auger\ e-}$ and $BE_{photo\ e-}$ terms are affected by charging and workfunction in equal and opposite amounts).

XPS spectra were analyzed with CasaXPS. A linear background was applied to all the 2p scans. For the 3p and $L_{23}VV$ scans, a linear background was

used to analyze the Co standards, but a Shirley background was used to analyze *in situ* AP-XPS data. All peaks had a 70:30 Gaussian-Lorentzian mix.

NEXAFS scans of the $L_{2,3}$ edges (corresponding to $2p_{1/2}$ and $2p_{3/2}$ electrons respectively) were also collected at ALS via partial electron yield detection (see Section 1.4.2.2). The KE of outgoing electrons measured was 350 eV, except for $NiCo_2O_4$ where the measured KE was 370 eV. NEXAFS spectra were analyzed with the Athena program.

5.3 Results and Discussion

In this section we present the results for the AP measurements on the Co standards and the changes in the AP measured in thermal redox tests of the $LaCoO_3$ pellet and LSC thin film. These data are compared to the NEXAFS $L_{2,3}$ spectra.

5.3.1 Auger Parameters of Co Standards

The Co standards show no obvious correlation between the AP and Co oxidation state, likely due to the complex differences in LVV line shapes. The $L_{23}VV$ spectrum is very broad, ill-defined, and complex due to the multitude of auger electrons produced with different KEs (see Section 1.4.1.6). Thus, there is no straightforward method to determine the relative intensities of each auger peak.

Figure 5.2 shows representative $L_{23}VV$ spectra from compounds of differing Co oxidation state: $Co(OH)_2$ (black), Co_3O_4 (blue), and $LaCoO_3$ (red). As described above, it is very difficult to ascertain the KE of a specific Auger electron. Instead, the KE corresponding to the maximum intensity of the *overall range* of $L_{23}VV$ peaks is measured. In other words, it is not important to identify each individual Auger electron peak within the spectrum (*e.g.* $L_3M_4M_4$ vs. $L_3M_4M_5$,

where M_4 and M_5 represent 3d valence electrons). What is of more importance is accurately determining the KE at which the maximum intensity is found. The spectra are fitted with an "envelope" constructed from adding numerous peaks (70:30 Gaussian-Lorentzian mix, in grey) which give the best fit of the data points. For example, the blue line in the Co_3O_4 $L_{23}VV$ spectrum is the envelope for that spectrum, and represents the sum of the grey peaks which do not correspond to specific Auger electrons. The highest intensity of the Co_3O_4 envelope, and defining value of the $KE_{L_{23}VV}$, is found at 774.2 eV.

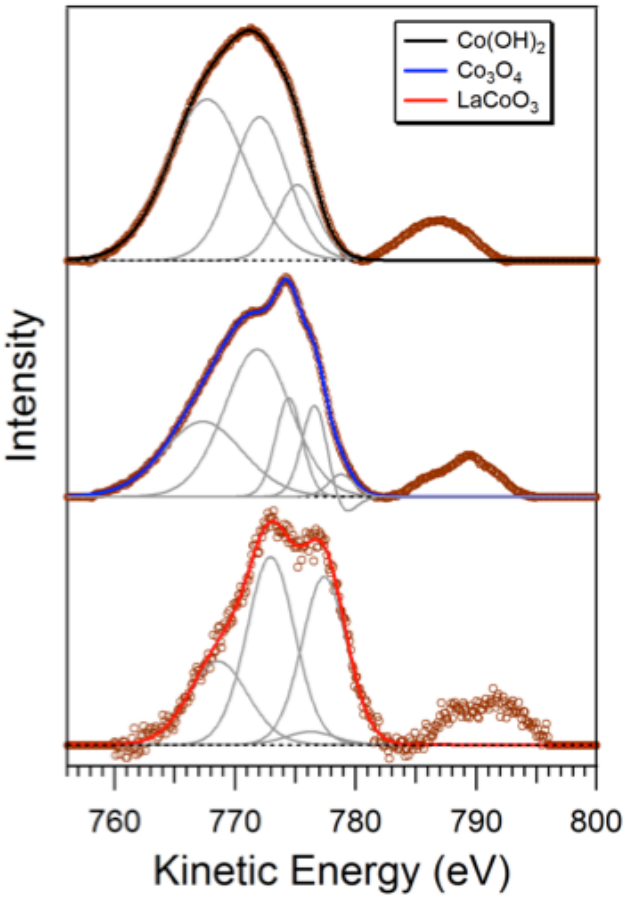

Figure 5.2. Representative $L_{23}VV$ spectra of Co in different Co oxidation state compounds: $Co(OH)_2$ (black), Co_3O_4 (blue), and $LaCoO_3$ (red). The high KE peak ~790 eV is the L_2VV region while the L_3VV region is fit with enough peaks (in grey) to create an envelope that fits the spectrum well. The background is represented by the dotted line.

Representative XPS Co 2p and 3p spectra for the same three compounds listed above are shown in Figure 5.3 and Figure 5.4, respectively.

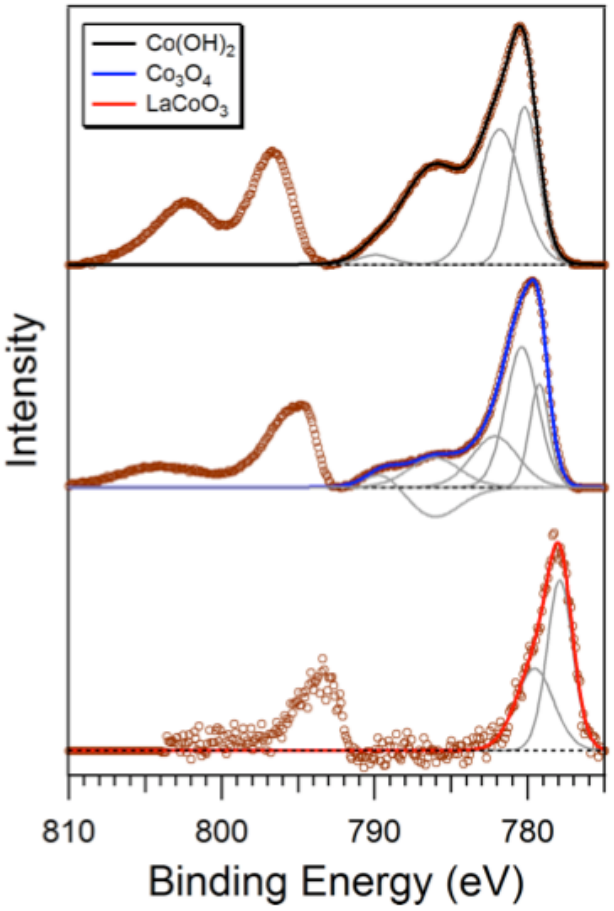

Figure 5.3. Representative Co 2p spectra of different Co oxidation state compounds: $Co(OH)_2$ (black), Co_3O_4 (blue), and $LaCoO_3$ (red). The low BE peak region at ~778 eV is comprised of $2p_{3/2}$ related peaks and is fit with enough peaks (in grey) to create an envelope that fits the spectrum well. The background is represented by the dotted line.

The 2p spectra show the two main $2p_{3/2}$ and $2p_{1/2}$ peaks separated by ~15 eV. These peaks are complicated by multiplet splitting[280,281] and in some cases charge transfer satellites that are typical of Co^{2+} octahedral, high spin compounds such as $Co(OH)_2$ and the mixed valent Co_3O_4.[188,278,279] However, as in the $L_{23}VV$ spectrum, our primary interest is in locating the maximum intensity of the Co $2p_{3/2}$ spectrum, so that peaks (in grey) are fit to create a well-fitting envelope and the relevant BE was measured.

The 3p spectrum is more convoluted than the 2p because the spin-orbit splitting is much smaller (~1eV) so that all of the peaks are mixed together. Once again, we fit as many peaks as necessary to create a well-fitting envelope with no concern regarding the physical meaning of the peaks themselves.

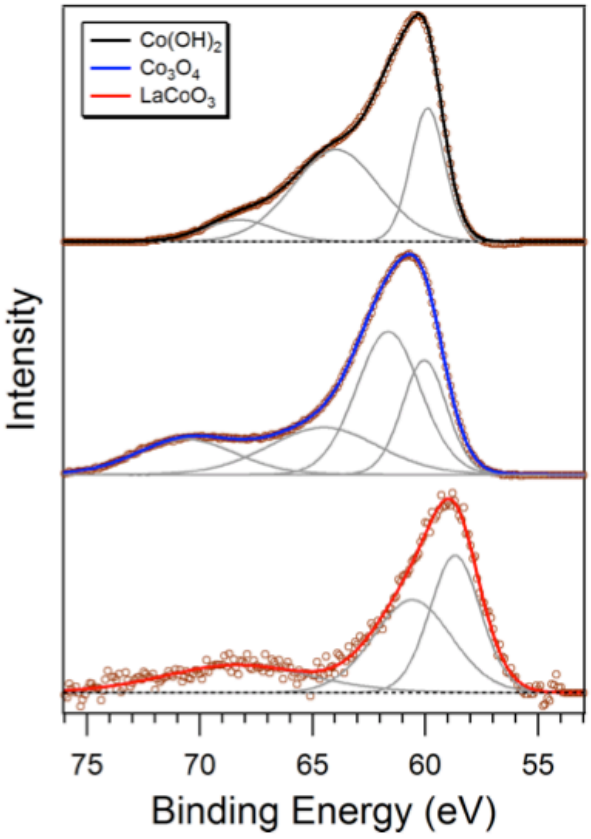

Figure 5.4. Representative Co 3p spectra of different Co oxidation state compounds: $Co(OH)_2$ (black), Co_3O_4 (blue), and $LaCoO_3$ (red). The spin-orbit peaks are too close to be deconvoluted and the spectrum is fit with enough peaks (in grey) to create an envelope that fits the spectrum well. The background is represented by the dotted line.

A summary of the AP data with respect to the 2p and 3p electrons are given in Figure 5.5 and Figure 5.6 in terms of Wagner plot analysis. A Wagner plot is a typical way of displaying AP measurements in which the KE of the Auger peak maximum (left axis) is plotted against the BE of the photoelectron peak maximum (bottom axis). The addition of these two terms gives the AP (right axis), which can be tracked by following the diagonal lines. For example, in Figure 5.5, $NiCo_2O_4$ has its $L_{23}VV$ maximum at 774.3 eV KE and $2p_{3/2}$ maximum at 779.7 eV BE, placing it on the diagonal line that leads to a AP measurement of 1554.0 eV (Co

oxidation states are color-coded as described in the figure caption). We were not able to acquire good XPS data on the LSC *powders* with 10 and 50 mol% Sr doping, and they are therefore omitted.

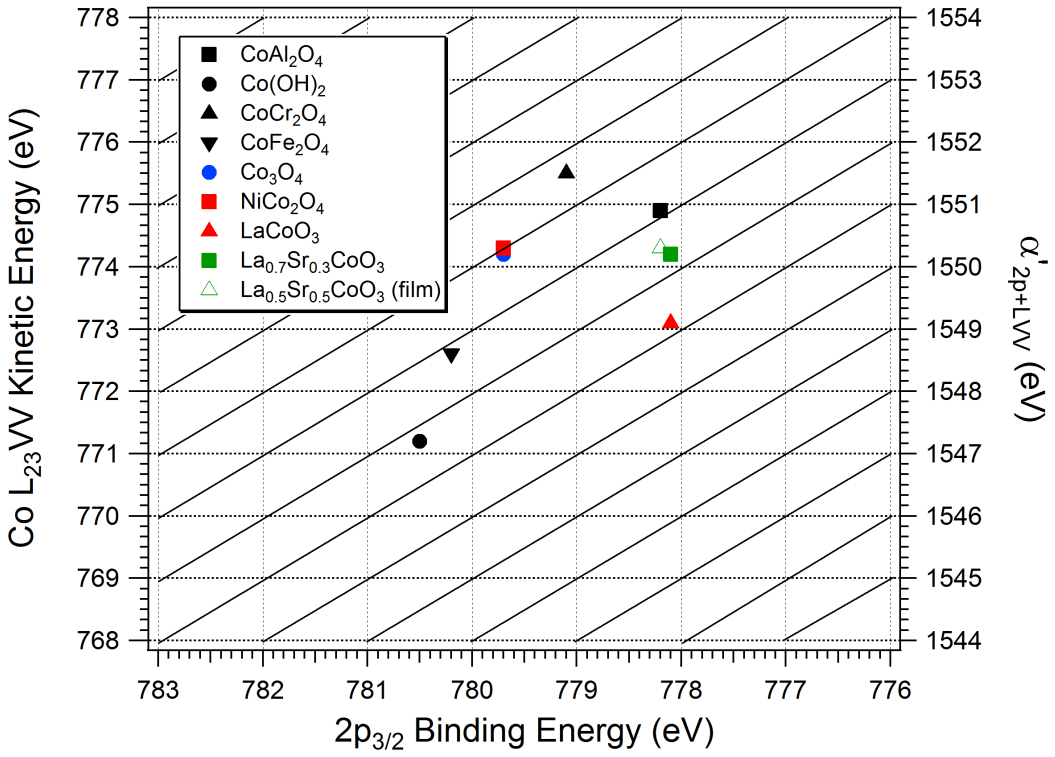

Figure 5.5. Wagner plot of the $L_{23}VV$ Auger electron KE vs. $2p_{3/2}$ BE of Co standards of varying oxidation state: 2+ (black), 2.66+ (blue), 3+ (red), >3+ (green)

The plots show little consistency in the AP values even between compounds of like oxidation state. There is also no clear trend between AP and increasing oxidation state. This lack of correlation may be due to the potential sensitivity of AP to coordination and electronic structure differences (*e.g.* spin state). As can be seen in Figure 5.2 the $L_{23}VV$ peak shape is very different between the three compounds. These types of differences are found between compounds of like oxidation state as well and can largely influence the calculated AP (SI Figure 5.4).

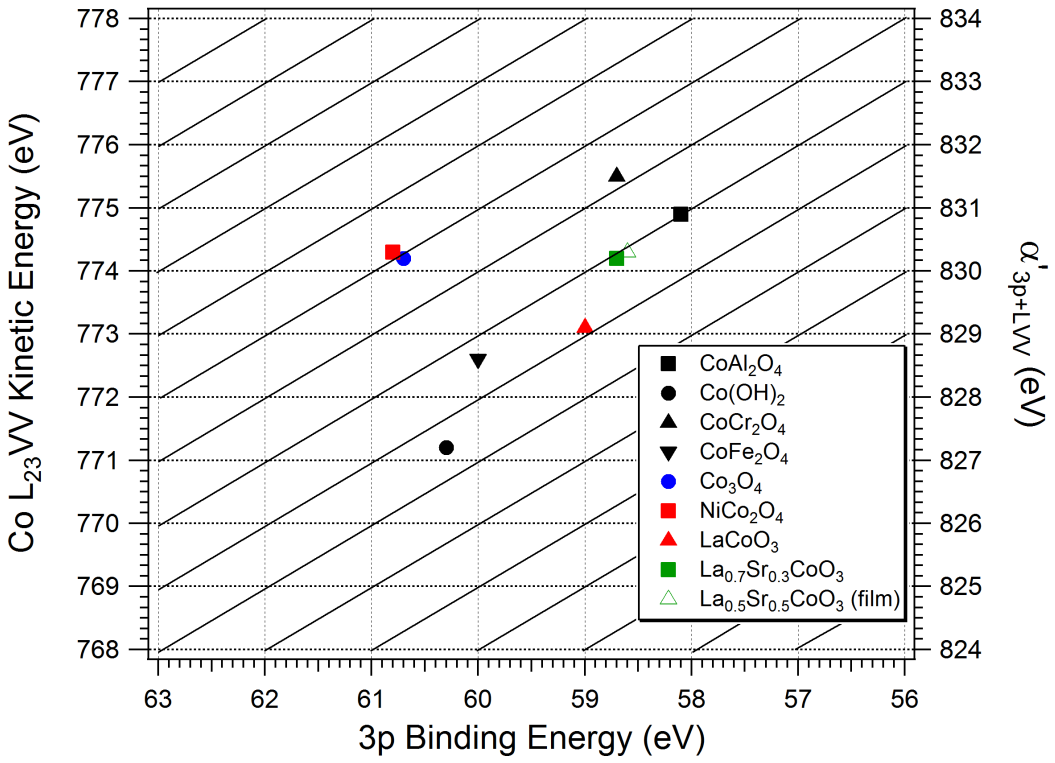

Figure 5.6. Wagner plot of the $L_{23}VV$ Auger electron KE vs. 3p BE of Co standards of varying oxidation state: 2+ (black), 2.66+ (blue), 3+ (red), >3+ (green)

5.3.2 Thermal Redox Tests

5.3.2.1 Thermal Redox Tests of $LaCoO_{3-\partial}$

The $LaCoO_3$ pellet was characterized by using NEXAFS and AP-XPS in different conditions (see Section 5.2.2.2), each giving different Co oxidation states. Evidence of the changing Co oxidation state may be seen in the $L_{2,3}$ edge NEXAFS spectra shown in Figure 5.7. The L_3 edge is located at ~778 eV while the L_2 edge is the less prominent feature at ~795 eV. Over the course of the experiment, the two edges move toward lower energies, signifying reduction[203,270,273] (see Section 1.4.2.1).

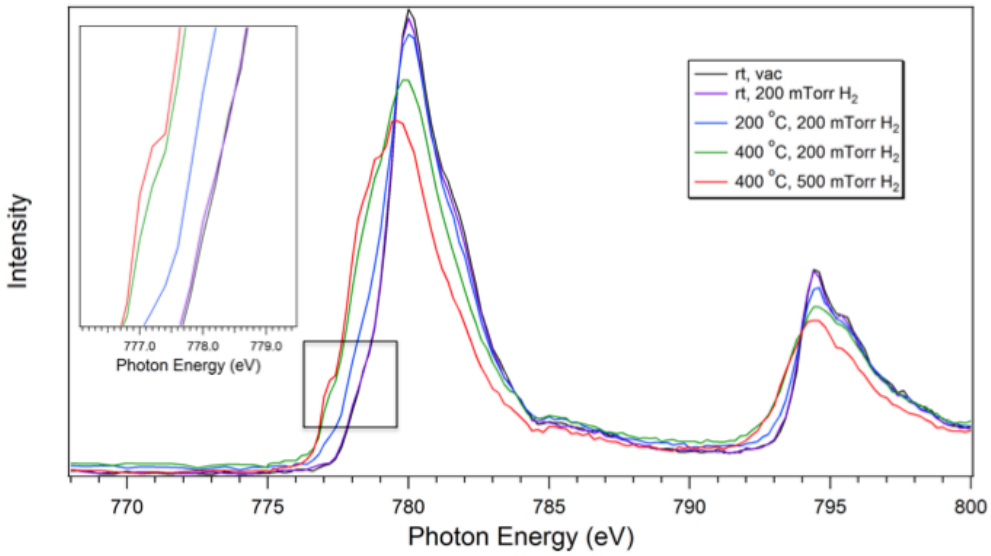

Figure 5.7. Co $L_{2,3}$ edge NEXAFS spectra for $LaCoO_3$ as it transitions between the environments: rt and vacuum (black), rt and 200 mTorr H_2 (purple), 200 ^oC and 200 mTorr H_2 (blue), 400 ^oC and 200 mTorr H_2 (green), and 400 ^oC and 500 mTorr H_2 (red). The inset shows an enlargement of the edge region.

Figure 5.8A shows Co 2p spectra taken at a photon energy of 1000 eV in the two most different conditions: rt and UHV (black) and 400 ^oC and 500 mTorr H_2 (red). Figure 5.8B shows the Co $L_{23}VV$ and 3p spectra under the same two conditions and were collected at 850 eV. At the photon energy of 850 eV, the KE of Co 3p is very close to the Co $L_{23}VV$ peaks, which facilitates the simultaneous collection of both features. However, there is some potential convolution from the Co 3p satellite.

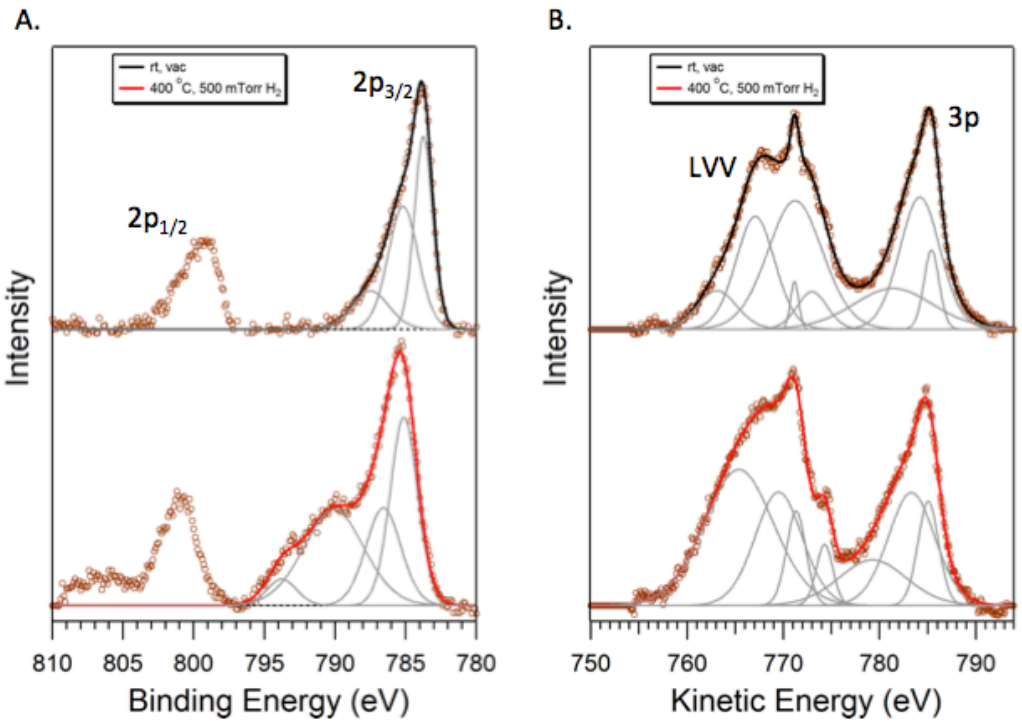

Figure 5.8. Spectra of (A) Co 2p and (B) $L_{23}VV$ and 3p peaks of $LaCoO_3$ under two conditions: rt and UHV (black) and 400 ^{o}C in 500 mTorr H_2 (red).

The $LaCoO_{3-\partial}$ spectra show a larger change in the Co $2p_{3/2}$ BE (from 783.9 eV to 785.1 eV) than the L_3VV peak KE (from 771.1 to 770.7), resulting in a total α'_{2p+LVV} increase from 1555.0 eV to 1556.2 eV as Co is reduced. Furthermore, the satellite typically observed in reduced Co^{2+} high spin compounds is observed in the 500 mTorr H_2 condition.

The potential trend of an increase in α'_{2p+LVV} with an increase in Co reduction is further emphasized in Figure 5.9, which plots α'_{2p+LVV} (black, left axis) as it changes with the increasingly reducing conditions shown in Figure 5.7. However, the α'_{3p+LVV} (red, right axis) shows very little change.

While the α'_{2p+LVV} results are promising, the potential convolution of the LVV peak with the Co 3p satellite could affect the measurements.

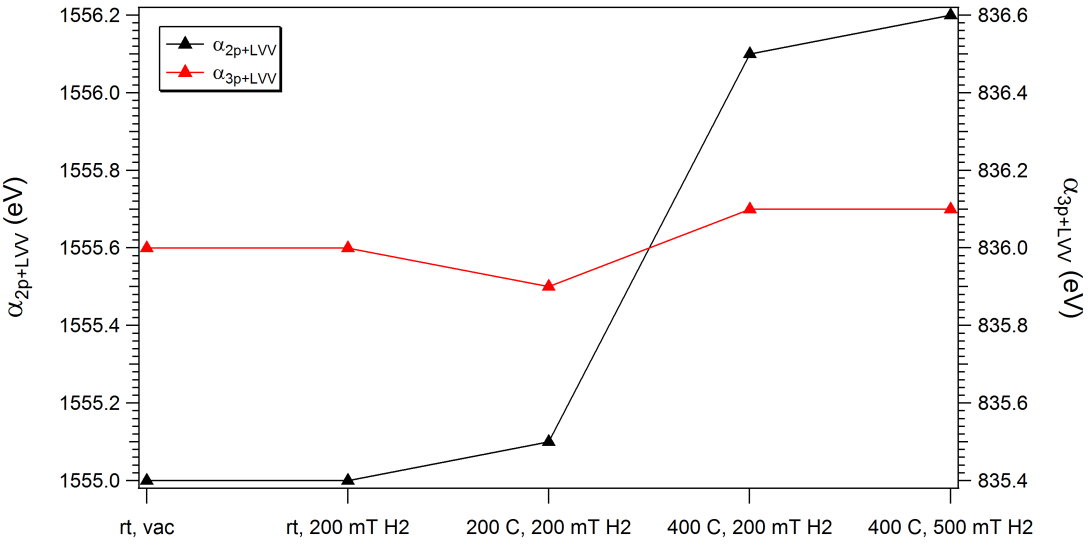

Figure 5.9. Auger parameter changes based on the 2p (black, left axis) and 3p (red, right axis) plotted vs. increasing reducing conditions.

5.3.2.2 LSC Thin Film

The LSC thin film was exposed to different reducing or oxidizing environments (H_2 and O_2, respectively) at different pressures and temperatures (see Section 5.2.2.2). Even in the most reducing and oxidizing conditions (500 mTorr of H_2 or O_2 at the highest temperatures), no changes were observed in the NEXAFS spectra (Figure 5.10) implying that the Co oxidation state was not affected by these different conditions within the sensitivity of our measurements.[203,270,273]

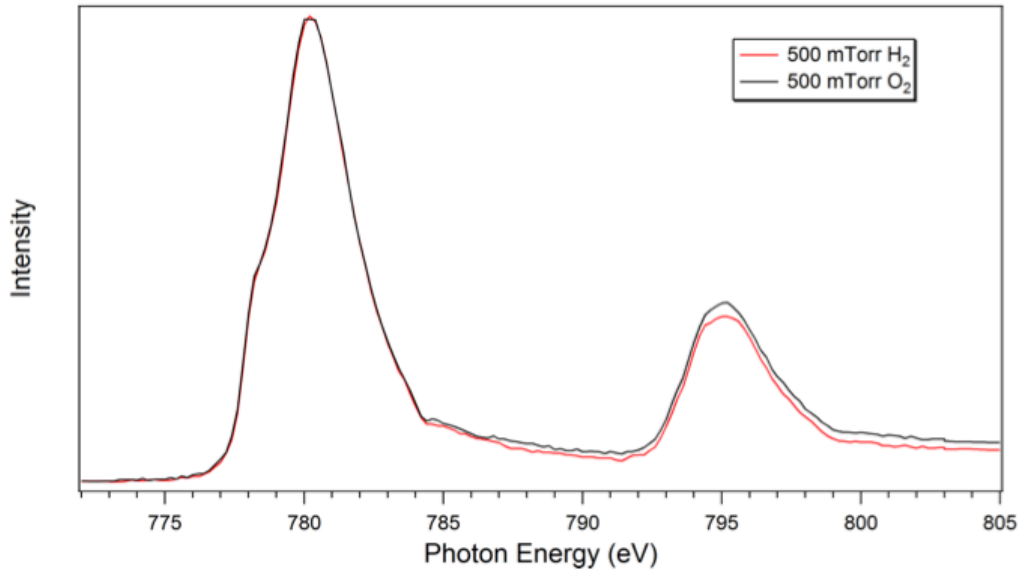

Figure 5.10. NEXAFS $L_{2,3}$ spectra of the LSC thin film in 500 mTorr H_2 (red) and 500 mTorr O_2 (black). The two curves are near superimposable, with no distinct shift in the L_2 edge or peak.

There is also no appreciable change in the α'_{2p+LVV} measurements for LSC in the oxidizing and reducing environments. Figure 5.11 shows spectra collected at a photon energy of 1020 eV of Co 2p (A) and the $L_{2,3}VV$ (B) peaks under 500 mTorr O_2 (black) and 500 mTorr H_2 (red). There is evidence of a Mo impurity in the L_2VV peak region, which shows peaks at KEs of ~785 and ~781 eV. These peaks do not interfere with the primary L_3VV region and the 1020 eV photon energy eliminates potential interference from the Co 3p satellite. However, the two sets of spectra between the two conditions show little-to-no change in the maximum values.

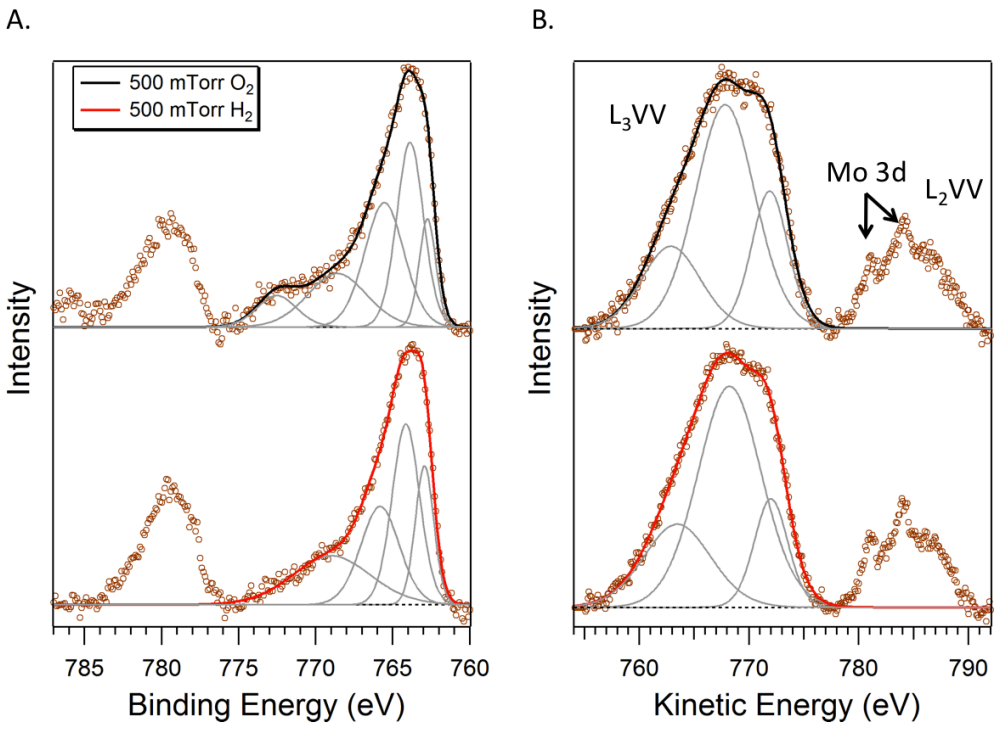

Figure 5.11. Spectra of (A) Co 2p and (B) the $L_{2,3}VV$ peaks of the LSC thin film under two conditions: 500 mTorr O_2 (black) and 500 mTorr H_2 (red). The L_2VV peak region is convoluted with Mo 3d peaks which do not interfere with the primary L_3VV region.

5.4 Conclusion

The AP between the $L_{23}VV$ Auger electrons and the 2p and 3p photoelectrons was measured by XPS for Co standard compounds of well-defined oxidation state. No clear relation between either AP and oxidation state was found among the samples. The lack of correlation is possibly due to differences in lattice structure (*i.e.* bond length) and coordination environments between the samples.

While constructing a calibration curve that is effective for measuring the oxidation state of all Co compounds may be impossible, the AP measured between the $L_{23}VV$ and 2p peaks does show a possible correlation with oxidation state changes within the *same* Co compound. For example, as the Co in $LaCoO_{3-\partial}$ was

reduced, the AP increased. Further studies are necessary to verify the feasibility of tracking and quantifying oxidation states with the AP in an operating SOC.

5.5 Supporting Information

5.5.1 Auger Parameter and Extra Atomic Relaxation Energy

The AP is related to an atom's environment via the "extra-atomic relaxation" energy of an atom. As stated in Section 1.4.1.4, this energy describes neighboring atom electrons relaxing to screen the core-hole that results from primary photoelectron emission. Extra atomic relaxation is dependent on a species' environment and oxidation state. While a full derivation is not presented here (see Ref. 191), shifts in the AP can be correlated to changes in the extra-atomic relaxation energy by noting the changes that occur with regard to the photoelectron BE and Auger electron KE when a free atom becomes part of a solid compound:

$$\Delta BE_{\text{photo e- (free atom}\rightarrow\text{ solid compound)}} = -R_{ea} + \Delta E_e \qquad \textbf{(Eq. 5.5)}$$

$$\Delta KE_{\text{Auger e- (free atom}\rightarrow\text{ solid compound)}} = 3R_{ea} - \Delta E_e \qquad \textbf{(Eq. 5.6)}$$

where R_{ea} is the extra atomic relaxation energy and ΔE_e is the change in the Hartree-Fock calculated energy of an electron in a solid compound (see Section 1.4.1.4). In turn, these two quantities change the BE of the core electron compared to its free atom value. By combining Eqs. 5.2, 5.5, and 5.6:

$$\Delta\alpha'_{\text{(free atom}\rightarrow\text{ solid compound)}} = +2R_{ea} \qquad \textbf{(Eq. 5.7)}$$

meaning that if a free atom is incorporated into a solid, the AP will shift by twice the extra atomic relaxation energy. If the atom transitions from one bonding environment to another (*e.g.* a metal is reduced), the R_{ea} will likely change, resulting in a further change in AP that can be calculated with Eq. 5.4.

5.5.2 NEXAFS Scans of Co Standards

Below are NEXAFS $L_{2,3}$ edge spectra for the Co standards. The L_3 and L_2 edges are located at ~778 eV and ~795 eV, respectively.

SI Figure 5.1 shows the $L_{2,3}$ edge spectra of Co^{2+} compounds, $Co(OH)_2$ (black), $CoFe_2O_4$ (red), $CoAl_2O_4$ (blue), and $CoCr_2O_4$ (green). $Co(OH)_2$ and $CoFe_2O_4$ display an extra feature at 777 eV that is observed only in Co^{2+} centers in an octahedral environment,[271,272,286] whereas the $CoAl_2O_4$ and $CoCr_2O_4$ show evidence of a tetrahedral environment. These results are in agreement with the co-ordinations provided in Table 5.1.

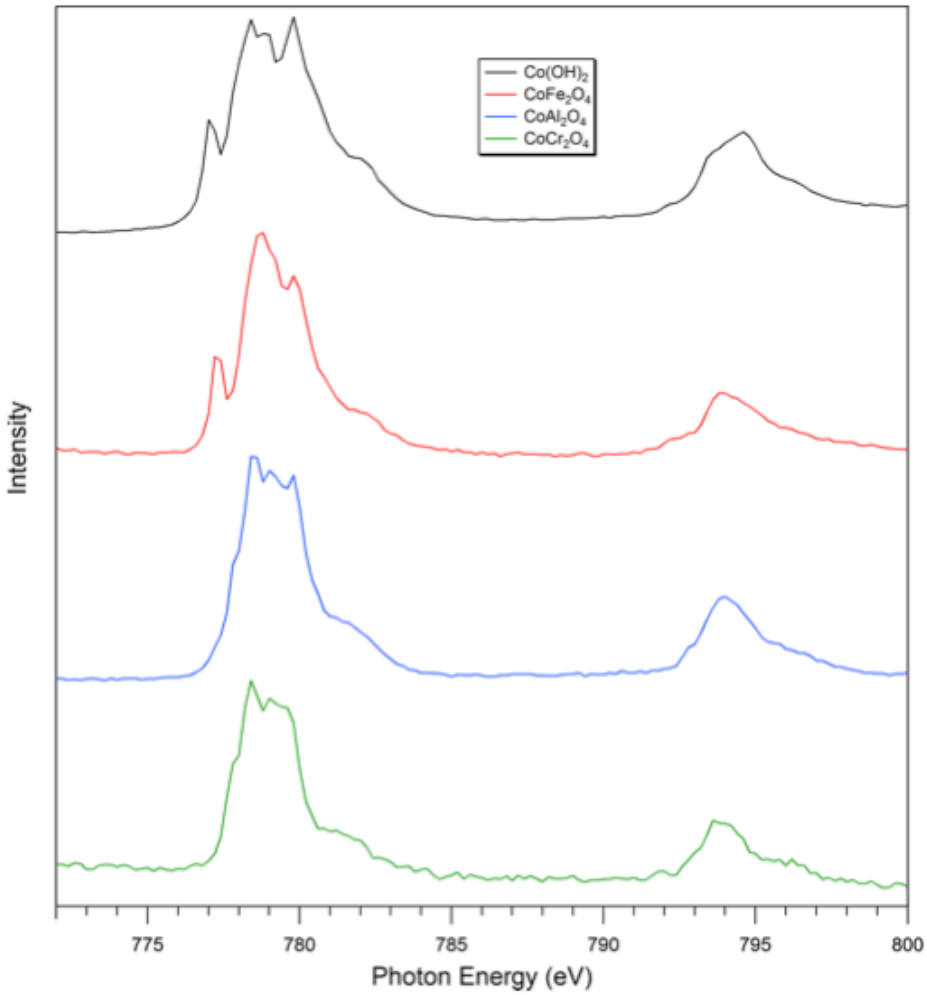

SI Figure 5.1. Co $L_{2,3}$ edge spectra of Co^{2+} compounds: $Co(OH)_2$ (black), $CoFe_2O_4$ (red), $CoAl_2O_4$ (blue), and $CoCr_2O_4$ (green). The feature at 777 eV in $Co(OH)_2$ and $CoFe_2O_4$ is indicative of an octahedral environment.

SI Figure 5.2 shows Co $L_{2,3}$ edge spectra of a $Co^{2.66+}$ compound (Co_3O_4, black) and Co^{3+} compounds, $NiCo_2O_4$ (red), and $LaCoO_3$ (blue). $NiCo_2O_4$ displays an extra feature compared to $LaCoO_3$ at 778.4 eV indicating that it is a high-spin complex.[293]

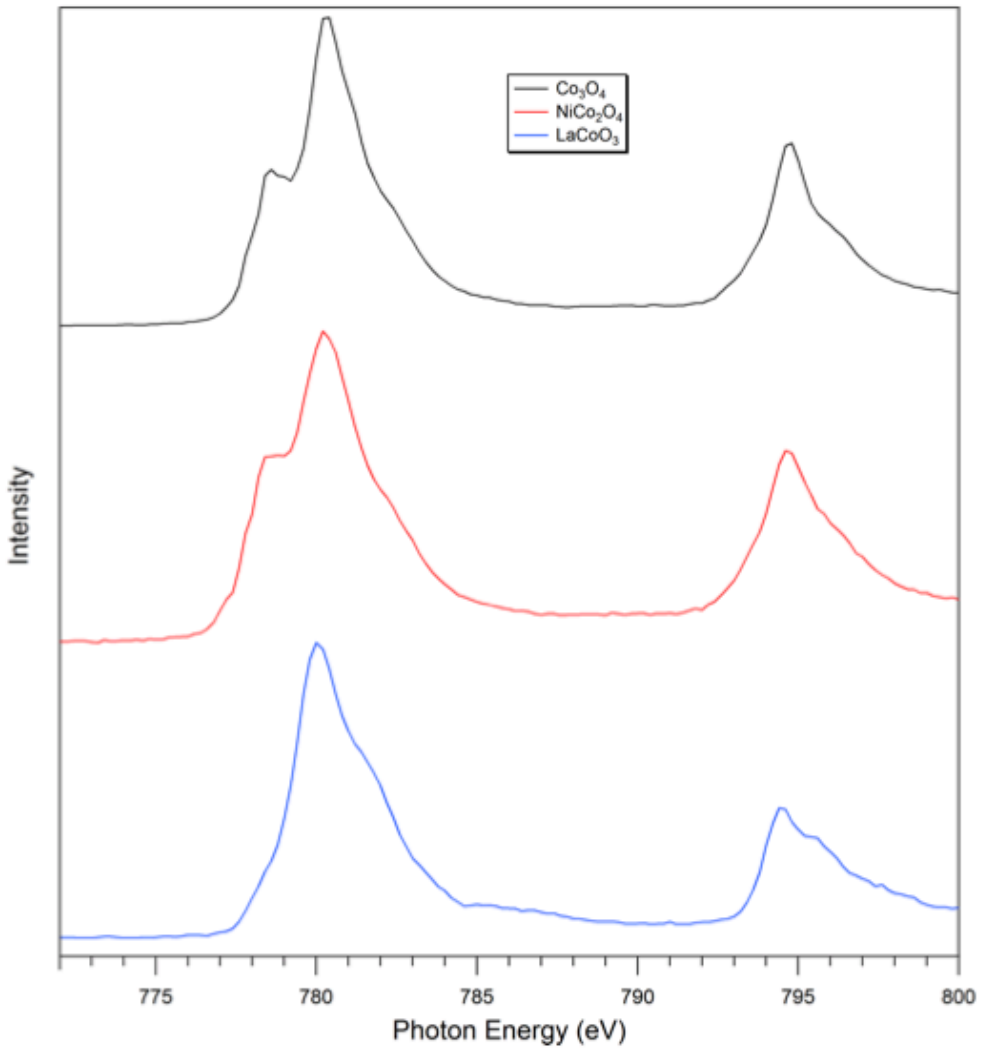

SI Figure 5.2. Co $L_{2,3}$ edge spectra of $Co^{2.66+}$ and Co^{3+} compounds: Co_3O_4 (black), $NiCo_2O_4$ (red), and $LaCoO_3$ (blue). The feature at 778.4 eV in $NiCo_2O_4$ is indicative of a high-spin complex.

SI Figure 5.3 shows the $L_{2,3}$ spectra of three LSC compounds with different Sr doping levels: $La_{0.9}Sr_{0.1}CoO_3$ (black), $La_{0.7}Sr_{0.3}CoO_3$ (red), and $La_{0.5}Sr_{0.5}CoO_3$ (blue). Spectra were normalized to the pre-edge background. As the Sr content increases, the Co oxidation state and edge energy increases as well (see inset for edge region enlargement).

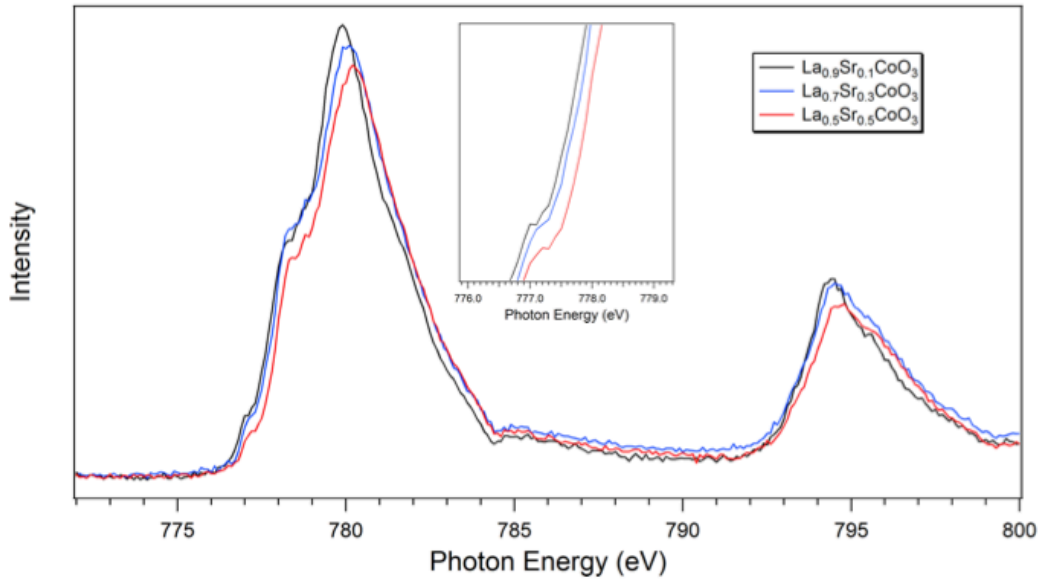

SI Figure 5.3. Co $L_{2,3}$ edge spectra of three LSC compounds: $La_{0.9}Sr_{0.1}CoO_3$ (black), $La_{0.7}Sr_{0.3}CoO_3$ (red), and $La_{0.5}Sr_{0.5}CoO_3$ (blue). The edge increases as Co oxidation state increases as can be seen in the inset which provide an enlargement of the edge region.

5.5.3 L_3VV spectra of Co^{2+} compounds

SI Figure 5.4 shows the L_3VV spectra of three Co^{2+} compounds, $Co(OH)_2$ (black), $CoAl_2O_4$ (blue), and $CoCr_2O_4$ (red). Spectra have all been calibrated with a C 1s peak (284.8 eV)[186] to help show the differences. The $CoAl_2O_4$ spectrum has a slight right hump relative to $Co(OH)_2$, while the $CoCr_2O_4$ spectrum exhibits a clear difference in shape, potentially due to structural differences.

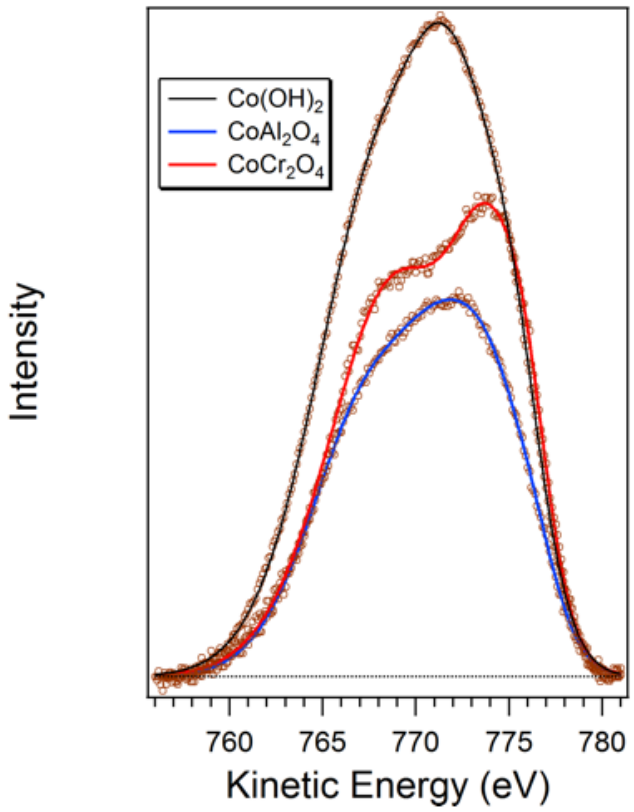

SI Figure 5.4. Co L_3VV spectra of Co^{2+} compounds: $Co(OH)_2$ (black), $CoAl_2O_4$ (blue), and $CoCr_2O_4$ (red).

6 Summary and Future Work

6.1 Introduction

The work presented in this dissertation focused on the development of *in operando* protocols and utilizing those protocols to elucidate mechanistic details behind solid oxide electrochemical cell (SOC) processes. Ambient pressure X-ray photoelectron spectroscopy (AP-XPS) was used to study the oxygen reduction reaction (ORR) and oxygen evolution reaction (OER) on the surface of the commonly used electrode, lanthanum strontium manganite (LSM). We further contrasted the behavior between LSM and a composite material made of LSM and yttria-stabilized zirconia (LSM/YSZ) toward thermal oxygen exchange. A method for measuring Co oxidation with AP-XPS in a promising cathode material, lanthanum strontium cobaltite (LSC), was also explored. Lastly, a technique for tracking Ce oxidation states and electrochemically active regions in ceria, another commonly used SOC material, with a near infrared (NIR) imaging camera was developed.

6.2 Summary of Major Results

6.2.1 Sr Surface Speciation and Mn Oxidation States

LSM ($La_{1-x}Sr_xMnO_{3\pm\delta}$) thin films were studied with AP-XPS in a 200 mTorr O_2 environment at temperatures ranging from 530 ^oC to 680 ^oC. Under open circuit voltage (OCV) conditions, Mn is more reduced toward the upper region of the surface, and Sr segregates to the surface predominantly as extruded SrO particles that lie on top of the electrode. Presumably, the Sr which remains in the upper LSM lattice surface exists in a Ruddlesden-Popper (RP) phase which may

partially account for the reduced Mn. The other influencing factor on Mn surface reduction is the generation of oxygen vacancies.

A cathodic bias induces further reduction of Mn (oxygen vacancy generation) and extrusion of SrO, while an anodic bias induces Mn oxidation (oxygen vacancy loss), but an ambiguous degree of SrO growth. These results imply that oxygen vacancies play a role in SrO surface extrusion.

Our spatially-resolved XPS measurements show that these phenomena occur throughout the LSM surface not in any specific region.

6.2.2 Electrochemically Active Regions and Voltage Drops on LSM Electrodes

The surface potentials between the two LSM electrodes (cathode and anode) under polarization were measured and potential drops were found, localized to the electrode/electrolyte interface. This result provides what we believe to be the first *in operando* spectroscopic evidence that all electrochemical activity occurs at the triple phase boundary (TPB), *i.e.* that LSM in these conditions behaves as an electronic conductor. The result is supported by spatially resolved Mn oxidation state data which shows electrons are conducted throughout the LSM electrodes in the form of either Mn reduction (cathode) or oxidation (anode).

Furthermore, a lower potential drop (and associated resistance) was observed on the LSM cathode compared to the LSM anode, demonstrating that LSM is a superior electrocatalyst for ORR promotion.

6.2.3 Vacancy Formation in LSM and LSM/YSZ Composites

In situ thermal AP-XPS studies were performed on LSM and LSM/YSZ powder-based samples. The samples were exposed to different combinations of O_2, H_2O, and CO_2 gases at temperatures ranging from 400 ^oC to 600 ^oC in analogy to bulk oxygen exchange studies conducted by Wachsman *et al.*[42,249] The LSM/YSZ composite consistently exhibited a larger concentration of surface oxygen vacancies, promoting the more facile exchange of oxygen observed on the composite relative to LSM in the bulk oxygen exchange studies.

6.2.4 Measuring Surface Co Oxidation States with the Auger Parameter

The Auger parameter (AP) between $L_{23}VV$ Auger electrons and 2p photoelectrons is shown to have potential use as a Co oxidation state probe of operating LSC electrodes. The AP of a $LaCoO_{3-\delta}$ sample was measured with AP-XPS, *in situ*, in different reducing environments (varied by temperature and H_2 pressure). The AP increased as Co reduction was increased, as corroborated by near edge X-ray absorption fine structure (NEXAFS) measurements.

6.2.5 Using a NIR Imaging Camera for Ce Oxidation State Tracking

A SOC with ceria (CeO_{2-x}) electrodes was fabricated based on prior AP-XPS research[23-27] and studied with a NIR imaging camera in true ambient, operating conditions that were analogous to the model conditions in AP-XPS experiments. Electrochemically active regions, signified by a reduction of Ce, were observed with NIR imaging that were commensurate with those found in AP-XPS studies. These observations support the use of a simple, accessible NIR imaging tool to track SOC activity, *in operando*, while bridging the gap between the model

conditions used in AP-XPS experiments, and more realistic conditions that are accessible with NIR imaging techniques.

6.3 Future Work

6.3.1 Further ORR and OER studies on LSM-Based Materials

While extensive *in operando* AP-XPS studies were conducted on a pure LSM electrode, the research on LSM/YSZ composites in this work was limited to *in situ*, thermal studies. Because LSM/YSZ is considered to behave closer to a mixed ionic/electronic conductor (MIEC) than pure LSM, the identification of electrochemically active regions and resistances to ORR and OER would be very useful for comparing and contrasting the composite's electrocatalytic ability with that of pure LSM. We showed that LSM/YSZ exhibits a larger concentration of surface oxygen vacancies than pure LSM under OCV conditions, but how these vacancies will factor into the composite's electrochemical activity under polarization remains unknown. These experiments can be further bolstered by *in operando* isotopic exchange experiments, as *in situ* experiments have yielded great insight on the thermal behavior of LSM and LSM/YSZ composites.

Additionally, OER on LSM-based materials should be of particular focus as there is a scarcity of *in operando* research in comparison with ORR studies, especially using spectroscopic tools (as stated previously, Yildiz *et al.*[175] appear to have published the only work of such nature). There is particular interest in the degradation of LSM performance over long-term anodic polarization. This "deactivation effect" has been suggested to occur by several processes including, delamination (the cause of which is uncertain),[177,294] a disintegration of LSM at the

interface,[176] or the formation of $La_2Zr_2O_7$ resistive phases.[178] However, these possibilities are currently only supported by *ex situ* characterizations. AP-XPS measurements are more accurate and can parse any of the proposed deactivation origins, as surface phenomena such as, changes in the interface surface chemistry or resistive phase formation, are potentially observable.

Lastly, in order to provide stronger evidence in support of the Sr-enriched RP phase formation in the LSM surface at lower temperatures, and disappearance of these RP phases at higher temperatures, *in operando* extended X-ray absorption fine structure (EXAFS) measurements should be taken on the LSM cells used in this work. The EXAFS will allow for assessment of Sr coordination environments of Sr and the relative importance of RP phases in the reduction of Mn compared to oxygen vacancy formation.

6.3.2 Auger Parameter and Potential Mapping on LSC

AP measurements have demonstrated potential for the quantification of Co surface oxidation states in LSC electrodes. However, in order to develop a meaningful calibration curve to compare Co oxidation states with the AP, Co standards within the same basic perovskite structure must be used, *i.e.* the standards should not be varied in structure (*e.g.* spinel vs. perovskite) or chemical composition (*e.g.* $CoAl_2O_4$ vs. $LaCoO_3$). This curve may be obtained by preparing LSC compounds of different Sr doping levels (to a more varied degree than those presented in Chapter 5), and running thermogravimetric analysis (TGA) characterizations on them. By determining the oxygen content of these samples at

different temperatures, and then mimicking those temperatures in an XPS set-up, a reliable calibration curve may be achievable.

Even if the AP can only be reliably used to qualitatively measure changes in Co oxidation states, *in operando* studies on LSC electrodes, in line with those performed on LSM, should be conducted. To the best of our knowledge, surface potentials have not been mapped on these materials, nor has there been any *in operando* XPS work done regarding OER performance in LSC. Identifying active regions, even if only by qualitative Co oxidation measurements and surface potential mapping, would prove invaluable toward understanding LSC behavior.

6.3.3 Co-Electrolysis of H_2O and CO_2

High temperature electrochemical syn-gas formation (a combination of H_2 and CO gases) from H_2O/CO_2 co-electrolysis is one of the most efficient means of synthetic fuel formation when run in a SOC, in theory.[295] Because of our extensive AP-XPS studies on independent SOC electrolysis reactions of water and CO_2,[23-27] we are poised to make important mechanistic contributions to the field of H_2O/CO_2 co-electrolysis. For example, it is possible that formates, bicarbonates, and other H-C-O molecular intermediates are formed during co-electrolysis that are excluded from the individual electrolysis reactions. AP-XPS can be used to identify these intermediates, and what conditions result in their formation.

Furthermore, the surface potential measurement technique can also shed light on the co-electrolysis mechanism. For example, water has been shown to be easier to reduce than CO_2 in Ni/YSZ systems despite the very similar thermodynamics of each individual reduction. Mechanistically, it is assumed that

water has a lower overpotential for electrolysis although there is currently no direct spectroscopic data to evaluate this theory.

6.3.4 Sulfur Batteries

While SOCs are an important developing technology to meet society's expanding energy storage and utilization needs, next generation batteries are also critical. However, the mechanisms behind battery operation are not well-understood. XPS measurements are precluded by the vapor pressures resulting from liquid electrolytes typically employed in these electrochemical systems. Furthermore, studying an electrode/electrolyte interface with a liquid electrolyte is not achievable with the majority of AP-XPS stations currently available. However, with the advent of "tender" X-rays (photon energies of 3000 ~ 5000 eV), these issues can be circumvented, and developing battery technologies can be better studied. For example, in collaboration with Dr. Chunshen Wang's group at the University of Maryland, new carbon/sulfur cathode-based batteries have been developed[296] that exhibit remarkable stability (near 100% capacity retained over 4000 cycles and 2+ years), but the fundamental chemistry behind their operation remains unknown.

Preliminary *ex-situ* XPS experiments suggest that the cycling stability of the electrode is due to an extremely electron-rich sulfur species that is present in the discharged electrode, but is not present in the charged electrode.[296] With tender X-ray experiments, the formation and disappearance of this electron rich sulfide during charge and discharge processes can be observed. In addition, the electrochemically active and inactive components of the electrode that are

reversibly interconverted with charge and discharge (*e.g.* $S_2 + 4e^- \rightleftharpoons 2S^{2-}$) can be separated, via surface potential measurements.

References

(1) Saunders, P.; White, D. R. *Int. J. Thermophys.* **2010**, *31* (8-9), 1583.

(2) Kan, C. C.; Kan, H. H.; Van Assche, F. M.; Armstrong, E. N.; Wachsman, E. D. *J. Electrochem. Soc.* **2008**, *155* (10), B985.

(3) Binet, C.; Daturi, M.; Lavalley, J. C. *Catal. Today* **1999**, *50*, 207.

(4) Wang, H.; Keum, J. K.; Hiltner, A.; Baer, E.; Freeman, B.; Rozanski, A.; Galeski, A. *Science* **2009**, *323* (5915), 757.

(5) Co, A. C.; Xia, S. J.; Birss, V. I. *J. Electrochem. Soc.* **2005**, *152* (3), A570.

(6) Pomfret, M. B.; Owrutsky, J. C.; Walker, R. A. *Annu. Rev. Anal. Chem.* **2010**, *3* (1), 151.

(7) Ormerod, R. M. *Chem. Soc. Rev.* **2002**, *32* (1), 17.

(8) Lu, X.; Faguy, P. W.; Liu, M. *J. Electrochem. Soc* **2002**, *149* (10), A1293.

(9) Sum, O. S. N.; Djurado, E.; Pagnier, T.; Rosman, N.; Roux, C.; Siebert, E. *Solid State Ionics* **2005**, *176* (35-36), 2599.

(10) Schlogl, R. *Handbook of Heterogeneous Catalysis*; Ertl, G., Knozinger, H., Schuth, F., Weitkamp, J., Eds.; Wiley-VCH: Weinheim, 2008.

(11) *Industrial Applications of Homogenious Catalysis*; D. Reidel Publishing Company: Dordrecht, 1988.

(12) Bertleff, W. *Ullmann's Encyclopedia of Industrial Chemistry*; Wiley-VCH: Weinheim, 2000.

(13) Caillol, N.; Pijolat, M.; Siebert, E. *Appl. Surf. Sci.* **2007**, *253* (10), 4641.

(14) Mizusaki, J. *Solid State Ionics* **2000**, *129* (1-4), 163.

(15) Jiang, S.; Wang, W. *Solid State Ionics* **2005**, *176* (13-14), 1185.

(16) Murray, E. P.; Barnett, S. A. *Solid State Ionics* **2001**, *143* (3-4), 265.

(17) Wang, W.; Jiang, S. P. *Solid State Ionics* **2006**, *177* (15-16), 1361.

(18) Mogensen, M.; Skaarup, S. *Solid State Ionics* **1996**, *86-8*, 1151.

(19) Fleig, J. R. *Phys. Chem. Chem. Phys.* **2005**, *7* (9), 2027.

(20) Fleig, J.; Kim, H. R.; Jamnik, J.; Maier, J. *Fuel Cells* **2008**, *8* (5), 330.

(21) Adler, S. B. *Chem. Rev.* **2004**, *104*, 4791.

(22) Wang, W.; Huang, Y.; Jung, S.; Vohs, J. M.; Gorte, R. J. *J. Electrochem. Soc.* **2006**, *153* (11), A2066.

(23) Yu, Y.; Mao, B.; Geller, A.; Chang, R.; Gaskell, K.; Liu, Z.; Eichhorn, B. W. *Phys. Chem. Chem. Phys.* **2014**, *16* (23), 11633.

(24) Yu, Y.; Geller, A.; Mao, B.; Chang, R.; Liu, Z.; Eichhorn, B. W. *ECS Trans.* **2013**, *57* (1), 3119.

(25) Zhang, C.; Yu, Y.; Grass, M. E.; Dejoie, C.; Ding, W.; Gaskell, K.; Jabeen, N.; Hong, Y. P.; Shavorskiy, A.; Bluhm, H.; Li, W.-X.; Jackson, G. S.; Hussain, Z.; Liu, Z.; Eichhorn, B. W. *J. Am. Chem. Soc.* **2013**, 11572.

(26) Zhang, C.; Grass, M. E.; Mcdaniel, A. H.; Decaluwe, S. C.; Gabaly, F. E.; Liu, Z.; Mccarty, K. F.; Farrow, R. L.; Linne, M. A.; Hussain, Z.; Jackson, G. S.; Bluhm, H.; Eichhorn, B. W. *Nature Mater.* **2010**, *9* (11), 944.

(27) Zhang, C.; Grass, M. E.; Yu, Y.; Gaskell, K. J.; Decaluwe, S. C.; Chang, R.; Jackson, G. S.; Hussain, Z.; Bluhm, H.; Eichhorn, B. W.; Liu, Z. *ACS*

Catal. **2012**, *2* (11), 2297.

(28) Crumlin, E. J.; Mutoro, E.; Hong, W. T.; Biegalski, M. D.; Christen, H. M.; Liu, Z.; Bluhm, H.; Shao-Horn, Y. *J. Phys. Chem. C* **2013**, *117* (31), 16087.

(29) Nenning, A.; Opitz, A. K.; Rameshan, C.; Rameshan, R.; Blume, R.; Hävecker, M.; Knop-Gericke, A.; Rupprechter, G.; Klötzer, B.; Fleig, J. *J. Phys. Chem. C* **2016**, *120* (3), 1461.

(30) Pomfret, M. B.; Steinhurst, D. A.; Owrutsky, J. C. *Energy Fuels* **2011**, *25* (6), 2633.

(31) Eigenbrodt, B. C.; Pomfret, M. B.; Steinhurst, D. A.; Owrutsky, J. C.; Walker, R. A. *J. Phys. Chem. C* **2011**, *115* (6), 2895.

(32) Pomfret, M. B.; Steinhurst, D. A.; Kidwell, D. A.; Owrutsky, J. C. *J. Power Sources* **2010**, *195* (1), 257.

(33) Brett, D. J. L.; Aguiar, P.; Clague, R.; Marquis, A. J.; Schöttl, S.; Simpson, R.; Brandon, N. P. *J. Power Sources* **2007**, *166* (1), 112.

(34) Ju, G.; Reifsnider, K.; Huang, X. *J. Fuel Cell Sci. Technol.* **2008**, *5* (3), 031006.

(35) Cumming, D. J.; Elder, R. H. *J. Power Sources* **2015**, *280* (C), 387.

(36) Robinson, J. B.; Brown, L. D.; Jervis, R.; Taiwo, O. O.; Millichamp, J.; Mason, T. J.; Neville, T. P.; Eastwood, D. S.; Reinhard, C.; Lee, P. D.; Brett, D. J. L.; Shearing, P. R. *J. Synchrotron Rad.* **2014**, *21*, 1134.

(37) Guo, H.; Wang, M.; Liu, J.; Nie, Z.; Ye, F.; Ma, C. *J. Power Sources* **2015**, *273*, 775.

(38) Geller, A.; Pomfret, M.; Steinhurst, D. A.; Yu, Y.; Liu, Z.; Owrutsky, J. C.; Eichhorn, B. W. *ChemElectroChem* **2015**, *2* (10), 1527.

(39) Kan, C. C.; Wachsman, E. D. *J. Electrochem. Soc.* **2009**, *156* (6), B695.

(40) Kan, C. C.; Wachsman, E. D. *Solid State Ionics* **2010**, *181* (5-7), 338.

(41) Armstrong, E. N.; Duncan, K. L.; Oh, D. J.; Weaver, J. F.; Wachsman, E. D. *J. Electrochem. Soc.* **2011**, *158* (5), B492.

(42) Huang, Y. L.; Pellegrinelli, C.; Wachsman, E. D. *J. Electrochem. Soc.* **2016**, *163* (3), F171.

(43) Sun, C.; Stimming, U. *J. Power Sources* **2007**, *171* (2), 247.

(44) EG&G Technical Services, Inc. *Fuel Cell Handbook*, 7 ed.; US Department of Energy: Morgantown, 2004; pp 1–427.

(45) Atkinson, A.; Barnett, S.; Gorte, R. J.; Irvine, J. T. S.; McEvoy, A. J.; Mogensen, M.; Singhal, S. C.; Vohs, J. *Nat. Mater.* **2004**, *3*, 17.

(46) Wachsman, E. D.; Lee, K. T. *Science* **2011**, *334* (6058), 935.

(47) Brett, D. J. L.; Atkinson, A.; Brandon, N. P.; Skinner, S. J. *Chem. Soc. Rev.* **2008**, *37* (8), 1568.

(48) Flipsen, S. F. J. *J. Power Sources* **2006**, *162* (2), 927.

(49) Park, S. D.; Vohs, J. M.; Gorte, R. J. *Nature* **2000**, *404* (6775), 265.

(50) Murray, E. P.; Tsai, T.; Barnett, S. A. *Nature* **1999**, *400* (6745), 649.

(51) Kishimoto, H.; Yamaji, K.; Horita, T.; Xiong, Y.; Sakai, N.; Brito, M. E.; Yokokawa, H. *J. Power Sources* **2007**, *172* (1), 67.

(52) Sumi, H.; Ukai, K.; Mizutani, Y.; Mori, H.; WEN, C.; Takahashi, H.; Yamamato, O. *Solid State Ionics* **2004**, *174* (1-4), 151.

(53) Taroco, H. A.; Santos, J. A. F.; Domingues, R. Z. *Advances in Ceramics - Synthesis and Characterization, Processing and Specific Applications*; Sikalidis, C., Ed.; InTech: Rijeka, 2011; pp 1–532.

(54) Lashtabeg, A.; Skinner, S. J. *J. Mater. Chem.* **2006**, *16* (31), 3161.

(55) *High temperature solid oxide fuel cells: fundamentals, design, and applications*; Singhal, S. C., Kendall, K., Eds.; Elsevier Science Ltd: Oxford, 2003.

(56) Jacobson, A. J. *Chem. Mater.* **2010**, *22* (3), 660.

(57) Badwal, S. *Solid State Ionics* **2001**, *143* (1), 39.

(58) Fergus, J. W. *J. Power Sources* **2006**, *162* (1), 30.

(59) Moon, P. K.; Tuller, H. L. *Solid State Ionics* **1988**, *28-30* (PART 1), 470.

(60) Abraham, F.; Boivin, J. C.; Mairesse, G.; Nowogrocki, G. *Solid State Ionics* **1990**, *40-1*, 934.

(61) Navrotsky, A. *J. Mater. Chem.* **2005**, *15* (19), 1883.

(62) Choudhary, C. B.; Maiti, H. S.; Subbarao, E. C. *Solid Electrolytes and their Applications*; Subbarao, E. C., Ed.; Plenum Press: New York, 1980.

(63) Shannon, R. D. *Acta Crystallographica Section A* **1976**, *32* (5), 751.

(64) Grolig, J. G.; Froitzheim, J.; Svensson, J. E. *J. Power Sources* **2014**, *248*, 1007.

(65) Yang, Z.; Xia, G.; Wang, C. M.; Nie, Z.; Templeton, J. D.; Singh, P.; Stevenson, J. W. *Investigation of AISI 441 Ferritic Stainless Steel and Development of Spinel Coatings for SOFC Interconnect Applications*; 2008.

(66) Molin, S.; Kusz, B.; Gazda, M.; Jasinski, P. *J. Solid State Electrochem.* **2009**, *13* (11), 1695.

(67) Mogensen, M.; Sammes, N. M.; Tompsett, G. A. *Solid State Ionics* **2000**, *129* (1-4), 63.

(68) Seo, D. J.; Ryu, K. O.; Park, S. B.; Kim, K. Y.; Song, R. H. *Materials Research Bulletin* **2006**, *41* (2), 359.

(69) Kharton, V. V.; Marques, F.; Atkinson, A. *Solid State Ionics* **2004**, *174* (1-4), 135.

(70) Dalslet, B.; Blennow, P.; Hendriksen, P. V.; Bonanos, N.; Lybye, D.; Mogensen, M. *J. Solid State Electrochem.* **2006**, *10* (8), 547.

(71) Nesaraj, A. S. *J. Sci. Ind. Res.* **2010**, *69* (3), 169.

(72) Fleig, J. *Annu. Rev. Mater. Res.* **2003**, *33* (1), 361.

(73) Mobius, H. *J Solid State Electrochem* **1997**, *1*, 2.

(74) Mizusaki, J.; Amano, K.; Yamauchi, S.; Fueki, K. *Solid State Ionics* **1987**, *22*, 313.

(75) Verkerk, M. J.; Hammink, M. W. J.; Burggraaf, A. J. *J. Electrochem. Soc.* **1983**, *130*, 70.

(76) Takahashi, T.; Iwahura, H.; Suzuki, Y. *Electrode Materials for High-Temperature Solid Electrolyte Fuel Cells*; Proceedings of the Third International Symposium on Fuel Cells, 1969; pp 113–119.

(77) Minh, N. *J. of Am. Ceram. Soc.* **1993**, *76* (3), 563.

(78) Button, D.; Archer, D. *J. Am. Ceram. Soc.* **1966**.

(79) Belardi, R.-M.; Deseure, J.; Brant, M. C.; Matencio, T.; Domingues, R.

Z. *Ionics* **2009**, *15* (2), 227.

(80) Brant, M. C.; Matencio, T.; Dessemond, L.; Domingues, R. Z. *Solid State Ionics* **2006**, *177* (9-10), 915.

(81) Sun, C.; Hui, R.; Roller, J. *J. Solid State Electrochem.* **2010**, *14* (7), 1125.

(82) *Ferroelectrics – Material Aspects*; Lallart, M., Ed.; InTech: Rijeka, 2011; pp 1–530.

(83) Jiang, S. P. *J. Mater. Sci.* **2008**, *43* (21), 6799.

(84) Vanroosmalen, J.; Cordfunke, E.; Helmholdt, R. B.; Zandbergen, H. W. *J. Solid State Chem.* **1994**, *110* (1), 100.

(85) Mitchell, J. F.; Argyriou, D. N.; Potter, C. D.; Hinks, D. G.; Jorgensen, J. D.; Bader, S. D. *Phys. Rev. B* **1996**, *54* (9), 6172.

(86) Alonso, J. A.; MartinezLope, M. J.; Casais, M. T.; MacManusDriscoll, J. L.; deSilva, P.; Cohen, L. F.; FernandezDiaz, M. T. *J. Mater. Chem.* **1997**, *7* (10), 2139.

(87) Tofield, B. C.; Scott, W. R. *J. Solid State Chem.* **1974**, *10* (3), 183.

(88) Yokokawa, H.; Horita, T.; Sakai, N.; Dokiya, M.; Kawada, T. *Solid State Ionics* **1996**, *86-8*, 1161.

(89) Tanasescu, S.; Totir, N. D.; Marchidan, D. I. *Electrochimica Acta* **1998**, *43* (12-13), 1675.

(90) Nowotny, J.; Rekas, M. *J. Am. Ceram. Soc.* **1998**, *81* (1), 67.

(91) Mizusaki, J.; Mori, N.; Takai, H.; Yonemura, Y.; Minamiue, H.; Tagawa, H.; Dokiya, M.; Inaba, H.; Naraya, K.; Sasamoto, T.; Hashimoto, T. *Solid State Ionics* **2000**, *129* (1-4), 163.

(92) Mizusaki, J.; Yonemura, Y.; Kamata, H.; Ohyama, K.; Mori, N.; Takai, H.; Tagawa, H.; Dokiya, M.; Naraya, K.; Sasamoto, T.; Inaba, H.; Hashimoto, T. *Solid State Ionics* **2000**, *132* (3-4), 167.

(93) Zheng, F.; Pederson, L. R. *J. Electrochem. Soc.* **1999**, *146* (8), 2810.

(94) Hammouche, A.; Schouler, E.; Henault, M. *Solid State Ionics* **1988**, *28*, 1205.

(95) Kuo, J. H.; Anderson, H. U.; Sparlin, D. M. *J. Solid State Chem.* **1990**, *87* (1), 55.

(96) Jiang, S. P. *Solid State Ionics* **2002**, *146* (1-2), 1.

(97) Tsipis, E. V.; Kharton, V. V. *J. Solid State Electrochem.* **2008**, *12* (11), 1367.

(98) Jiang, S. P. *J. Solid State Electrochem.* **2007**, *11* (1), 93.

(99) Siebert, E.; Hammouche, A.; Kleitz, M. *Electrochimica Acta* **1995**, *40* (11), 1741.

(100) Virkar, A. V.; Chen, J.; Tanner, C. W.; Kim, J. W. *Solid State Ionics* **2000**, *131* (1-2), 189.

(101) Juhl, M.; Primdahl, S.; Manon, C.; Mogensen, M. *J. Power Sources* **1996**, *61* (1-2), 173.

(102) Bae, J. M.; Steele, B. *Solid State Ionics* **1998**, *106* (3-4), 247.

(103) Oishi, N.; Atkinson, A.; Brandon, N. P.; Kilner, J. A.; Steele, B. *J. Am. Ceram. Soc.* **2005**, *88* (6), 1394.

(104) Dusastre, V.; Kilner, J. A. *Solid State Ionics* **1999**, *126* (1-2), 163.

(105) Martins, R. F.; Brant, M. C.; Domingues, R. Z.; Paniago, R. M.; Sapag,

K.; Matencio, T. *Materials Research Bulletin* **2009**, *44* (2), 451.

(106) Spacil, H. S. 1970.

(107) Matsuzaki, Y.; Yasuda, I. *Solid State Ionics* **2000**, *132* (3-4), 261.

(108) Zhu, W. Z.; Deevi, S. C. *Mater. Sci. Eng., A* **2003**, *362* (1-2), 228.

(109) Brandon, N. P.; Brett, D. J. *Phil. Trans. R. Soc. A* **2006**, *364* (1838), 147.

(110) Jiang, S. P.; Chan, S. H. *J. Mater. Sci.* **2004**, *39* (14), 4405.

(111) Holtappels, P.; Vinke, I. C.; de Haart, L.; Stimming, U. *J. Electrochem. Soc.* **1999**, *146* (8), 2976.

(112) Dees, D. W.; Claar, T. D.; Easler, T. E.; Fee, D. C.; Mrazek, F. C. *J. Electrochem. Soc.* **1987**, *134* (9), 2141.

(113) Iwata, T. *J. Electrochem. Soc.* **1996**, *143* (5), 1521.

(114) *Denki Kayaku*.

(115) Majumdar, S.; Claar, T.; Flandermeyer, B. *J. Am. Ceram. Soc.* **1986**, *69* (8), 628.

(116) Steele, B. *Solid State Ionics* **1996**, *86-8*, 1223.

(117) Toebes, M. L.; Bitter, J. H.; van Dillen, A. J.; de Jong, K. P. *Catalysis Today* **2002**, *76* (1), 33.

(118) Ruiz-Morales, J. C.; Canales-Vazquez, J.; Savaniu, C.; Marrero-Lopez, D.; Zhou, W. Z.; Irvine, J. *Nature* **2006**, *439* (7076), 568.

(119) Sun, C.; Li, H.; Chen, L. *Energy Environ. Sci.* **2012**, *5* (9), 8475.

(120) Schwarz, K. *Proc. Natl. Acad. Sci. U.S.A.* **2006**, *103* (10), 3497.

(121) Mobius, H. H.; Rohland, B. April 9, 1968.

(122) Ruloph, V. J.; Naturforsch, Z. **1959**, *14a*, 727.

(123) Blumenthal, R. N.; Panlener, R. J. *J. Phys. Chem. Solids* **1970**, *31* (5), 1190.

(124) Tuller, H. L.; Nowick, A. S. *J. Phys. Chem. Solids* **1977**, *38* (8), 859.

(125) Naik, I. K.; Tien, T. Y. *J. Phys. Chem. Solids* **1978**, *39* (3), 311.

(126) Bishop, S. R.; Stefanik, T. S.; Tuller, H. L. *Phys. Chem. Chem. Phys.* **2011**, *13* (21), 10165.

(127) McIntosh, S.; Gorte, R. J. *Chem. Rev* **2004**, *104* (10), 4845.

(128) Hauch, A.; Ebbesen, S. D.; Jensen, S. H.; Mogensen, M. *J. Mater. Chem.* **2008**, *18* (20), 2331.

(129) Donitz, W.; Erdle, E.; Streicher, R. *Electrochemical Hydrogen Technologies. Electrochemical Production and Combustion of Hydrogen*; Wendt, H., Ed.; Elsevier: Amsterdam, 1990; pp 215–259.

(130) Nath, K.; Das, D. *J. Sci. Ind. Res.* **2007**, *66* (9), 701.

(131) Ebbesen, S. D.; Jensen, S. H.; Hauch, A.; Mogensen, M. B. *Chem. Rev.* **2014**, *114* (21), 10697.

(132) Laguna-Bercero, M. A. *J. Power Sources* **2012**, *203*, 4.

(133) Koh, J.; Yoon, D.; Oh, C. H. *J. Nucl. Sci. Technol.* **2010**, *47* (7), 599.

(134) Ni, M.; Leung, M. K. H.; Leung, D. C. *Int. J. Hydrogen Energy* **2007**, *32* (18), 4648.

(135) Mitterdorfer, A.; Gauckler, L. *Solid State Ionics* **1999**.

(136) Mitterdorfer, A.; Gauckler, L. *Solid State Ionics* **1999**.

(137) Crumlin, E. J.; Mutoro, E.; Hong, W. T.; Biegalski, M. D.; Christen, H. M.; Liu, Z.; Bluhm, H.; Shao-Horn, Y. *J. Phys. Chem. C* **2013**, *117* (31),

16087.

(138) Ostergard, M. J. L.; Clausen, C.; Bagger, C.; Mogensen, M. *Electrochimica Acta* **1995**, *40* (12), 1971.

(139) Decorse, P. *Solid State Ionics* **1999**, *117* (1-2), 161.

(140) Li, Z.; Bosman, M.; Yang, Z.; Ren, P.; Wang, L.; Cao, L.; Yu, X.; Ke, C.; Breese, M. B. H.; Rusydi, A.; Zhu, W.; Dong, Z.; Foo, Y. L. *Adv. Funct. Mater.* **2012**, *22* (20), 4312.

(141) Lee, Y.-L.; Morgan, D. *ECS Trans.* **2009**, *25* (2), 2769.

(142) Fister, T. T.; Fong, D. D.; Eastman, J. A.; Baldo, P. M.; Highland, M. J.; Fuoss, P. H.; Balasubramaniam, K. R.; Meador, J. C.; Salvador, P. A. *Appl. Phys. Lett.* **2008**, *93* (15).

(143) Katsiev, K.; Yildiz, B.; Balasubramaniam, K.; Salvador, P. A. *Appl. Phys. Lett.* **2009**, *95* (9).

(144) Harrison, W. A. *Phys. Rev. B* **2011**, *83* (15).

(145) Jalili, H.; Han, J. W.; Kuru, Y.; Cai, Z.; Yildiz, B. *J. Phys. Chem. Lett.* **2011**, *2* (7), 801.

(146) Lee, W.; Han, J. W.; Chen, Y.; Cai, Z.; Yildiz, B. *J. Am. Chem. Soc* **2013**, *135* (21), 7909.

(147) vanHeuveln, F. H.; Bouwmeester, H. *J. Electrochem. Soc.* **1997**, *144* (1), 134.

(148) Chen, X. J.; Khor, K. A.; Chan, S. H. *Solid State Ionics* **2004**, *167* (3-4), 379.

(149) McEvoy, A. J. *Solid State Ionics* **2000**, *135* (1-4), 331.

(150) Jiang, S. P.; Love, J. G. *Solid State Ionics* **2003**, *158* (1-2), 45.

(151) Wang, W.; Jiang, S. P. *J. Solid State Electrochem.* **2004**, *8* (11), 914.

(152) Kuznecov, M.; Otschik, P.; Obenaus, P.; Eichler, K.; Schaffrath, W. *Solid State Ionics* **2003**, *157* (1-4), 371.

(153) Huber, A.-K.; Falk, M.; Rohnke, M.; Luerßen, B.; Amati, M.; Gregoratti, L.; Hesse, D.; Janek, J. *Journal of Catalysis* **2012**, *294*, 79.

(154) Backhaus-Ricoult, M.; Work, K.; Adib, K.; Gregoratti, L.; Amati, M. *ECS Trans.* **2014**, *61*, 3.

(155) Backhaus-Ricoult, M.; Adib, K.; Clair, T. S.; Luerssen, B.; Gregoratti, L.; Barinov, A. *Solid State Ionics* **2008**, *179* (21-26), 891.

(156) Jiang, S. P.; Wang, W. *Electrochem. Solid-State Lett.* **2005**, *8* (2), A115.

(157) van Heuveln, F. H. *J. Electrochem. Soc.* **1997**, *144* (1), 126.

(158) van Heuveln, F. H. *J. Electrochem. Soc.* **1997**, *144* (1), 134.

(159) Mizusaki, J.; Saito, T.; Tagawa, H. *J. Electrochem. Soc.* **1996**, *143* (10), 3065.

(160) Brichzin, V.; Fleig, J.; Habermeier, H. U.; Cristiani, G.; Maier, J. *Solid State Ionics* **2002**, *152*, 499.

(161) Siebert, E.; Hammouche, A.; Kleitz, M. *Electrochimica Acta* **1995**, *40* (11), 1741.

(162) Lauret, H.; Hammou, A. *J. Eur. Ceram. Soc.* **1996**, *16* (4), 447.

(163) Laguna-Bercero, M. A.; Kilner, J. A.; Skinner, S. J. *Solid State Ionics* **2011**, *192* (1), 501.

(164) Yang, C.; Coffin, A.; Chen, F. *Int. J. Hydrogen Energy* **2010**, *35* (8),

3221.

(165) Chen, K.; Ai, N.; Jiang, S. P. *J. Electrochem. Soc.* **2010**, *157* (11), P89.

(166) Ebbesen, S. D.; Mogensen, M. *J. Power Sources* **2009**, *193* (1), 349.

(167) Yang, C.; Jin, C.; Coffin, A.; Chen, F. *Int. J. Hydrogen Energy* **2010**, *35* (11), 5187.

(168) Eguchi, K.; Hatagishi, T.; Arai, H. *Solid State Ionics* **1996**, *86-8*, 1245.

(169) Marina, O. A.; Pederson, L. R.; Williams, M. C.; Coffey, G. W.; Meinhardt, K. D.; Nguyen, C. D.; Thomsen, E. C. *J. Electrochem. Soc.* **2007**, *154* (5), B452.

(170) Svensson, A. M.; Sunde, S.; Nisancioglu, K. *J. Electrochem. Soc.* **1998**, *145* (4), 1390.

(171) O'Brien, J. E.; Stoots, C. M.; Herring, J. S.; Lessing, P. A.; Hartvigsen, J. J.; Elangovan, S. *J. Fuel Cell Sci. Technol.* **2005**, *2* (3), 156.

(172) Jensen, S. H.; Larsen, P. H.; Mogensen, M. *Int. J. Hydrogen Energy* **2007**, *32* (15), 3253.

(173) Chen, K.; Liu, S.-S.; Ai, N.; Koyama, M.; Jiang, S. P. *Phys. Chem. Chem. Phys.* **2015**, *17*, 31308.

(174) Liang, M.; Yu, B.; Wen, M.; Chen, J.; Xu, J.; Zhai, Y. *J. Power Sources* **2009**, *190* (2), 341.

(175) Yildiz, B.; Myers, D. J.; Carter, D. J.; Chang, K.-C.; You, H. 2007; pp 1–12.

(176) Chen, K.; Jiang, S. P. *Int. J. Hydrogen Energy* **2011**, *36* (17), 10541.

(177) Virkar, A. V. *Int. J. Hydrogen Energy* **2010**, *35* (18), 9527.

(178) Keane, M.; Mahapatra, M. K.; Verma, A.; Singh, P. *Int. J. Hydrogen Energy* **2012**, *37* (22), 16776.

(179) Li, N.; Keane, M.; Mahapatra, M. K.; Singh, P. *Int. J. Hydrogen Energy* **2013**, *38* (15), 6298.

(180) Ladas, S.; Kennou, S.; Vayenas, C. G. *J. Phys. Chem* **1993**, *97* (35), 8845.

(181) Ogletree, D. F.; Bluhm, H.; Lebedev, G.; Fadley, C. S.; Hussain, Z.; Salmeron, M. *Rev. Sci. Instrum.* **2002**, *73* (11), 3872.

(182) Grass, M. E.; Karlsson, P. G.; Aksoy, F.; Lundqvist, M.; Wannberg, B.; Mun, B. S.; Hussain, Z.; Liu, Z. *Rev. Sci. Instrum.* **2010**, *81* (5), 053106.

(183) Crumlin, E. J.; Mutoro, E.; Liu, Z.; Grass, M. E.; Biegalski, M. D.; Lee, Y.-L.; Morgan, D.; Christen, H. M.; Bluhm, H.; Shao-Horn, Y. *Energy Environ. Sci.* **2012**, *5* (3), 6081.

(184) Chueh, W. C.; Mcdaniel, A. H.; Grass, M. E.; Hao, Y.; Jabeen, N.; Liu, Z.; Haile, S. M.; Mccarty, K. F.; Bluhm, H.; Gabaly, El, F. *Chem. Mater.* **2012**, *24* (10), 1876.

(185) Mueller, D. N.; Machala, M. L.; Bluhm, H.; Chueh, W. C. *Nat. Commun.* **2015**, *6*, 6097.

(186) *NIST Standard Reference Database 20, Version 4.1*, 4 ed.

(187) *NIST Standard Reference Database 20, Version 4.1 http://srdata.nist.gov/xps/Default.aspx*; 2013.

(188) Briggs, D.; Seah, M. P. *Practical Surface Analysis*, 2nd ed.; Wiley: New York, 1993; Vol. 1.

(189) Wagner, C. D.; Riggs, W. M.; Davis, L. E.; Moulder, J. F.; Muilenberg,

G. E. *Handbook of X-ray Photoelectron Spectroscopy*; Muilenberg, G. E., Ed.; Perkin-Elmer Corporation: Eden Prairie, 1979.

(190) Corcoran, C. J.; Tavassol, H.; Rigsby, M. A.; Bagus, P. S.; Wieckowski, A. *J. Power Sources* **2010**, *195* (24), 7856.

(191) Wagner, C. D. *Faraday Discuss. Chem. Soc.* **1975**, *60*, 291.

(192) Cerrato, J. M.; Hochella, M. F., Jr.; Knocke, W. R.; Dietrich, A. M.; Cromer, T. F. *Environ. Sci. Technol.* **2010**, *44* (15), 5881.

(193) Galakhov, V. R.; Demeter, M.; Bartkowski, S.; Neumann, M.; Ovechkina, N. A.; Kurmaev, E. Z.; Logachevskaya, N. I.; Mukovskii, Y. M.; Mitchell, J.; Ederer, D. L. *Phys. Rev. B* **2002**, *65* (11).

(194) Demeter, M.; Neumann, M.; Galakhov, V. R.; Oveckkina, N. A.; Kurmaev, E. Z.; Labachevskaya, N. I. *Acta Physica Polonica A* **2000**, *98* (5), 587.

(195) Shih, S.-J.; Sharghi-Moshtaghin, R.; De Guire, M. R.; Goettler, R.; Xing, Z.; Liu, Z.; Heuer, A. H. *J. Electrochem. Soc.* **2011**, *158* (10), B1276.

(196) Shirley, D. A. *Physica Scripta* **1975**, *11* (3-4), 117.

(197) Brabers, V. A. M.; van Setten, F. M.; Knapen, P. S. A. *J. Solid State Chem.* **1983**, *49* (1), 93.

(198) Sunding, M. F.; Hadidi, K.; Diplas, S.; Løvvik, O. M.; Norby, T. E.; Gunnæs, A. E. *J. Electron. Spectrosc. Relat. Phenom.* **2011**, *184* (7), 399.

(199) Spanjaard, D.; Guillot, C.; Desjonquères, M.-C.; Tréglia, G.; Lecante, J. *Surf. Sci. Rep* **1985**, *5* (1-2), 1.

(200) *https://als.lbl.gov/wp-content/uploads/2016/06/quick-facts.pdf*.

(201) *http://www.lbl.gov*.

(202) Crumlin, E. J.; Bluhm, H.; Liu, Z. *J. Electron. Spectrosc. Relat. Phenom.* **2013**, *190*, 84.

(203) Brena, B.; Siegbahn, P. E. M.; Ågren, H. *J. Am. Chem. Soc* **2012**, *134* (41), 17157.

(204) Hähner, G. *Chem. Soc. Rev.* **2006**, *35* (12), 1244.

(205) Hiraya, A.; Watanabe, M.; Sham, T. K. *Rev. Sci. Instrum.* **1995**, *66* (2), 1528.

(206) Frazer, B. H.; Gilbert, B.; Sonderegger, B. R.; De Stasio, G. *Surf. Sci.* **2003**, *537* (1-3), 161.

(207) May 4, 2008, pp 1–10.

(208) Patsalas, P.; Logothetidis, S.; Metaxa, C. *Appl. Phys. Lett.* **2002**, *81* (3), 466.

(209) Patsalas, P.; Logothetidis, S.; Sygellou, L.; Kennou, S. *Phys. Rev. B* **2003**.

(210) Jung, W.; Tuller, H. *Energy Environ. Sci.* **2012**.

(211) Chen, Y.; Jung, W.; Cai, Z.; Kim, J. J.; Tuller, H. L.; Yildiz, B. *Energy Environ. Sci.* **2012**, *5* (7), 7979.

(212) Mizusaki, J.; Saito, T.; Tagawa, H. *J. Electrochem. Soc.* **1996**, *143* (10), 3065.

(213) Jensen, S. H.; Larsen, P. H.; Mogensen, M. *Int. J. Hydrogen Energy* **2007**, *32* (15), 3253.

(214) Risch, M.; Stoerzinger, K. A.; Maruyama, S.; Hong, W. T.; Takeuchi, I.; Shao-Horn, Y. *J. Am. Chem. Soc* **2014**, *136* (14), 5229.

(215) Zhang, C.; Li, C.-J.; Zhang, G.; Ning, X.-J.; Li, C.-X.; Liao, H.; Coddet, C. *Materials Science and Engineering: B* **2007**, *137* (1-3), 24.

(216) Kurumada, M.; Hara, H.; Iguchi, E. *Acta Materialia* **2005**, *53* (18), 4839.

(217) Decorse, P.; Quenneville, E.; Poulin, S.; Meunier, M.; Yelon, A.; Morin, F. *J. Vac. Sci. Technol. A* **2001**, *19* (3), 910.

(218) Mullica, D. F.; Lok, C. K. C.; Perkins, H. O. *Phys. Rev. B* **1985**, *31*, 31.

(219) Nelson, A. J.; Reynolds, J. G.; Christou, G. *J. Appl. Phys.* **2003**, *93* (5), 2536.

(220) Cumpson, P. J. *Surf. Interface Anal.* **2000**, *29* (6), 403.

(221) Strohmeier, B. R. *Surf. Interface Anal.* **1990**, *15* (1), 51.

(222) Teterin, Y. A.; Teterin, A. Y.; Lebedev, A. M.; Ivanov, K. E. *J. Electron. Spectrosc. Relat. Phenom.* **2004**, *137-140*, 607.

(223) Cerrato, J. M.; Hochella, M. F., Jr.; Knocke, W. R.; Dietrich, A. M.; Cromer, T. F. *Environ. Sci. Technol.* **2010**, *44* (15), 5881.

(224) Wu, Q.-H.; Liu, M.; Jaegermann, W. *Mater. Lett.* **2005**, *59* (16), 1980.

(225) De Souza, R. A. *Phys. Chem. Chem. Phys.* **2006**, *8* (7), 890.

(226) Ishihara, T. *Solid State Ionics* **1998**, *113-115* (1-2), 593.

(227) Mazzaferro, J.; Balseiro, C. A.; Alascio, B. *J. Phys. Chem. Solids* **1985**, *46* (12), 1339.

(228) Huang, K.; Goodenough, J. B. *Solid Oxide Fuel Cell Technology: Principles, Performance and Operations*; Woodhead Publishing Limited: Cambridge, 2009.

(229) Huang, Y.-L.; Pellegrinelli, C.; Wachsman, E. D. *ACS Catal.* **2016**, *6* (9),

6025.

(230) Dulli, H.; Dowben, P. A.; Liou, S. H.; Plummer, E. W. *Phys. Rev. B* **2000**, *62* (22), R14629.

(231) Szot, K.; Speier, W.; Herion, J.; Freiburg, C. *Appl Phys A* **1996**, *64* (1), 55.

(232) Szot, K.; Speier, W. *Phys. Rev. B* **1999**, *60* (8), 5909.

(233) Liang, Y.; Bonnell, D. A. *Surf. Sci.* **1994**, *310* (1-3), 128.

(234) Jarry, A. *Figure Preparation*.

(235) Kuru, Y.; Marrocchelli, D.; Bishop, S. R.; Chen, D.; Yildiz, B.; Tuller, H. L. *J. Electrochem. Soc.* **2012**, *159* (11), F799.

(236) Kushima, A.; Yip, S.; Yildiz, B. *Phys. Rev. B* **2010**, *82* (11), 115435.

(237) Yeh, J. J.; Lindau, I. *At. Data Nucl. Data Tables* **1985**, *32* (1), 1.

(238) Powell, C. J. 1st ed. National Institute of Standards and Technology: Gaithersburg.

(239) Sun, X.; Chen, M.; Liu, Y. L.; Hjalmarsson, P.; Ebbesen, S. D.; Jensen, S. H.; Mogensen, M. B.; Hendriksen, P. V. *J. Electrochem. Soc.* **2013**, *160* (9), F1074.

(240) Ertl, G.; Knozinger, H.; Schuth, F.; Weitkamp, J. *Handbook of Heterogeneous Catlysis*; Ertl, G., Knozinger, H., Eds.; Wiley-VCH: Weinheim, 2008.

(241) Uchida, H.; Osada, N.; Watanabe, M. *Electrochem. Solid-State Lett.* **2004**, *7* (12), A500.

(242) Brisse, A.; Schefold, J.; Zahid, M. *Int. J. Hydrogen Energy* **2008**, *33* (20),

5375.

(243) Chauveau, F.; Mougin, J.; Bassat, J. M.; Mauvy, F.; Grenier, J. C. *J. Power Sources* **2010**, *195* (3), 744.

(244) Ferrero, D.; Lanzini, A.; Leone, P.; Santarelli, M. *Chemical Engineering Journal* **2015**, *274* (C), 143.

(245) Ni, M.; Leung, M. K. H.; Y C Leung, D. *J. Power Sources* **2006**, *163* (1), 460.

(246) Ni, M.; Leung, M. K. H.; Leung, D. Y. *J. Power Sources* **2008**, *177* (2), 369.

(247) Jin, X.; Xue, X. *J. Power Sources* **2010**, *195* (19), 6652.

(248) Kazempoor, P.; Braun, R. J. *Int. J. Hydrogen Energy* **2014**, *39* (11), 5955.

(249) Huang, Y.-L.; Pellegrinelli, C.; Geller, A.; Liou, S.-C.; Jarry, A.; Wang, L.; Yu, Y.; Bluhm, H.; Crumlin, E. J.; Eichhorn, B. W.; Wachsman, E. D. *Submitted*.

(250) Tsai, T.; Barnett, S. A. *Solid State Ionics* **1997**, *93* (3-4), 207.

(251) Murray, E. P.; Tsai, T.; Barnett, S. A. *Solid State Ionics* **1998**, *110* (3-4), 235.

(252) Kenjo, T.; Nishiya, M. *Solid State Ionics* **1992**, *57* (3-4), 295.

(253) Jorgensen, M. J.; Mogensen, M. *J. Electrochem. Soc.* **2001**, *148* (5), A433.

(254) Ostergard, M.; Clausen, C.; Bagger, C.; Mogensen, M. *Electrochimica Acta* **1995**, *40* (12), 1971.

(255) Wang, S. Z.; Jiang, Y.; Zhang, Y. H.; Yan, J. W.; Li, W. Z. *Solid State*

Ionics **1998**, *113* (1-2), 291.

(256) Stoerzinger, K. A.; Risch, M.; Suntivich, J.; Lue, W. M.; Zhou, J.; Biegalski, M. D.; Christen, H. M.; Ariando; Venkatesan, T.; Shao-Horn, Y. *Energy Environ. Sci.* **2013**, *6* (5), 1582.

(257) Kirtley, J. D.; Halat, D. M.; McIntyre, M. D.; Eigenbrodt, B. C.; Walker, R. A. *Anal. Chem.* **2012**, *84* (22), 9745.

(258) Pomfret, M. B.; Owrutsky, J. C.; Walker, R. A. *J. Phys. Chem. B* **2006**, *110* (35), 17305.

(259) Sum, O.; Djurado, E.; Pagnier, T.; Rosman, N.; Roux, C. *Solid State Ionics* **2005**, *176* (35-36), 2599.

(260) Li, X.; Lee, J.-P.; Blinn, K. S.; Chen, D.; Yoo, S.; Bin Kang; Bottomley, L. A.; El-Sayed, M. A.; Park, S.; Liu, M. *Energy Environ. Sci.* **2014**, *7* (1), 306.

(261) Brightman, E.; Maher, R.; Offer, G. J.; Duboviks, V.; Heck, C.; Cohen, L. F.; Brandon, N. P. *Rev. Sci. Instrum.* **2012**, *83* (5), 053707.

(262) Kirtley, J.; Singh, A.; Halat, D.; Oswell, T.; Hill, J. M.; Walker, R. A. *J. Phys. Chem. C* **2013**, *117* (49), 25908.

(263) Maher, R. C.; Cohen, L. F.; Lohsoontorn, P.; Brett, D. J. L.; Brandon, N. P. *J. Phys. Chem. A* **2008**, *112* (7), 1497.

(264) Laachir, A.; Perrichon, V.; Badri, A.; Lamotte, J.; Catherine, E.; Lavalley, J. C.; Fallah, El, J. F.; Hilaire, L.; Le Normand, F. L.; Qu m r, E.; Sauvion, G. N. L.; Touret, O. *Faraday Trans.* **1991**, *87* (10), 1601.

(265) Binet, C.; Badri, A.; Lavalley, J. C. *J. Phys. Chem* **1994**, *98*, 6392.

(266) Pomfret, M. B.; Walker, R. A.; Owrutsky, J. C. *J. Phys. Chem. Lett.* **2012**, *3*, 3053.

(267) Bergman, T. L.; Lavine, A. S.; Incropera, F. P.; DeWitt, D. P. *Fundamentals of Heat and Mass Transfer*, 3rd ed.; Wiley, 1990.

(268) Balakrishnan, G.; Sundari, S. T.; Kuppusami, P.; Mohan, P. C.; Srinivasan, M. P.; Mohandas, E.; Ganesan, V.; Sastikumar, D. *Thin Solid Films* **2011**, *519* (8), 2520.

(269) Hueso, J. L.; Holgado, J. P.; Pereñíguez, R.; Mun, S.; Salmeron, M.; Caballero, A. *J. Solid State Chem.* **2009**, *183* (1), 27.

(270) Orikasa, Y.; Ina, T.; Nakao, T.; Mineshige, A.; Amezawa, K.; Oishi, M.; Arai, H.; Ogumi, Z.; Uchimoto, Y. *J. Phys. Chem. C* **2011**, *115* (33), 16433.

(271) Hsieh, Y.-H.; Kuo, H.-H.; Liao, S.-C.; Liu, H.-J.; Chen, Y.-J.; Lin, H.-J.; Chen, C.-T.; Lai, C.-H.; Zhan, Q.; Chueh, Y.-L.; Chu, Y.-H. *Nanoscale* **2013**, *5* (14), 6219.

(272) Gautam, S.; Thakur, P.; Bazylewski, P.; Bauer, R.; Singh, A. P.; Kim, J. Y.; Subramanian, M.; Jayavel, R.; Asokan, K.; Chae, K. H.; Chang, G. S. *Mater. Chem. Phys.* **2013**, *140* (1), 130.

(273) Chou, T.-L.; Chan, T.-S.; Chen, J.-M.; Yamauchi, H.; Karppinen, M. *J. Solid State Chem.* **2013**, *202*, 27.

(274) Lin, S. S. Y.; Do Heui Kim; Engelhard, M. H.; Ha, S. Y. *Journal of Catalysis* **2010**, *273* (2), 229.

(275) Ovari, L.; Calderon, S. K.; Lykhach, Y.; Libuda, J.; Erdőhelyi, A.; Papp,

C.; Kiss, J.; Steinrück, H. P. *Journal of Catalysis* **2013**, *307* (C), 132.

(276) McIntyre, N. S.; Cook, M. G. *Anal. Chem.* **1975**, *47*, 2208.

(277) Chen, Y.; Zhao, S.; Liu, Z. *Phys. Chem. Chem. Phys.* **2015**, *17*, 14012.

(278) Petitto, S. C.; Marsh, E. M.; Carson, G. A.; Langell, M. A. *J. Mol. Catal. A: Chem.* **2008**, *281* (1-2), 49.

(279) Ivanova, T.; Naumkin, A.; Sidorov, A.; Eremenko, I.; Kiskin, M. *J. Electron. Spectrosc. Relat. Phenom.* **2007**, *156-158*, 200.

(280) Van der Heide, P. A. W. *J. Electron. Spectrosc. Relat. Phenom.* **2008**, *164* (1-3), 8.

(281) Biesinger, M. C.; Payne, B. P.; Grosvenor, A. P.; Lau, L. W. M.; Gerson, A. R.; Smart, R. S. C. *Appl. Surf. Sci.* **2011**, *257* (7), 2717.

(282) Van Campen, D. G.; Klebanoff, L. E. *Phys. Rev. B* **1994**, *49*, 2040.

(283) Zhao, J.; Jones, C. M.; Poirier, D. M. *J. Vac. Sci. Technol. B* **1999**, *17* (6), 2570.

(284) Wagner, C. D.; Gale, L. H.; Raymond, R. H. *Anal. Chem.* **1979**, *51* (4), 466.

(285) Biesinger, M. C.; Lau, L. W. M.; Gerson, A. R.; Smart, R. S. C. *Phys. Chem. Chem. Phys.* **2012**, *14* (7), 2434.

(286) Hsieh, Y.-H.; Kuo, H.-H.; Liao, S.-C.; Liu, H.-J.; Chen, Y.-J.; Lin, H.-J.; Chen, C.-T.; Lai, C.-H.; Zhan, Q.; Chueh, Y.-L.; Chu, Y.-H. *Nanoscale* **2013**, *5* (14), 6219.

(287) Li, W.; Li, J.; Guo, J. *Intermetallics* **2003**, *23*, 2289.

(288) Tristan, N.; Hemberger, J.; Krimmel, A.; Krug von Nidda, H.-A.;

Tsurkan, V.; Loidl, A. *Phys. Rev. B* **2005**, *72* (17), 174404.

(289) Lei, S.; Liu, L.; Wang, C.; Shen, X.; Wang, C.; Guo, D.; Zeng, S.; Cheng, B.; Xiao, Y.; Zhou, L. *CrystEngComm* **2014**, *16* (2), 277.

(290) Marco, J. F.; Gancedo, J. R.; Gracia, M.; Gautier, J. L.; Ríos, E.; Berry, F. J. *J. Solid State Chem.* **2000**, *153* (1), 74.

(291) Jasaitis, D.; Beganskiene, A.; Senvaitiene, J.; Kareiva, A.; Ramanauskas, R.; Juskenas, R.; Selskis, A. *Chemija* **2011**, *22*, 125.

(292) Klissurski, D. G.; Uzunova, E. L. *Chem. Mater.* **1991**, *3*, 1060.

(293) Montoro, L. A.; Abbate, M.; Almeida, E. C.; Rosolen, J. M. *Chem. Phys. Lett* **1999**, *309*, 14.

(294) Momma, A.; Kato, T.; Kaga, Y.; Nagata, S. *Journal of the Ceramic Society of Japan* **1997**, *105* (5), 369.

(295) Graves, C.; Ebbesen, S.; Mogensen, M. ... *and Sustainable Energy* ... **2011**.

(296) Xu, Y.; Wen, Y.; Zhu, Y.; Gaskell, K.; Cychosz, K. A.; Eichhorn, B.; Xu, K.; Wang, C. *Adv. Funct. Mater.* **2015**, *25* (27), 4312.